

Exploring and Constraining New Physics in the Dark Sector

by

Francis-Yan Cyr-Racine

B.Sc., McGill University, 2005

M.Sc., McGill University, 2008

A THESIS SUBMITTED IN PARTIAL FULFILLMENT OF
THE REQUIREMENTS FOR THE DEGREE OF

DOCTOR OF PHILOSOPHY

in

The Faculty of Graduate Studies

(Physics)

THE UNIVERSITY OF BRITISH COLUMBIA

(Vancouver)

October 2012

© Francis-Yan Cyr-Racine 2012

Abstract

The standard cosmological model that has emerged in the last decades describes an acceleratingly expanding universe where the familiar baryonic matter accounts for a very small fraction of the overall energy budget. The vast majority of the energy content of the Universe appears to belong to an elusive dark sector made up of dark matter and dark energy. In this thesis, we explore the cosmological consequences of new physics that could govern this unknown dark sector.

We first consider a model where dark matter can annihilate to Standard-Model particles through a Breit-Wigner resonance. We show in this case that the energy released by dark matter annihilating in the first proto-halos is likely substantial. We determine that the bounds on the allowed energy injection into the primordial gas and the energy density of the diffuse gamma-ray background strongly constrain the magnitude of the resonantly-enhanced annihilation cross section.

We then perform a thorough analysis of a dark sector made of atom-like bound states. This so-called Atomic Dark-Matter model predicts novel dark-matter properties on small scales but retains the success of cold dark matter on cosmological scales. We revisit the atomic physics necessary to capture the thermal history of the dark atoms and discuss the required improvements over the hydrogen calculation. To solve the perturbation equations, we develop a second-order tight-coupling approximation and further discuss its implications for the baryon-photon case. We compute the matter power spectrum in this model and show that it displays strong dark-matter acoustic oscillations and a cutoff on small scales. Interestingly, we also identify key cosmic microwave background signatures that distinguish the atomic dark matter scenario from other dark matter theories. We determine that

Abstract

astrophysical constraints on this model generally favour dark atoms that are both more massive and have higher binding energies than standard atomic hydrogen.

We finally consider how oscillations in the bispectrum of primordial fluctuations affects the clustering of dark-matter halos. We discover that features in the inflaton potential such as oscillations and bumps become imprinted in the mass dependence of the non-Gaussian halo bias. This finding opens the possibility of characterizing the inflationary potential with large-scale-structure surveys.

Preface

This thesis is partly based on three published papers and on a fourth manuscript that is close to submission.

A version of chapter 2 has been published. I performed all the calculations and analyses, made the plots and drafted the manuscript. Professor Profumo provided the branching ratios for the different annihilation channels. Professor Sigurdson performed a cross-check of our results with a more detailed Press-Schechter analysis, and provided guidance and comments on the manuscript. Sigurdson and I performed the final editing of the manuscript.

A version of chapter 3 has been published. All calculations, analyses and plots were made by me. I drafted the original manuscript. Professor Sigurdson provided guidance and comments on the manuscript.

I led the study of dark atoms presented in chapters 4 and 5. I performed all the analytical calculation, did the required analyses, produced all the figures and wrote the manuscript. A preliminary version of the Boltzmann code used in chapters 4 and 5 was provided by Dr. Antony Lewis. I heavily edited this code. The dark-recombination code used to produce some of the plots is based on a code initially written by Professor Douglas Scott. Again, this code was heavily edited to suit our needs. The differential equations were solved numerically with a stiff solver provided by Dr. Jens Chluba. The recombination coefficients were computed using a code provided by Dr. Yacine Ali-Haïmoud.

A version of chapter 6 has been published. I carried out all calculations and produced all the plots. I wrote the initial draft of the manuscript. Dr. Schmidt included one paragraph in the introduction and added a section in the conclusion. Schmidt and I performed the final editing of the manuscript.

Journal Papers

1. F.-Y. Cyr-Racine, S. Profumo, and K. Sigurdson, “Protohalo Constraints to the Resonant Annihilation of Dark Matter,” *Phys.Rev.*, vol. D80, p. 081302, 2009.
2. F.-Y. Cyr-Racine and K. Sigurdson, “Photons and Baryons before Atoms: Improving the Tight-Coupling Approximation,” *Phys.Rev.*, vol. D83, p. 103521, 2011.
3. F.-Y. Cyr-Racine and F. Schmidt, “Oscillating Bispectra and Galaxy Clustering: A Novel Probe of Inflationary Physics with Large-Scale Structure,” *Phys.Rev.*, vol. D84, p. 083505, 2011.

Table of Contents

Abstract	ii
Preface	iv
Table of Contents	vi
List of Tables	x
List of Figures	xi
List of Abbreviations	xv
Acknowledgements	xvi
Dedication	xviii
1 Introduction	1
1.1 The Standard Cosmological Model	3
1.2 Inflation	5
1.3 Dark Matter	8
1.3.1 Possible Small-Scale Dark-Matter Anomalies	9
1.3.2 Relic Abundance	11
1.3.3 Kinetic and Thermal Decoupling	12
1.3.4 Direct-Detection	13
1.3.5 Indirect-Detection	14
1.4 Cosmological Observables	16
1.4.1 Cosmic Microwave Background	16
1.4.2 Matter Power Spectrum	23
1.4.3 Halo Clustering and Bias	25
1.5 Structure of the Thesis	27
1.5.1 Protohalo Constraints to the Resonant Annihilation of Dark Matter	28

Table of Contents

1.5.2	Photons and Baryons before Atoms: Improving the Tight-Coupling Approximation	28
1.5.3	The Theory of Atomic Dark Matter	29
1.5.4	Oscillating Bispectra and Galaxy Clustering	30
2	Protohalo Constraints to the Resonant Annihilation of Dark Matter	32
2.1	Introduction	32
2.2	Breit-Wigner Resonance	33
2.3	Annihilation in Protohalos	35
2.4	Constraints from the Diffuse Background	36
2.5	Constraints on Energy Injection into Primordial Gas	38
2.6	Discussion	39
2.7	Summary	43
3	Photons and Baryons before Atoms: Improving the Tight-Coupling Approximation	44
3.1	Introduction	44
3.2	Solution to the Exact Equations	45
3.2.1	Initial Conditions	46
3.2.2	Convergence of the Stiff Integration	47
3.3	Second-Order Scheme	48
3.3.1	Photon-Baryon Slip	50
3.3.2	Photon Quadrupole Moment	51
3.3.3	Computational Procedure	52
3.3.4	Accuracy of the Second-Order Scheme	53
3.4	Bias on Cosmological Parameters	56
3.5	Reducing the Computational Runtime	58
3.6	Discussion and Conclusion	60
4	The Theory of Atomic Dark Matter I: Thermal History and Evolution of Fluctuations	62
4.1	Introduction	62
4.2	The Model	65
4.3	Thermal History	66
4.3.1	BBN Limit on Dark-Sector Temperature	67
4.3.2	Dark Recombination	70
4.3.3	Thermal Decoupling of Atomic Dark Matter	75
4.3.4	Joint-Evolution of DM Temperature and Ionization Fraction	83

Table of Contents

4.3.5	Existence of Dark Atoms	89
4.4	Evolution of Dark-Matter Perturbations	91
4.4.1	Perturbation Equations	91
4.4.2	Dark Opacity and Kinetic Decoupling	93
4.4.3	Regimes of the Dark Plasma	96
4.4.4	Numerical Solutions	102
4.4.5	Real-Space Evolution: DAO Scale	104
5	The Theory of Atomic Dark Matter II: Cosmological and Astrophysical Implications	109
5.1	Cosmological Implications	109
5.1.1	Matter Power Spectrum	111
5.1.2	Cosmic Microwave Background	117
5.2	Astrophysical Constraints on Atomic Dark Matter	129
5.2.1	Ellipticity of DM Halos	130
5.2.2	Cooling of DM Halos	140
5.3	Direct Detection	141
5.4	Discussion	143
6	Oscillating Bispectra and Galaxy Clustering: A Novel Probe of Inflationary Physics with Large-Scale Structure	147
6.1	Introduction	147
6.2	Non-Gaussian Halo Bias in the Peak-Background Split Formalism	150
6.2.1	Nonlocal Kernel	150
6.2.2	Halo Bias in Peak-Background Split	151
6.3	Oscillatory Bispectra and their Scale-dependent Bias	154
6.3.1	Resonant Non-Gaussianity	154
6.3.2	Features in the Inflaton Potential	158
6.4	Discussion	165
6.5	Conclusion	167
7	Conclusions	170
	Bibliography	174
 Appendices		
A	Second-Order Tight-Coupling Appendices	197
A.1	Perturbation Equations	197

Table of Contents

A.2	Initial Conditions	198
A.3	Tight-Coupling Approximation to Second Order in τ_c	201
B	Atomic Dark-Matter Appendices	202
B.1	Relations between Dark Parameters	202
B.2	Effective Number of Relativistic Degrees of Freedom	202
B.3	Thermal Rates	203
	B.3.1 Photo-Ionization Heating Rate	203
	B.3.2 Photo-Recombination Cooling Rate	204
	B.3.3 Free-Free Cooling and Heating	205
	B.3.4 Rayleigh Heating	207
B.4	Atomic Cross-Sections	208
	B.4.1 H-H Cross-Section	208
	B.4.2 H-p and H-e Cross-Sections	213

List of Tables

3.1	χ^2 values between fiducial Planck data and theoretical spectra obtained with the first- and second-order codes for different accuracy boost.	57
3.2	Biases of the 6-parameter Λ CDM model in unit of the standard deviation.	58

List of Figures

1.1	The CMB temperature angular power spectrum	22
1.2	The matter power spectrum for the Λ CDM paradigm.	24
2.1	The functional form of the resonance function $f(\gamma, \delta, x)$	35
2.2	Fraction of the initial energy that is converted to photons and electron-induced photons.	39
2.3	The enhancement factor of σ_0 for an unphysical and a physical pole.	40
2.4	Upper bound on $\sigma_0 B_{35}$ for both leptonic and hadronic annihilation of dark matter.	42
3.1	Fractional change in C_l^{TT} and C_l^{EE} versus multipole moments as the relative tolerance of the stiff integrator is varied.	48
3.2	Fractional change in C_l^{TT} and C_l^{EE} versus multipole moments as the three CAMB accuracy boost factors are increased.	49
3.3	Fractional difference of C_l^{TT} between the usual first-order tight-coupling approximation and the benchmark integration, and between the second-order approximation and the benchmark integration (default accuracy).	54
3.4	Fractional difference of C_l^{TT} between the usual first-order tight-coupling approximation and the benchmark integration and the second-order approximation and the benchmark integration (accuracy factor 5).	55
3.5	Marginalized posterior probability distribution for the vanilla Λ CDM model.	60
3.6	Residuals between the photon perturbation computed using the exact equations and the solutions obtained with the first- and second-order tight-coupling approximation.	61
4.1	Effective number of DS relativistic degrees of freedom at the time of nucleosynthesis as a function of α_D and B_D	68

List of Figures

4.2	Joint BBN constraints on the present-day DS temperature and on the effective number of DS relativistic degrees of freedom at the time of nucleosynthesis.	70
4.3	Comparison between recombination rates.	76
4.4	Comparison between the rates of different energy-exchange mechanism.	80
4.5	Comparison between the rates of different energy-exchange mechanism.	81
4.6	Comparison between our improved treatment of dark recombination and the standard treatment for a strongly-coupled model.	86
4.7	Comparison between our improved treatment of dark recombination and the standard treatment for a Compton-heating-dominated dark sector.	87
4.8	Comparison between our improved treatment of dark recombination and the standard treatment for a weakly-coupled dark sector.	88
4.9	Late-time ionized fraction as a function of m_D and α_D for a dark-atom model with $B_D = 10$ keV.	90
4.10	Redshift evolution of an atomic DM fluctuation with $k = 70$ Mpc^{-1} in synchronous gauge.	101
4.11	Redshift evolution of an atomic DM fluctuation with $k = 70$ Mpc^{-1} in synchronous gauge.	102
4.12	Redshift evolution of an initially Gaussian-shaped density fluctuation in configuration space.	106
4.13	Redshift evolution of an initially Gaussian-shaped density fluctuation in configuration space.	107
4.14	Late-time redshift evolution of an initially Gaussian-shaped density fluctuation in configuration space.	108
5.1	Total linear matter power spectrum at $z = 0$ for two atomic DM models.	112
5.2	Total linear matter power spectrum at $z = 0$ for an atomic DM model.	113
5.3	Linear matter correlation function.	115
5.4	Dimensionless linear matter power spectrum at $z = 0$ for a single dark-atom model for different values of ξ	118
5.5	Comparison between the CMB temperature angular power spectrum of atomic DM and that of a Λ CDM model with an equivalent number of extra neutrinos.	120

List of Figures

5.6	Comparison between the CMB polarization angular power spectrum of atomic DM and that of a Λ CDM model with an equivalent number of extra neutrinos.	121
5.7	Illustration of the constant phase shift between an atomic DM model and a Λ CDM model containing an equivalent number of relativistic species.	123
5.8	CMB angular power spectra in the atomic DM scenario for different values of ξ	126
5.9	CMB temperature power spectra in the atomic DM scenario for different values of ξ	128
5.10	Halo-ellipticity and Ly- α forest constraints on the parameter space of atomic DM.	136
5.11	Halo ellipticity and Ly- α forest constraints on the parameter space of atomic DM.	137
5.12	Halo ellipticity and Ly- α forest constraints on the parameter space of atomic DM.	138
6.1	Non-Gaussian correction to the halo bias for the resonant non-Gaussianity model as a function of scale.	156
6.2	Non-Gaussian spectral moment σ_W^2 for the resonant model as a function of halo mass.	157
6.3	Non-Gaussian correction to the halo bias for the resonant non-Gaussianity model as a function of halo mass.	158
6.4	Absolute value of the non-Gaussian spectral moment σ_W^2 for the feature model as a function of halo mass.	161
6.5	The two contributions to the non-Gaussian halo bias correction as a function of mass for the model with a feature at $k_f = 0.5h\text{Mpc}^{-1}$	162
6.6	Mass-dependence of the non-Gaussian correction to the halo bias for the model with a feature in the inflaton potential. . .	163
6.7	Scale-dependence of the non-Gaussian correction to the halo bias for the model with a feature in the inflaton potential. . .	164
6.8	Comparison between $\Delta b_1(M)$ obtained with a spherical tophat filter and with a Gaussian filter.	168
B.1	Universal dimensionless fitting functions for the photo-ionization heating rate.	204
B.2	Universal dimensionless fitting function for the photo-recombination cooling rate.	205

List of Figures

B.3	Momentum-transfer cross-section for hydrogen and positronium self-scattering.	212
B.4	Momentum-transfer cross-section for electron-hydrogen scattering obtained from direct computation, from rescaling the proton-hydrogen cross-section, and from rescaling the electron-positronium cross-section.	215

List of Abbreviations

ATIC	Advanced Thin Ionization Calorimeter
BAO	Baryon Acoustic Oscillation
BBN	Big-Bang Nucleosynthesis
CAMB	Code for Anisotropies in the Microwave Background
CDM	Cold Dark Matter
CMB	Cosmic Microwave Background
COBE	Cosmic Background Explorer
CosmoMC	Cosmological Monte Carlo
DAO	Dark Acoustic Oscillation
DM	Dark Matter
DR	Dark Radiation
DS	Dark Sector
dSph	Dwarf Spheroidal
LAT	Large Area Telescope
PAMELA	Payload for Antimatter Matter Exploration and Light-nuclei Astrophysics
PPB-BETS	Polar Patrol Balloon - Balloon-borne Electron Telescope with Scintillating fibers
SM	Standard Model
SPT	South Pole Telescope
WIMP	Weakly Interacting Massive Particle
WMAP	Wilkinson Microwave Anisotropy Probe

Acknowledgements

There are a few people without whom I would not be writing this thesis today. First, thanks to Christian Guay-Poliquin for convincing me that day in a math class 13 years ago that I should go to university and “get a Ph.D.”. Well, here I am! I would most likely not be studying physics today without the devotion of CEGEP teacher Martin Charest. Thanks Martin for those amazing lectures on electromagnetism and for the countless evenings spent in your office or in coffee shops talking about physics. I must thank Robert Brandenberger for triggering my interest in theoretical cosmology and for patiently answering all my questions at every possible hour of day and night.

In my early days as an undergraduate student, many professors at McGill University encouraged me to surpass myself and have ambitious goals. I especially want to thank Charles Gale, Sangyong Jeon, Charles Roth, Jim Cline, and Robert Rutledge for their continued encouragement.

I would like to thank my fellow officemates during my early graduate years at McGill. Thanks to Jean, Nima, Andrew, Aaron, Anke, Paul, and Jamie for thought-provoking discussions, for our year-long game of Diplomacy, for all these beer nights at Thomson House, and for teaching me everything I know about string theory! You guys were the best officemates I will ever have! I also wish to thank Guy Moore for his inspiring lectures on quantum field theory and for always welcoming me into his office (did you get any research done that year?). Of course, I would not be here today without the devotion and continuous support of my masters thesis advisor Robert Brandenberger.

My largest thanks goes to my advisor Kris Sigurdson for his advice, encouragement and for believing in my potential. He instilled a healthy dose of criticisms in my work and his comments on my research were always correct and useful. I admire his dedication that often went way beyond the usual call of duty. It was a true honor to be his first Ph.D. student.

I wish to thank the collaborators that have made possible some of the research presented in this thesis. Thanks to Yacine Ali-Haïmoud, Jens Chluba, Antony Lewis, Adam Moss, Stefano Profumo, and Fabian Schmidt. I also wish to thank the OMEGA collaboration for welcoming me as one of their

Acknowledgements

own, especially Leonidas Moustakas, Chuck Keeton, Ross Fadely, Annika Peter and Gregory Dobler. I thank my Ph.D. committee for useful comments on my work. I also thank the members of the particle-cosmology group here at UBC.

I dearly thank my muse and inspiration Diana for all her love and encouragement. Thanks for accompanying me through this journey and keeping me afloat in hard times. Life would be so different without you.

Thank to all my friends in Vancouver for their support and diversions over the last four years: Thomas Busigny, Jakob and Carmen Emmel, Michael McCormick, Jaya Viswanathan, Christophe Corbel, Katherin Brenker, Valeria Castellanos, Pierre, and Elsa. I would like to thank Mike, Valeria and Federico Urban for accompanying me to all those heavy metal concerts. Thanks to Mert Celikin, Agnieszka Barszcz and Cédric Migliorini for their friendship and support, despite the long distance separating us.

I especially thank my bandmates Dan Mazur, Liam Huber and Ludovic Van Waerbeke for helping me stay sane during my years as a Ph.D. student. Thanks for rocking out with me every week and putting up with my love for heavy music and my humongous drumkit! Keep rocking when I leave!

I thank my parents and my sister for encouraging me to pursue the academic route. Thank you for understanding and putting up with my constant absence. I miss you dearly.

I acknowledge the generous support of the National Science and Engineering Research Council (NSERC) of Canada through the Canada Graduate Scholarship program and the Michael Smith Foreign Study Supplement program. I also acknowledge the financial support from the Four-Year Fellowship program at UBC. I also wish to thank the California Institute of Technology where some of the work presented in this thesis was completed. Infrastructure funded by the Canada Foundation for Innovation (CFI) Leaders Opportunity Fund was essential to completing this thesis.

À Thomas, en souvenir de tous les bons moments passés ensemble.

Chapter 1

Introduction

We live in a dark Universe. It should come as a humbling fact for humanity that despite centuries of scientific advances, mankind only understands about five percent of the content of the Universe. While we do not yet fully comprehend these dark constituents, astronomers do see light being bent by vast amounts of unobservable matter, they notice galaxies rotating faster than they should simply based on their visible mass, and they observe far-away objects receding from us at an accelerating pace. The elegant names “dark matter” and “dark energy” invented to catalogue these phenomena are merely bookkeeping devices parametrizing our ignorance. Yet, the dark sector plays a vital role in the evolution of the Universe. In the absence of dark matter, galaxy formation would be implausible, altering dramatically the possible development of intelligent life. Therefore, understanding the nature of dark matter is intrinsically linked to lifting the mystery of our own origins and of the structure around us. As a data-driven theoretical cosmologist, my research is focused on shedding light on this conundrum.

A large part of this thesis focuses on exploring and constraining possible new physics that could govern this unknown “Dark Sector” (DS) of the Universe. In this work, the cosmic DS encompasses all the new (non-baryonic) particles and fields that are necessary to describe cosmological and astrophysical observations. In particular, it comprises all the physics controlling the elusive dark-matter (DM) sector. Current cosmological observations point to a DM sector that is cold, collisionless and which seems to be interacting with the Standard Model (SM) particles only through the gravitational force. A key question for cosmologists is to quantify how much departure from this simple cold-dark-matter (CDM) picture is allowed by the current data.

The core of this thesis is dedicated to the study of two different DM scenarios incorporating new physics beyond the plain CDM paradigm. We first present a short study (Chapter 2) of a DM model capable of annihilating through a resonance. We then carry out in chapters 4 and 5 an in-depth analysis of a scenario in which DM is made of atom-like bound states. This atomic DM model constitutes a very general testbed for studying physics beyond CDM since it can describe a plethora of possible DS phenomena using a minimal set of ingredients. At the preliminary stage of this work, it became clear that some of our early results concerning an approximation used to solve the perturbed Boltzmann equations could be of interest to the broader cosmological science community. We thus published those results separately and we also present them here as an independent chapter (see chapter 3).

While studying the *fundamental nature* of DM is an eminent research question in itself, we can also learn a substantial amount of information about the primeval Universe by examining how DM is *distributed* across the cosmos today. Indeed, the very rich cosmological and astrophysical structures currently populating the Universe were seeded in the very first moments of its existence by quantum processes in an epoch called inflation¹. By carefully studying the statistics of how objects are distributed across the cosmos, one can hope to extract useful information about the physics governing the primordial inflationary epoch. This thesis addresses this important issue in chapter 6 by considering how the clustering of DM halos is affected when the bispectrum of primeval fluctuations oscillates with scale.

Put concisely, the science goal of this thesis is to explore new physics in the DS to unveil its potential tell-tale signatures in key cosmological observables such as the CMB, the matter power spectrum and the scale-dependent halo bias. This research is particularly relevant today since there are so many DM or inflation models on the market that it is difficult to separate the wheat from the chaff. Studying economical models that predict *new* observable phenomena (such as atomic DM) is essential to advance our

¹While inflation is by far the most discussed paradigm of the very early Universe, there are competing theories such as the Ekpyrotic scenario and the Pre-Big-Bang Models.

knowledge of cosmology.

We begin this thesis by reviewing the Standard Cosmological Model that has emerged in the last three decades. We then give a broad overview of the current state of affairs in DM science. In section 1.4, we review the key cosmological observables that we use to explore and constrain new physics in the DS. We finally give a brief synopsis of each thesis chapter.

1.1 The Standard Cosmological Model

In the last three decades, cosmology has transitioned from being a mostly qualitative field of study to establishing itself as a data-intensive precision science. Amazingly, various observations of physically distinct phenomena on vastly different scales all seem to point to the same cosmological model. This so-called “Concordance” or “Standard” cosmological model describes an acceleratingly expanding Universe where the baryonic matter we are familiar with from our everyday experience only constitutes a very small fraction of the overall energy budget of the Universe [1]. The remainder of the energy is either in the form of cold non-baryonic dark matter or in the form of a smooth unclustered fluid often called dark energy.

This model has not emerged overnight. It took the best part of the twentieth century and the work of thousands of scientists to gradually develop the currently accepted model of the Universe. The first step toward a unified and testable theory of the Universe was taken with the establishment of general relativity by Einstein [2]. This development allowed physicists to understand how the energy content of the Universe affects the fabric of space-time. The discovery that the Universe is expanding by Edwin Hubble in 1929 [3] brought us the first hint of the dynamical nature of the cosmos surrounding us. Shortly after in 1933, Zwicky’s observation [4, 5] of the Coma cluster gave us the first clue that a non-baryonic matter component could play a major role in the Universe.

As evidence about the expansion of the Universe grew in importance, it became relevant for physicists to reverse the arrow of time and ask about the initial state of the Universe. From these considerations emerged the Big

1.1. The Standard Cosmological Model

Bang picture in which the Universe originates from an initial singularity in a hot and dense state [6–8]. The high temperature of the cosmic plasma a few seconds after the Big Bang made possible the synthesis of the light nuclear elements in roughly the right proportions to explain observations, hence successfully establishing the theory of Big-Bang Nucleosynthesis (BBN) [9]. It was then postulated in the late 1940s that relic radiation from this early hot epoch should still permeate the Universe today [10–12]. The discovery of this cosmic radiation background by Penzias and Wilson [13, 14] established the Big-Bang model as our main theoretical framework to understand the Universe we live in.

Precise observations of galactic rotation curves by Rubin and Ford [15] in the 1970s firmly established the existence of a non-baryonic matter component in the Universe². By the early 1980s, a somewhat coherent model of an expanding universe populated by dark and baryonic matter as well as photons and neutrinos was beginning to emerge. This so-called Friedmann-Lemaitre-Robertson-Walker (FLRW) model was however plagued with some serious problems. It was indeed realized that the CMB was very uniform across causally disconnected patches of the sky, an observation that the causally expanding FLRW Universe could not elucidate. This issue is usually referred to as the *horizon* problem [16]. Furthermore, to explain the current state of the Universe, its energy density would have to be fine-tuned to lie extremely close to the critical value at the Big Bang [17], an issue known as the *flatness* problem.

An important step toward solving these problems was taken with the introduction of cosmic inflation [18–22]. This paradigm postulates that the Universe underwent an early period of exponential expansion, effectively stretching small causally-connected regions of the cosmos to extremely large sizes. The inflationary model naturally solves the horizon problem since all regions of the sky were in causal contact before inflation. Moreover,

²Other physical mechanisms based on modified gravity have been able to successfully explain the observed galaxy rotation curves. However, such theories have been so far unsuccessful at correctly predicting the spectrum of the CMB and have therefore not gain traction among the broader scientific community.

the inflationary paradigm readily alleviates the flatness problem by bringing the energy density of the Universe exceedingly close to its critical value. Above all, inflation provides a mechanism for seeding the primordial inhomogeneities [23, 24] that eventually evolve into all the rich structures that we observe in the Universe today.

Observations of the primary CMB anisotropies by the COBE satellite [25] and other experiments have confirmed some of the basic predictions of inflation, hence establishing this model as our leading paradigm for the very early Universe. The next breakthrough in our understanding of the cosmos came in 1998 when observations of distant Type Ia supernovae suggested that the expansion of Universe is *accelerating* [26, 27]. Since then, many independent measurements have confirmed this accelerated expansion and determined that a majority of the energy in the Universe is made of an unknown diffuse component often called “dark energy”.

At the dawn of the twenty-first century, many experiments corroborated this emerging picture of an accelerating spatially-flat universe mostly filled with DM and dark energy, most notably the WMAP satellite [28] which provided measurements of the key parameters describing our Universe with unprecedented accuracy. In parallel, observations of the distribution of galaxies (see e.g. [29]), the Lyman- α forest flux spectrum [30], the distribution of matter through weak lensing surveys [31–34], and the precise determination of the Hubble expansion rate [35] all contributed to the rise of the concordance cosmological model. To this day, evidence continues to accumulate toward this standard cosmological model (commonly denoted as the Λ CDM model) and it now forms the baseline from which theoretical physicists study more extended cosmological scenarios.

1.2 Inflation

The theory of cosmic inflation was initially introduced [18–22] to solve the horizon and flatness problems described above. The inflationary era describes a period during which small causally-connected regions of the early Universe are stretched to large cosmological distances. This has for conse-

1.2. Inflation

quence of establishing large-scale correlations beyond the causal horizon of the Universe. The rapid expansion of the Universe during inflation requires the pressure and energy density to obey the following relation [36]

$$p < -\frac{\rho}{3}, \quad (1.1)$$

where p is the pressure and ρ is the energy density of the Universe. Such negative pressure cannot be obtained from regular matter or radiation, and we must therefore invoke new physics to explain this apparent period of accelerated expansion. Most inflation models postulate that the energy density of the early Universe is dominated by a *scalar field* φ , often referred to as the *inflaton*. The energy density and pressure for an homogeneous scalar field is given by [36]

$$\rho_\varphi = \frac{1}{2}\dot{\varphi}^2 + V(\varphi), \quad p_\varphi = \frac{1}{2}\dot{\varphi}^2 - V(\varphi), \quad (1.2)$$

where $\dot{\varphi}$ denotes the time-derivative of the scalar field, $(1/2)\dot{\varphi}^2$ is the kinetic energy of the scalar field, and $V(\varphi)$ is the potential energy of the scalar field. If the kinetic energy is subdominant compared to the potential energy of the scalar field, then the inequality given in Eq. (1.1) is automatically satisfied since $p_\varphi \simeq -\rho_\varphi$. Therefore, most single-field inflation models can be built by specifying a potential $V(\varphi)$ in which the scalar field evolves slowly such that the kinetic energy is always subdominant. Such inflation theories are usually referred to as *slow-roll* inflation models [21, 22]. We discuss in chapter 6 of this thesis a novel way to characterize the potential $V(\varphi)$ responsible for inflation.

Beside providing a mechanism to explain the causal structure of the Universe, inflation also gives rise to the primordial density fluctuations [23, 24] that later evolve to form all the objects populating the Universe. Indeed, quantum fluctuations of the scalar field φ that are spatially stretched to cosmological distances during inflation provide the necessary seeds for the density fluctuations observed in the Universe. The small perturbations seeded by slow-roll inflation models obey *Gaussian* statistics [37], which implies that

1.2. Inflation

their statistical properties are completely specified by their two-point auto-correlation function or its Fourier transform, the fluctuation power spectrum $P_\Phi(k)$, which is defined by the relation

$$\langle \Phi(\mathbf{k})\Phi(\mathbf{k}') \rangle = (2\pi)^3 P_\Phi(k) \delta^3(\mathbf{k} - \mathbf{k}'), \quad (1.3)$$

where the angular brackets denote an average over all possible directions of \mathbf{k} and \mathbf{k}' , and $\delta^3(\mathbf{k})$ stands for the three-dimensional delta function. Here, Φ is the gravitational potential perturbation. Most inflationary theories predict a nearly scale-invariant spectrum of primordial fluctuations, that is, one for which $k^3 P_\Phi(k)$ is almost independent³ of k [36]. In slow-roll inflation models, all higher-order correlation function (e.g. $\langle \Phi\Phi\Phi \rangle$, $\langle \Phi\Phi\Phi\Phi \rangle$, etc) are either directly computed from P_Φ (even correlators) or vanish entirely (odd correlators). Current observations [1] indicate that the primeval fluctuations obey Gaussian statistics to better than one part in 10^3 . There is nevertheless a large ongoing scientific effort devoted to the detection of possible small deviations from Gaussianity in the statistics governing primordial fluctuations.

Indeed, the detection of a non-Gaussian signature in the statistics of primeval perturbations could inform us about potential deviations from slow-roll inflation in the early Universe. At first order, deviations from Gaussianity is usually parametrized in terms of the three-point correlation function

$$\langle \Phi(\mathbf{k}_1)\Phi(\mathbf{k}_2)\Phi(\mathbf{k}_3) \rangle = (2\pi)^3 \delta^3(\mathbf{k}_1 + \mathbf{k}_2 + \mathbf{k}_3) B_\Phi(\mathbf{k}_1, \mathbf{k}_2, \mathbf{k}_3), \quad (1.4)$$

where $B_\Phi(\mathbf{k}_1, \mathbf{k}_2, \mathbf{k}_3)$ denotes the *bispectrum*. The delta function enforces that the three momenta \mathbf{k}_1 , \mathbf{k}_2 , and \mathbf{k}_3 form a closed triangle in Fourier space. This triangle can have different shapes which characterize the type of non-Gaussianity present in the primordial density field. For instance, if

³The spectrum of primordial fluctuations is usually parametrized as $k^3 P_\Phi(k) \sim k^{n_s-1}$, where n_s is called the scalar spectral index. The case $n_s = 1$ corresponds to a scale-invariant spectrum of primordial fluctuations. Current observations seem to indicate that n_s is slightly smaller than 1 [1].

the three-point function has a maximum when two of the momenta are much larger than the third one, that is, $k_2, k_3 \gg k_1$, then the bispectrum is said to have a *local* or *squeezed* shape [38]. If the three-point function peaks when the three momenta are similar, that is, $k_1 \sim k_2 \sim k_3$, then the bispectrum is said to have an *equilateral* shape [39]. Other possible shapes include the *orthogonal* form [40] which is constructed such that it is orthogonal to both the local and equilateral shapes, and the *folded* form for which $k_3 \approx k_1 + k_2$ [41]. More general shapes are also possible. For instance, in chapter 6 of this thesis, we focus on bispectra displaying oscillations as the sizes of the different momenta are varied. For all possible shapes, we emphasize that the detection of a non-zero bispectrum of primordial fluctuations can provide us with a wealth of information about the physics governing inflation. We discuss below in section 1.4.3 a possible way to detect a non-vanishing bispectrum by observing the clustering of matter in the Universe.

1.3 Dark Matter

The standard cosmological model indicates that $\sim 25\%$ of the energy density is in the form of non-baryonic dark matter [1]. Phenomenologically, this matter component is able to clump into large gravitationally-bound halos, appears to be collision-less (no self-interaction), and only weakly couples (if at all) with the regular SM particles. DM scenarios can roughly be classified into three broad categories: cold, warm, and hot. Hot DM consists of ultra-relativistic particles that can free-stream over cosmological distances. A prime example of hot DM is the neutrino⁴. A warm DM particle [43–46] was relativistic in the past but is massive enough to become non-relativistic before matter-radiation equality⁵. Sterile neutrinos with a mass in the keV range fall into this category. In contrast, cold DM [47, 48] is made of particles that have been non-relativistic since a very early epoch and are therefore unable to free-stream over large distances. This last category has received

⁴The Standard-Model neutrinos cannot however form the bulk of the DM because they violate the Gunn-Tremaine bound [42].

⁵The epoch of matter-radiation equality corresponds to the time at which the energy density of relativistic radiation is equal to that of non-relativistic matter.

the most attention in the last two decades since CDM can easily clump and form the large halos surrounding galaxies and clusters. Particle candidates for CDM includes the popular Weakly Interacting Massive Particle (WIMP), the axion [49], as well as many models of asymmetric DM (see e.g. [50]).

It was rapidly realized that hot DM has too much pressure to form self-bound structures in the Universe [51]. It is therefore unlikely that hot DM can form the majority of the non-baryonic matter, even though it could still make up a small fraction of its overall energy density. On the other hand, warm DM could constitute most of the DM in the Universe. Since it was relativistic in the recent past, warm DM had enough kinetic energy to stream over a certain distance, effectively wiping out any inhomogeneities on scales smaller than this free-streaming length. Warm DM thus modifies the distribution of matter on small scales while sharing the properties of CDM on larger scales. This indicates that observations of the DM distribution on the smallest scales are crucial to solve the cold-versus-warm DM puzzle.

Beyond the cold and warm labels, DM could also have some self interactions [52]. From a particle physics point of view, we naturally expect DM particles to interact at some level [53]. For example, WIMPs are expected to have weak-scale cross section that could lead to an annihilation signal near the center of DM halos. However, observations of the apparent ellipticity (see e.g. [54]) of DM halos and the analysis of images of the Bullet Cluster [55] both severely constraint the size of the interaction cross section. Again, this indicates that we must focus our attention on sub-galactic scales to identify key signatures of possible interactions in the DM sector.

1.3.1 Possible Small-Scale Dark-Matter Anomalies

Intriguingly, observations of small satellite galaxies in the last decade have provided us with *possible* hints about the nature of DM. First, numerical simulations of structure formation in a CDM model indicate that a Milky Way-type galaxy should be surrounded by many faint satellite galaxies. While we have indeed found a fair number of such satellites around our own and other large galaxies, there is still a large discrepancy between the numerical

predictions and the observations [56–58]. Detailed simulations of the star formation efficiency and other feedback mechanisms inside these so-called dwarf galaxies have somewhat alleviated the problem [59–66] but there is still a fair amount of controversy about whether baryonic physics alone can solve this “missing satellite” problem. In any case, there is no doubt that modifying the properties of DM on short scales could bring the faint end of the galaxy luminosity function in line with observations.

Second, measurements of the inner mass profile of dwarf spheroidal (dSph) galaxies suggest that they are consistent with a constant-density core while CDM-based simulations predict a steeper cuspy density profile [67–69]. Again, baryonic physics feedbacks have been proposed to explain this apparent discrepancy [70] although there is still no consensus about whether these are sufficient to mitigate this issue [71]. Moreover, one should keep in mind that there might be large systematic uncertainties in the measurements of the inner density profile of dSphs galaxies [72] and that the current data is still very sparse. Nevertheless, it has been shown that self-interacting DM [73] can naturally predict a central core inside dSph galaxies.

Third, it was recently realized that simulated CDM subhalos surrounding large galactic halos are generally too dense to host any of the brightest dwarf galaxies orbiting the Milky Way [74, 75]. Indeed, satellites of our own galaxy attain their maximum circular velocity at larger radii than the simulated halos, implying that the former are more diffuse than the latter. Again, baryonic feedback has been proposed to alleviate this problem [76]. This might also indicate that galaxy formation is intrinsically stochastic in low-mass halos [77], although such a large level of stochasticity is probably incompatible with other observations [78]. Interestingly, it has been shown that warm DM [79] and self-interacting DM [73] generally produce more diffuse halos that can replicate those of the Milky Way satellites. Again, we see that modifying the short-scale behavior of DM physics can economically bring our theoretical predictions in line with the observations.

1.3.2 Relic Abundance

The microphysics governing the DM sector not only affects astrophysical objects at redshift zero but also largely determines its cosmological and particle physics properties in the early Universe. In particular, the fundamental physics of the DS fixes the DM relic abundance, which has been precisely measured by the WMAP satellite [1]. Various physical mechanisms could be responsible for setting this primordial abundance of DM. For instance, DM could have been in chemical equilibrium with the SM plasma through reactions of the type $\chi\bar{\chi} \leftrightarrow f\bar{f}$, where χ stands for a DM particle and f for any SM fermion. Once the rate of this process became smaller than the expansion rate of the Universe, the annihilation reaction effectively froze-out, leaving a relic abundance of χ and $\bar{\chi}$ particles. To accurately describe this freeze-out process, one needs in general to solve the Boltzmann equation [36] for the DM number density as a function of time. To a good approximation, the relic abundance is given by [80]

$$\Omega_{\text{D}}h^2 \simeq \frac{3 \times 10^{-27} \text{ cm}^3/\text{sec}}{\langle\sigma v\rangle}, \quad (1.5)$$

where σ is the total annihilation cross-section, v is the relative velocity of the DM particles and $\langle\dots\rangle$ denotes thermal averaging. Interestingly, if the cross section has the magnitude of a typical electroweak scale process ($\langle\sigma v\rangle \sim 3 \times 10^{-26} \text{ cm}^3/\text{sec}$), then we automatically obtain the correct DM relic abundance. This fact largely explains why WIMPs have garnered so much attention in the literature [53].

There exists also a large class of DM models for which the density of χ is not equal to that of $\bar{\chi}$, effectively mimicking the asymmetry in the baryonic sector where there is slightly more baryons than anti-baryons. In these asymmetric DM models [50], the symmetric part of the energy density annihilates away completely, leaving only the excess of χ particle as the relic DM density. Thus, in asymmetric DM models, the relic abundance is completely set by the initial size of the asymmetry. For example, the atomic DM model considered in this thesis falls in this category.

1.3.3 Kinetic and Thermal Decoupling

After DM chemically decouples from the cosmic plasma, it can still maintain thermal contact with the plasma through scattering reactions of the form $\chi f \rightarrow \chi f$. As long as such processes are in equilibrium (i.e. their rates are much faster than the Hubble expansion rate), they transfer both energy and momentum to the DM sector. As a consequence, the DM and the rest of the cosmic plasma share a common temperature and the DM density fluctuations are tightly-coupled to those in the plasma. DM density fluctuations cannot significantly grow in this regime since the plasma pressure is very effective at counteracting the gravitational pull on DM particles.

When the momentum-transfer rate between the plasma and the DM falls below the expansion rate, the DM particles effectively cease to be dragged by the rest of the plasma and is said to have *kinematically* decoupled from the rest of the particles. We define the kinetic decoupling temperature T_{kd} as the temperature of the plasma when the momentum-transfer rate Γ_{mt} is equal to the Hubble expansion rate

$$\Gamma_{\text{mt}}|_{T_{\text{kd}}} = H|_{T_{\text{kd}}}. \quad (1.6)$$

After kinetic decoupling, DM density fluctuations are free to grow by gravitational infall. Thus, the time of kinetic decoupling (also called the drag epoch) constitutes a very important period since it indicates when DM can start forming over-densities that would eventually turn into cosmological and astrophysical structures at late times. Moreover, the drag epoch also defines a length scale below which no DM inhomogeneity persists. Indeed, the plasma pressure can force DM particles to diffuse out of over-densities on scales that enter the Hubble horizon before kinetic decoupling. Thus, the Fourier mode with wavenumber $k_{\text{kd}} = H|_{T_{\text{kd}}}$ determines an approximate cutoff scale below which we expect to find no self-bound structure. At late times, this cutoff translates into a minimal DM halo mass [81]

$$M_{\text{min}} \simeq \frac{4\pi}{3} \rho_{\text{crit}} \Omega_{\text{D}} \left(\frac{\pi}{k_{\text{kd}}} \right)^3, \quad (1.7)$$

1.3. Dark Matter

where ρ_{crit} is the critical density of the Universe and $\Omega_{\text{D}} = \rho_{\text{D}}/\rho_{\text{crit}}$ with ρ_{D} being the energy density of DM.

When the energy-transfer rate between the plasma and the DM falls below the expansion rate of the Universe, these two constituents cease to share a common temperature. We define the temperature of thermal decoupling T_{td} through the relation

$$\Gamma_{\text{et}}|_{T_{\text{td}}} = H|_{T_{\text{td}}}, \quad (1.8)$$

where Γ_{et} is the energy transfer rate. Before thermal decoupling, the DM temperature scales as $T_{\text{DM}} \propto a^{-1}$, while after thermal decoupling, it scales as $T_{\text{DM}} \propto a^{-2}$, where a is the scale factor.

We note that in the special case where the DS is made of a single type of particle (together with its anti-particle), then kinetic and thermal decoupling happen simultaneously [81], that is, $T_{\text{kd}} = T_{\text{td}}$. This is usually the case for WIMP DM. However, if the DS is made of a mix of light and heavy particles, then thermal decoupling can be significantly delayed compared to kinetic decoupling. A classical example is the baryon-photon plasma where the baryons kinematically decouple from the plasma around $z_{\text{kd}} = 1020$ but thermally decouple only at $z_{\text{td}} \sim 200$ (see e.g. [36]). For most of its parameter space, the atomic DM scenario considered in this thesis falls into this latter category.

1.3.4 Direct-Detection

Our Milky Way galaxy resides in a large mostly-smooth DM halo. As the solar system revolves around the galactic center, the Earth is continuously being struck by DM particles from this smooth component of the halo. In scenarios where DM interacts with SM particles, one could hope that some of these particles could be detected as they make their way through the Earth. In the last two decades, several detectors have been built with the purpose of directly detecting DM in the laboratory. To this day, there has been no unambiguous and uncontroversial detection of DM particles. In the following, we give a summary of the current status of direct-detection experiments.

The oldest and perhaps most controversial claim of DM detection is from the DAMA/LIBRA collaboration [82]. The collaboration claims a high-significance detection of an annual-modulation signal with the right phase and amplitude to be attributable to DM scattering in their NaI crystal. Unfortunately, other experiments, most notably CDMS-II [83] and XENON100 [84], were unable to reproduce this result and even excluded the region of parameter space favored by the DAMA in the case of standard WIMP DM. To confuse matter further, the CoGeNT experiment [85] also reported the detection of excess events that could be interpreted as DM scattering in their detector and even observed an annual modulation signal, but with a different phase than the DAMA signal. This claimed detection is also in serious tension with the CDMS-II and XENON100 results. Finally, the CRESST collaboration [86] reported the detection of a significant number of events that could be interpreted as WIMPs scattering in their detector. Again, this last result is under serious stress when compared with the null results of CDMS-II and XENON100.

We therefore see that there is currently a fair amount of confusion about whether DM has been directly detected or not. In this thesis, we focus on the cosmological aspect of DM and leave the couplings between the DS and the SM unspecified. Thus, we do not further consider constraints from direct detection.

1.3.5 Indirect-Detection

If DM is able to annihilate into SM particles, then we might be able to detect the by-products of these annihilation events, giving us indirect evidence of the particle nature of DM. Since the annihilation rate of DM particles scales as the square of the local density, the largest signal is expected from regions in the local Universe that have a large DM density like the Galactic centre and dwarf galaxies. DM can either annihilate into a pair of SM fermions or into two energetic photons. The key element for DM indirect-detection is to be able to disentangle the DM signal from the large astrophysical foregrounds and backgrounds.

In the last few years, several collaborations announced the discovery of peculiar signals that could be interpreted as DM annihilating in the galactic center. For instance, PAMELA [87] reported an anomalously high ratio of positrons over electrons at energies up to 100 GeV while the Fermi-LAT collaboration [88] revealed an unexpectedly large sum of positrons and electrons all the way to the TeV scale. Interpreted as DM annihilation, these signals however require unconventionally large astrophysical enhancement factors as well as very specific leptophilic models of DM annihilation [89]. Moreover, this signal could also be explained by standard astrophysical sources such as pulsars or supernova remnants [90]. At present, the DM interpretation of this anomaly cannot be completely ruled out, but there is considerable tension with more recent data [91].

Perhaps the clearest signal from DM annihilation comes from gamma-ray detection. Gamma rays provide a cleaner signal than charged fermions since they generally have a low probability of scattering while traveling from their emission point to the detector. This implies that they usually point back to the region where DM annihilation is taking place, allowing us to target our searches toward the most promising sources. The drawback is however that the rate for DM to annihilate directly to photons is usually loop-suppressed. In the last decade, numerous gamma-ray signal that could tentatively be attributed to DM annihilation were reported. We give here a brief overview of the most propitious signals. Data from the Fermi-LAT indicate a possible excess in the gamma-ray flux at energies of a few GeV from an extended region near the Galactic centre [92, 93]. It was proposed that this excess could be explained by a 10 GeV DM candidate annihilating in the central part of our galaxy. At the time of writing, this result has however not been confirmed by the Fermi-LAT collaboration. More intriguingly, a sharp feature in the gamma-ray spectrum in the energy range between 130 and 150 GeV was recently found in publicly-available Fermi data [94, 95]. This feature was shown to be compatible with a narrow gamma-ray line or to be the result of internal bremsstrahlung, two signals that are easily explained in terms of DM annihilation [96]. However, as this signal originates from the Galactic centre, it is again very difficult to draw strong conclusions about

the exact nature of this feature. As more data is accumulated, this situation may however rapidly change [97].

Instead of considering the gamma-ray flux from a specific object or a particular region of the sky, chapter 2 of this thesis puts constraints on DM annihilation by considering the magnitude of the *diffuse* gamma-ray background from DM annihilating in the first protohalos that form at redshift $z \sim 40$. We also consider constraints on annihilating DM from the allowed amount of energy that could have been injected in the primordial gas from these annihilation processes. While these constraints do not allow the identification of tell-tale signatures of DM, they do provide conservative bounds on the possible physics governing the DS.

1.4 Cosmological Observables

To explore and constrain new physics in the DS, this thesis makes great use of three key cosmological observables. These are the CMB, the matter power spectrum, and the halo bias. We briefly review here the essential physics behind each of these measurable quantities.

1.4.1 Cosmic Microwave Background

To this day, observations of the CMB has provided us with the most precise picture [1, 98, 99] of the Universe as it stood roughly 380, 000 years after the Big Bang. At that epoch, photons cease to interact with the baryons and can begin to free-stream over large cosmological distances. The expansion of the Universe stretches their wavelength so that these photons appear today as an *almost-uniform* background of low-energy microwave photons. The fact that the microwave background is not totally uniform is essential to extract crucial information about the early Universe. Indeed, small temperature variations in the CMB inform us about the size and distribution of primordial fluctuations. As we mentioned above, these tiny fluctuations are thought to be the result of quantum processes that took place during inflation [23, 24]. By studying the *statistics* of these fluctuations, we can

learn a great deal about the physics governing the early Universe.

A key characteristic of the primeval fluctuations is that they have *small* amplitude. This simple fact greatly simplifies the CMB analysis since it implies that we can use linear perturbation theory to obtain accurate predictions (see e.g. [100]). To compute the theoretical CMB power spectrum, we need to evolve forward in time the primordial fluctuations resulting from inflation from early times until the photons decouple from the baryons, and then follow their trajectory as they free-stream from that epoch to our detectors today. In the following, we qualitatively describe the different ingredients entering this calculation. We first discuss the background evolution of the SM plasma (i.e. how its temperature and ionized fraction evolve) and then turn our attention to the fluctuations about this background. This is a particularly worthwhile exercise at this point since the atomic DM scenario is governed by very similar physics and many concepts introduced here will be discussed in that context in chapters 4 and 5.

Background Evolution

After electron-positron annihilation but prior to photon decoupling, the Universe is composed of protons, electrons, helium nuclei and photons, all tightly-coupled into an almost-perfect fluid. In addition, there are free-streaming neutrinos that are decoupled from the plasma, and DM which we assume here to be standard CDM. As the Universe cools down due to the Hubble expansion, it becomes energetically favorable for the free electrons to recombine with the helium nuclei and the free protons [101, 102]. As helium has a higher binding energy, it recombines first. Hydrogen recombination⁶ follows shortly after at redshift $z \sim 1100$. The end result is a mostly-neutral gas of hydrogen and helium atoms that is kinematically decoupled from the photon bath. The photons themselves effectively decouple from the plasma shortly after the onset of hydrogen recombination [36].

The baryons and photons are thermally coupled via Compton scattering.

⁶As we will describe in details the recombination process of *dark* atoms (which is similar to that of hydrogen) in chapter 4, we do not include further details about recombination at this point.

This process alone keeps the baryon temperature close to the photon temperature well after the end of recombination [102]. Indeed, due to the large photon-to-baryon ratio, even the small relic fraction of free electron ($\sim 10^{-4}$) left after recombination is sufficient to maintain thermal contact between the matter and the radiation. Once the energy-exchange rate through Compton scattering falls below the Hubble expansion rate, adiabatic cooling takes over and the matter temperature ceases to track that of radiation.

Perturbation Evolution

We now turn our attention to the small matter and radiation fluctuations that evolve on top of this uniform background. The equations governing the evolution of baryons, photons, neutrinos, and DM perturbations are listed in appendix A.1. Heuristically, these equations describe the competing force of gravity, which tends to make perturbations grow, and of the pressure, which tends to prohibit the growth of fluctuations. These equations are usually simultaneously solved numerically with initial conditions set at very early time when all length scales of interest are frozen outside of the Hubble horizon [100]. In this thesis, we only consider the adiabatic mode⁷, which is observed to be the dominant mode in CMB data [1]. In the following, we qualitatively describe the solutions of the perturbation equations for each constituents.

Dark Matter: In the simple CDM scenario, DM does not interact with the rest of the plasma and gravity is therefore the sole force acting on its particles. During radiation domination, the gravitational potential is dominated by photons and neutrinos which are unable to clump together due to their relativistic motion. This causes the gravitational potential to decay during this era. Paradoxically, the decaying potential boosts the amplitude of the DM fluctuations as they enter the horizon. Once inside the horizon, the DM fluctuations grow logarithmically with the scale factor until the period of matter-radiation equality. At that epoch, DM fluctuations begin to grow via gravitational infall at a much faster pace, that is, linear with the

⁷This mode of the cosmological perturbation equations takes the entropy per particle to be constant. It is the mode excited in most simple inflationary scenarios.

scale factor. DM is responsible for establishing the gravitational potential wells that will eventually host baryonic objects such as galaxies at late times. In chapters 4 and 5, we consider a model where DM is initially coupled to a radiation bath of “dark” photons. As we shall see there, the evolution of DM fluctuations described above is considerably modified in this case.

Neutrinos: Like CDM, neutrinos are also decoupled from the rest of the plasma. They however experience a significant amount of pressure due to their relativistic nature. As neutrino fluctuations enter the Hubble horizon, they can immediately free-stream out of over-densities (and into under-densities). Since neutrinos have a higher sound speed than the baryon-photon plasma, their fluctuations can propagate further in a given time interval, effectively establishing a gravitational potential perturbation beyond the photon sound horizon. Moreover, the free-streaming of neutrinos leads to the growth of anisotropic stress associated with the development of a significant quadrupole moment ($F_{\nu 2}$). These two effects combined lead to a small phase shift of the baryon-photon acoustic oscillations and a small reduction of their amplitude [103]. As we will discuss in chapter 5, this subtle but important signature is key in distinguishing free-streaming radiation from tightly-coupled “dark” radiation.

Photons and Baryons: Prior to recombination, the baryons and photons form a tightly-coupled fluid. The important quantity to consider here is the mean free-path τ_c of a photon between successive collisions with free electrons. If τ_c is much smaller than the physical size of the fluctuation or a Hubble time⁸, than the tight-coupling approximation holds and we can consider the baryon-photon plasma as a single almost-perfect fluid. This regime is however hard to capture numerically since the corresponding equations are very stiff. The solution is usually to expand the equations to first order in the small quantities $k\tau_c$ and τ_c/τ [104], where k is the wavenumber of the fluctuation and τ is the conformal time. In this thesis, we develop for the first time a *second-order* tight-coupling scheme which is shown in chapter 3 to be more accurate than the first-order approximation. In the opposite

⁸We take the speed of light to be equal to unity such that distance and time intervals are equivalent.

case, where τ_c is similar to the length scale of a fluctuations or is comparable to a Hubble time, the tight-coupling approximation breaks down and we need to consider the baryons and photons perturbations separately.

Photons: In the tightly-coupled regime, the solution to the baryon-photon equations corresponds to sound wave propagating in the plasma. As the mean free-path of the photons grows, photons are able to diffuse out of the baryon perturbations, effectively smoothing out fluctuations on scales shorter than this diffusion length [105, 106]. When photons begin scattering on electrons less than once per Hubble time, they can escape the baryons fluctuations and start to free-stream. Since finite time has elapsed between horizon entry and this decoupling epoch, the plasma sound wave can only propagate over a finite distance. This distance, called the sound horizon at decoupling, remains imprinted on the photon density field, appearing as the mean separation between maximally-correlated photon fluctuations. Once decoupled from the baryons, the photons must however escape the gravitational potential wells established by the DM. Photons escaping over-dense regions are effectively red-shifted while photons traveling out of under-dense regions are blue-shifted compared to the smooth background (a process known as the Sachs-Wolfe effect [107]). As the CMB photons free-stream from their emission point to our detectors, they encounter various gravitational potential wells. If those are static, the photon energy is unchanged as it falls and climb out of the potential wells (the blue-shift is exactly canceled by the red-shift). However, if the potential wells decay with time (i.e. because of radiation or dark energy), then the photons can experience a net blue shift. This last effect is called the Integrated Sachs-Wolfe effect.

Baryons: Once the momentum-transfer rate falls below the Hubble expansion rate, the baryons cease to be pushed around by the photons. They are then free to fall into the gravitational potential wells set by the DM. As in the case of the photons, the size of the sound horizon at the drag epoch remains imprinted as a key length scale in the baryon density field. At late times, matter fluctuations separated by this so-called Baryon Acoustic Oscillation (BAO) scale display an enhanced correlation between themselves.

Because of its universality, the BAO scale provides a standard ruler that allows us to test the expansion history of the Universe. Since the distribution of baryons is mostly determined by the DM potential wells, studies of the distribution of luminous baryonic objects in the Universe can inform us about the fundamental properties of DM.

Temperature Power Spectra

Having described the essential physical processes taking place when photons last-scatter around redshift $z \sim 1090$, we now turn our attention toward the statistical tools used to characterize the photon fluctuations. As the photons escape the baryons and DM fluctuations and travel all the way to the current epoch, they obtain small temperature fluctuations $\Delta T(\hat{n})$ compared to the background blackbody spectrum. These temperature perturbations can be expanded in terms of spherical harmonics Y_{lm} as

$$\frac{\Delta T(\hat{n})}{T} = \sum_{l=1}^{\infty} \sum_{m=-l}^l a_{lm} Y_{lm}(\hat{n}), \quad (1.9)$$

where \hat{n} is a unit vector pointing in the direction of the incoming photons. We are mainly interested in the two-point correlation function of these temperature fluctuations which we can write as [108]

$$\left\langle \frac{\Delta T(\hat{n})}{T} \frac{\Delta T(\hat{n}')}{T} \right\rangle = \frac{1}{4\pi} \sum_{l=0}^{\infty} (2l+1) C_l^{\text{TT}} P_l(\hat{n} \cdot \hat{n}'), \quad (1.10)$$

where the angular brackets denote an average over all possible directions of \hat{n} and \hat{n}' and P_l stands the Legendre polynomial of order l . We note that the two-point correlation function only depends on the angle separating the two unit vectors \hat{n} and \hat{n}' , a result that follows from the homogeneity and isotropy of the primeval plasma. The C_l coefficients can be themselves expressed as

$$C_l^{\text{TT}} = (4\pi)^2 \int k^2 dk P_p(k) |\mathcal{T}_{Tl}(k)|^2, \quad (1.11)$$

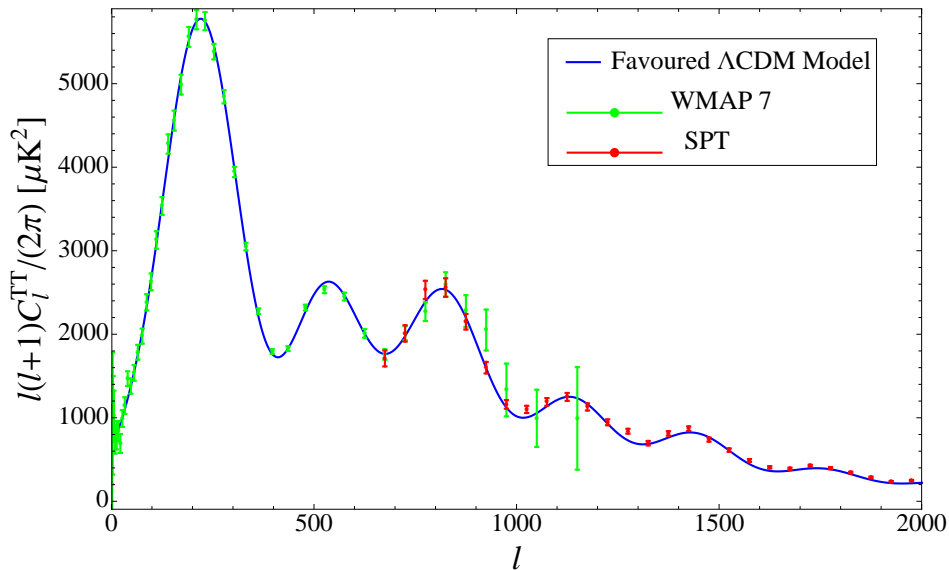


Figure 1.1: The CMB temperature angular power spectrum. We show the data from the 7-year observations of the WMAP experiment [1] and from the South Pole Telescope (SPT) experiment [99]. The blue solid line displays the Λ CDM model currently favoured by the data.

where $P_p(k)$ is the primordial power spectrum of fluctuations and $\mathcal{T}_{Tl}(k)$ is the transfer function for the temperature anisotropies. The latter can be obtained via the line-of-sight integral of the source function $S_T(k, \tau)$ [108]

$$\mathcal{T}_{Tl}(k) = \int_0^{\tau_0} S_T(k, \tau) j_l[k(\tau_0 - \tau)] d\tau, \quad (1.12)$$

where j_l is the spherical Bessel function of order zero and τ_0 is the conformal time at the present epoch. All the physics described in the previous subsection is encoded in the source function. To compute the C_l s, we therefore need to solve numerically the perturbation equations given in appendix A.1, compute the source functions and substitute it in the above equations. We display the currently-favoured CMB temperature power spectrum in Fig. 1.1. A similar calculation applies to the polarization anisotropies, for which we need to substitute the proper polarization source function in Eq. 1.12.

By carefully measuring the CMB temperature and polarization angular power spectra, we can determine many important cosmological parameters such as the DM and baryon densities, the amplitude and slope of the primordial power spectrum, and the amount of relativistic species present at photon decoupling. Subtle hints of new DS physics may lie hidden in the CMB spectra and new high-quality data from the Planck satellite [109] will be crucial in informing this question.

1.4.2 Matter Power Spectrum

The matter power spectrum describes the distribution of matter throughout the Universe. More specifically, it is the Fourier transform of the two-point correlation function of the matter density field. In terms of the Fourier-space density fluctuations $\delta_m(\mathbf{k})$, the matter power spectrum $P_m(k)$ is defined as

$$\langle \delta_m(\mathbf{k})\delta_m(\mathbf{k}') \rangle = (2\pi)^3 \delta^3(\mathbf{k} - \mathbf{k}') P_m(k). \quad (1.13)$$

The total matter fluctuations can be obtained from combining the DM and baryons density perturbations

$$\delta_m = \frac{\rho_b \delta_b + \rho_c \delta_c}{\rho_b + \rho_c}. \quad (1.14)$$

Again, the baryon and DM density fluctuations are given by the solution of the set of Boltzmann equations shown in appendix A.1. As we discussed above, DM fluctuations that enter the horizon during the radiation-dominated epoch only grow logarithmically with the scale factor. Conversely, matter fluctuations crossing into the horizon during matter domination grow linearly with a . We thus expect the matter power spectrum to display the following behaviour. On very large cosmological scales (small k), fluctuations only entered the horizon recently and did not have a lot of time to grow. As the wave-number is progressively increased, fluctuations had more and more time to grow in amplitude and we thus expect the matter power spectrum to have a positive slope on large scales. Fourier modes that enter the horizon just after matter-radiation equality experience the largest

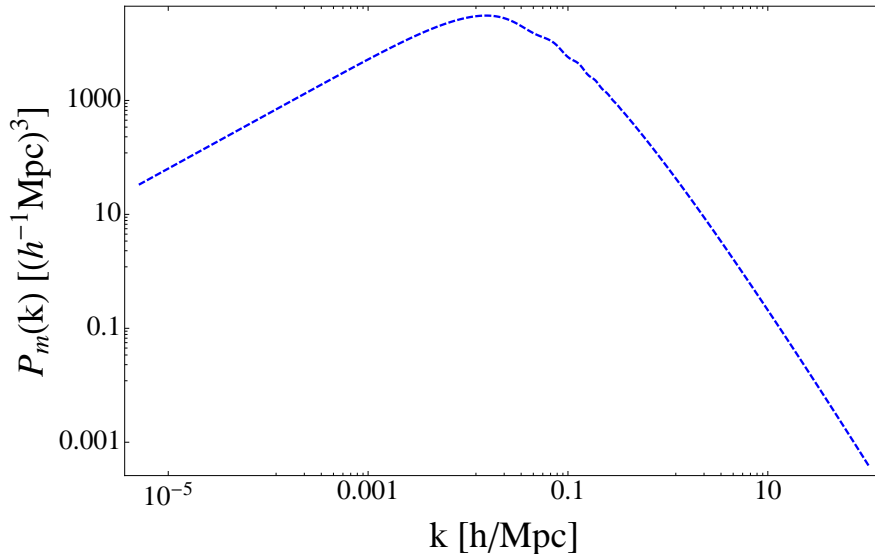


Figure 1.2: The matter power spectrum for the Λ CDM paradigm. The small oscillations around $k \sim 0.1 h\text{Mpc}^{-1}$ are due to the baryon acoustic oscillations. Here, h stands for the reduced dimensionless Hubble parameter.

growth since they spend the most time in the linear growing regime. We thus expect the matter power spectrum to have a maximum at k_{eq} , the Fourier mode that enters the horizon at equality. Finally, length scales becoming subhorizon while radiation is still dominating will be suppressed compared to modes with $k \sim k_{\text{eq}}$ since they grow much more slowly. We thus expect the matter power spectrum to have a negative slope for $k \gtrsim k_{\text{eq}}$. We display the CDM matter power spectrum in Fig. 1.2 where the features described above are clearly visible.

Since $\rho_c \simeq 5\rho_b$, the matter power spectrum is most sensitive to the DM. Thus, it could in theory provide a good probe of new physics in the DS. One must however be careful as the predictions obtained by solving the linear perturbation equations fail at short length scales ($k \gtrsim 0.2 h\text{Mpc}^{-1}$) since non-linearities become very important for these modes. Nevertheless, as we will briefly discuss in chapter 5, strong-lensing studies of galactic substructures could be used to estimate the shape of the non-linear tail of

the matter power spectrum.

1.4.3 Halo Clustering and Bias

The majority of the information we know about the distribution of matter through the Universe comes from the study of luminous objects such as galaxies and clusters of galaxies. Since most matter populating the cosmos is actually dark, we may ask if these luminous objects are good tracers of the overall matter density field. We show in this section that galaxies and galaxy clusters (together with their surrounding DM halos) are actually *biased* tracers of the large-scale matter field [110]. This bias is very sensitive to the statistical distribution of fluctuations in the density field and could be used to extract a wealth of information about the statistics of the primordial perturbations.

We divide the matter field into a small-amplitude long-wavelength contribution δ_l having a coherence length l_l and a high-amplitude short-wavelength contribution δ_s correlated over a much shorter distance $l_s \ll l_l$. The total matter field δ_m is the sum of these two components

$$\delta_m = \delta_l + \delta_s. \quad (1.15)$$

Let us consider a region of size l such that $l_s \ll l \ll l_l$. In this region, the short-wavelength field displays many fluctuations while the long-wavelength mode is approximately constant. Astrophysical objects such as galaxy clusters form when the peaks of the short-wavelength density field exceed a given threshold $\nu\sigma$, where σ is the rms density fluctuation. The threshold ν therefore denotes the number of standard deviations separating a density peak from the average density. We would like to calculate the probability of finding such an object at position \mathbf{x} in the region defined above. If this region happens to be located near a maximum of the long-wavelength field δ_l , then it is effectively over-dense compared to an averaged region of the Universe. We intuitively expect such over-dense regions to contain more collapsed objects. Conversely, if the above region lies near a minimum of δ_l , then it is under-dense and we expect it to contain less collapsed objects

compared to an average region of the Universe. Equivalently, we can say the the critical density threshold necessary to form a collapsed astrophysical objects is *modulated* by the long-wavelength density field δ_1 such that $\nu_{\text{eff}} = \nu - \delta_1(\mathbf{x})/\sigma$.

The probability of having a collapsed object at position \mathbf{x} is given by [110].

$$\begin{aligned} P(> \nu, \mathbf{x}) &= P(> \nu - \delta_1(\mathbf{x})/\sigma) \\ &\simeq P(> \nu) \left(1 - \frac{1}{P(> \nu)\sigma} \frac{dP(> \nu)}{d\nu} \delta_1(\mathbf{x}) \right), \end{aligned} \quad (1.16)$$

where $P(> \nu)$ is the probability that the overall matter density field δ_m exceeds the threshold ν . Since $dP(> \nu)/d\nu$ is negative⁹, we see that the probability of finding a collapsed object at position \mathbf{x} is enhanced compared to $P(> \nu)$ if $\delta_1(x)$ is positive (i.e. over-dense). We can absorb this enhancement factor into the long-wavelength density field by defining a new density contrast for the DM halos of collapsed objects [110].

$$\delta_h(\mathbf{x}) \equiv - \left(\frac{dP(> \nu)/d\nu}{\sigma P(> \nu)} \right) \delta_1(\mathbf{x}). \quad (1.17)$$

Defining the two-point correlation function as $\xi \equiv \langle \delta(\mathbf{x})\delta(\mathbf{y}) \rangle$, we observe that the correlation between halos is enhanced over the correlation present in the large-scale density field

$$\xi_h(r) = \left(\frac{dP(> \nu)/d\nu}{\sigma P(> \nu)} \right)^2 \xi_1(r). \quad (1.18)$$

The factor multiplying ξ_1 is called the bias. Note that it only depends on the statistics of the underlying matter fluctuation field. The bias basically measures the relative strength of halo clustering compared to that of the matter field. In the case of a Gaussian density field (as describe in section 1.2), δ_s and δ_1 are completely independent of each other and the above

⁹The probability of finding a region exceeding a given threshold shrinks as the threshold is increased. This is reasonable: very massive objects (such as superclusters) are rather rare while less massive objects (i.e. galaxies) are much more common.

expression simplifies to [110, 111].

$$\xi_h(r) \approx \frac{\nu^2}{\sigma^2} \xi_l(r), \quad (1.19)$$

which is valid for $\nu \gg 1$. We see that the most biased collapsed objects are those with the highest collapse threshold, that is, the most massive. We also note that for a Gaussian density field, the bias is independent of scale (i.e. of the correlation distance r). In this thesis, we will mostly consider the Fourier transform of Eq. (1.18)

$$P_h(k) = b_l^2 P_m(k), \quad (1.20)$$

where b_l is the Lagrangian bias and $P_h(k)$ is the power spectrum of DM halos.

If the density field is non-Gaussian, then the short-wavelength modes δ_s are *not* independent of the long-wavelength modes δ_l . This last case is particularly interesting and is the focus of chapter 6 of this thesis. There, we focus on non-Gaussian fluctuations having a non-zero three-point function (see section 1.2). We show in chapter 6 that theories having a non-zero bispectrum generally predict a *scale-dependent* halo bias [111–114]. This implies that the detection of a scale-dependent bias can inform us about the statistics of the primordial density fluctuations. In particular, since the simplest inflation models predict an almost-Gaussian spectrum of perturbations [37], the discovery of a scale-dependent bias could rule out a large swath of inflation theories. Competitive bounds on the amount of non-Gaussianities in primeval fluctuations have been obtained using this technique [113].

1.5 Structure of the Thesis

In the following sections, we provide a brief synopsis of each chapter included in this thesis, emphasizing the main ideas and results.

1.5.1 Protohalo Constraints to the Resonant Annihilation of Dark Matter

DM annihilating into SM particles has been put forward [89, 92, 93] as an explanation for the anomalous excess of charged fermions measured by cosmic ray experiments [87, 90, 115, 116]. If true, this interpretation requires an annihilation cross section that is enhanced compared to that required to obtain the correct thermal relic abundance (see e.g. [117]). It has been proposed that the annihilation cross section may possess a low-energy resonance that effectively boost the rate at which DM is converted to SM particles [118, 119]. In chapter 2, we show that such resonance leads to a flash of annihilation when the first DM protohalos collapse at redshift $z \sim 40$. The energy emitted by these annihilation events is either absorbed by the primordial gas or appears today as a diffuse gamma-ray background. In both cases, astrophysical and cosmological observations strongly limit the amount of energy that could have been injected by DM annihilation [120]. This in turn gives rise to a bound on the low-energy resonant annihilation cross section of DM. We discuss these constraints in the case where DM annihilates mostly to e^+e^- , $\mu^+\mu^-$ and $\tau^+\tau^-$ pairs, as well as to an hadronic final state. For each of these channels, we do a detailed analysis to determine which fraction of the emitted energy is locally absorbed by the gas and which fraction contributes to the gamma-ray background. We find that a resonant DM annihilation cross section is in serious tension with observations, making annihilating DM an unlikely source of the observed excess of charged fermions.

1.5.2 Photons and Baryons before Atoms: Improving the Tight-Coupling Approximation

Prior to recombination photons, electrons, and atomic nuclei rapidly scattered and behaved, almost, like a single tightly-coupled baryon-photon plasma. The equations of motion describing the evolution of fluctuations in this regime are very stiff and therefore difficult to solve numerically. We investigate in chapter 3 the accuracy of the tight-coupling approximation [121]

commonly used to numerically evolve the baryon and photon perturbation equations at early times. By solving the exact perturbations equations with a stiff solver starting deep in the radiation-dominated epoch we find the level of inaccuracy introduced by resorting to the standard first-order tight-coupling approximation. Most importantly, we develop a new second-order approximation in the inverse Thomson opacity expansion and show that it closely tracks the full solution, at essentially no extra numerical cost. We find the bias on estimates of cosmological parameters introduced by the first-order approximation is, for most parameters, negligible. Finally, we show that our second-order approximation can be used to reduce the time needed to compute cosmic microwave background angular spectra by as much as 17%. The new equations developed in this chapter are now a standard staple of modern CMB codes such as `CAMB` [122] or `CLASS` [123]. While this chapter focuses on the baryon-photon case, this work was initially motivated by our study of atomic DM for which a similar analysis can be carried out.

1.5.3 The Theory of Atomic Dark Matter

In chapters 4 and 5, we perform a thorough analysis a DM model in which the dark sector, due to a new $U(1)$ dark force, is made of atom-like bound states. This so-called “atomic” DM model [124–126] predicts novel DM properties on small scales but retains the success of CDM on cosmological scales. Moreover, this model takes fully advantage of all the atomic physics that has been developed since the dawn of the quantum revolution. This scenario naturally incorporates a dark radiation component which could explain the seemingly large number of relativistic degrees of freedom currently seen by CMB experiments [98, 99]. Since dark atoms typically have a large geometric cross section, this model constitutes an example of self-interacting DM with a velocity-dependent cross section. As such, we show that this model has the potential to address the current problems facing the dwarf spheroidal galaxies (see section 1.3.1). In chapter 4, we revisit the atomic physics necessary to capture the thermal history of the DS and show significant improvements over the standard hydrogen calculation are

generally required to make accurate predictions. We solve numerically the Boltzmann equations governing the evolution of cosmological fluctuations in this model and discuss in details in chapter 5 the impact of the atomic DM scenario on the matter power spectrum and on the CMB. We show that this scenario introduces a new important length scale in the density field corresponding to the size of the sound horizon at the epoch when DM kinematically decouples from the dark plasma. This “DAO” scale determines the minimal DM halo mass at late times which is typically orders of magnitude larger than in a typical WIMP scenario. Interestingly, we identify key CMB signatures that distinguish the atomic DM scenario from a standard Λ CDM model containing extra relativistic degrees of freedom. We finally discuss constraints on atomic DM from galactic dynamics, the Lyman- α forest data and BBN. We determine that the ellipticity of DM halos is the most constraining observations for atomic DM.

1.5.4 Oscillating Bispectra and Galaxy Clustering

Many models of inflation predict oscillatory features in the bispectrum of primordial fluctuations [41, 127–132]. Since it has been shown that primordial non-Gaussianity can lead to a scale-dependent halo bias [111–114], we investigate in chapter 6 the effect of oscillations in the three-point function on the clustering of dark-matter halos. Interestingly, we find that features in the inflaton potential such as oscillations (resonant non-Gaussianities) or sharp steps get imprinted in the mass dependence of the non-Gaussian halo bias. In both cases, we find a strong scale dependence for the non-Gaussian halo bias with a slope similar to that of the local non-Gaussian model. In the resonant case, we find that the non-Gaussian bias oscillates with halo mass, a novel feature that is unique to this type of models. In the case of a sharp feature in the inflaton potential, we find that the clustering of halos is enhanced at the mass scale corresponding to the Fourier mode that exited the horizon when the inflaton was crossing the feature in the potential. Both of these are new effects that open the possibility of characterizing the inflationary potential with large-scale-structure surveys. We briefly discuss

1.5. Structure of the Thesis

the prospects for detecting these non-Gaussian effects.

Chapter 2

Protohalo Constraints to the Resonant Annihilation of Dark Matter

2.1 Introduction

Recent data reported by several experiments may suggest the existence of a new source of cosmic ray positrons. Indeed, PAMELA [87] has reported an excess in the positron fraction from 10 to 100 GeV while the ATIC [115] and PPB-BETS [116] experiments have detected an overabundance of charged leptons in the total positron-electron (e^+e^-) energy spectrum between 300 and 800 GeV (see also the Fermi LAT results [88]). A very interesting explanation of these data invokes the annihilation of dark-matter particles with a mass at the TeV scale in the Galactic halo. However, in conventional models the dark-matter annihilation cross section needed to account for the excess is much larger [by a factor $\mathcal{O}(100 \text{ to } 1000)$] than the value deduced from the observed dark-matter relic abundance $\Omega_{\text{D}}h^2 \simeq 0.11$. To account for this, Refs. [118, 119, 133, 134] propose that this “enhancement factor” can be explained by a resonance in the dark-matter annihilation cross section.

In this chapter, we calculate the number and spectrum of photons and e^+e^- pairs produced by the annihilation of dark matter to standard model particles in the first protohalos that form at redshift $z \lesssim 40$. We find that experimental constraints from the diffuse gamma-ray background and on the amount of energy injection allowed into the primordial medium can be difficult to reconcile with the large annihilation cross sections $\sigma \sim 10^{-6}$ to

10^{-7} GeV^{-2} required to account for the observed Galactic lepton excess¹⁰.

While we focus here on models with a Breit-Wigner resonance in the dark-matter annihilation cross section, our constraints to σ_0 , the low-velocity-dispersion annihilation cross section, are model independent and apply to any model in which dark matter annihilates predominately to standard model final states (for instance, Ref. [117]). We briefly review the resonant enhancement mechanism before deriving constraints on the cross section from protohalo collapse. We then use current experimental bounds on diffuse backgrounds and energy injection into primordial gas to constrain the parameter space of the resonant cross section.

2.2 Breit-Wigner Resonance

We consider a model in which two dark-matter particles of mass m and energy $E_{i=1,2}$ annihilate via a narrow resonance of mass M . This type of resonance is very common in high-energy particle collisions such as those taking place at the Large Hadron Colliders (LHC). The main difference here is that the resonance occurs for low-energy collisions. Such low-energy resonance requires a mild level of fine-tuning as the masses of the particles involved in the annihilation process need to approximately obey $4m^2 \approx M^2$. We note however that such mass coincidence can naturally arise in Kaluza-Klein dark-matter models [135]. Following Refs. [118, 119], we parametrize this resonance using $M^2 = 4m^2(1 - \delta)$, $|\delta| \ll 1$. For $\delta < 0$, we have a physical pole (particle state), while for $\delta > 0$, we have an unphysical pole. In both cases, the cross section times velocity takes the form

$$\hat{\sigma}(z) \equiv 4E_1 E_2 \sigma v \propto \frac{(1+z)\gamma^2}{(z+\delta)^2 + \gamma^2}, \quad \gamma \equiv \Gamma/M, \quad (2.1)$$

where the Mandelstam variable $s_M = 4m^2(1+z)$ and Γ is the decay width of the resonance, that is, the inverse lifetime of the resonance. The dimensionless variable z represents the total kinetic energy of the colliding DM particles, expressed as a fraction of their total squared mass. We note that

¹⁰ $1 \text{ GeV}^{-2} \simeq 3.88 \times 10^{-28} \text{ cm}^2 = 38.8 \text{ millibarn}$.

2.2. Breit-Wigner Resonance

the cross section given in Eq. 2.1 is locally enhanced when $z = -\delta$, hence the name Breit-Wigner *resonance*. To calculate the relic abundance of dark matter, we thermally average the annihilation cross section σ with respect to a relativistic Maxwell-Boltzmann distribution,

$$\langle\sigma v\rangle_{\text{T}} = \frac{g_i^2}{n_{\text{EQ}}^2} \frac{m^4}{8\pi^4 x} \int_0^\infty dz \sqrt{z} \hat{\sigma}(z) K_1(2x\sqrt{1+z}), \quad (2.2)$$

where $x \equiv m/T$ and $n_{\text{EQ}} = (g_i m^3/2\pi^2)K_2(x)/x$. Here $K_1(x)$ and $K_2(x)$ are modified Bessel functions and g_i is the number of helicity states of a dark-matter particle. In this chapter, we set $c = k_{\text{B}} = 1$. Evaluating the integral (2.2), we can write the thermal cross section as $\langle\sigma v\rangle_{\text{T}} = \sigma_0 f(\delta, \gamma, x)$, where the function f encodes all the information about the resonance and has the property $f(\delta, \gamma, x \gg 1) = 1$. While there is no simple analytic expression for f , it can straightforwardly be found numerically (see Fig. 2.1). To determine the relic density, we solve the Boltzmann equation

$$\frac{dY}{dx} = -\frac{\lambda}{x^2} f(\delta, \gamma, x)(Y^2 - Y_{\text{EQ}}^2) \quad (2.3)$$

for the dark-matter yield, $Y = n/s$, where n is the number density of dark matter and s is the entropy density. Here, $\lambda = \sqrt{8\pi^2 g_*/45} M_{\text{pl}} m \sigma_0$ where g_* is the number of relativistic degrees of freedom, M_{pl} is the reduced Planck mass, and $Y_{\text{EQ}} = (45/4\sqrt{2}\pi^{7/2})(g_i/g_*)x^{3/2}e^{-x}$ is the equilibrium dark-matter yield. In the usual nonresonant scenario with $f \rightarrow 1$, Y tracks Y_{EQ} until the annihilation rate falls below the Hubble expansion rate and the interactions freeze out. The freeze-out temperature $T_{\text{f}} = m/x_{\text{f}}$ is conventionally determined when $Y - Y_{\text{EQ}} \simeq \mathcal{O}(Y_{\text{EQ}})$ — when the yield Y deviates substantially from equilibrium. The relic abundance is then given by the solution for Y at late time, $Y_\infty \simeq x_{\text{f}}/\lambda$.

However, in the presence of a resonance, the annihilation process does not freeze out when $Y - Y_{\text{EQ}} \simeq \mathcal{O}(Y_{\text{EQ}})$ as $f(\delta, \gamma, x)$ is increasing with x (for all $\delta > 0$ and some cases with $\delta < 0$). Instead, the dark matter keeps annihilating until a much lower temperature $T_{\text{b}} = m/x_{\text{b}} \ll T_{\text{f}}$, and the relic abundance is given by the asymptotic solution $Y_\infty^{\text{res}} \simeq x_{\text{b}}/\lambda$. The

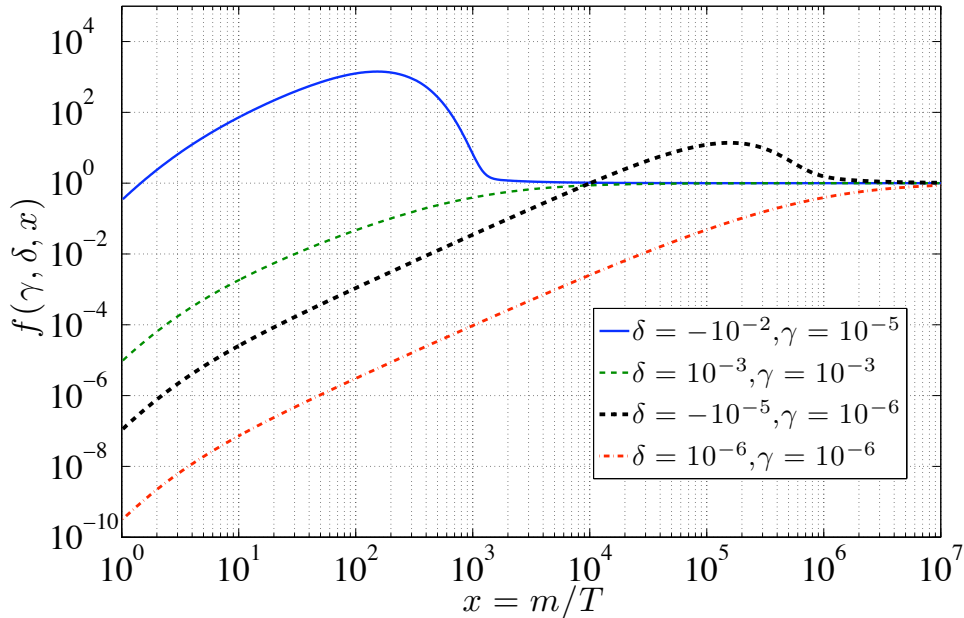


Figure 2.1: The functional form of the resonance function $f(\gamma, \delta, x)$ for various δ and γ with $g_i = 2$.

resonant case must have a higher λ (and thus σ_0) to obtain a relic abundance compatible with cosmological observations. In particular, if this higher σ_0 leads to an important production of positron-electron pairs in the Galactic halo, then one could explain the anomalous leptonic excess as was argued in Ref. [118, 119].

2.3 Annihilation in Protohalos

After matter-radiation equality, perturbations in the dark matter start to grow via gravitational instability and form protohalos — the first nonlinear structures in the Universe. The formation of protohalos triggers a flash of annihilation of dark-matter particles at redshift $z_f \sim 40$ [120, 136]. As they have a small mass and a low velocity dispersion [137], the annihilation cross section in these protohalos is given by σ_0 . If dark matter annihilates into standard model particles, a significant fraction of the initial energy will

be converted to high-energy photons and e^+e^- pairs. A photon generated can either travel freely through the Universe if its energy is within the gap between $0.1 \text{ MeV} \lesssim E_\gamma \lesssim 0.3 \text{ TeV}$ ¹¹ in which the Universe is essentially transparent [138], or it is absorbed by the primordial gas. The e^+e^- pairs produced rapidly inverse-Compton scatter off CMB photons resulting in gamma rays that are similarly either absorbed by the primordial gas or freestream if their energies are in the transparent gap. Experimental bounds on the diffuse extragalactic background of gamma rays and on the energy injection into the primordial gas constrain the number of e^+e^- pairs and photons that could have been created in the first dark matter halos. As we now show, this bounds the dark matter cross section to annihilate into e^+e^- pairs.

2.4 Constraints from the Diffuse Background

As the density inside a virialized protohalo is ~ 180 times higher than the mean cosmological density at redshift z_f , the average fractional annihilation rate $\bar{\Gamma} \equiv -\langle \dot{n} \rangle / \langle n \rangle = B \langle n \rangle \langle \sigma v \rangle_T$ in protohalos is

$$\bar{\Gamma} \simeq 4.9 \times 10^{-6} \left(\frac{B\sigma_0}{\text{GeV}^{-2}} \right) \left(\frac{m}{\text{TeV}} \right)^{-1} \left(\frac{z_f}{40} \right)^3 \text{ Myr}^{-1}, \quad (2.4)$$

assuming the present dark-matter density to be $\Omega_D h^2 \simeq 0.11$ and where n stands for number density and $\langle \dots \rangle$ denotes spatial averaging over a protohalo. We have introduced the standard boost factor $B \equiv \langle n^2 \rangle / \langle n \rangle^2$ to account for the nonuniform distribution of dark matter in these halos. Plausible values for B range between 3 and 60 depending on the concentration and density profile of the halos [139].

As the Universe expands nonlinear structures form via hierarchical collapse and the total fraction of dark-matter particles bound in collapsed ob-

¹¹A photon with an energy above the transparency window has a high probability of scattering off a CMB photon or produce a particle-antiparticle pair of SM fermions. On the other hand, a photon with an energy below the transparency gap is likely to photoionize a neutral hydrogen or helium atom. In contrast, a photon emitted in the transparency gap loses most of its energy by redshifting.

2.4. Constraints from the Diffuse Background

jects increases [140]. Protohalos eventually merge into more massive halos with a lower mean density and mean annihilation rate — although the dense cores of first-generation halos likely continue to shine relatively brightly for some time as dense substructures in larger halos.

We find the fraction Θ of dark-matter particles that annihilate in protohalos and other dense structures to be

$$\Theta \simeq 3.9 \times 10^{-4} \left(\frac{B\sigma_0}{\text{GeV}^{-2}} \right) \left(\frac{m}{\text{TeV}} \right)^{-1} \left(\frac{z_f}{40} \right)^{3/2}, \quad (2.5)$$

where $\Theta \simeq (1/3)\bar{\Gamma}\Delta t|_{z_f \simeq 40}$. We model dense structures that collapse at redshift z to annihilate efficiently for an expansion (e -folding) time Δt before being disrupted so that annihilation shuts off. At redshift z_f , $\Delta t \sim 2.4 \times 10^2 (z_f/40)^{-3/2}$ Myr and the factor of $1/3$ accounts for the facts that: (i) only a fraction of the Universe has collapsed into nonlinear structure at the redshifts of interest; (ii) structure forming at $z \lesssim z_f$ and $z \gtrsim z_f$ also contributes to the mean annihilation rate of the Universe. We find Eq. (2.5) evaluated in the “flash approximation” at redshift z_f is a good estimate for detailed calculations of the mean annihilation rate using Press-Schechter theory. The main uncertainties in these calculations, which could alter the estimate by factors of order unity or less, are the form of the mass function (which determines the collapse fraction) and estimates of the high-redshift survival lifetime of dense structures.

If the photons generated are not absorbed by the primordial gas, then they contribute to the diffuse background of gamma rays with energy density $\rho_\gamma = \Theta \rho_{\text{crit}} \Omega_D / z_f$, where ρ_{crit} is the critical density of the Universe today and we have accounted for the redshift of the photons. Using Eq. (2.5), we find

$$\rho_\gamma \simeq 1.1 \times 10^{-11} \left(\frac{\Omega B \sigma_0}{\text{GeV}^{-2}} \right) \left(\frac{m}{\text{TeV}} \right)^{-1} \left(\frac{z_f}{40} \right)^{\frac{1}{2}} \frac{\text{GeV}}{\text{cm}^3}, \quad (2.6)$$

where Ω is the fraction of the initial energy that is converted to photons (or electron-induced photons) whose energies lie inside the transparent gap. A fit from EGRET [141] to the gamma-ray spectrum of unresolved astrophysical sources yields the bound $\rho_\gamma^{\text{EGRET}} \approx 5.7 \times 10^{-16} (E_\gamma/\text{GeV})^{-0.1} \text{ GeV cm}^{-3}$.

2.5. Constraints on Energy Injection into Primordial Gas

Assuming that this energy excess is entirely accounted for by annihilating dark matter in the first structures, we obtain

$$\sigma_0 \lesssim \frac{5.0 \times 10^{-5}}{B\Omega} \left(\frac{m}{\text{TeV}}\right) \left(\frac{z_f}{40}\right)^{-\frac{1}{2}} \left(\frac{E_\gamma}{\text{GeV}}\right)^{-0.1} \text{GeV}^{-2}. \quad (2.7)$$

This bound is a conservative upper limit on the annihilation cross section as other contributions (e.g. blazars) to the gamma-ray background are likely present.

Above we take the limit that all the photons with energies above ~ 0.3 TeV are absorbed locally and therefore do not contribute to the diffuse gamma-ray background. This places a lower limit on the contribution to the diffuse gamma-ray background. For completeness, we also give gamma-ray background constraints in the alternative limiting case in which all photon energy (prompt and electron-induced) generated by dark-matter annihilation contributes to the diffuse background.

2.5 Constraints on Energy Injection into Primordial Gas

We now consider the case for which the energy released by the annihilating dark matter is absorbed by the primordial gas. The absorbed energy heats and ionizes the primeval gas which has for consequence of increasing its opacity to CMB photons and leading to measurable changes in their fluctuation power spectrum. Detailed modeling of CMB and large-scale-structure data [142] yields a bound $\Theta \lesssim 3 \times 10^{-10}$ on the fraction of the total rest mass energy of dark matter that could have been injected in the primordial gas when the age of the Universe was $t_f \sim 67$ Myr. Using Eq. (2.5), we then find

$$\sigma_0 \lesssim \frac{7.6 \times 10^{-7}}{B\Omega'} \left(\frac{m}{\text{TeV}}\right) \left(\frac{z_f}{40}\right)^{-\frac{3}{2}} \text{GeV}^{-2}, \quad (2.8)$$

where Ω' is the fraction of the initial energy that is injected in the form of photons whose energies lie above the transparent gap (i.e. photons with $E_\gamma \gtrsim 300$ GeV either generated promptly or via inverse-Compton scatter-

ing). Forthcoming results from the Planck satellite are likely to strengthen this bound.

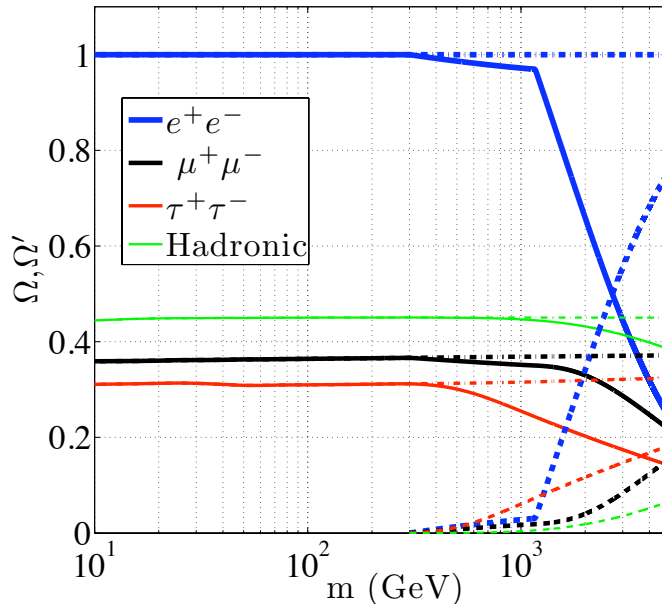


Figure 2.2: Fraction of the initial energy that is converted to photons and electron-induced photons with energies inside (Ω , solid lines) the transparent gap ($0.1 \text{ MeV} \lesssim E_\gamma \lesssim 0.3 \text{ TeV}$) and outside (Ω' , dashed lines) the transparent gap ($E_\gamma \gtrsim 0.3 \text{ TeV}$) as a function of the dark-matter mass for different annihilation channels. We also give the values of Ω computed under the assumption that all the energy released contribute to the diffuse gamma-ray background (dash-dot lines).

2.6 Discussion

If the anomalous leptonic signal is accounted for by annihilating dark matter, the value of the cross section to e^+e^- pairs in the Galaxy must be in the range $\sigma_{e^+e^-} \sim 10^{-6}$ to 10^{-7} GeV^{-2} . The total annihilation cross section in the Galaxy today, σ_G , is related to σ_0 by a transfer function $g(\delta, \gamma) \equiv \sigma_G/\sigma_0 \simeq f(\delta, \gamma, x_G)$, where we take $x_G \sim 3 \times 10^6$ in the Galactic halo [118]. This function accounts for differences between σ_0 and σ_G for very small γ

2.6. Discussion

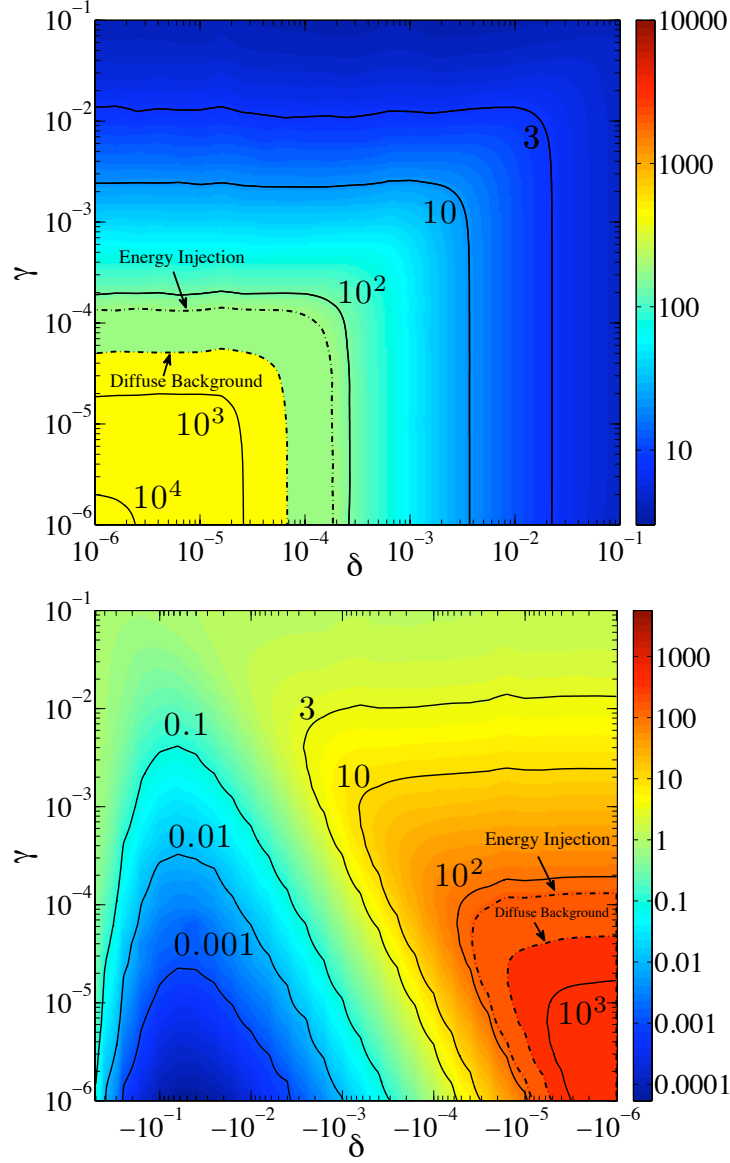


Figure 2.3: The enhancement factor ($\equiv Y_{\infty}^{\text{res}}/Y_{\infty}$) of σ_0 for an unphysical (top panel) and a physical (bottom panel) pole in models that have $\Omega_{\text{D}}h^2 \simeq 0.11$. Dash-dot lines show regions where values of (δ, γ) are excluded by (2.9) and (2.10). Shading in excluded regions reflects the value on the constraint boundary.

2.6. Discussion

and δ ($\delta, \gamma \lesssim 10^{-5}$). We find $g \sim 0.67$ to 1 for $10^{-4} \geq \delta, \gamma \geq 10^{-6}$ and $g \sim 1$ to 1.65 for $-10^{-6} \leq \delta, \gamma \leq -10^{-4}$ while for $|\delta|, \gamma \gtrsim 10^{-4}$, we find $g(\delta, \gamma) = 1$. As the cross section to e^+e^- pairs is necessarily smaller than the total annihilation cross section, we have $\sigma_{e^+e^-} \leq g(\delta, \gamma)\sigma_0$.

To calculate the fraction of the total initial energy that is converted to photons (and electron-induced photons) inside (Ω) and outside (Ω') the transparent energy gap, we use Monte Carlo simulations of the photon and e^+e^- pairs spectra and yields obtained from DARKSUSY [143]. To accurately determine the energy injected via electron-induced photons, we use the exact photon distribution expected from high-energy inverse-Compton scattering with a Klein-Nishina (KN) cross section (see Appendix A of Ref. [144]). This is important because for electron energies $E_e \sim \text{TeV}$ typical CMB photons at $z \sim 40$ have energies comparable to m_e in the electron rest frame and KN corrections are significant.

We consider four fiducial cases in which the dark matter annihilates either only into $\tau^+\tau^-$, $\mu^+\mu^-$ or e^+e^- pairs, or only into hadrons, with equal probability of annihilating into any of the $q\bar{q}$ pairs or to a gluon pair. For the hadronic case, prompt photons dominate while electron-induced photons contribute at most $\sim 40\%$ to Ω or Ω' . Electron-induced photons dominate for the muon channel while prompt photons dominate the tau channel. In Fig. 2.2, we plot Ω (solid lines) as a function of the dark-matter mass for the four channels. A realistic model might include a mixture of hadronic and leptonic annihilations (although current Galactic data may favor a leptophilic process) which would lead to an energy fraction $0.31 \lesssim \Omega \lesssim 1$ for $m = 200$ GeV. Using the constraint Eq. (2.7) and taking $B \sim 35$, $m = 200$ GeV, $z_f = 40$, and $\Omega \sim 0.6$, we obtain

$$\sigma_0 \lesssim 3.8 \times 10^{-7} \text{GeV}^{-2}, \quad (2.9)$$

where we take $E_\gamma \sim 10$ GeV, the energy with the highest flux for $m = 200$ GeV. This constraint is shown in Fig. 2.3 by the dash-dot line labeled ‘‘Diffuse Background’’. For the allowed values of δ and γ , $g(\delta, \gamma)$ is between 0.97 and 1.3 , and therefore the constraint on the cross section to e^+e^- pairs is

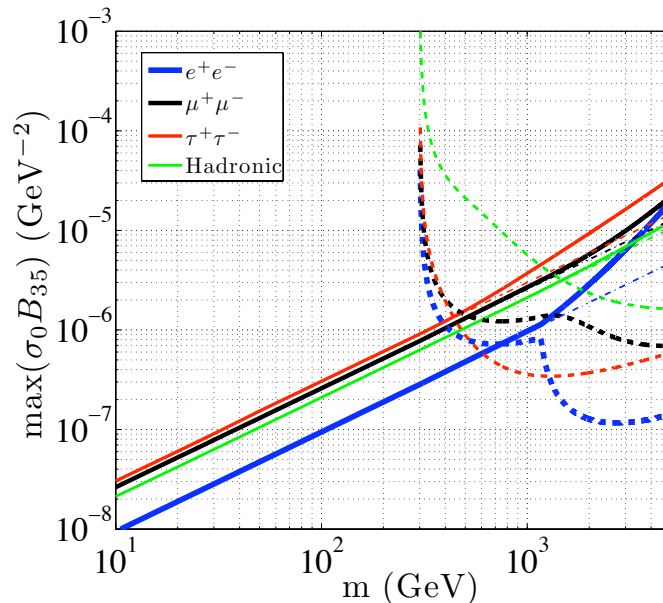


Figure 2.4: Upper bound on $\sigma_0 B_{35}$ from (2.9) and (2.10) for both leptonic and hadronic annihilation of dark matter ($z_f = 40$). The regions above the curves are excluded. The full lines show the diffuse background constraint while the dashed show the energy injection constraint. We also display the former constraint assuming that all the energy emitted by dark-matter annihilation contribute to the gamma-ray background (thin dash-dot lines). Note that $B_{35} \equiv B/35$.

$\sigma_{e^+e^-} \lesssim (3.7-4.9) \times 10^{-7} \text{GeV}^{-2}$. This bound excludes the resonant enhancement mechanism as a solution for the positron fraction excess problem for some of the plausible range for m and B (although for a low enough value of B/m , a solution might still be found).

For $m \gtrsim 600$ GeV, a stronger bound can be put on the cross section to positron-electron pairs using Eq. (2.8). In Fig. 2.2, the dashed lines show Ω' as a function of m for the three leptonic cases and the hadronic case. Again, a realistic model might involve some mixture of the two and therefore $0.01 \lesssim \Omega' \lesssim 0.34$ at $m = 2$ TeV. With $\Omega' \sim 0.3$, $z_f = 40$ and $B \sim 35$ in Eq. (2.8), we find

$$\sigma_0 \lesssim 1.4 \times 10^{-7} \text{GeV}^{-2}. \quad (2.10)$$

2.7. Summary

This constraint is shown in Fig. 2.3 by the dash-dot lines labeled “Energy Injection”. Equation (2.10) translates directly to a bound on $\sigma_{e^+e^-}$. Such a cross section is not large enough to account for the e^+e^- excess observed by the satellite experiments. One could weaken this constraint by allowing for a smaller value of B/m .

Finally, generalizing Eqs. (2.9) and (2.10) gives the model-independent upper bounds on $\sigma_0 B_{35}$ shown in Fig. 2.4 ($B_{35} \equiv B/35$). We see that light dark matter ($m < 100$ GeV) is excluded by the diffuse background constraint if the anomalous leptonic signal is to be explained by dark matter annihilating in the Galactic halo. The energy injection constraints for charged lepton-pair production disfavor a dark-matter mass at the TeV scale.

Models have also been proposed where the pair annihilation of dark matter proceeds through metastable scalar particles that subsequently decay into lepton pairs, yielding a different electron-positron and gamma-ray spectrum from final state radiation. Examples include the models discussed in Refs. [117, 145]. Although we do not consider these models explicitly here, the resulting spectra and constraints are very similar, though with slightly softer spectra, to the case of one single lepton pair (see e.g. Fig. 4 in Ref. [146]).

2.7 Summary

We have shown that a resonant dark-matter annihilation cross section to e^+e^- pairs large enough to explain the Galactic lepton anomalies is in tension with data from the diffuse gamma-ray background and limits on energy injection into primordial gas. The high enhancement regions of the parameter space are difficult to reconcile with these bounds assuming that protohalos are not exceptionally diffuse. Forthcoming data from the Fermi satellite might detect telltale signatures of dark-matter annihilation or yield even more stringent constraints to resonant annihilation models.

Chapter 3

Photons and Baryons before Atoms: Improving the Tight-Coupling Approximation

3.1 Introduction

The cosmic microwave background (CMB) radiation provides us with a picture of the Universe as it looked when the first atoms formed, about 380,000 years after the big bang. At that time, photons and baryonic matter practically ceased interacting and the Universe became transparent to radiation, allowing CMB photons to free-stream through space. To extract accurate cosmological information from CMB data it is crucial to understand the evolution of the photon-baryon plasma before decoupling. This involves solving the Boltzmann equations for both photons and baryons coupled by a Thomson-scattering collision term [100, 121, 147–151]. However, the large value of the Thomson opacity (τ_c^{-1}) before recombination renders these equations stiff, and hence difficult to solve numerically. This difficulty is usually circumvented by making use of the so-called “tight-coupling” approximation [121]. In this scheme, an alternative (approximate) form of the equations is found and used to find the solution by systematically expanding the problematic terms to first order in τ_c . At late times, once the Thomson opacity drops below a certain threshold, one switches back to the exact equations to determine the final answer.

Recently, it has been suggested that uncertainties in the cosmological recombination process may lead to a bias in estimates of cosmological parameters [152–154]. Could the tight-coupling approximation also result in such a bias and affect the final result of modern Boltzmann codes such as CAMB [122] or CMBFAST [108]? In this chapter, we first investigate the accuracy of the tight-coupling approximation by directly solving the exact set of equations at all times using a stiff integration scheme. This necessitates calculating more accurate cosmological initial conditions than has been done in the past. While not efficient, solving the exact equations allows us to determine the level of inaccuracy introduced by resorting to the tightly-coupled limit at early times. We then design a higher-order expansion scheme and show that at second order in $k\tau_c$ and $\dot{\tau}_c$, the final solution very closely tracks that obtained by solving the exact set of equations. We are then able to compute the bias on cosmological parameter estimates introduced by resorting to the first-order tight-coupling approximation and show that it is indeed small for most cosmological parameters. Finally, and most importantly, we describe how our second-order expansion can be used to speed up the computation of CMB power spectra without loss of overall accuracy.

3.2 Solution to the Exact Equations

The first step in testing the validity of the tight-coupling approximation is to evolve the exact set of equations from early times. This requires the use of a differential equation solver able to solve stiff systems with adaptive step sizes. We utilize the LSODA [155] solver which is based on the backward differentiation formula method. We find that the stiff integrator can solve the exact Boltzmann equations provided suitably accurate initial conditions are given. Indeed, the usual initial conditions for the perturbation variables used by modern Boltzmann codes are valid only in the limit of perfect coupling between photons and baryons [100, 156]. In this limit, the dipole moments of the photon and baryon distributions are exactly equal to each other and the photon quadrupole moment vanishes. However, in order to solve the

3.2. Solution to the Exact Equations

exact equations at early times, one needs to initialize the relative dipole moment (usually called the slip) between the photons and baryons and the photon quadrupole moment to nonzero values. We describe our approach to this problem in the next subsection. We then verify the convergence of the solution obtained with the stiff integrator to ensure it is stable to changes in the numerical tolerance and accuracy settings.

3.2.1 Initial Conditions

To find suitable initial conditions to the system of exact equations, we expand each perturbation variable in powers of $k\tau$ and $\epsilon \equiv \tau_c/\tau$

$$\Delta(\tau, \epsilon) = \sum_{m,n} (C_\Delta)_{mn} (k\tau)^m \epsilon^n \quad (3.1)$$

and substitute the result in the system of coupled differential equations (see Appendix A.1 for details concerning the notation). Here k is the Fourier wave number, τ is conformal time and $\Delta(\tau, \epsilon)$ stands for any of the following perturbation variables: $\delta_c, \delta_\gamma, \theta_\gamma, F_{\gamma 2}, \delta_b, S_b \equiv \theta_b - \theta_\gamma, \delta_\nu, \theta_\nu, F_{\nu 2}$, and η (our notation closely follows that of [100]). We then match coefficients of like powers of $k\tau$ and ϵ to obtain a set of linear equations for the series coefficients $(C_\Delta)_{mn}$. We solve these linear equations to find a global series solution, demanding that the tightly-coupled solutions (adiabatic or isocurvature) are retrieved in the limit $\epsilon \rightarrow 0$. In principle, one could try to solve the full recursion relation and obtain a closed-form expression for the $(C_\Delta)_{mn}$. In practice however, finding the first few terms of the series is sufficient to set accurate initial conditions. Using this method, we obtain the leading-order contribution to the initial value of the slip between baryons and photons for the adiabatic mode

$$S_b(\tau) \equiv \theta_b(\tau) - \theta_\gamma(\tau) = \frac{\beta_1 R_b}{6(1 - R_\nu)} \omega k^4 \tau^4 \epsilon + \mathcal{O}(\epsilon^2), \quad (3.2)$$

where $\beta_l = 1 - l(l+2)K/k^2$ is a normalization constant, $R_\nu \equiv \rho_\nu/(\rho_\nu + \rho_\gamma)$, $R_b \equiv \rho_b/\rho_m$ and $\omega = H_0 \Omega_m / \sqrt{\Omega_r}$. Here, $\Omega_m \equiv \rho_m/\rho_{\text{crit}}$, where $\rho_m = \rho_c + \rho_b$

3.2. Solution to the Exact Equations

is the total energy density of non-relativistic matter and ρ_{crit} is the critical density of the Universe¹². Similarly, $\Omega_r \equiv \rho_r/\rho_{\text{crit}}$, where $\rho_r = \rho_\gamma + \rho_\nu$ is the total energy density of relativistic radiation. The leading-order contribution of the photon quadrupole moment of the adiabatic mode is

$$F_{\gamma 2}(\tau) = \left[\frac{16}{9} + \frac{(8R_\nu - 5)\omega\tau}{3(2R_\nu + 15)} \right] \frac{4k^2\tau^2\epsilon}{(4R_\nu + 15)} + \mathcal{O}(\epsilon^2). \quad (3.3)$$

We list the initial conditions for all of the relevant perturbation variables in Appendix A.2.

3.2.2 Convergence of the Stiff Integration

We verify the convergence of the stiff integrator by running several computations with increasing accuracy and comparing the resulting angular power spectra. In **CAMB**, the desired accuracy is usually selected by choosing the appropriate ‘‘accuracy boost factors’’ which control, among other things, the Fourier mode sampling of the CMB anisotropy sources, the time step of the integrator, the number of multipoles kept in photon and neutrino hierarchies and the sampling of the final angular power spectrum. See Ref. [157] for a complete list. Here, we increase the accuracy boost factors to verify convergence but we also vary independently the tolerance of the stiff integrator to single out any error that is introduced by the solver itself. Throughout this section, we use as a benchmark model the WMAP seven-year cosmological parameter best-values [1]. Figure 3.1 shows the fractional change in both C_l^{TT} and C_l^{EE} as a function of the multipole moment l as the relative tolerance of the integrator is increased by an order of magnitude from 10^{-6} to 10^{-7} . The average fractional change in the angular power spectra is approximately 3×10^{-7} , hence showing that the integration process has converged. Figure 3.2 shows the fractional change in both C_l^{TT} and C_l^{EE} as the three **CAMB** accuracy boost factors are increased from 5 to 6. We see that the C_l computed with the stiff integrator have an accuracy of 0.01% or better with the accuracy boost factors set to 5. We shall use this spectrum

¹²The critical density corresponds to the required energy density for the Universe to have a flat (Euclidean) spatial geometry.

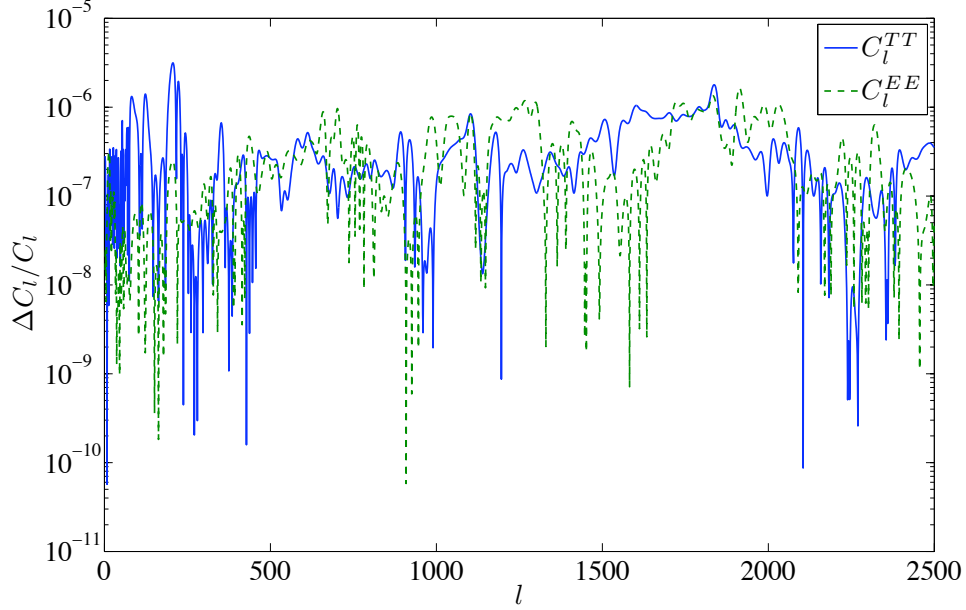


Figure 3.1: Fractional change in C_l^{TT} and C_l^{EE} versus multipole moments as the relative tolerance of the stiff integrator is varied from 10^{-6} to 10^{-7} . Here the CAMB accuracy boost factors are set equal to 5. The average change is 3.5×10^{-7} for C_l^{TT} and 3.3×10^{-7} for C_l^{EE} .

as our benchmark for testing the accuracy of our second-order tight-coupling approximation scheme which we now present in the next section.

3.3 Second-Order Scheme

In the usual tight-coupling approximation, the photon and baryon dipole moments are obtained by solving the two exact equations [158]

$$\dot{\theta}_\gamma = \frac{R}{1+R} k^2 \left(\frac{1}{4} \delta_\gamma - \beta_1 \frac{F_{\gamma 2}}{2} \right) + \frac{1}{1+R} \left(k^2 c_s^2 \delta_b - \frac{\dot{a}}{a} \theta_b - \dot{S}_b \right), \quad (3.4)$$

$$\dot{\theta}_b = \frac{1}{1+R} \left(k^2 c_s^2 \delta_b - \frac{\dot{a}}{a} \theta_b \right) + \frac{R}{1+R} \left[k^2 \left(\frac{1}{4} \delta_\gamma - \beta_1 \frac{F_{\gamma 2}}{2} \right) + \dot{S}_b \right], \quad (3.5)$$

3.3. Second-Order Scheme

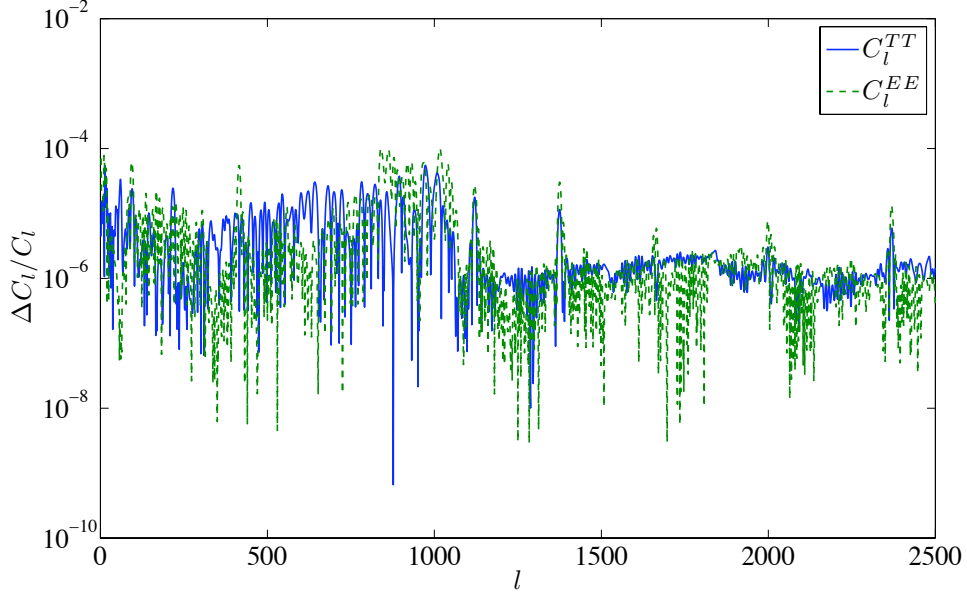


Figure 3.2: Fractional change in C_l^{TT} and C_l^{EE} versus multipole moments as the three CAMB accuracy boost factors are increased from 5 to 6. The maximum change is about 1×10^{-4} for C_l^{EE} and 6×10^{-3} for C_l^{TT} .

where a stands for the scale factor and dots represent derivatives with respect to conformal time. The exactness of the solution to the above equations of motion depends strongly on the accuracy at which we can determine both \dot{S}_b and $F_{\gamma 2}$. Current CMB Boltzmann codes use a first-order expansion in τ_c to approximate the photon-baryon slip and the photon quadrupole moment. Here, we propose a method to obtain the second-order corrections in τ_c to these quantities. See [159] for a related expansion in the context of magnetogenesis.

3.3.1 Photon-Baryon Slip

Our starting point is the exact equation for the slip obtained from combining Eq. (A.8) and the time derivative of Eq. (A.11) [158]:

$$\begin{aligned} \dot{S}_b = & \frac{1}{1 + 2\frac{\dot{a}}{a}\frac{\tau_c}{1+R}} \left\{ \left[\frac{\dot{\tau}_c}{\tau_c} - \frac{\dot{a}}{a} \frac{2}{1+R} \right] S_b + \frac{\tau_c}{1+R} \left[-\frac{\ddot{a}}{a} \theta_b - \ddot{S}_b \right. \right. \\ & \left. \left. - k^2 \frac{\dot{a}}{a} \left(\frac{1}{2} \delta_\gamma - \beta_1 F_{\gamma 2} \right) + k^2 \left(c_s^2 \dot{\delta}_b - \frac{1}{4} \dot{\delta}_\gamma + \beta_1 \frac{\dot{F}_{\gamma 2}}{2} \right) \right] \right\}. \end{aligned} \quad (3.6)$$

Usually, one sets $\ddot{S}_b = F_{\gamma 2} = \dot{F}_{\gamma 2} = 0$ and neglect the prefactor on the right-hand side of Eq. (3.6) since they contribute terms of order τ_c^2 and higher. However, to obtain an equation for the photon-baryon slip valid at second order in τ_c , an approximation for \ddot{S}_b , $F_{\gamma 2}$ and $\dot{F}_{\gamma 2}$ accurate to first order in τ_c is necessary.

The second derivative of the photon-baryon slip is computed by taking the time derivative of the right-hand side of Eq. (3.6). Here, we neglect terms proportional to $d^3 S_b/d\tau^3$ and $\ddot{F}_{\gamma 2}$. We then use the time derivative of Eqs. (A.7) and (A.10) to eliminate the second derivatives of δ_γ and δ_b . \ddot{h} is eliminated by using the space-space component of the perturbed Einstein equation

$$\ddot{h} + 2\frac{\dot{a}}{a}(2k\sigma - 6\dot{\eta}) - 2k^2\beta_1\eta = -8\pi G a^2 \sum_i 3\rho_i w_i \delta_i, \quad (3.7)$$

where $\sigma = (\dot{h} + 6\dot{\eta})/2k$ is the shear. We further eliminate $\dot{\theta}_\gamma$ using Eq. (A.8) and set $F_{\gamma 2} = \dot{F}_{\gamma 2} = 0$ since they contribute terms of order τ_c^2 to \ddot{S}_b . We finally substitute the time-evolution equations for the parameters R , c_s^2 , τ_c and $\dot{a}/a \equiv \mathcal{H}$:

$$\begin{aligned} \dot{R} &= -\mathcal{H}(1 - 3c_s^2)R, & \dot{c}_s^2 &= -\mathcal{H}c_s^2 \\ \dot{\tau}_c &= 2\dot{\mathcal{H}}\tau_c + 2\mathcal{H}\dot{\tau}_c, & \dot{\mathcal{H}} &= -3\mathcal{H}\dot{\mathcal{H}} - \mathcal{H}^3. \end{aligned}$$

Now armed with an expression for \ddot{S}_b , we substitute it into Eq. (3.6) and solve algebraically for \dot{S}_b . The result is given in Appendix A.3.

3.3.2 Photon Quadrupole Moment

To obtain an expression for $F_{\gamma 2}$ and $\dot{F}_{\gamma 2}$ accurate to second order in τ_c , we use the recursion relation between higher photon multipole moments [100]

$$\dot{F}_{\gamma l} = \frac{k}{2l+1} [lF_{\gamma(l-1)} - (l+1)\beta_l F_{\gamma(l+1)}] - \frac{1}{\tau_c} F_{\gamma l}, \quad (3.8)$$

which is valid for $l \geq 3$. We begin by setting $F_{\gamma 5} = 0$ and solve Eq. (3.8) with $l = 4$ for $F_{\gamma 4}$. We then take the derivative with respect to proper time, setting $\ddot{F}_{\gamma 4} = 0$. We finally solve the resulting equation for $\dot{F}_{\gamma 4}$ and substitute back the result in Eq. (3.8). This last equation leads to an expression for $F_{\gamma 4}$ valid to fourth order in τ_c (remembering that $F_{\gamma 3} \propto k^2 \tau_c^2$ and that $\dot{\tau}_c \propto \tau_c/\tau$):

$$F_{\gamma 4} \simeq \frac{4}{9} k \tau_c F_{\gamma 3} (1 - \dot{\tau}_c) - \frac{4}{9} k \tau_c^2 \dot{F}_{\gamma 3} + \mathcal{O}(\tau_c^5). \quad (3.9)$$

Substituting the above in Eq. (3.8) evaluated at $l = 3$ and using a similar procedure, we obtain an expression for $F_{\gamma 3}$ valid to fourth order in τ_c

$$F_{\gamma 3} \simeq \frac{3}{7} k \tau_c F_{\gamma 2} (1 - \dot{\tau}_c + \dot{\tau}_c^2) - \frac{3}{7} k \tau_c^2 \dot{F}_{\gamma 2} (1 - \dot{\tau}_c) - \frac{16}{147} k^3 \tau_c^3 F_{\gamma 2} + \mathcal{O}(\tau_c^5). \quad (3.10)$$

The last step in deriving expansions for the quadrupole moment and its derivative is to express the polarization multipole $G_{\gamma 2}$ in terms of $\dot{F}_{\gamma 2}$ and $F_{\gamma 2}$. Similar to the above calculation, this is accomplished by using the recursion relation for the polarization multipole moments [160]

$$\dot{G}_{\gamma l} = \frac{k}{2l+1} \left[l G_{\gamma(l-1)} - \frac{(l+3)(l-1)}{l+1} \beta_l G_{\gamma(l+1)} \right] - \frac{1}{\tau_c} \left[G_{\gamma l} - \frac{2}{15} \left(\frac{3}{4} F_{\gamma 2} + \frac{9}{2} G_{\gamma 2} \right) \delta_{l2} \right], \quad (3.11)$$

3.3. Second-Order Scheme

where δ_{ij} is the Kronecker delta. Again, we set $G_{\gamma 5} = 0$ and follow the method outlined above to obtain

$$G_{\gamma 2} \simeq \frac{F_{\gamma 2}}{4} - \frac{5}{8}\tau_c \dot{F}_{\gamma 2} \left(1 - \frac{5}{2}\dot{\tau}_c + \frac{25}{4}\dot{\tau}_c^2\right) - \frac{5}{56}k^2\tau_c^2 F_{\gamma 2}(1 - 6\dot{\tau}_c) + \frac{15}{27}k^2\tau_c^3 \dot{F}_{\gamma 2}, \quad (3.12)$$

which is accurate to fourth order in τ_c . We now have all the necessary tools to derive approximate expressions for $F_{\gamma 2}$ and $\dot{F}_{\gamma 2}$. We substitute Eqs. (3.12) and (3.10) in Eq. (A.9) and solve for $F_{\gamma 2}$. We then take the derivative with respect to conformal time and set $\ddot{F}_{\gamma 2} = 0$. We finally solve for $\dot{F}_{\gamma 2}$ and obtain

$$\dot{F}_{\gamma 2} = \frac{32}{45}\dot{\tau}_c(\theta_\gamma + k\sigma) \left(1 - \frac{11}{6}\dot{\tau}_c\right) + \frac{32}{45}\tau_c(\dot{\theta}_\gamma + k\dot{\sigma}) \left(1 - \frac{11}{6}\dot{\tau}_c\right) + \mathcal{O}(\tau_c^3). \quad (3.13)$$

Substituting the above back in Eq. (A.9) we ultimately arrive at the desired expression for the photon quadrupole moment

$$F_{\gamma 2} = \frac{32}{45}\tau_c(\theta_\gamma + k\sigma) \left(1 - \frac{11}{6}\dot{\tau}_c\right) + \frac{32}{45}\tau_c^2(\dot{\theta}_\gamma + k\dot{\sigma}) \left(-\frac{11}{6}\right) + \mathcal{O}(\tau_c^3). \quad (3.14)$$

3.3.3 Computational Procedure

As we can see from Eq. (3.14), our second-order expression for the photon quadrupole moment depends on $\dot{\theta}_\gamma$. From a practical perspective, this is problematic since it is the quantity that we are trying to determine in the first place. We overcome this difficulty by computing each quantity order by order in τ_c until the desired level of accuracy is reached.

The first step is to obtain an approximation to $F_{\gamma 2}$ using Eq. (3.14) but keeping only the terms linear in τ_c , which are independent of $\dot{\theta}_\gamma$. We then use this expression to calculate $\dot{\sigma}$ to first order in τ_c using the traceless

3.3. Second-Order Scheme

space-space part of the perturbed Einstein equation

$$k\dot{\sigma} + 2\frac{\dot{a}}{a}k\sigma - k^2\eta = -8\pi G a^2 (\rho_\nu F_{\nu 2} + \rho_\gamma F_{\gamma 2}). \quad (3.15)$$

Next, we calculate a zeroth-order expression for $\dot{\theta}_\gamma$ using Eq. (3.4) with \dot{S}_b and $F_{\gamma 2}$ set to zero. We then use our two formulas for $\dot{\sigma}$ and $\dot{\theta}_\gamma$ to compute $\dot{F}_{\gamma 2}$ to first order in τ_c using Eq. (3.13).

We now have all the necessary tools to calculate the photon-baryon slip to second order in τ_c using Eq. (A.26). We finally use this last expression to obtain a first order approximation to $\dot{\theta}_\gamma$ using Eq. (A.8) which in turn is used to obtain $\dot{F}_{\gamma 2}$ and $F_{\gamma 2}$ accurate to second order in τ_c .

3.3.4 Accuracy of the Second-Order Scheme

We test the accuracy of the second-order scheme by comparing the final angular power spectrum with both the stiff integrator benchmark and the usual first-order tight-coupling approximation. To isolate the effect of the second-order terms in the equations of motion, we leave untouched the algorithm that switches from the tightly-coupled equations to the exact system of equations. Improvements to the switching criteria will be discussed in Sec. 3.5. As mentioned above, all the results presented in this section are valid for the WMAP seven-year best-fit values for cosmological parameters. We find that at default accuracy setting (“accuracy boost” = 1) for all three computations, the fractional difference between the second-order scheme and the benchmark integration averaged over multipoles is about an order of magnitude smaller than the average fractional difference between the usual first-order tight-coupling approximation and the benchmark integration (see Fig. 3.3). Hence, the second-order scheme reproduces more accurately the solution to the exact equations.

As the accuracy boost factors are increased, the second-order scheme keeps providing, on average, a more accurate answer than the first-order tight-coupling approximation. Figure 3.4 compares the angular power spec-

3.3. Second-Order Scheme

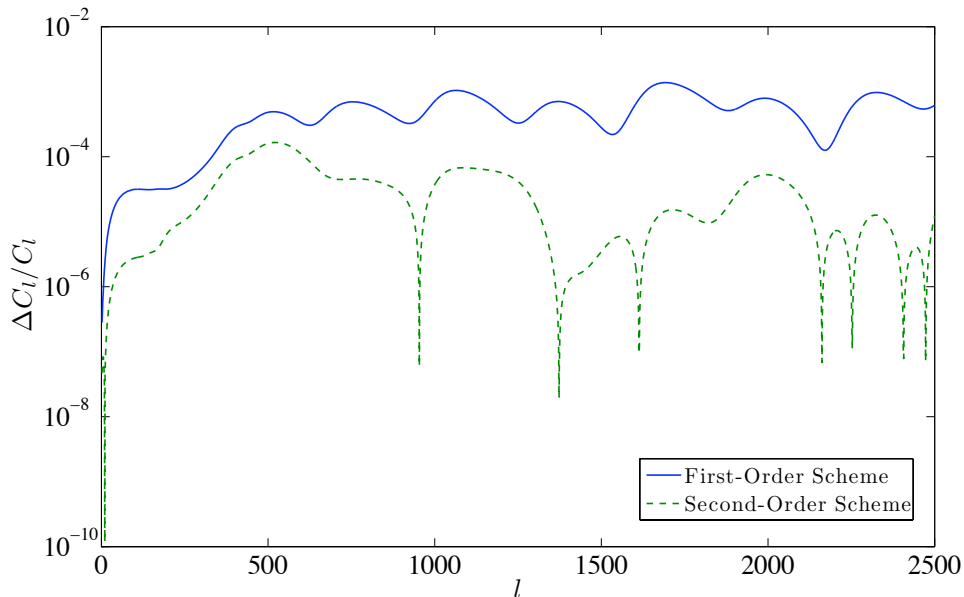


Figure 3.3: Fractional difference of C_l^{TT} between the usual first-order tight-coupling approximation and the benchmark integration (full line), and between the second-order approximation and the benchmark integration (dashed line). Here, the three sets of C_l s have been computed with default accuracy. The average fractional difference is 6.6×10^{-4} for the first-order approximation and 5×10^{-5} for the second-order approximation.

tra from the two schemes with those found by integrating the exact system of equations. Although, the difference between the two codes might be insignificant for current CMB experiments, it illustrates that the next-to-leading-order code is better capturing what is happening during the tightly-coupled epoch, especially for the low multipoles. The key point however is that this better accuracy comes at almost *no* additional computational cost, a point that we shall emphasize in Sec. 3.5.

In summary, we have shown that the second-order tight-coupling approximation reproduces more closely the result found by solving the exact equations, hence showing that the tight-coupling expansion is converging toward the exact solution. For practical applications however, the percentage change in the angular power spectrum between the usual first-order

3.3. Second-Order Scheme

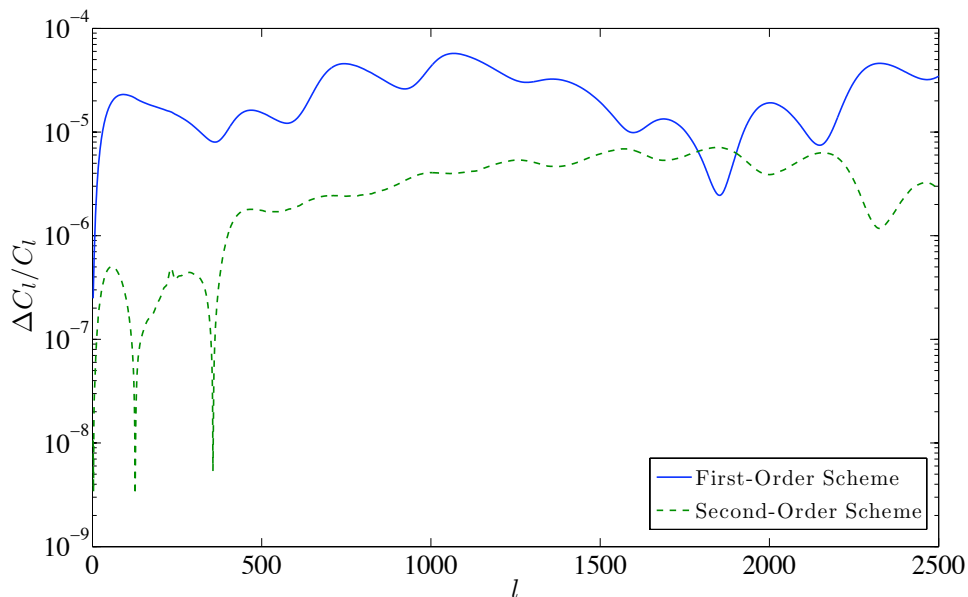


Figure 3.4: Fractional difference of C_l^{TT} between the usual first-order tight-coupling approximation and the benchmark integration (full line) and the second-order approximation and the benchmark integration (dashed line). Here, all the C_l s have been computed with the three accuracy boost factors set to 5. The average fractional difference is 2.4×10^{-5} for the first-order approximation and 3.5×10^{-6} for the second-order approximation.

approximation and the exact solution is small and well within the quoted precision from CAMB (0.3% at default accuracy). This implies that the first-order tight-coupling approximation should be sufficient for most practical purposes. Nevertheless, as we will describe in the next few sections, it is possible to use our second-order expansion to reduce the potential bias on cosmological parameter estimates and to speed up the code.

We mention in passing that the precision (i.e., the size of the numerical noise) of individual C_l is almost unaffected by the introduction of the second-order terms in the equations of motion. Indeed, the precision of the final angular power spectrum is mainly determined by the number of k -modes evolved by the code, the number of photon multipoles that are solved for, as well as various interpolation errors. Since our new tight-coupling approx-

imation does not modify any of the above, it is therefore natural to expect that the precision of the second-order power spectrum to remain unchanged.

3.4 Bias on Cosmological Parameters

In today's era of precision cosmology, the main purpose of CMB codes is to generate theoretical spectra that are then compared with data for cosmological parameter estimation purpose. However, numerical errors in the theoretical spectra could lead to a slight bias on estimates of cosmological parameters [157]. Since our improved tight-coupling approximation scheme leads to more accurate values of the power spectra, it is interesting to see how the bias is affected. To answer this question, we need to compute the effective χ^2 between our theoretical spectra and a fiducial data set which we take to have Planck-level noise. The effective χ^2 is defined by [157]

$$\chi^2 = \sum_l (2l+1) f_{\text{sky}} \left[\text{Tr} \left(\tilde{\mathbf{C}}_l^{-1} \hat{\mathbf{C}}_l \right) + \ln \frac{|\tilde{\mathbf{C}}_l|}{|\hat{\mathbf{C}}_l|} - 2 \right], \quad (3.16)$$

where f_{sky} is the observed sky fraction and $\tilde{\mathbf{C}}_l = \{C_l^{XX'} + \mathcal{N}_l^{XX'}\}$ is the theoretical covariance matrix. Here, X runs over temperature (T) and polarization (E). $\hat{\mathbf{C}}_l$ is the data covariance matrix. If we assume that the likelihood $\mathcal{L} = \exp(-\chi^2/2)$ is a multivariate Gaussian and that the prior probability densities are flat, then the bias on any cosmological parameter cannot exceed $\sqrt{\chi^2}$ standard deviations. In practice however, this bound is rarely saturated. Nonetheless, a small χ^2 between the data and the theory is still necessary to ensure a minimal bias.

We generate a fiducial data set up to $l = 2500$ using the method outlined in Ref. [157] but with the C_l obtained from the stiff solver. Again, we use the WMAP 7-year best-fit values for cosmological parameters. We take the noise to be Gaussian and isotropic with power spectrum given by

$$\mathcal{N}_l^{XX'} = \delta_{XX'} \theta_{\text{beam}}^2 \Delta_X^2 \exp \left[l(l+1) \frac{\theta_{\text{beam}}^2}{8 \ln 2} \right], \quad (3.17)$$

3.4. Bias on Cosmological Parameters

Code	χ^2	Time (s)
CAMB accuracy = 1	2.3	4.8
2nd Order acc. = 1	1.3	4.8
CAMB accuracy = 2	0.17	18.2
2nd Order acc. = 2	0.091	18.2
Opt. CAMB acc. = 2	1.1	15.1
Opt. 2nd Order acc. = 2	0.10	15.1

Table 3.1: χ^2 values between fiducial Planck data and theoretical spectra gotten with the first- and second-order codes for different accuracy boost. We also give the computational time needed to generate the theoretical spectra in order to show that the greater accuracy comes at no extra numerical cost. The computational times displayed here are for a single-processor machine.

where θ_{beam} is the beam width and Δ_X is the sensitivity per pixel. As an example, we consider the 143 GHz channel of the HFI instrument aboard Planck [109] which has $\theta_{\text{beam}} = 7.1'$, $\Delta_T = 6.0\mu K$ and $\Delta_E = 11.4\mu K$, assuming 14 months of integrated observation. We assume a sky coverage of $f_{\text{sky}} = 0.65$.

We list in Table 3.1 the values of χ^2 computed between our fiducial Planck data and our improved second-order code. For comparison, we also give the χ^2 values for unmodified CAMB at similar accuracy boost. We see that the higher-order tight-coupling approximation leads to a better fit to the fiducial data and therefore to a smaller theoretical maximal bias on cosmological parameters at no extra numerical cost. To estimate the real biases on cosmological parameters, we run several Markov chains using both the first- and second-order tight-coupling code together with the publicly available code CosmoMC [161]. We restrict ourselves to the “vanilla” 6-parameter Λ CDM model and made sure that the Gelman-Rubin “ $R - 1$ ” convergence criteria [162] is smaller than 0.005 for all the parameters under consideration.

We list in Table 3.2 the biases between the results from our second-order CMB code and the results from a code that used the same accuracy setting as the fiducial spectra (mimicking an error-free analysis). For comparison, we also give the biases for the usual first-order code. At default accuracy, we

3.5. Reducing the Computational Runtime

Code	$\Omega_b h^2$	$\Omega_c h^2$	θ	τ	n_s	$\ln(10^{10} A_s)$
CAMB accuracy = 1	0.24	0.15	0.31	0.11	0.40	0.19
2nd Order acc. = 1	0.25	0.16	0.15	0.12	0.33	0.15
CAMB accuracy = 2	0.02	0.006	0.03	0.013	0.03	0.03
2nd Order acc. = 2	0.03	0.003	0.01	0.016	0.017	0.015

Table 3.2: Biases of the 6-parameter Λ CDM model in unit of the standard deviation. We contrast the first- and second-order tight-coupling approximation and give the value of the accuracy boost factors used for each computation. Here, θ is the ratio of the size of the baryon-photon sound horizon at decoupling to the angular diameter distance to the last-scattering surface, τ is the reionization optical depth, n_s is the scalar spectral index, and A_s is the amplitude of primordial scalar fluctuations.

see that the difference between the two codes in terms of the bias is rather slim, with θ being the most dramatically affected by the second-order code. This stems from the fact that our second-order code better captures the position of the first peak, as can be seen from Figs. 3.3 and 3.4. We conclude that the numerical errors due to the first-order tight-coupling approximation does introduce a small bias to the estimate of θ at default accuracy, although it is clear that other numerical errors (k -sampling, interpolation, etc) contribute the most significant part to the biases of cosmological parameters for both codes. As the accuracy of the codes is increased, the difference in bias between the two codes becomes insignificant for parameter estimation purposes. Therefore, if one sets the accuracy of the theoretical spectra to be large enough that the bias from numerical errors other than the first-order tight-coupling is small, then the usual tightly-coupled equations are appropriate for cosmological parameter estimation.

3.5 Reducing the Computational Runtime

Up to this point, we have used the second-order expansion in τ_c to improve the accuracy of CMB Boltzmann codes. In this section, we adopt a different point of view and take advantage of our improved tight-coupling scheme to reduce the computational time needed to evolve the perturbation equations.

3.5. Reducing the Computational Runtime

Indeed, the new $\mathcal{O}(\tau_c^2)$ terms in the tightly-coupled perturbation equations allow one to switch to the exact equations at a later time while keeping the same accuracy as the usual first-order expansion. Since the approximate tightly-coupled equations are easier to solve than their exact counterparts, precious computational time can be saved. Moreover, the higher accuracy of the second-order equations lets us use a larger minimal time step for the numerical integrator, hence reducing the total number of steps taken by the integrator and further cutting down the computational time.

Our approach here is to degrade the accuracy of the second-order code by modifying the tight-coupling switching criteria, using larger time steps and cutting down the photon hierarchy until the output from this “optimized” code somewhat matches that of the unmodified first-order code. We then compute the χ^2 value between our fiducial Planck data and the output from this optimized code and compare it to a similar calculation done with the regular CAMB code. The results are shown on the two last rows of Table 3.1 where we see that we achieve a $\sim 17\%$ computational time reduction while still retaining the accuracy of the first-order code at accuracy boost 2.

Although this gain in computational efficiency is modest, it can significantly reduce the amount of time necessary to run Markov chains for cosmological parameter estimation. To demonstrate this, we run 8 chains with our optimized second-order code at accuracy boost 2, generating 20000 samples per chain. We also run the similar chains with regular CAMB at accuracy boost 2 and make sure to have $R - 1 \lesssim 0.005$. Figure 3.5 shows that the results for the marginalized posterior distribution are very similar between the two codes, with the distribution for θ being the most affected, although very mildly (0.09 standard deviation). However, the most important difference between the two results is that our optimized second-order code took on average $\sim 16\%$ less time to complete. Hence, our second-order tight-coupling code, in addition to leading to more accurate angular CMB spectra, can instead be used to speed up the computational time and make more efficient use of computing resources.

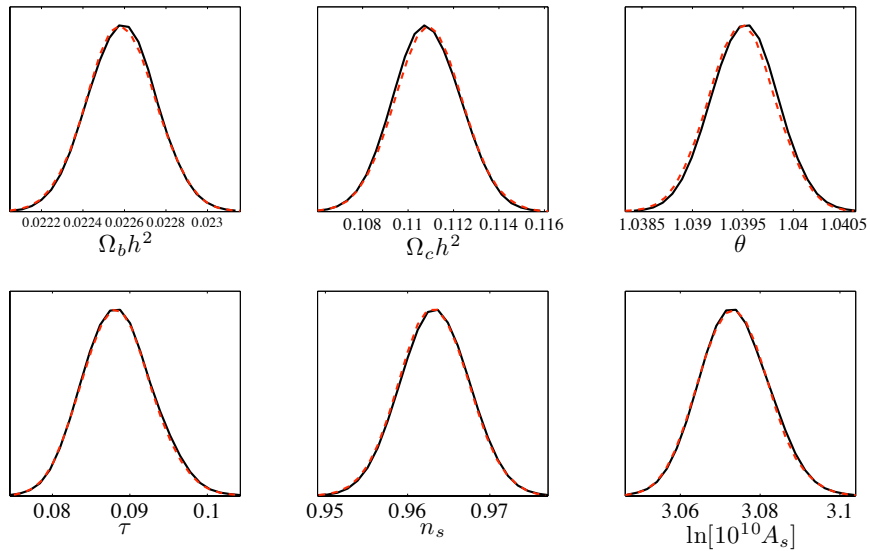


Figure 3.5: Marginalized posterior probability distribution for the vanilla Λ CDM model. The full black line represents the result obtained using the first-order code at accuracy boost 2 while the red dotted line was obtained using our optimized second-order code.

3.6 Discussion and Conclusion

We have developed a second-order tight-coupling approximation to the photon-baryon perturbation equations and shown that it closely reproduces the solution to the nonapproximated equations. In practice, the main reason why our second-order tight-coupling code produces more accurate power spectra is that it better tracks the evolution of the photon perturbations. Figure 3.6 shows the residuals between the photon perturbation δ_γ computed using the exact equations and the solutions obtained with the first- and second-order tight-coupling approximation. We see that the second-order scheme deviates much less from the exact solution than the usual first-order scheme, leading to a more accurate value of the source term needed for the line-of-sight integration [108]. We could in principle extend our analysis to develop a third-order tight-coupling approximation scheme. However, the long mathematical expressions associated with such a scheme are likely to

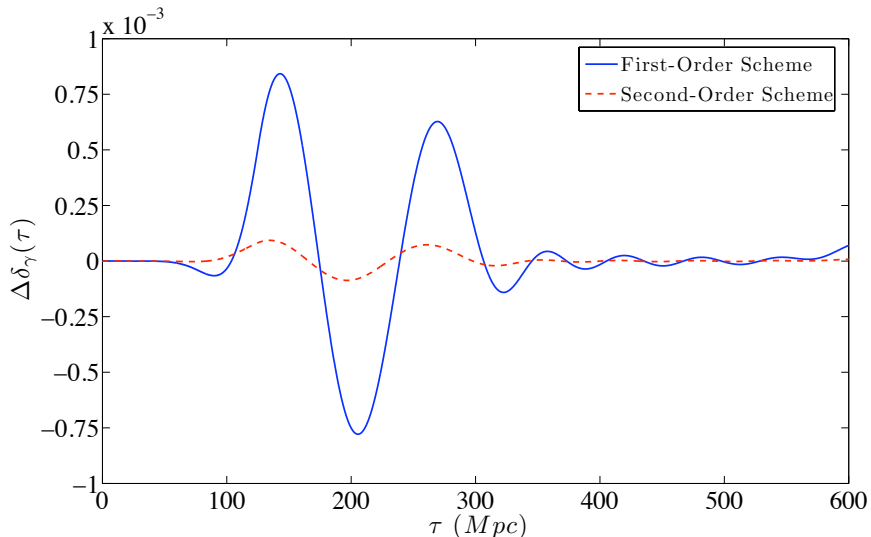


Figure 3.6: Residuals ($\Delta\delta_\gamma \equiv \delta_\gamma^{\text{exact}} - \delta_\gamma^{\text{approx}}$) between the photon perturbation δ_γ computed using the exact equations and the solutions obtained with the first- and second-order tight-coupling approximation.

lead to numerical inaccuracies that could overwhelm the accuracy gained by including the third-order terms.

In conclusion, we have investigated the accuracy of the tight-coupling approximation by solving the exact equations at all times using a stiff numerical solver. We have shown that the first-order tight-coupling approximation leads to a small accuracy lost compared to the exact solution and that this change is well within the quoted precision of the angular power spectra. We have discussed how our second-order code has a smaller maximal possible bias on cosmological parameters than its first-order counterpart. We have shown that the bias introduced by the first-order tight-coupling is insignificant for today’s cosmological experiments, unless `CAMB`’s default accuracy is used. Finally, we have shown that the improved accuracy of our second-order approximation allows one to optimize the tight-coupling switching criteria and integration parameters in order to modestly reduce the computational time of the code. Our second-order scheme has now been implemented in the main code of publicly-available CMB software such as `CAMB` or `CLASS`.

Chapter 4

The Theory of Atomic Dark Matter I: Thermal History and Evolution of Fluctuations

4.1 Introduction

Although dark matter (DM) has been known to exist for several decades [4, 5, 15], its physical nature remains one of the deepest mysteries of modern science. Observations show that DM is mostly cold, collisionless and interacts very weakly (if at all) with Standard-Model (SM) particles. Many models that fit this picture very well have been proposed through the years, including the prominent weakly-interacting-massive-particle (WIMP) models. Distinguishing between these different scenarios is crucial if we have any hope to pinpoint the nature of DM. In this respect, models incorporating new physics that predict novel observational signatures have a clear advantage in disentangling the DM puzzle.

While the cold Dark-Matter (CDM) paradigm [47, 48] has been extremely successful at describing observations from cosmological scales to galactic scales, recent observations of small nearby galaxies seem to be in tension with the CDM scenario. In addition to the so-called “missing satellite problem” [56–58] which refers to the apparent under-abundance of light Milky-Way satellites, observations of the inner mass profiles of Dwarf Spheroidal (dSph) galaxies indicate that they are consistent with a core

while CDM simulations favor a cuspier profile [67–69]. Further, it has been pointed out recently that the most massive galactic subhalos from CDM simulations are too dense to host the brightest Milky Way satellites [74, 75]. While it is plausible that these problems could be alleviated by including the appropriate baryonic physics in CDM simulations [59–66, 70, 77, 163, 164], these observations may be pointing toward physics beyond the vanilla CDM paradigm.

We adopt here the point of view that the above tensions between the Λ CDM paradigm and the astrophysical observations may be resolved by modifying the microphysics of the DM sector. Various scenarios have been proposed along those lines in the literature, most of which could either be classified as interacting DM models [52] or warm DM scenarios [43–46]. The former is tightly constrained by the observed ellipticity of DM halos [165, 166] and by the apparent survivability of DM halos to evaporation in clusters [167], while the latter is unlikely to be able to address all of the CDM issues discussed above [168]. It was realized recently [73, 169, 170] that interacting DM with a velocity-dependent cross section could avoid the ellipticity and evaporation constraints while alleviating the tension between the simulations and the Milky-Way satellites.

In this chapter, we investigate in detail the cosmology of a Dark Sector (DS) made of hidden hydrogen-like bound states [124–126, 171]. This so-called “Atomic Dark Matter” model retains the success of CDM on large cosmological scales but modifies the DM dynamics on sub-galactic scales. Similar to conventional atoms, atomic DM is kinematically coupled to a thermal bath of “dark” radiation (DR) until late times, which significantly delays the growth of matter perturbations on small scales. During the decoupling epoch, diffusion and acoustic damping substantially reduce the amplitude of sub-horizon perturbations, effectively wiping out structures on scales below this damping horizon, hence mimicking the effect of free-streaming. This model thus naturally provides a way to suppress the faint end of the galaxy luminosity function. After kinematic decoupling, the acoustic oscillations of the dark plasma remain imprinted on the small-scale matter power spectrum. Note that these physical processes also take place in a canonical

WIMP scenario [81, 137, 172]. The crucial difference here is that the kinematic decoupling of atomic DM typically happens much later than that of a WIMP and therefore can have an impact on much larger, if not observable, scales.

Beyond its effect on the matter power spectrum, the atomic DM scenario also impacts the cosmic microwave background (CMB) through the effects of the DR on the amplitude and phases of cosmological perturbations. We identify a key CMB signature that distinguishes the atomic DM scenario from a simple Λ CDM model incorporating extra relativistic degrees of freedom. Indeed, while models incorporating extra radiation always assume it to free-stream like neutrinos, the DR in the atomic DM model can only start free-streaming after it decouples from the DM. Cosmological modes entering the Hubble horizon before the onset of the free-streaming display a slightly different behavior than Fourier modes crossing the causal horizon after the decoupling of the DR.

Since dark atoms have a much larger geometric cross section than point particles, this scenario falls into the category of interacting DM models. Interestingly, the atomic physics naturally gives rise to a velocity-dependent interaction cross section. It is therefore possible that atomic DM could address some of the dSph-galaxy problems while evading the ellipticity and evaporation constraints. In the following, we focus on the ellipticity constraint and show that while it strongly constrains the parameter space of the model, there are plenty of parameter values for which the galactic dynamics is unaffected.

For clarity and completeness, it is important to mention that the term “dark atoms” has been used in various contexts in the literature. For example, dark atoms naturally appears in Mirror DM models [173, 174]. In [175, 176], the term “dark atom” refers to a bound state between a new stable particle charged under ordinary electromagnetism and a helium nucleus. The authors of [177] explored a model in which dark matter is made of supersymmetric dark atoms. In the present work, the phrase “dark atom” is exclusively used to describe the bound state of two dark fermions (i.e. neutral under the SM gauge group) oppositely charged under a new gauge

$U(1)_D$ interaction.

This chapter is organized as follow. In section 4.2, we introduce the atomic DM model and discuss the parameters necessary to describe the theory. In section 4.3, we analyze the thermal history of atomic DM from its initial hot plasma state to its cold and collisionless stage at late times. We include a thorough discussion of the thermal and kinetic decoupling epoch and present an in-depth analysis of the dark-recombination process. In section 4.4, we solve the modified cosmological perturbation equations and discuss the different regimes that a DM fluctuation encounters. The cosmological and astrophysical implications of this model are discussed in chapter 5.

4.2 The Model

The atomic DM model [124–126] is composed of two oppositely-charged massive fermions interacting through a dark massless (or nearly massless) $U(1)_D$ gauge boson¹³. In analogy with the regular baryonic sector, we call the lighter fermion “dark electron”, the heavier fermion “dark proton” and the massless gauge boson “dark photon”. In this work, we assume that the DM relic abundance is set by some UV physics in the early Universe. Since we are mostly interested in the late-time cosmological and astrophysical impacts of atomic DM, we do not expect the details of this high-energy completion to play any role in our results. See [126, 178, 179] for examples of DM production mechanism that can lead to atom-like DM particles.

Four parameters are necessary to fully characterize the physics of the DS in this model. These are the DM mass (i.e. the mass of the bound state) m_D , the dark fine-structure constant α_D , the binding energy of the bound state B_D and the present-day ratio of the DR temperature to the CMB temperature $\xi \equiv (T_D/T_{\text{CMB}})|_{z=0}$. Other combinations of parameters are possible but this particular set is physically transparent since B_D/ξ

¹³We note that dark atoms do not have to be made of two spin-1/2 fermions. For instance, they could arise from a bound state of two scalar particles or from a bound state of a spin-1/2 fermion with a scalar particle.

4.3. Thermal History

fixes the redshift of dark recombination, m_D fixes the number density of DM particles and α_D governs the microscopic interactions between the DS constituents. These parameters are subject to the consistency constraint

$$\frac{m_D}{B_D} \geq \frac{8}{\alpha_D^2} - 1, \quad (4.1)$$

which ensures that $m_{\mathbf{e},\mathbf{p}} \leq (m_D + B_D)/2$. This bound is saturated when the two fermions have equal masses. Here, $m_{\mathbf{e}}$ and $m_{\mathbf{p}}$ stand for the dark-electron mass and the dark-proton mass, respectively. We give their values in terms of m_D , B_D , and α_D in appendix B.1.

On a more general level, the atomic DM scenario can be considered as a toy model of a more complete theory involving a dark plasma in the early Universe. Indeed, atomic DM contains the all key ingredients of a dark-plasma theory (dark radiation, multiple particles, kinetic and thermal decoupling, modified growth of DM fluctuations, long-range and short-range interactions, etc) with only minimal physical inputs. As such, the results presented in this chapter should be understood in the broader context of a generalized dark-plasma theory.

Interestingly, the atomic DM scenario naturally englobes the hidden charged DM models discussed in [180, 181] as special cases. Moreover, in the limit of very large atomic binding energy and large dark fine-structure constant, dark atoms become basically undistinguishable from standard CDM particles. Therefore, the atomic DM scenario is a rather general testbed for physics beyond the vanilla WIMP/CDM paradigm.

4.3 Thermal History

In the early Universe, the DS forms a tightly-coupled plasma much like the standard baryon-photon plasma. As the Universe cools down, three important transitions need to carefully be taken into account. First, once the DS temperature falls below B_D , it becomes energetically favorable for the dark fermions to recombine into neutral dark atoms. Second, once the momentum transfer rate between the DR and the dark fermions falls below the

Hubble expansion rate (kinetic decoupling), the DM effectively ceases to be dragged along by the radiation and can start to clump and form structures. Finally, once the energy transfer rate between the DM and the DR falls below the Hubble rate (thermal decoupling), the DM temperature T_{DM} ceases to track that of DR and start cooling adiabatically. Accurately capturing these transitions and computing their impact on cosmological observables is a major goal of this chapter.

We begin this section by determining the Big Bang Nucleosynthesis (BBN) bound on the dark-photon temperature. We then discuss the recombination of dark atoms and their thermal coupling to the DR, emphasizing the differences between dark atoms and regular atomic hydrogen. We finally present the solutions to the joint evolution of the dark-atom ionized fraction and temperature.

4.3.1 BBN Limit on Dark-Sector Temperature

Observations of the relative abundance of light elements put a bound on the possible number of relativistic degrees of freedom at the time of BBN. This limit is usually quoted in terms of the effective number of light neutrino species in thermal equilibrium at BBN; here we shall use the conservative estimate $N_\nu = 3.24 \pm 1.2$ (95% confidence) derived in Ref. [182]. More recent estimates [183–187] of N_ν are statistically consistent with this value. Assuming that the DS contributes $g_{*,D}^{\text{BBN}}$ relativistic degrees of freedom during BBN and further assuming three species of SM neutrinos, we obtain the bound

$$g_{*,D}^{\text{BBN}} \xi_{\text{BBN}}^4 \leq 2.52, \quad (4.2)$$

where ξ_{BBN} is the ratio of the DS and visible temperatures at the time of nucleosynthesis. In the minimal atomic DM scenario considered in this thesis, DM is totally decoupled from SM particles and therefore the entropy of the DS and the visible sector are separately conserved

$$\frac{g_{*,D}^{\text{BBN}} \xi_{\text{BBN}}^3}{g_{*,D}^{\text{today}} \xi^3} = \frac{g_{*,\text{vis}}^{\text{BBN}}}{g_{*,\text{vis}}^{\text{today}}}, \quad (4.3)$$

4.3. Thermal History

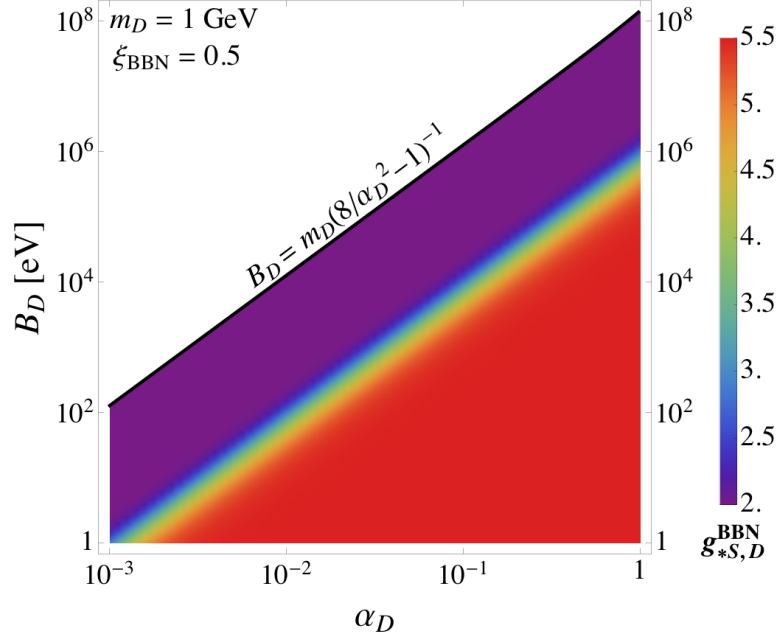


Figure 4.1: Effective number of DS relativistic degrees of freedom at the time of nucleosynthesis as a function of α_D and B_D for dark atoms with mass $m_D = 1$ GeV. Here, we have fixed the ratio of the DR temperature to the visible-sector temperature at BBN, $\xi_{\text{BBN}} = 0.5$. We also display the consistency constraint given by Eq. 4.1 above which dark atoms do not exist.

where $g_{*S,D}$ is the present-day effective number of degrees of freedom contributing to the entropy of the DS, $s_D \propto g_{*S,D} T_D^3$. For the simplest model of dark atoms considered here, we have $g_{*S,D}^{\text{today}} = 2$ (i.e. only dark photons contribute). Similarly, $g_{*S,\text{vis}}$ is the effective number of degrees of freedom contributing to the entropy of the visible sector. For the particle content of the SM, we have $g_{*S,\text{vis}}^{\text{BBN}} = 10.75$ and $g_{*S,\text{vis}}^{\text{today}} = 3.94$. During BBN, both dark photons and dark electrons (together with their antiparticles) can contribute to $g_{*S,D}^{\text{BBN}}$ (we assume that the dark proton is massive enough to be non-relativistic at the time of BBN). These dark components are kept in thermal equilibrium through Compton scattering and we therefore always have $g_{*S,D}^{\text{BBN}} = g_{*D}^{\text{BBN}}$. Figure 4.1 shows the dependence of $g_{*S,D}^{\text{BBN}}$ on α_D and B_D for dark atoms with mass $m_D = 1$ GeV and for $\xi_{\text{BBN}} = 0.5$. We see that

4.3. Thermal History

there is a large parameter space for which dark electrons are relativistic at BBN, leading to $g_{*,S,D}^{\text{BBN}} = 11/2$ for these models. At late times, the ratio of the DS and visible-sector temperatures is given by

$$\xi = \left(\frac{g_{*,S,\text{vis}}^{\text{today}} g_{*,S,D}^{\text{BBN}}}{g_{*,S,\text{vis}}^{\text{BBN}} g_{*,S,D}^{\text{today}}} \right)^{1/3} \xi_{\text{BBN}}. \quad (4.4)$$

Note that if $g_{*,S,D}^{\text{BBN}} = 11/2$, that is, if the dark electrons and anti-electrons annihilate after BBN, then $\xi \approx \xi_{\text{BBN}}$ since both the visible and dark sector are reheated by the same amount in this case (assuming the dark electron is a Dirac fermion). Substituting Eq. 4.4 into Eq. 4.2, we obtain the constraint

$$\frac{\xi}{(g_{*,D}^{\text{BBN}})^{1/12}} \lesssim 0.71 \quad (95\% \text{ confidence}). \quad (4.5)$$

We display this constraint in Fig. 4.2 where we observe that $\xi \geq 1$ is disfavored by at least 4 standard deviations if we consider BBN alone. Note that atomic DM models generally predict a different number of effective relativistic degrees of freedom at BBN than at the time of hydrogen recombination. Given a choice of dark parameters $(\alpha_D, B_D, m_D, \xi)$, we can compute $g_{*,D}(T_D)$ using Eq. B.3. The evolution of the dark-radiation temperature is then given by the implicit equation

$$T_D(z) = T_D^{\text{today}} (1+z) \left(\frac{g_{*,D}^{\text{today}}}{g_{*,D}(T_D)} \right)^{1/3}. \quad (4.6)$$

This equation can easily be solved iteratively by substituting the zeroth order solution $T_D(z) = T_D^{\text{today}} (1+z)$ into $g_{*,D}(T_D)$. In practice however, the annihilation of dark electron and dark positron has very little effect on the cosmological evolution and to a very good approximation, we can take ξ to be constant.

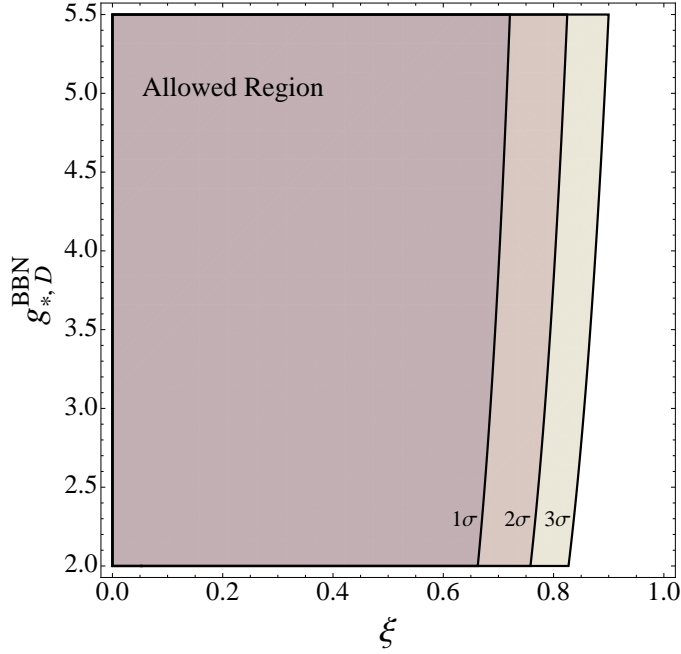


Figure 4.2: Joint BBN constraints on the present-day DS temperature and on the effective number of DS relativistic degrees of freedom at the time of nucleosynthesis. As indicated, we display contours corresponding to 1-, 2-, and 3- σ constraints.

4.3.2 Dark Recombination

Once $T_D \ll B_D$, it becomes energetically favourable for the dark plasma to recombine into neutral dark atoms. Letting n_e and n_D denote the number densities of *dark electrons* and of *dark protons* (both free and those bound in dark atoms) respectively, we can define the ionization fraction of the dark plasma as $x_D \equiv n_e/n_D$. Like regular hydrogen, dark atoms cannot directly recombine to their ground state as this results in the emission of a dark photon that can immediately ionize another dark atom [101]. Recombination needs therefore to proceed through excited states of the dark atoms. Once a dark electron has reached an excited state, it rapidly cascades down to the $n = 2$ state. Dark electrons can then reach the ground state via the $2s-1s$ two-photon transition or by emitting a Lyman- α dark photon which

4.3. Thermal History

redshifts out of the line wing. The recombination process is thus governed by the rate of escape of the dark Lyman- α photons out of their resonance line and by the rate of two-photon decay [101, 102]. While these two rates are comparable for regular baryonic hydrogen, they may differ significantly in the case of dark atoms.

To solve for the ionization history of the DS, we follow the Effective Multi-Level Atom (EMLA) method presented in Ref. [188]. For our purpose, we consider a four-level effective dark atom consisting of the two interface states $2s$ and $2p$, the ground state ($1s$), and a continuum. The recombination process is then governed by a set of Boltzmann equations of the form

$$\frac{dx_D}{dz} = \frac{x_D^2 n_D (\mathcal{A}_D^{2s} + \mathcal{A}_D^{2p}) - \mathcal{B}_D^{2s} x_{2s} - \mathcal{B}_D^{2p} x_{2p}}{H(z)(1+z)}, \quad (4.7)$$

$$\begin{aligned} \frac{dx_{2s}}{dz} = & \frac{\mathcal{B}_D^{2s} x_{2s} - x_D^2 n_D \mathcal{A}_D^{2s} + \mathcal{R}_{2p,2s}(3x_{2s} - x_{2p})}{H(z)(1+z)} \\ & + \frac{\Lambda_{2s,1s}(x_{2s} - (1-x_D)e^{-\frac{3B_D}{4T_D}})}{H(z)(1+z)}, \end{aligned} \quad (4.8)$$

$$\begin{aligned} \frac{dx_{2p}}{dz} = & \frac{\mathcal{B}_D^{2p} x_{2p} - x_D^2 n_D \mathcal{A}_D^{2p} + \mathcal{R}_{2p,2s}(x_{2p} - 3x_{2s})}{H(z)(1+z)} \\ & + \frac{R_{\text{Ly}\alpha}(x_{2p} - 3(1-x_D)e^{-\frac{3B_D}{4T_D}})}{H(z)(1+z)}, \end{aligned} \quad (4.9)$$

where $\mathcal{A}_D^{nl} = \mathcal{A}_D^{nl}(T_{\text{DM}}, T_D)$ is the effective recombination coefficient to the interface state nl , $\mathcal{B}_D^{nl} = \mathcal{B}_D^{nl}(T_D)$ is the effective photoionization rate of the interface state nl , $H(z)$ is the Hubble expansion rate and z is the redshift which we use here as a time variable. $R_{\text{Ly}\alpha}$ is the rate at which dark Lyman- α photons escape the Ly α resonance due to the expansion of the Universe [101]

$$R_{\text{Ly}\alpha} = \frac{(3B_D)^3 H}{(8\pi)^2 n_D (1-x_D)}. \quad (4.10)$$

4.3. Thermal History

Here and in the remainder of this chapter, we set $\hbar = c = k_B = 1$. $\Lambda_{2s,1s}$ denotes the rate of the forbidden two-photon transition between the $2s$ state and the ground state. It is given by [189–191]

$$\Lambda_{2s-1s} = \left(\frac{\alpha_D}{\alpha_{\text{em}}} \right)^6 \left(\frac{B_D}{B_H} \right) 8.22458 \text{ s}^{-1}. \quad (4.11)$$

Here α_{em} is the SM fine-structure constant and $B_H \simeq 13.6 \text{ eV}$ is the binding energy of regular hydrogen. $\mathcal{R}_{2p,2s}$ is the effective transition rate between the interface states $2s$ and $2p$ and is given by [188]

$$\mathcal{R}_{2p,2s} \equiv \sum_{nl} R_{2p \rightarrow nl} P_{nl \rightarrow 2s}, \quad (4.12)$$

where $R_{2p \rightarrow nl}$ is the bound-bound transition rate between the $2p$ state and the “interior” state nl ($n > 2$) and $P_{nl \rightarrow 2s}$ stands for the probability that a dark atom in a state nl will decay to the $2s$ state. Details of the computation of $R_{2p \rightarrow nl}$ and $P_{nl \rightarrow 2s}$ can be found in [188].

Previous studies of atomic DM have used an approximate recombination coefficient given by [100, 192]

$$\mathcal{A}_D(T_{\text{DM}}) = 0.448 \frac{64\pi}{\sqrt{27}\pi} \frac{\alpha_D^2}{\mu_D^2} \left(\frac{B_D}{T_{\text{DM}}} \right)^{1/2} \ln \left(\frac{B_D}{T_{\text{DM}}} \right). \quad (4.13)$$

This rate is problematic for three reasons. First, since it is only a function of the DM temperature, it fails to take into account the contribution from stimulated recombination which explicitly depends on T_D . Second, it does not take into account the effect of transitions among the high- n atomic states (an approximately 14% correction). Finally, it is inaccurate for $T_{\text{DM}} \gtrsim B_D$ and $T_{\text{DM}} \ll B_D$. To improve this situation and obtain an accurate picture of dark recombination, we compute a new recombination coefficient using the method outlined in Ref. [188]. Our recombination coefficient is given by

$$\mathcal{A}_D^{nl}(T_{\text{DM}}, T_D) \equiv \alpha_{nl} + \sum_{n'l'} \alpha_{n'l'} P_{n'l' \rightarrow nl}. \quad (4.14)$$

4.3. Thermal History

Here, $P_{n'l' \rightarrow nl}$ stands for the probability that a dark atom in a state $n'l'$ will decay to a state nl . The volumetric recombination rate to an atomic state nl is

$$\alpha_{nl}(T_{\text{DM}}, T_D) = \frac{(2\pi)^{3/2}}{(\mu_D T_{\text{DM}})^{3/2}} \int_0^\infty e^{-B_D \kappa^2 / T_{\text{DM}}} \gamma_{nl}(\kappa) \times [1 + f_{\text{BB}}(B_D(\kappa^2 + n^{-2}), T_D)] d(\kappa^2). \quad (4.15)$$

Here, κ denotes the momentum of the incoming dark electron in units of $\alpha_D/2B_D$ and $f_{\text{BB}}(E, T) \equiv (e^{E/T} - 1)^{-1}$ is the dark-photon distribution function at energy E for a blackbody spectrum at temperature T . The details of the atomic physics are encoded in the γ_{nl} factor [188]

$$\gamma_{nl}(\kappa) \equiv \frac{1}{3\pi n^2} \alpha_D^3 B_D (1 + n^2 \kappa^2)^3 \sum_{l'=l\pm 1} \max(l, l') |g(n, l, \kappa, l')|^2, \quad (4.16)$$

where $g(n, l, \kappa, l')$ denotes the bound-free radial matrix elements [193]. Numerically computing the momentum integral in Eq. (4.15) for each state nl and performing the sums in Eq. (4.14) up to $n_{\text{max}} = 250$ yield a recombination coefficient of the form

$$\mathcal{A}_D^{nl}(T_{\text{DM}}, T_D) = \frac{2\sqrt{2\pi}\alpha_D^3}{3\mu_D^{3/2}\sqrt{T_{\text{DM}}}} G_{250}^{nl}\left(\frac{T_D}{B_D}, \frac{T_{\text{DM}}}{T_D}\right), \quad (4.17)$$

where G_{250}^{nl} are universal dimensionless functions encoding the details of the atomic physics and its interaction with the radiation field. These functions are independent of the model parameters (α_D, m_D, B_D, ξ) and therefore need to be computed only once. For the purpose of numerical computation, we tabulate G_{250}^{2s} and G_{250}^{2p} on a grid of T_D/B_D and T_{DM}/T_D values and use an interpolation scheme to obtain accurate values of the effective recombination coefficients. The photoionization rates are related to the above photorecombination coefficients through detailed balance

$$\mathcal{B}_D^{nl}(T_D) = \left(\frac{\mu_D T_D}{2\pi}\right)^{3/2} e^{-\frac{B_D}{n^2 T_D}} \mathcal{A}_D^{nl}(T_{\text{DM}} = T_D, T_D). \quad (4.18)$$

4.3. Thermal History

In terms of the universal dimensionless functions, this reads

$$\mathcal{B}_D^{nl}(T_D) = \frac{\alpha_D^3 T_D}{3\pi} e^{-\frac{B_D}{n^2 T_D}} G_{250}^{ml}\left(\frac{T_D}{B_D}, 1\right). \quad (4.19)$$

In Fig. 4.3, we compare the effective total recombination rate $\mathcal{A}_D(T_{\text{DM}}, T_D) \equiv \mathcal{A}_D^{2s}(T_{\text{DM}}, T_D) + \mathcal{A}_D^{2p}(T_{\text{DM}}, T_D)$ with the approximate rate given by Eq. (4.13). The top panel compares the recombination rate when the DM and the DR are in thermal equilibrium with $T_{\text{DM}} = T_D$. We see that the approximate rate (4.13) performs reasonably well over the temperature range where most of the recombination is happening ($0.007 \lesssim T_D/B_D \lesssim 0.02$). Most of the difference between Eq. (4.13) and our exact computation can be traced to the fact that the former neglects the transitions between the high- n atomic levels. As shown in Ref. [194], this could in principle be taken into account by multiplying Eq. (4.13) by a fudge factor ~ 1.14 . We also show the recombination rate derived in Pequignot et al. [195] corrected by this fudge factor as used in `Recfast` [194]. Not surprisingly, this last rate is an excellent fit to the exact rate over most of the important temperature range. However, we see that both the Pequignot et al. and the rate given in Eq. (4.13) fails at high temperature and to a lesser extent, at low temperature. For regular atomic hydrogen, these errors are inconsequential since most of the baryonic plasma is ionized until $T_{\text{CMB}}/B_{\text{H}} \sim 0.02$ and has mostly recombined before $T_{\text{CMB}}/B_{\text{H}} \sim 0.003$. For weakly-coupled dark atoms however, these errors can have a substantial effect on the late-time ionization fraction of the DS.

The lower panel of Fig. 4.3 compares the different recombination rates when the DM temperature differs significantly from that of the DR. This can happen for example for a weakly-coupled DS which thermally decouples from the DR before the onset of or during recombination. In this case, both the canonical rate (4.13) and that of Pequignot et al. fail to capture the correct temperature dependence over most of the important temperature range. This should not come as a surprise as these two rates are purely functions of T_{DM} and cannot therefore capture the contribution from stimulated recombination which is a function on the DR temperature, T_D . For regular atomic hydrogen, this effect is unimportant since thermal decoupling

of baryons happens well after recombination. Note that Eq. (4.13) systematically underestimates the recombination rate leading to an artificially large late-time ionization fraction for weakly-coupled dark atoms. Given the sensitivity of the recombination rate on the DM temperature, it is important to accurately capture its evolution through the stage of thermal decoupling which we discuss in the next section.

Without solving any differential equation, it is possible to obtain an estimate for the late-time ionized fraction of the DS \bar{x}_D by solving the condition

$$\bar{x}_D n_D (\mathcal{A}_D^{2s} + \mathcal{A}_D^{2p}) \simeq H, \quad (4.20)$$

which determines the ionized fraction when the recombination process goes out of equilibrium. Using the above expression for the recombination rates and evaluating them at $T_D/B_D \sim 0.007$, we obtain

$$\bar{x}_D \sim 2 \times 10^{-16} \frac{\xi}{\alpha_D^6} \left(\frac{\Omega_D h^2}{0.11} \right)^{-1} \left(\frac{m_D}{\text{GeV}} \right) \left(\frac{B_D}{\text{keV}} \right), \quad (4.21)$$

where $\Omega_D \equiv \rho_{\text{DM}}/\rho_{\text{crit}}$ and $h = H_0/(100 \text{ km/s/Mpc})$ is the reduced Hubble constant. While this expression is only accurate up to a factor as large as 10, it illustrates how the relic ionized fraction scales with the dark parameters.

4.3.3 Thermal Decoupling of Atomic Dark Matter

In the early Universe, frequent interactions between the dark photons and the dark fermions keep the DS in thermal equilibrium at a single temperature. Dark photons Compton scatter off dark electrons, hence transferring energy to the DM gas. This energy is then redistributed among the DS fermions through Coulomb scattering between the dark electrons and the dark protons. The typical timescale for this process is [159]

$$\begin{aligned} \tau_{\mathbf{e-p}} &= \frac{\sqrt{\mu_D} T_{\text{DM}}^{3/2}}{\sqrt{2\pi} \alpha_D^2 n_D x_D \ln \Lambda} \\ &\simeq \frac{3.8 \times 10^{-4} \xi^{\frac{3}{2}}}{\alpha_D^2 x_D \ln \Lambda} \left(\frac{0.11}{\Omega_D h^2} \right) \left(\frac{m_D}{\text{GeV}} \right) \left(\frac{\mu_D}{\text{MeV}} \right)^{\frac{1}{2}} \left(\frac{T}{\text{eV}} \right)^{-\frac{3}{2}} \text{ s}, \end{aligned} \quad (4.22)$$

4.3. Thermal History

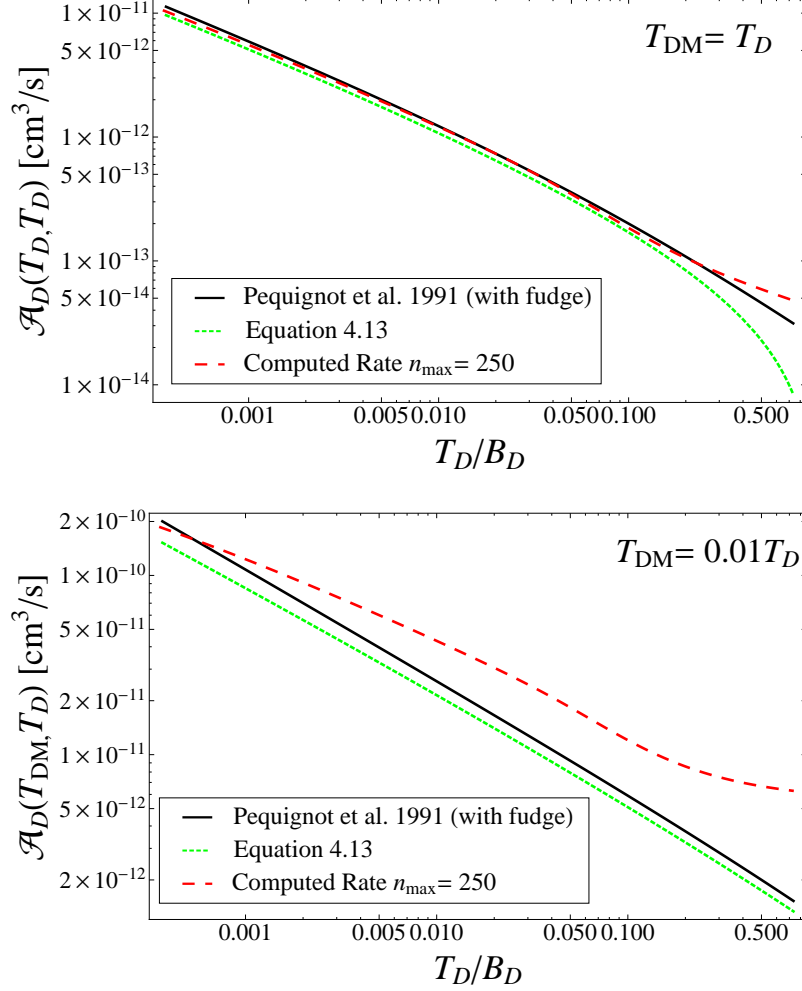


Figure 4.3: Comparison between recombination rates. We have chosen the DS parameters such that they match those of regular atomic hydrogen. We plot the approximate recombination rate given by Eq. (4.13) (green short-dashed line) as well as our rate computed according to Eq. (4.17) including all shells up to $n_{\max} = 250$ (red long-dashed line). For comparison, we also show the recombination rate given in Ref. [195] corrected by a fudge factor of 1.14 as used in `Recfast` [194] (black solid line). *Top Panel:* We compare the rates when the DM and DR are in thermal equilibrium such that $T_{\text{DM}} = T_D$. *Lower Panel:* Similar to the top panel but with $T_{\text{DM}} = 0.01T_D$.

4.3. Thermal History

where we have assumed $T_{\text{DM}} = T_D$ in going from the first line to the second equality. This timescale should therefore be considered as an upper limit since after thermal decoupling, we generally have $T_{\text{DM}} < T_D$. Here, $\ln \Lambda$ is the Coulomb logarithm and is approximately given by

$$\ln \Lambda \simeq \ln \left[\frac{T_{\text{DM}}^{3/2}}{\sqrt{\pi n_D x_D \alpha_D}^{3/2}} \right], \quad (4.23)$$

and has value $\ln \Lambda \sim 30 - 60$ over the parameter space of interest. The Coulomb rate should be compared to the Hubble timescale during radiation domination

$$\tau_{\text{H}} \equiv \frac{1}{2} H^{-1} \simeq \frac{2.42 \times 10^{12}}{\sqrt{3.36 + g_{*,D} \xi^4}} \left(\frac{T}{\text{eV}} \right)^{-2} \text{ s}. \quad (4.24)$$

For all interesting atomic DM parameter space, we always have $\tau_{\mathbf{e}-\mathbf{p}} \ll \tau_{\text{H}}$ and therefore, we can always assume that the dark fermions are in thermal equilibrium among themselves at a single temperature T_{DM} . The neutral dark atoms maintain thermal contact with the dark fermions through elastic collisions. To a good approximation, the cross section for a collision between a dark electron of energy $E_{\mathbf{e}}$ and a dark atom in its ground state is given by [196]

$$\sigma_{\mathbf{e}-\mathbf{H}}(E_{\mathbf{e}}) \simeq \frac{320 \alpha_D^2}{B_D^2} \frac{1}{\sqrt{1 + \gamma (E_{\mathbf{e}}/B_D)^2}}, \quad (4.25)$$

which is valid for $E_{\mathbf{e}} < B_D$ and where $\gamma \simeq 15.69$ is a best-fit parameter. Averaging this cross-section over the Maxwell-Boltzmann velocity distribution of the dark electrons and multiplying by the number density of neutral atoms, we obtain the elastic collision rate between dark atoms and dark electrons

$$\begin{aligned} \Gamma_{\mathbf{e}-\mathbf{H}} &\simeq \frac{5.3 \times 10^8 \alpha_D^2 (1 - x_D)}{\left(1 + 15.07 \left(\frac{T_{\text{DM}}}{B_D} \right)^{\frac{3}{2}} \right)^{0.576}} \left(\frac{T_{\text{DM}}}{m_{\mathbf{e}}} \right)^{\frac{1}{2}} \\ &\times \left(\frac{\Omega_D h^2}{0.11} \right) \left(\frac{B_D}{\text{eV}} \right)^{-2} \left(\frac{m_D}{\text{GeV}} \right)^{-1} \left(\frac{T}{\text{eV}} \right)^3 \text{ s}^{-1}, \end{aligned} \quad (4.26)$$

4.3. Thermal History

which is valid for $T_{\text{DM}}/B_D \lesssim 1$. Again, the timescale associated with this collisional process $\tau_{\mathbf{e}-\mathbf{H}} \equiv \Gamma_{\mathbf{e}-\mathbf{H}}^{-1}$ is much shorter than the Hubble time over most of the dark atom parameter space. We can therefore safely assume that the whole DM sector (ions + neutral dark atoms) is always in thermal equilibrium at a single temperature T_{DM} . For the remaining of this chapter, we thus focus our attention on the interaction between the dark fermions and the DR.

Due to its steep dependence on the DR temperature, Compton heating is always the dominant energy-transfer mechanism between DM and DR at early times. The Compton heating rate is given by [102]

$$\Gamma_{\text{Compton}} = \left[1 + \left(\frac{m_{\mathbf{e}}}{m_{\mathbf{p}}} \right)^3 \right] \frac{64\pi^3 \alpha_D^2 T_D^4}{135 m_{\mathbf{e}}^3} \frac{x_D}{1 + x_D}, \quad (4.27)$$

where $m_{\mathbf{e}}$ and $m_{\mathbf{p}}$ are the masses of the dark electron and dark proton, respectively. The prefactor in the square bracket accounts for Compton heating of both dark electrons and protons. For regular atomic hydrogen, the large photon-to-baryon ratio ensures that Compton heating alone efficiently maintains thermal contact between baryons and the photon bath well after the former recombine into neutral hydrogen and helium. For dark atoms however, there is a large parameter space for which Compton heating becomes inefficient at early times (i.e. for $T_D \gg B_D$). In this case, one must consider other possible energy-exchange mechanisms between the DR and DM. Before dark recombination, photo-ionization heating and photo-recombination cooling are the most important mechanisms that can maintain thermal contact between DM and DR once Compton heating falls out of equilibrium. Free-free (Bremsstrahlung) cooling and free-free heating are also relevant energy-exchange mechanisms for dark atoms. Finally, dark photons can exchange energy with neutral dark atoms through Rayleigh scattering. The volumetric energy-exchange rates for these processes are (in energy per unit time per unit volume, see Appendix B.3)

$$\Pi_{\mathbf{p}-\mathbf{i}}(T_D) = \frac{\alpha_D^3 T_D^2}{3\pi} x_{2s} n_D e^{-\frac{B_D}{4T_D}} F_{\mathbf{p}-\mathbf{i}}(T_D/B_D), \quad (4.28)$$

4.3. Thermal History

$$\Pi_{\text{p-r}} = \frac{2\alpha_D^3 \sqrt{2\pi T_{\text{DM}}}}{3\mu_D^{3/2}} x_D^2 n_D^2 F_{\text{p-r}}\left(\frac{T_D}{B_D}, \frac{T_{\text{DM}}}{T_D}\right), \quad (4.29)$$

$$\Pi_{\text{ff}} \simeq \frac{16\alpha_D^3 \bar{g}_{ff} \sqrt{2\pi T_{\text{DM}}} x_D^2 n_D^2}{(3\mu_D)^{3/2}} \left(\frac{\pi^2 \epsilon (1 + 2\epsilon) - 6\zeta(3)\epsilon^2}{6} \right), \quad (4.30)$$

$$\Pi_{\text{R}} \simeq \frac{430080\zeta(9)\alpha_D^2 n_D (1 - x_D) T_D^9 \epsilon}{\pi^2 B_D^4 m_D m_e^2}, \quad (4.31)$$

where $\Pi_{\text{p-i}}$, $\Pi_{\text{p-r}}$, Π_{ff} and Π_{R} are the photo-ionization heating, photo-recombination cooling, the net free-free heating rate, and the net Rayleigh heating rate, respectively. $F_{\text{p-i}}$ and $F_{\text{p-r}}$ are universal dimensionless functions parametrizing the details of the atomic physics and its interaction with the radiation field. These functions are independent of the model parameters $(\alpha_D, B_D, m_D, \xi)$ and therefore need to be computed only once. The fractional temperature difference is denoted by $\epsilon \equiv (T_D - T_{\text{DM}})/T_D$.

It is instructive to compare the relative magnitude of the different energy-exchange mechanisms. The typical timescale required by the thermal processes to transfer an $\mathcal{O}(1)$ fraction of the kinetic energy of the DM is given by

$$\tau_i \equiv \Gamma_i^{-1} = \left(\frac{2\Pi_i}{3T_{\text{DM}} n_D (1 + x_D)} \right)^{-1}, \quad (4.32)$$

where we have assumed the equipartition of energy among all dark constituents. Comparing Eqs. (4.29) and (4.30), we see that the free-free processes and the bound-free processes have similar leading-order amplitudes. Explicitly taking ratio of the Compton heating rate to that of photo-recombination cooling, we obtain

$$\frac{\Gamma_{\text{Compton}}}{\Gamma_{\text{p-r}}} \sim 10^{-3} \frac{\alpha_D^2}{x_D} \left(\frac{T_{\text{DM}}}{B_D} \right)^{\frac{1}{2}} \left(\frac{m_D}{B_D} \right) \frac{\xi^4 (1 + z)}{F_{\text{p-r}}}. \quad (4.33)$$

We first notice that it is always possible to find a high-enough redshift such that Compton heating dominates over the bound-free energy-exchange channels. As the Universe cools down, the photo-heating can become the

4.3. Thermal History

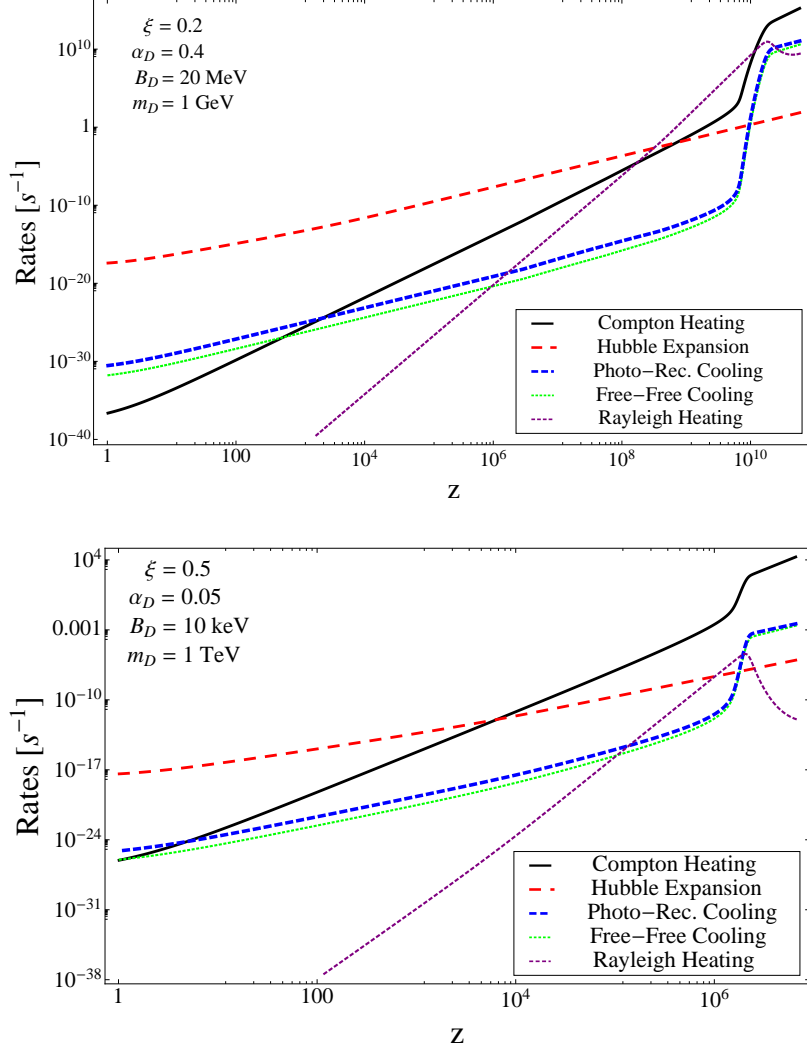


Figure 4.4: Comparison between the rates of different energy-exchange mechanism. We display the rates for Compton heating (solid, black), photo-recombination cooling (short-dashed, blue), and free-free cooling (dotted, green). We also show the Hubble expansion rate (long-dashed, red). The upper panel displays the evolution of the thermal rates for an atomic DM model with $\Upsilon_{\text{BF}} \sim 700$ and $\Upsilon_{\text{R}} \sim 6 \times 10^{-6}$, while the lower panel has $\Upsilon_{\text{BF}} \sim 280$ and $\Upsilon_{\text{R}} \sim 400$.

4.3. Thermal History

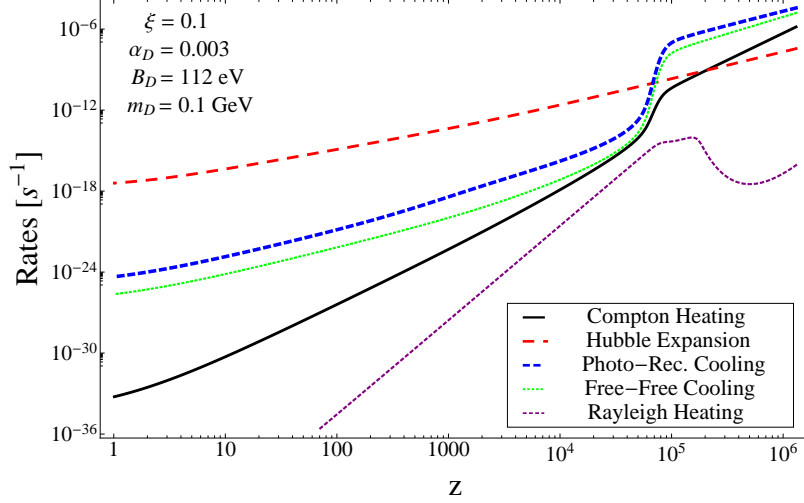


Figure 4.5: Same as Fig. 4.4 but for a model with $\Upsilon_{\text{BF}} \sim 5 \times 10^{-4}$ and $\Upsilon_{\text{R}} \sim 4$.

dominant energy-exchange mechanism for low values of α_D , for a cold DS ($\xi \ll 1$), or for a light DM candidate. Generally, photo-recombination cooling, photo-ionization heating, and the free-free processes must be taken into account when

$$\Upsilon_{\text{BF}} \equiv \left. \frac{\Gamma_{\text{Compton}}}{\Gamma_{\text{p-r}}} \right|_{z_{\text{drec}}} \simeq 5.6 \times 10^5 \alpha_D^2 \xi^3 \left(\frac{0.11}{\Omega_D h^2} \right) \left(\frac{m_D}{\text{GeV}} \right) \lesssim 1. \quad (4.34)$$

Here, z_{drec} is the redshift at which dark atoms recombine. For standard atomic hydrogen, we have $\Upsilon_{\text{BF}} \sim 10^2$ and can therefore neglect any contribution beyond Compton heating.

For relatively large values of the coupling constant α_D , recombination is generally very efficient, resulting in a considerably low ionized fraction $x_D \ll 1$ at late times. Consequently, thermal coupling mechanisms that depend on the presence of free ions to proceed such as Compton heating and free-free heating become relatively inefficient. When this happens, the only remaining mechanism that can maintain thermal equilibrium between the DR and DM for these models is Rayleigh heating. Generally, Rayleigh

4.3. Thermal History

heating takes over Compton heating as the dominant heat-exchange channel after dark recombination if the condition

$$\Upsilon_{\text{R}} \equiv \frac{\Gamma_{\text{Compton}}}{\Gamma_{\text{R}}} \Big|_{z_{\text{drec}}} \simeq \frac{5 \times 10^4 x_D}{1 - x_D} \left(\frac{m_D}{m_{\text{e}}} \right) \lesssim 1, \quad (4.35)$$

is satisfied. This indicates that only models with very small left-over ionization fraction and moderate value of the ratio m_D/m_{e} can obtain a non-negligible contribution from Rayleigh heating. In Figs. 4.4 and 4.5, we compare the rates for the four dominant energy-exchange mechanisms to the Hubble rate. The upper panel of Fig. 4.4 shows a relatively strongly-coupled dark-atom model with $\Upsilon_{\text{R}} \sim 6 \times 10^{-6}$ and $\Upsilon_{\text{BF}} \sim 700$ where Rayleigh heating becomes the dominant thermal-coupling mechanism after the onset of dark recombination. In the lower panel of Fig. 4.4, we illustrate a model with $\Upsilon_{\text{BF}} \sim 280$ and $\Upsilon_{\text{R}} \sim 400$ where Compton heating is the only important mechanism until adiabatic cooling takes over at late times. Figure 4.5 displays an alternate scenario with $\Upsilon_{\text{BF}} \sim 5 \times 10^{-4}$ and $\Upsilon_{\text{R}} \sim 4$ where photo-ionization heating and photo-recombination cooling dominate from early times until adiabatic cooling takes over after recombination.

We therefore see that the thermal evolution of atomic DM strongly depends on the specific choice of dark parameters. In contrast to regular atomic hydrogen whose thermal history can be accurately captured by only considering Compton heating, it is necessary in general to include complementary thermal coupling channels to precisely determine the thermal-decoupling temperature of dark atoms. Put differently, the thermal history of the baryon-photon plasma represents only one possibility among all the regimes that a plasma in an expanding universe can explore. In this respect, it is interesting to realize that the thermal evolution of the baryon-photon plasma is rather simple compared to what it could have been, had the parameters of SM been different.

Putting the different pieces together, the Boltzmann equation governing

the evolution of the DM temperature is then [102]

$$(1+z)\frac{dT_{\text{DM}}}{dz} = 2T_{\text{DM}} + \frac{2(\Pi_{\text{p-r}} - \Pi_{\text{p-i}} - \Pi_{\text{ff}} + \Pi_{\text{R}})}{3k_{\text{B}}n_{\text{D}}(1+x_{\text{D}})H(z)} + \frac{64\pi^3\alpha_{\text{D}}^2T_{\text{D}}^4}{135m_{\text{e}}^3H(z)}\frac{x_{\text{D}}(T_{\text{DM}} - T_{\text{D}})}{1+x_{\text{D}}}\left[1 + \left(\frac{m_{\text{e}}}{m_{\text{p}}}\right)^3\right], \quad (4.36)$$

where the first term of the right-hand side corresponds to adiabatic cooling due to the expansion of the Universe, the second term takes into account the contribution from bound-free and free-free processes as well as Rayleigh scattering, and the last term describes the Compton heating of the DM gas. Note that we have neglected collisional processes such as collisional cooling¹⁴ in the above analysis. These processes are expected to be subdominant compared to the radiative channels considered here, unless $\rho_{\gamma,\text{D}}/\rho_{\text{DM}} \sim \mathcal{O}(1)$, where $\rho_{\gamma,\text{D}}$ is the energy density of the DR.

4.3.4 Joint-Evolution of DM Temperature and Ionization Fraction

The thermal history of the DS sector is specified by simultaneously solving Eqs. (4.7), (4.8), (4.9), and (4.36) together with the initial conditions

$$\begin{aligned} x_{\text{D}}(z_{\text{i}}) &= x_{\text{D,Saha}}(z_{\text{i}}) & x_{2\text{s}}(z_{\text{i}}) &= e^{-\frac{3B_{\text{D}}}{4T_{\text{D}}}}(1 - x_{\text{D}}(z_{\text{i}})) \\ x_{2\text{p}}(z_{\text{i}}) &= 3x_{2\text{s}}(z_{\text{i}}) & T_{\text{DM}}(z_{\text{i}}) &= T_{\text{D}}(z_{\text{i}}), \end{aligned}$$

where $x_{\text{D,Saha}}$ is the Saha equilibrium ionization fraction and z_{i} is the initial redshift. It is obtained by solving the Saha equation

$$\frac{x_{\text{D,Saha}}^2}{1 - x_{\text{D,Saha}}} = \frac{1}{n_{\text{D}}}\left[\left(\frac{m_{\text{e}}m_{\text{p}}T_{\text{D}}}{2\pi m_{\text{D}}}\right)^{3/2}e^{-B_{\text{D}}/T_{\text{D}}}\right]. \quad (4.37)$$

¹⁴The collisional excitation of a neutral dark atom followed by the emission of a dark photon. The result of this process is a net energy transfer from the DM gas to the DR thermal bath, hence the name collisional *cooling*.

4.3. Thermal History

These ionization and temperature evolution equations are extremely stiff at early times and therefore require the use of a stiff solver. We assume that adiabatic cooling dominates the evolution of the DR temperature such that

$$T_D(z) = T_{\text{CMB}}^{(0)} \xi(1+z), \quad (4.38)$$

where $T_{\text{CMB}}^{(0)}$ is the temperature of the CMB today. Note that dark recombination always happens after the dark electrons and positrons annihilate¹⁵ and we have therefore neglected the change in the number of relativistic species (see Eq. 4.6). Equation (4.38) is valid as long as we can neglect the energy injected into the dark radiation bath in a Hubble time, that is

$$\frac{\delta\rho_{\gamma,D}}{\rho_{\gamma,D}} \simeq \frac{\Pi_{\text{p-r}}\tau_{\text{H}}}{\rho_{\gamma,D}} \ll 1. \quad (4.39)$$

In the above, we have only included the contribution from photo-recombination. In practice, all mechanisms leading to a net energy transfer from the DM to the DR should be included. Before DM recombination, the right-hand side of Eq. (4.39) is almost a constant and is equal to

$$\frac{\delta\rho_{\gamma,D}}{\rho_{\gamma,D}} \sim 10^2 \frac{\alpha_D^6}{\xi^4} \left(\frac{m_D}{\text{GeV}}\right)^{-2} \left(\frac{B_D}{\text{eV}}\right)^{-1} \ll 1. \quad (4.40)$$

Models not respecting this bound are likely to require a more involved analysis since the DR field cannot be taken to be thermal in these cases. A full solution to the energy-transfer problem is out of the scope of this thesis and we therefore focus on models obeying Eq. (4.40).

We can now compare our improved treatment of the dark-atom recombination and thermal decoupling to the “standard treatment” described in Ref. [125]. The “standard treatment” combines Eqs. (4.7), (4.8), and (4.9) into a single differential equation for x_D and uses the approximate recombination rate given in Eq. (4.13). Its DM temperature evolution equation only includes Compton heating and adiabatic cooling. In Fig. 4.6, we display the

¹⁵Since $B_D \simeq (1/2)\alpha_D^2 m_e$ and dark recombination takes place for $T_D \ll B_D$, we always have $T_D \ll m_e$ at the onset of dark recombination as $\alpha_D < 1$.

4.3. Thermal History

ionized-fraction and temperature evolution for a model with $\Upsilon_{\text{R}} \sim 6 \times 10^{-6}$ and $\Upsilon_{\text{BF}} \sim 700$. We see that the redshift evolution of our improved ionization calculation closely matches the standard treatment at early times. At late times however, our improved calculation predicts an ionization fraction that differs from the standard treatment by as much as 60%. The very good agreement at early times follows from the fact that the ionized fraction of the DS is initially mostly controlled by the Saha equilibrium condition, and therefore insensitive to the exact value of the recombination coefficient. At late times however, the Saha approximation breaks down and the ionized fraction becomes sensitive to the recombination rates. As can be seen in the lower panel of Fig. 4.6, the inclusion of Rayleigh scattering postpones the thermal decoupling of DM, resulting in a DM gas that is hotter than one would expect by considering only Compton heating. Since the recombination coefficient is very sensitive to the DM temperature, this explains the somewhat large difference in x_{D} at low redshift.

Figure 4.7 displays the ionization and temperature evolution of a dark-atom model for which Compton heating is the dominant thermal coupling mechanism until late times ($\Upsilon_{\text{BF}} \sim 2 \times 10^5$ and $\Upsilon_{\text{R}} \sim 10^2$). In this case, the usual calculation accurately captures the behaviour of both the ionization evolution and the DM temperature. This is not a surprise, since the standard treatment was designed to capture this specific regime of the dark plasma. The small difference in the ionization fraction (up to $\sim 12\%$) at late times is entirely due to our more accurate recombination coefficient which includes the effects of high- n shells on the recombination process. In Fig. 4.8, we display the ionization history (upper panel) and temperature evolution (lower panel) for a model with $\Upsilon_{\text{BF}} \sim 5 \times 10^{-4}$ ($\Upsilon_{\text{R}} \sim 4$). Not only does the standard calculation fail to predict the right recombination redshift, it also underestimates the late-time ionization fraction by more than 50%. Since the Saha equilibrium does not hold for these weakly-coupled models, their ionization evolution is strongly determined by the value of the recombination coefficient. In the lower panel, we see that the inclusion of the bound-free and free-free processes delays the thermal decoupling of DM, hence postponing the onset of dark recombination. As the recombination coefficient is

4.3. Thermal History

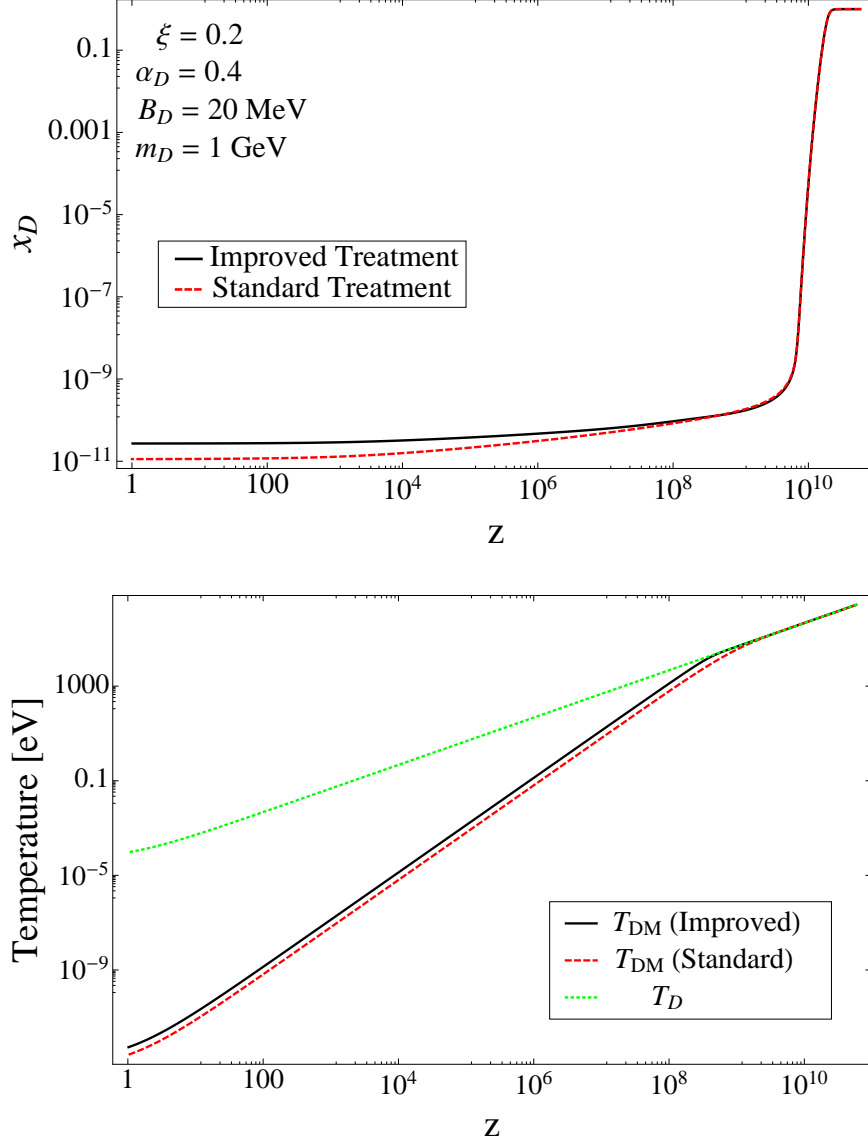


Figure 4.6: Comparison between our improved treatment of dark recombination and the standard treatment. We display results for a relatively strongly-coupled DS with $\Upsilon_R \sim 6 \times 10^{-6}$ and $\Upsilon_{BF} \sim 700$. The upper panel shows the evolution of the ionization fraction as a function of redshift while the lower panel shows the corresponding evolution of the DM and DR temperatures.

4.3. Thermal History

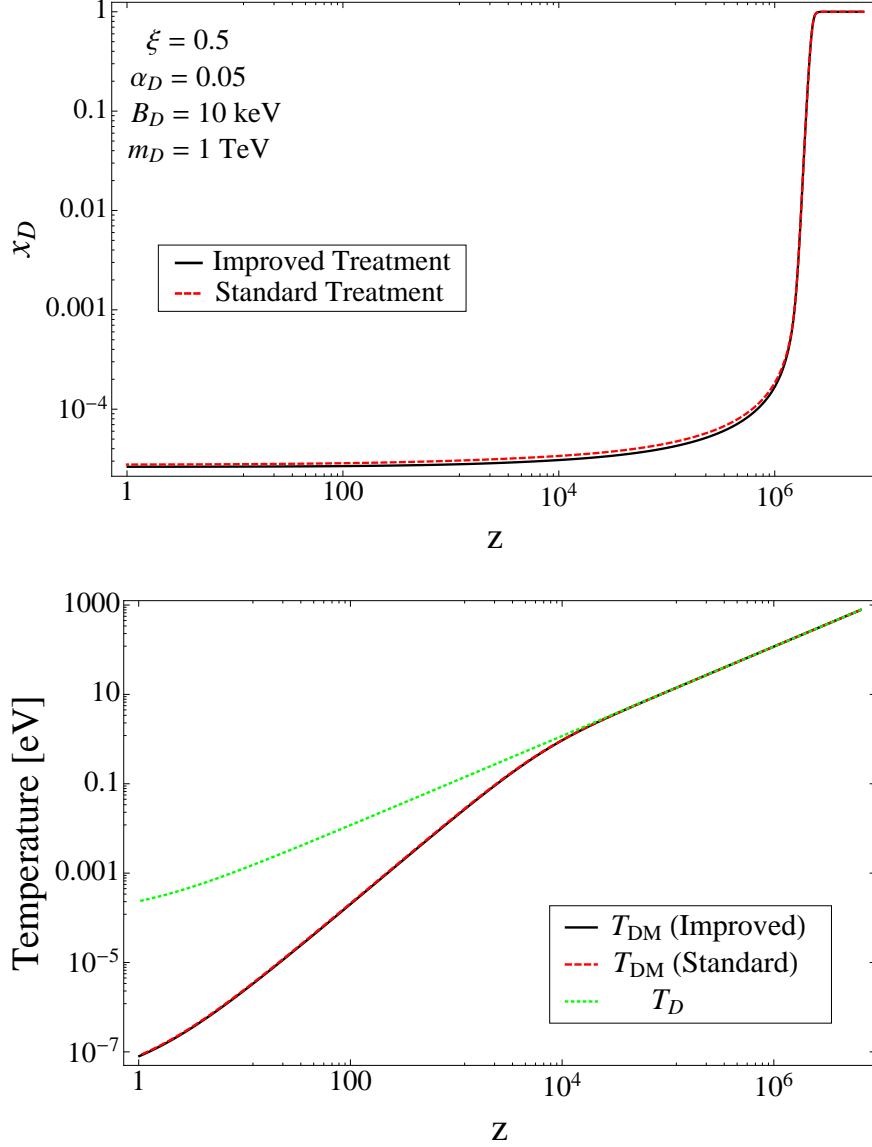


Figure 4.7: Comparison between our improved treatment of dark recombination and the standard treatment. We display results for a DS where Compton heating always dominates the thermal coupling between the DR and DM. Here, $\Upsilon_{BF} \sim 1.8 \times 10^5$ and $\Upsilon_R \sim 10^2$. The upper panel shows the evolution of the ionization fraction as a function of redshift while the lower panel shows the corresponding evolution of the DM and DR temperatures.

4.3. Thermal History

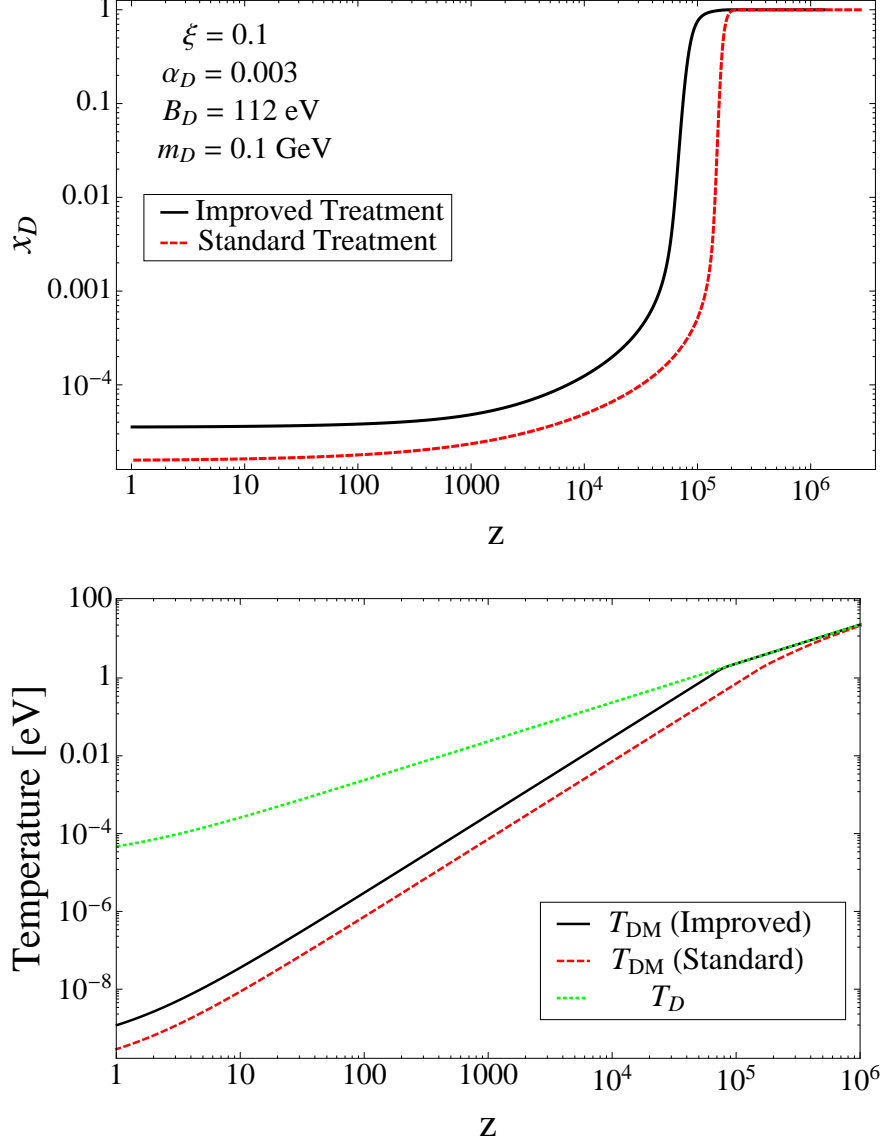


Figure 4.8: Comparison between our improved treatment of dark recombination and the standard treatment. We display results for a weakly-coupled DS with $\Upsilon_{\text{BF}} \sim 5 \times 10^{-4}$ and $\Upsilon_{\text{R}} \sim 4$. The upper panel shows the evolution of the ionization fraction as a function of redshift while the lower panel shows the corresponding evolution of the DM and DR temperatures.

very sensitive to the DM temperature (see Fig. 4.3), this delayed thermal decoupling acts to suppress the recombination rate, hence leaving a larger ionized fraction at late times.

In summary, the standard recombination treatment originally described in [101] can only be accurately applied to dark-atom models for which both bound-free and Rayleigh heating are negligible. For these scenarios, the late-time difference between our improved calculation and the standard treatment is almost entirely due our more accurate recombination coefficient, which properly accounts for the effects of excited atomic states and for the difference between the DM and DR temperature. On the other hand, the standard treatment generally overestimates the thermal-decoupling temperature for atomic DM models with $\Upsilon_{\text{BF}} \lesssim 1$ or $\Upsilon_{\text{R}} \lesssim 1$. As a consequence, the standard treatment tends to underestimate the DM ionized fraction at late times for these types of models.

4.3.5 Existence of Dark Atoms

As the dark fine-structure constant is decreased and the mass of the dark proton is increased, it becomes progressively more difficult for oppositely-charged dark fermions to find each other and form neutral bound states. There exist critical values of the masses and coupling constants beyond which dark atoms do not form and the dark plasma remains ionized even for $T_D \ll B_D$. Generally, this happens if the recombination rate is smaller than the Hubble expansion rate, when it becomes energetically favourable to form dark atoms. Using Eqs. (4.17) and (4.24), dark atoms can form only if the following condition is satisfied

$$\frac{\alpha_D^6}{\xi} \left(\frac{\Omega_D h^2}{0.11} \right) \left(\frac{m_D}{\text{GeV}} \right)^{-1} \left(\frac{B_D}{\text{keV}} \right)^{-1} \gtrsim 1.5 \times 10^{-16}, \quad (4.41)$$

where we have used $T_D \simeq T_{\text{DM}} \simeq 0.02 B_D$ which corresponds to the usual DS temperature at the onset of dark recombination. Models violating this bound are effectively hidden charged DM models similarly to those discussed in Refs. [180, 181]. For standard atomic hydrogen, the left-hand side of

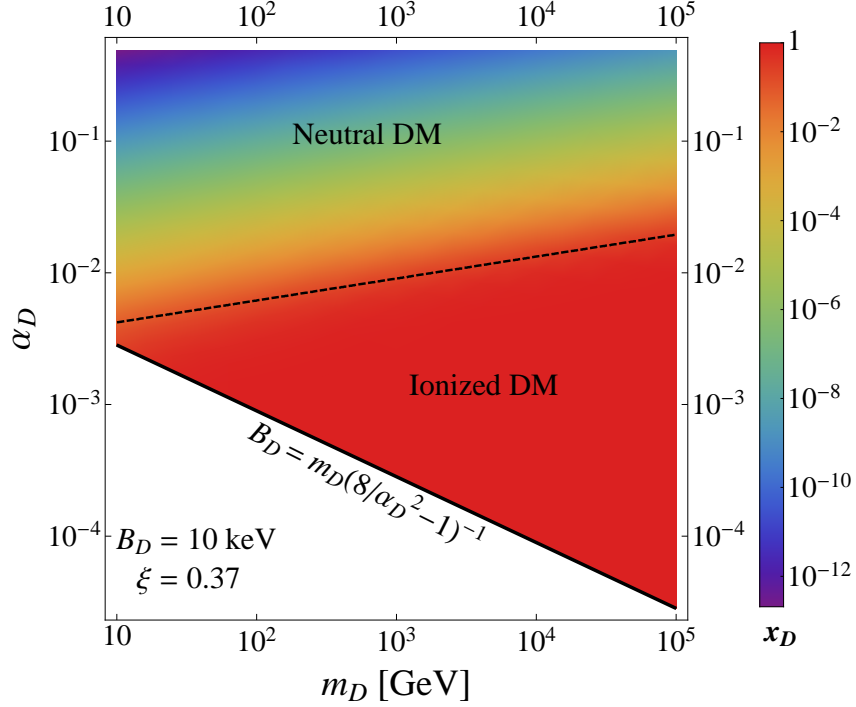


Figure 4.9: Late-time ionized fraction as a function of m_D and α_D for a dark-atom model with $B_D = 10$ keV. The dashed line corresponds to the bound given in Eq. (4.41), delimiting the mostly ionized models (below the line) from the region of parameter space dominated by dark atoms at late times (above the line).

Eq. (4.41) is equal to 2.4×10^{-12} , which is well above the bound as expected. We display the constraint (4.41) in Fig. 4.9 (dashed line) together with the values of the late-time ionized fraction for a model with $B_D = 10$ keV. We see that Eq. (4.41) delimits very well the region where the DS is mostly ionized at late times.

4.4 Evolution of Dark-Matter Perturbations

Having determined the evolution of the background ionized fraction and temperatures, we now turn our attention to the evolution of cosmological perturbations in the atomic DM scenario. In this theory, the DM and DR form a tightly-coupled plasma in the early Universe, much like the baryon-photon fluid. Once modes enter the horizon, the pressure provided by the relativistic dark photons gives rise to a restoring force opposing the gravitational infall of DM, hence leading to dark acoustic oscillations (DAO) in the plasma. Compared to a CDM model, the presence of these DAOs delays the onset of DM fluctuation growth until the epoch of kinetic decoupling. In addition, atomic DM fluctuations miss out on the kick due to the decaying gravitational potential when they cross inside the Hubble horizon [81]. We therefore generically expect DM fluctuations to be suppressed on small scales in atomic DM models.

We begin this section by giving the key equations describing the DM and DR perturbations, emphasizing the new collision term between these two constituents of the DS. We then discuss the different contributions to the opacity of the dark plasma and study their impact on the kinetic decoupling epoch. We then describe the various regimes that the perturbations in the dark plasma encounter as they evolve through the cosmic ages. We finally present numerical examples of these different regimes, both in Fourier space and in configuration space.

4.4.1 Perturbation Equations

The equations governing the evolution of atomic DM fluctuations are very similar to those describing the baryon-photon plasma. Special care must however be taken to include all the relevant contribution to the opacity of the DM to DR. The Boltzmann equations for DM are

$$\dot{\delta}_D + \theta_D - 3\dot{\phi} = 0, \tag{4.42}$$

$$\dot{\theta}_D + \frac{\dot{a}}{a}\theta_D - c_D^2 k^2 \delta_D - k^2 \psi = \frac{R_D}{\tau_D}(\theta_{\tilde{\gamma}} - \theta_D), \quad (4.43)$$

where we closely followed the notation of Ref. [100] in conformal Newtonian gauge. Here, δ_D is the DM density contrast, θ_D and $\theta_{\tilde{\gamma}}$ are the divergence of the DM and DR velocity, respectively; ϕ and ψ are the gravitational scalar potentials, $R_D \equiv 4\rho_{\tilde{\gamma}}/3\rho_D$, c_D is the sound speed of DM, k is the wavenumber of the mode and τ_D^{-1} is the opacity of the dark plasma. Here, the subscript $\tilde{\gamma}$ always refers to the dark photons. The right-hand side of Eq. (4.43) represents the collision term between the DM and the DR. At early times, we generally have $R_D \gg 1$ and $\tau_D \ll \tau_H$, implying that the DM is effectively dragged along by the DR. The latter evolves according to the following Boltzmann equations:

$$\dot{\delta}_{\tilde{\gamma}} + \frac{4}{3}\theta_{\tilde{\gamma}} - 4\dot{\phi} = 0; \quad (4.44)$$

$$\dot{\theta}_{\tilde{\gamma}} - k^2\left(\frac{1}{4}\delta_{\tilde{\gamma}} - \frac{F_{\tilde{\gamma}2}}{2}\right) - k^2\psi = \frac{1}{\tau_D}(\theta_D - \theta_{\tilde{\gamma}}); \quad (4.45)$$

$$\dot{F}_{\tilde{\gamma}2} = \frac{8}{15}\theta_{\tilde{\gamma}} - \frac{3}{5}kF_{\tilde{\gamma}3} - \frac{9}{10\tau_D}F_{\tilde{\gamma}2}; \quad (4.46)$$

$$\dot{F}_{\tilde{\gamma}l} = \frac{k}{2l+1} [lF_{\tilde{\gamma}(l-1)} - (l+1)F_{\tilde{\gamma}(l+1)}] - \frac{1}{\tau_D}F_{\tilde{\gamma}l}. \quad (4.47)$$

Eqs. (4.44) and (4.45) describe the evolution of the dark-photon over-densities ($\delta_{\tilde{\gamma}}$) and of the dark-photon velocity, respectively. It is also necessary to solve for the hierarchy of dark-photon multipoles (Eqs. (4.46) and (4.47)) to properly account for DR diffusion and its impact on DM perturbations. Since our focus is to describe the clustering of DM in this model, we do not solve for the DR polarization, which in any case has a negligible impact on DM fluctuations.

During the radiation-dominated epoch, the energy density of the DR is generally subdominant compared to the contribution from regular photons and neutrinos (see Eq. (4.5)). Therefore, the time-dependence of the grav-

4.4. Evolution of Dark-Matter Perturbations

itational potentials ϕ and ψ is very similar to the standard CDM case for which we have [36]

$$\phi \simeq -\phi_{\text{p}} \left[\frac{\sin(k\tau/\sqrt{3}) - (k\tau/\sqrt{3}) \cos(k\tau/\sqrt{3})}{(k\tau/\sqrt{3})^3} \right], \quad (4.48)$$

where τ stands for the conformal time and ϕ_{p} is the primordial amplitude. Since the gravitational potential is an oscillatory function, Eqs. (4.42) and (4.44) essentially describe driven harmonic oscillators where the driving force is provided by the baryon-photon plasma. Indeed, taken as a whole, the equations describing the dark plasma and the baryon-photon plasma in the early Universe correspond to a system of coupled harmonic oscillators. Such a system is known to exhibit resonance phenomena whenever the driving frequency approaches the natural frequency of the oscillator. For the dark plasma however, we always have

$$R_D \ll R \equiv \frac{4\rho_{\gamma}}{3\rho_{\text{b}}}, \quad (4.49)$$

where ρ_{γ} and ρ_{b} are the energy densities of regular photons and baryons, respectively. As the sound speed of a plasma is approximately given by $c_{\text{p}} = 1/\sqrt{3(1+R^{-1})}$, Eq. (4.49) implies that the sound speed of the dark plasma is always smaller than that of the baryon-photon plasma. Thus, the dark plasma is never driven close to its resonance threshold¹⁶.

4.4.2 Dark Opacity and Kinetic Decoupling

The opacity of the dark plasma dictates the strength of the coupling between DM and DR. Heuristically, τ_D can be considered as the mean free path a dark photon travels between collisions with a dark ion or a dark atom. As such, R_D/τ_D is approximately the momentum-transfer rate between the DR and the DM. As in the case of the thermal coupling of DM to DR, many mechanisms contribute to the exchange of momentum between the two dark

¹⁶While resonant enhancement does not occur for the simple atomic DM scenario considered in this thesis, it is nevertheless possible to construct a model where such resonance happens. This is an interesting possibility that we leave for future work

4.4. Evolution of Dark-Matter Perturbations

component. In addition to the usually-considered Compton-scattering term, we also include the contribution from Rayleigh scattering as well as the contribution from bound-free processes. The opacity is then

$$\tau_D^{-1} = \tau_{\text{Compton}}^{-1} + \tau_{\text{R}}^{-1} + \tau_{\text{p-i}}^{-1}. \quad (4.50)$$

The Compton scattering term is given by

$$\tau_{\text{Compton}}^{-1} = an_D x_D \sigma_{\text{T},D} \left[1 + \left(\frac{m_{\text{e}}}{m_{\text{p}}} \right)^2 \right], \quad (4.51)$$

where $\sigma_{\text{T},D} \equiv 8\pi\alpha_D^2/(3m_{\text{e}}^2)$ is the dark Thomson cross section and a is the scale factor. The factor in the bracket accounts for Compton scattering off dark protons. The contribution from Rayleigh scattering can be written as

$$\tau_{\text{R}}^{-1} = an_D(1-x_D)\langle\sigma_{\text{R}}\rangle \simeq 32\pi^4 an_D(1-x_D)\sigma_{\text{T},D} \left(\frac{T_D}{B_D} \right)^4, \quad (4.52)$$

which is valid for $T_D \ll B_D$. Here σ_{R} is the cross-section for Rayleigh scattering (see Eq. (B.17)) and $\langle \dots \rangle$ denotes a thermal average with respect to the Planck function describing the distribution of dark photons. Finally, the photoionization contribution is

$$\begin{aligned} \tau_{\text{p-i}}^{-1} &= a \sum_{n,l} n_{nl} \langle \sigma_{nl} \rangle \\ &\simeq an_D x_{2s} \frac{\pi\alpha_D^3}{6\zeta(3)T_D^2} e^{-B_D/(4T_D)} G_{250}^{2s} \left(\frac{T_D}{B_D}, 1 \right), \end{aligned} \quad (4.53)$$

where n_{nl} and σ_{nl} are the number density and the photoionization cross-section for dark atoms in quantum state nl , and $\zeta(x)$ is the Riemann zeta function.

For most atomic DM models, the Compton scattering contribution to the opacity dominates before dark recombination, with photoionization giving a subdominant contribution for models with $\Upsilon_{\text{BF}} \lesssim 1$. Once a significant number of dark atoms has recombined, Rayleigh scattering can become the dominant source of opacity for models with $\Upsilon_{\text{R}} \lesssim 1$.

4.4. Evolution of Dark-Matter Perturbations

The DR effectively begins free-streaming when its mean-free path becomes comparable to the size of the Hubble horizon, that is, $\tau_D^{-1} \simeq H$. In a model for which Compton scattering dominates the interactions between the DR and the DM, the onset of the free-streaming epoch is independent of the temperature and only depends of the fraction of ionized dark atoms,

$$x_D|_{\text{dec}}^{\text{Compt}} \simeq \min \left[1, \frac{3.7 \times 10^{-10}}{\alpha_D^6} \left(\frac{\Omega_D h^2}{0.11} \right)^{-1} \left(\frac{B_D}{\text{keV}} \right)^2 \left(\frac{m_D}{\text{GeV}} \right) \right], \quad (4.54)$$

where we have assumed that the DR decoupling happens in the radiation-dominated epoch and have neglected the contribution from dark protons. If the second argument in the $\min[.,.]$ function is larger than unity, it indicates that dark photons begin free-streaming at a very early epoch, making them difficult to distinguish from massless neutrinos. For a strongly-coupled DS which have $\Upsilon_R \lesssim 1$, the decoupling of dark photons happens much later and is governed by Rayleigh scattering of dark photons off neutral dark atoms. This leads to a decoupling temperature

$$\frac{T_D}{B_D} \Big|_{\text{dec}}^{\text{R}} \simeq \frac{7 \times 10^{-4}}{\alpha_D^{3/2}} \left[\left(\frac{\Omega_D h^2}{0.11} \right)^{-1} \left(\frac{B_D}{\text{keV}} \right)^2 \left(\frac{m_D}{\text{GeV}} \right) \right]^{\frac{1}{4}}, \quad (4.55)$$

where we have taken the limit $x_D|_{\text{dec}} \ll 1$. It is important to note that for most atomic DM scenarios, Compton scattering alone is responsible for the DM-DR coupling.

The key quantity governing the size of the smallest DM structure in the Universe is the temperature at which DM kinematically decouples from the DR (i.e. the dark drag epoch). This temperature can approximately be determined by solving the condition $R_D/\tau_D \simeq H$. For models dominated by Compton scattering, this leads to a kinetic decoupling temperature given by

$$\frac{T_D}{B_D} \Big|_{\text{drag}}^{\text{Compt}} \simeq \frac{5.8 \times 10^{-13}}{\alpha_D^6 \xi^4 x_D|_{\text{drag}}} \left(\frac{B_D}{\text{keV}} \right) \left(\frac{m_D}{\text{GeV}} \right). \quad (4.56)$$

This is effectively an implicit equation for the drag-epoch temperature since

the right-hand side involves the ionized fraction of dark atoms evaluated at that epoch. Taking $x_D|_{\text{drag}} \sim 1$ leads to a lower bound on the temperature at which DM ceases to be dragged along by the DR. If $\Upsilon_R \lesssim 1$, the kinetic decoupling occurs when Rayleigh scattering becomes ineffective. In this case, we obtain

$$\left. \frac{T_D}{B_D} \right|_{\text{drag}}^{\text{R}} \simeq 7 \times 10^{-4} \left[\frac{1}{\alpha_D^6 \xi^3} \left(\frac{B_D}{\text{keV}} \right) \left(\frac{m_D}{\text{GeV}} \right) \right]^{\frac{1}{5}}, \quad (4.57)$$

where we have used $x_D|_{\text{drag}} \ll 1$, which is a necessary condition for Rayleigh scattering to dominate over Compton scattering.

DM fluctuations on subhorizon length scales at the drag epoch have a significantly different evolution than those of a standard Λ CDM model. In particular, the suppression of small-scale power due to the dark-photon pressure leads to a minimal halo mass at late times. We will discuss this effect further in section 5.1.1.

4.4.3 Regimes of the Dark Plasma

We now turn our attention to the formal solutions to Eqs. (4.42) to (4.47). These admits different regimes depending on the relative values of the opacity, wavenumber, and Hubble expansion rate. These regimes are

1. **Superhorizon Regime:** This regime occurs when the wavelength characterizing a mode is still larger than the Hubble scale, $k < H$. As for the CDM case, cosmological perturbations do not significantly evolve in this regime. We therefore do not discuss this case any further since atomic DM is indistinguishable from standard CDM for these modes.
2. **Dark-Acoustic-Oscillation (DAO) Regime:** Once modes cross into the Hubble horizon, the microphysics governing the interaction between the DM and the DR becomes effective. If the mean-free-path of dark photons between collisions with dark fermions is much smaller than the wavelength of a given mode ($k\tau_D \ll 1$), then we can

consider the DM and the DR to be tightly-coupled and to form an almost perfect fluid at this scale. In this case, the DR pressure can effectively counteract the pull from the gravitational potential, leading to the propagation of acoustic oscillations in the dark plasma. This DAO regime occurs for wavelengths larger than the diffusion length scale of the dark photons, that is,

$$H < k < k_D, \quad (4.58)$$

where k_D is diffusion damping scale and is defined by [36]

$$\frac{1}{k_D^2(\tau)} = \int_0^\tau \frac{\tau_D d\tau'}{6(1 + R_D^{-1})} \left[\frac{1}{R_D^2 + R_D} + \frac{8}{9} \right]. \quad (4.59)$$

Heuristically, $1/k_D$ corresponds approximately to the average distance travelled by a dark photon in a Hubble time. Note that Eq. (4.59) is the result of a first-order expansion in $k\tau_D$ of the dispersion relation of DAOs and therefore is only accurate in the limit $k\tau_D \ll 1$. In the DAO regime, DM fluctuations undergo constant-amplitude oscillations

$$\delta_D \sim \exp \left\{ ik \int d\tau \tilde{c}_p \right\}, \quad (4.60)$$

where $\tilde{c}_p = 1/\sqrt{3(1 + R_D^{-1})}$ is the sound speed of the dark plasma. Due to these oscillations, DM fluctuations entering the horizon in this regime miss out on both the logarithmic growth and the horizon kick. Thus, despite the absence of damping in the DAO regime (besides the small contribution from Hubble expansion), DM perturbations still generally display smaller amplitudes at these scales when compared to a standard CDM model.

3. **Diffusion-Damping Regime:** Once the average distance travelled by a dark photon during a Hubble time becomes comparable with the wavelength of a given mode, DR can effectively diffuse out of overdensities at these scales. If the momentum transfer rate between the

DR and the DM is larger than the plasma oscillation frequency,

$$k_D < k < \frac{1}{\tilde{c}_p} \frac{R_D}{\tau_D}, \quad (4.61)$$

then DM is dragged along by the escaping dark photons, effectively erasing DM fluctuations on these scales. The time-dependence of the DM perturbations is then given by

$$\delta_D \sim \exp \left\{ ik \int d\tau \tilde{c}_p \right\} \exp \left\{ -\frac{k^2}{k_D^2} \right\}, \quad (4.62)$$

leading to an exponential damping on fluctuations on scale smaller than the diffusion length. As before, we have assumed the dark plasma is tightly-coupled ($k\tau_D \ll 1$) in deriving Eq. (4.62). When this condition ceases to be satisfied, the damping of DM fluctuations is no longer exponential and Eq. (4.62) breaks down. Note that the diffusion damping regime ends when $k\tilde{c}_p \sim R_D/\tau_D$, since DM ceases to be dragged by the DR when this condition is satisfied.

4. **Acoustic-Damping Regime** When the mean-free-path of dark photons becomes comparable to the wavelength of a given mode ($k\tau_D \gtrsim 1$), the dark plasma ceases to behave like a single perfect fluid. Due to the slow reaction of DM to the motion of dark photons in this regime, acoustic oscillations in the DM fluid start to significantly lag those propagating in the DR fluid. This in turns leads to viscous dissipation in the dark plasma resulting in the damping of DM fluctuations at these scales. Note however that this acoustic damping is weaker than the exponential damping characteristic of the tightly-coupled diffusion regime. Generally, acoustic damping occurs for modes satisfying the condition

$$H < \frac{1}{\tau_D} < k < \frac{R_D}{\tilde{c}_p \tau_D}. \quad (4.63)$$

The last inequality ensures that a significant amount of momentum is still transferred to the DM during acoustic damping. Physically, this regime is characterized by the development of anisotropic stress in the

dark fluid associated with a significant dark-photon quadrupole moment. As such, it is therefore difficult to obtain an analytical solution to the evolution of DM fluctuations in this regime.

5. **Gravitationally-Dominated Regime:** When the momentum transfer rate between the DR and atomic DM falls below the oscillation frequency of the dark photons, that is

$$H < \frac{R_D}{\tau_D} < k\tilde{c}_p, \quad (4.64)$$

the dark plasma ceases to behave like a single fluid and we must consider the DM and the DR fluctuations separately. In this regime, the evolution of the DM perturbations is determined by a competition between the gravitational potential dominated by the baryon-photon plasma and the remaining pressure of the DR. Since both of these contributions are oscillatory in nature, the evolution of the DM fluctuations in this regime can be rather complex. Essentially, we can view DM perturbations as forced oscillators driven by two distinct forces oscillating with difference frequencies. Explicitly, the equation governing the evolution of DM fluctuations is

$$\ddot{\delta}_D + \left(H + \frac{R_D}{\tau_D}\right) \dot{\delta}_D = S_G(k, \tau) - \frac{R_D}{\tau_D} \theta_{\tilde{\gamma}}, \quad (4.65)$$

where the gravitational source term is given by

$$S_G(k, \tau) = 3\ddot{\phi} - k^2\psi + 3\dot{\phi} \left(H + \frac{R_D}{\tau_D}\right). \quad (4.66)$$

The dark-photon driving term can be obtained from rearranging Eqs. (4.45) and (4.44)

$$\theta_{\tilde{\gamma}} = \theta_D + \frac{3\tau_D}{4} \left[\ddot{\delta}_{\tilde{\gamma}} + \frac{k^2}{3} \delta_{\tilde{\gamma}} + \frac{k^2}{6} F_{\tilde{\gamma}2} - 4\dot{\phi} + \frac{4}{3} k^2 \psi \right]. \quad (4.67)$$

In the limit that a DM fluctuation enters this regime after being exponentially damped by the diffusion of dark photons, the evolution of DR

perturbations is dominated by the gravitational potential. Neglecting the small quadrupole moment of the dark photons, this implies that the term in the square bracket of Eq. (4.67) is very close to zero. We thus have $\theta_{\tilde{\gamma}} \simeq \theta_D$ in this limit and Eq. (4.65) reduces to

$$\ddot{\delta}_D + H\dot{\delta}_D = 3\ddot{\phi} - k^2\psi + 3H\dot{\phi}. \quad (4.68)$$

Eq. (4.68) is to the usual equation describing the growth of standard CDM fluctuations. It implies that DM fluctuations grow logarithmically with the scale factor during the radiation-dominated epoch.

On the other hand, for modes that enter the gravitationally-dominated regime before being substantially damped by photon diffusion, the dark-photon driving term cannot be neglected in Eq. (4.65). In this case, the dark-photon quadrupole moment is non-negligible in Eq. (4.67), leading to an oscillatory pressure term with

$$\theta_{\tilde{\gamma}} \sim e^{\frac{ik\tau}{\sqrt{3}}}. \quad (4.69)$$

The gravitational potential contribution $S_G(k, \tau)$ also oscillates, but with a somewhat lower frequency $\sim k/\sqrt{3(1+R)}$. As these oscillators can randomly go in-phase and out-of phase, some damping or even some amplification can occur in this regime. However, since the momentum transfer rate R_D/τ_D is decaying more rapidly than $S_G(k, \tau)$, the gravitational potential rapidly becomes the dominant contribution to the evolution of DM fluctuations. Indeed, while $R_D/\tau_D \propto \tau^{-n}$ with $n \geq 3$ (depending on which process dominates the calculation of the opacity), $S_G(k, \tau) \propto \tau^{-2}$. Therefore, the DM fluctuations rapidly settle into the logarithmic growing mode.

6. **Kinetically-Decoupled Regime:** As the momentum transfer rate between atomic DM and DR falls below the Hubble rate, $R_D/\tau_D < H$, DM essentially stops interacting with the dark photons and begin behaving like the standard CDM. Modes entering this regime during radiation domination begin growing logarithmically with the scale factor

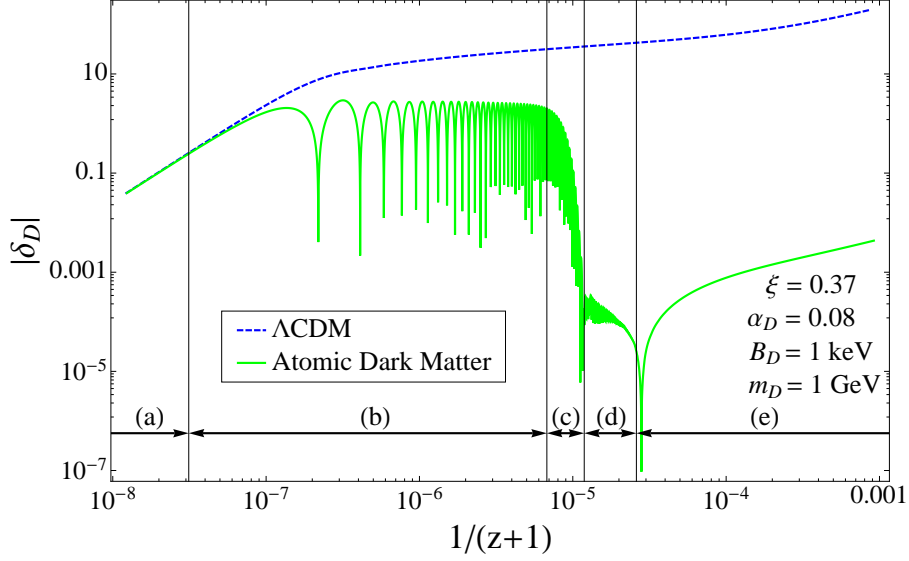


Figure 4.10: Redshift evolution of an atomic DM fluctuation with $k = 70 \text{ Mpc}^{-1}$ in synchronous gauge (green solid line). We identify on the figure the different regimes that the DM fluctuation encounters during its evolution. These are: (a) superhorizon; (b) DAO; (c) diffusion damping; (d) gravitationally-dominated; and (e) kinetically-decoupled. For the case displayed here, the fluctuation enters the horizon while the dark plasma is tightly-coupled and therefore undergoes acoustic oscillations. Once $k_D \sim k$, the fluctuation becomes exponentially damped by dark-photon diffusion. This damping ceases to be effective when the rate of momentum transfer between the DR and DM falls below the oscillation frequency of dark-photon fluctuations. When this happens, the fluctuation enters the gravitationally-dominated regime where the perturbation rapidly settles into the logarithmic growing mode. The sharp feature around $(z+1)^{-1} = 3 \times 10^{-5}$ is an artifact of plotting the absolute value of the fluctuation. For comparison, we also show the behavior of a CDM fluctuation with the same wavenumber.

while modes entering during matter domination grow linearly with a . In all cases, modes that enter the Hubble horizon after kinetic decoupling are undistinguishable from those of standard CDM.

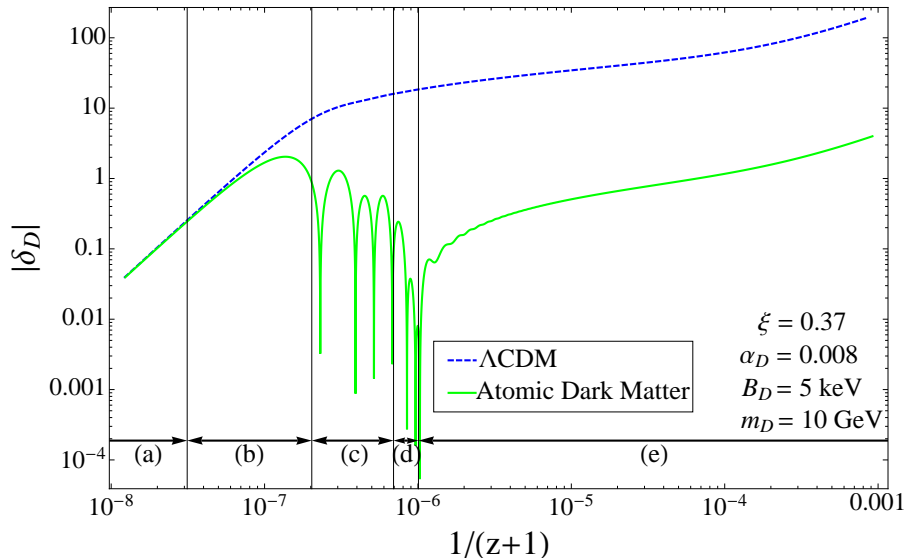


Figure 4.11: Redshift evolution of an atomic DM fluctuation with $k = 70 \text{ Mpc}^{-1}$ in synchronous gauge (green solid line). We identify on the figure the different regimes that the DM fluctuation encounters during its evolution. These are: (a) superhorizon; (b) DAO; (c) Acoustic damping; (d) gravitationally-dominated; and (e) kinetically-decoupled. For the case displayed here, the fluctuation enters the horizon while the dark plasma is weakly-coupled and therefore transitions to the acoustic damping regime very rapidly. This damping ceases to be effective when the rate of momentum transfer between the DR and DM falls below the oscillation frequency of dark-photon fluctuations. When this happens, the fluctuation enters the gravitationally-dominated regime where the perturbation is further damped before it settles into the logarithmic growing mode. For comparison, we also show the behavior of a CDM fluctuation with the same wavenumber.

4.4.4 Numerical Solutions

We solve numerically Eqs. (4.42-4.47) together with the standard Boltzmann equations describing the evolution of baryons, photon and neutrinos [100]. We use a modified version of the publicly-available code CAMB [122] assuming that all of the DM is made of dark atoms. We modify the perturbed Einstein equation to include the new contributions from DM and DR. We use a flat

4.4. Evolution of Dark-Matter Perturbations

background cosmology compatible with WMAP 7-year release [1]: $\Omega_b h^2 = 0.0226$, $\Omega_D h^2 = 0.1123$, $H_0 = 70.4$ km/s/Mpc, $\Delta_{\mathcal{R}}^2 = 2.3 \times 10^{-9}$, $n_s = 0.963$, and $\tau_{\text{re}} = 0.088$. We consider pure adiabatic initial conditions

$$\delta_D(z_i) = \delta_b(z_i) \quad \delta_{\tilde{\gamma}}(z_i) = \delta_{\gamma}(z_i), \quad (4.70)$$

$$\theta_D(z_i) = \theta_{\tilde{\gamma}}(z_i) = \theta_{\gamma}(z_i), \quad (4.71)$$

$$F_{\tilde{\gamma}l} = 0, \quad l \geq 2. \quad (4.72)$$

where z_i is the initial redshift which is determined such that all modes are superhorizon at early times, $k\tau(z_i) \ll 1$. We first pre-compute the ionization and thermal history of the DS as described in section 4.3 and use the result to compute the opacity of the dark plasma as given in Eq. (4.50) above. The ionization history of the baryon-photon sector is pre-computed in the usual way using **RecFast** [194]. The linear perturbation equations are then evolved forward in time from z_i to $z = 0$. At early times when $k\tau_D \ll 1$ and $\tau_D/\tau \ll 1$, Eqs. (4.43) and (4.45) are very stiff and we use a second-order tight-coupling scheme similar to that used for the baryon-photon plasma at early times [104, 197, 198].

In Fig. 4.10, we show the time evolution of a single Fourier mode for relatively strongly-coupled dark atoms. We clearly identify the different regimes that the fluctuation encounters from its horizon crossing to its late-time growth. For the particular choice of parameters displayed here, this Fourier mode enters the horizon in the DAO regime and oscillates until dark-photon diffusion exponentially suppresses its amplitude. Once DR kinematically decouples from DM, the fluctuation can start growing like regular CDM but from a much-reduced amplitude.

To contrast, we show in Fig. 4.11 the redshift evolution of the same Fourier mode for a weakly-coupled model of dark atoms. In this case, $k\tau_D \sim 1$ shortly after the mode enters the horizon and therefore it only briefly experiences the DAO regime. It then rapidly transitions to the acous-

tic damping regime where its amplitude decays, though not as quickly or strongly as in the diffusion damping regime. After kinetic decoupling, the mode finally settles into the logarithmic growing mode.

4.4.5 Real-Space Evolution: DAO Scale

The Fourier-space description of cosmological fluctuations allows one to qualitatively understand the different stages of their evolution and to obtain accurate numerical solutions to their equations of motion. Ultimately however, physical density fluctuations evolve in configuration space and it is thus important to translate their Fourier-space behaviour into this latter space.

In Figs. 4.12, 4.13, and 4.14, we display the configuration-space redshift evolution of a Gaussian adiabatic density fluctuation. In the upper panel of Fig. 4.12, we see both a dark-plasma and a baryon-photon plasma density wave traveling outward from the initial over-density. Since the dark plasma generically has a lower sound speed than the regular baryon-photon plasma, density waves propagating in the former do not travel as far in a given time interval as waves propagating in the latter. This results in the dark-plasma density wave lagging behind its baryon-photon counterpart. The upper panel of Fig. 4.12 also clearly shows the damping of the initial density fluctuation at short length-scales resulting from the outward propagation of acoustic waves.

The lower panel of Fig. 4.12 presents a snapshot of the outward-moving waves shortly after dark photons cease to be tightly-coupled to the DM. The upper panel of Fig. 4.13 further shows the DR diffusing out of the DM fluctuation after they kinematically decouple from each other. After the dark decoupling epoch, DM fluctuations begin to grow while DR continues to propagate out of the initial overdensity, eventually overtaking the baryon-photon sound horizon. Note that the sound horizon of the dark plasma remains imprinted on the DM fluctuations, resulting in a preferred scales in the late-time density field similar to the standard BAO scale. This so-called DAO scale constitutes a tell-tale signature of the presence of a dark plasma

distinct from the standard baryon-photon plasma in the early Universe. We will discuss its cosmological implications in the next section.

The inset in the lower panel of Fig. 4.13 shows that the dark-photon density wave can actually overtake the baryon-photon plasma wave after the former decouples from the DM. As in the case of free-streaming neutrinos, this effectively establishes gravitational-potential perturbations beyond the sound horizon of the baryon-photon plasma. It has been shown [103] that such supersonic gravitational-potential perturbations can have a measurable impact on the CMB power spectrum. This indicates that DR fluctuations could in principle have an impact on the CMB, which we consider chapter 5.

Fig. 4.14 shows the late-time decoupling of photons and baryons. As in the standard CDM scenario, baryons fall in the gravitational potential wells established by DM once they cease to be dragged along by the photons. In the atomic DM scenario however, the DAO scale becomes imprinted on the baryons as they fall toward DM in a process similar to how the BAO scale is imprinted on the DM as it falls toward the baryons at late times.

In summary, compared to a vanilla Λ CDM cosmology, the atomic DM scenario has an additional cosmological length scale corresponding to the size of the dark-plasma sound horizon when the DR kinematically decouples from the DM. Since the dark plasma decouples earlier and has a lower sound speed than the baryon-photon plasma, this DAO scale is generically much smaller than the BAO scale. Furthermore, the amplitude of density fluctuations on length scales smaller than the DAO scale is severely suppressed, leading to a minimal mass for the first objects that collapse at late times. We discuss the cosmological implications of atomic DM in the next chapter.

4.4. Evolution of Dark-Matter Perturbations

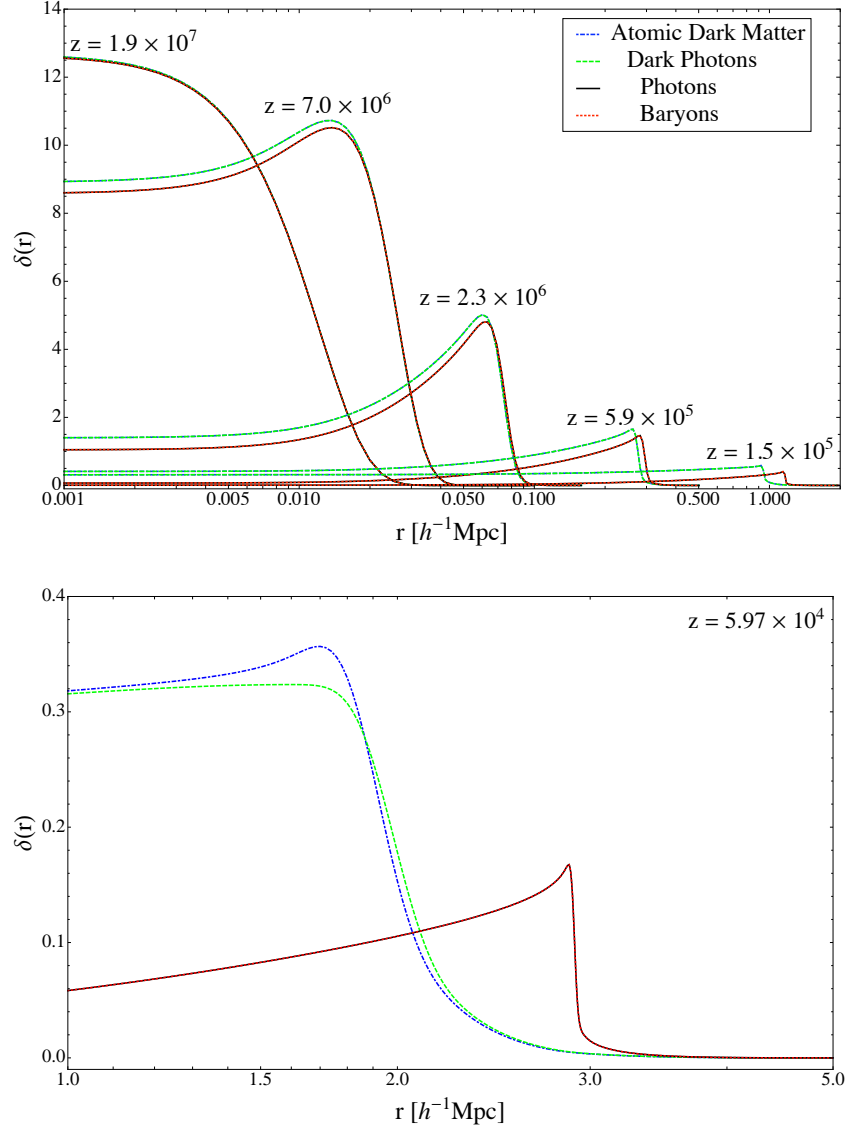


Figure 4.12: Redshift evolution of an initially Gaussian-shaped density fluctuation in configuration space. We take the fluctuation to be adiabatic. Here, $\alpha_D = 0.08$, $B_D = 1$ keV, $m_D = 1$ GeV, $\xi = 0.37$, and r stands for the comoving spatial separation. We display the evolution of the DM (dot-dashed, blue), DR (dashed, green), baryons (dotted, red), and photons (solid, black). The upper and lower panels show the initial Gaussian density fluctuation together with five snapshots of the outgoing density waves at lower redshifts. Note the changing axes from panel to panel.

4.4. Evolution of Dark-Matter Perturbations

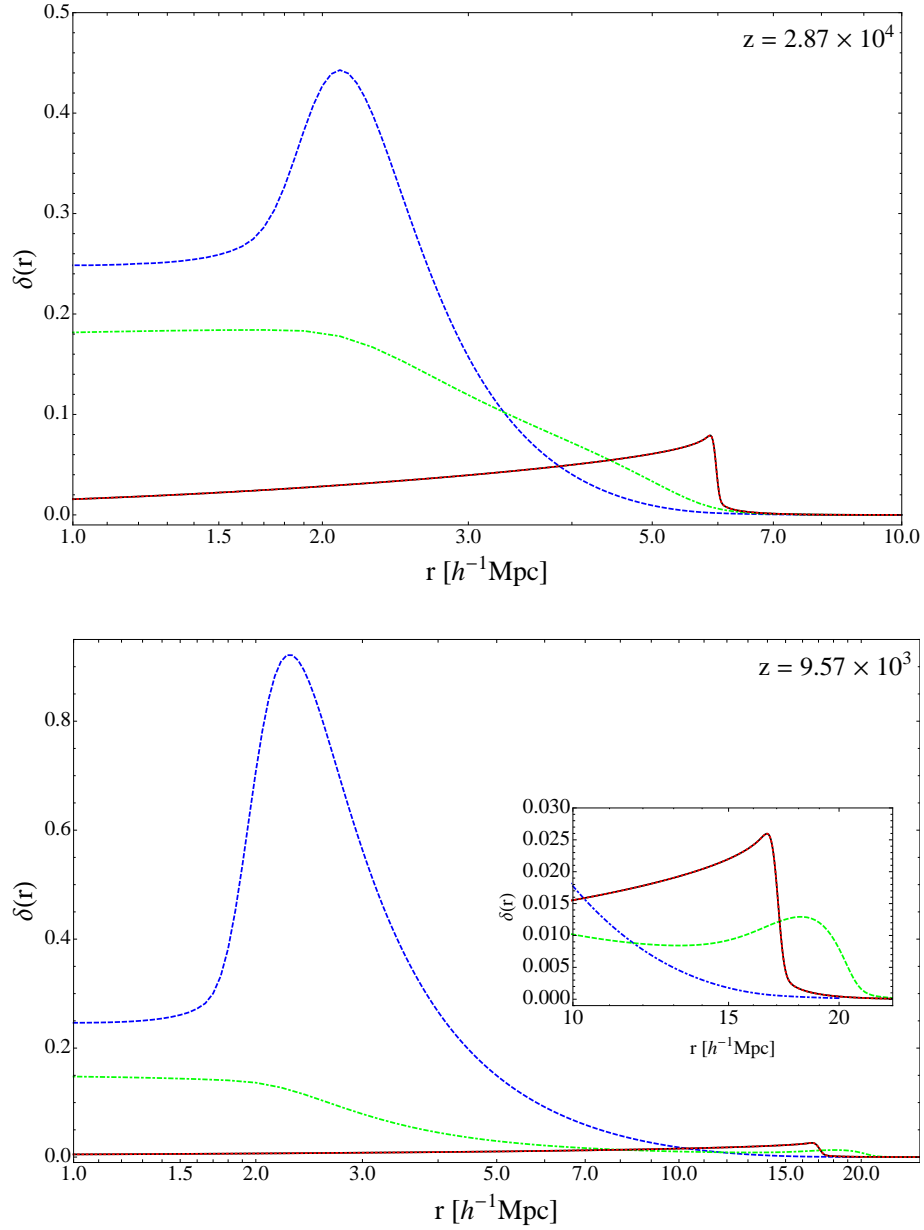


Figure 4.13: Same as Fig. 4.12 but for later redshifts. Note the changing axes from panel to panel. The inset in the lower panel focuses on the progression of the baryon-photon sound horizon.

4.4. Evolution of Dark-Matter Perturbations

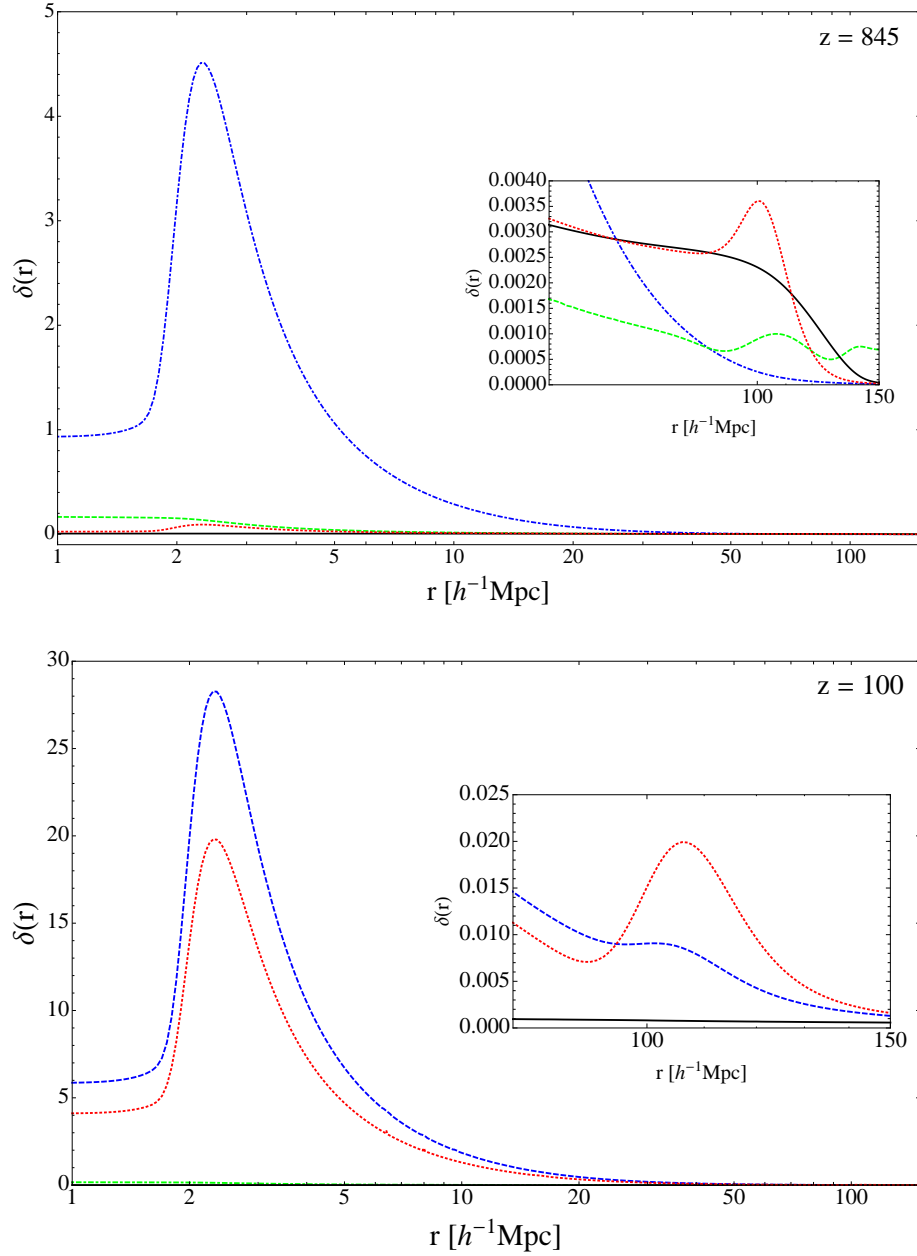


Figure 4.14: Same as Fig. 4.12 but for later redshifts. The insets focus on the progression of the baryon-photon sound horizon. At late times, two key lengthscales emerge: the standard BAO scale at $r_{\text{BAO}} \simeq 147$ Mpc and the new DAO scale at $r_{\text{DAO}} \simeq 3.3$ Mpc (for the model plotted here).

Chapter 5

The Theory of Atomic Dark Matter II: Cosmological and Astrophysical Implications

In chapter 4, we have described the physics of dark atoms as well as the solutions to the perturbed Boltzmann equations. We now turn our attention to the impacts of atomic DM on cosmological and astrophysical observations. In section 5.1, we present an analysis of the new features in the matter power spectrum and in the CMB due to the dark atomic physics. We also discuss the Lyman- α (Ly- α) forest bounds on the parameter space of atomic DM. In section 5.2, we consider the stringent astrophysical constraints on the model that are obtained by imposing that DM is effectively collisionless inside galactic halos. We revisit in section 5.3 the direct-detection signatures of atomic DM proposed in the literature in light of our new analysis. We finally discuss our results in section 5.4 and point out possible new avenues of research.

5.1 Cosmological Implications

The atomic DM scenario alters cosmological observables in two possible ways. On the one hand, the presence of dark relativistic degrees of freedom modifies the cosmological *expansion history* of the Universe. On the other hand, the gravity and pressure of the dark-photon *perturbations* impacts the evolution of DM and baryon-photon fluctuations, hence affecting late-time observables such as the CMB and the matter power spectrum.

5.1. Cosmological Implications

Unfortunately, the former case does not lead to unique effects on observable cosmological probes since the background cosmology of atomic DM is indistinguishable from that of a standard Λ CDM model that contains extra relativistic species. As the impact of relativistic neutrinos on the CMB and the matter power spectrum has been extensively studied in the literature (see e.g. [103, 199]), we shall only briefly review their key effects in the two following subsections.

Conversely, dark-photon *perturbations* can affect cosmological observables in a way that distinguish them from Λ CDM models containing extra neutrinos. This stems from the fact that relativistic neutrinos can free-stream from a very early epoch while dark photons can only do so after they decouple from the DM. Cosmological modes entering the horizon while the dark photons are free-streaming are expected to behave similarly to a Λ CDM model with an equivalent number of relativistic neutrinos. On the other hand, modes crossing the horizon while the dark photons are tightly-coupled to the DM do not experience the damping and phase shift of acoustic oscillations [103] usually associated with the presence of extra radiation. Therefore, we expect the atomic DM scenario to leave a *distinct* imprint on the CMB if dark photons begin free-streaming when the length scales relevant for this cosmological probe are crossing into the Hubble horizon. A corollary of this statement is that a dark-atom model for which dark photons decouple very early is, as far as the CMB is concerned, indistinguishable from a Λ CDM universe containing extra neutrinos.

Atomic DM itself alters cosmological observations through the modified growth of its density fluctuations. As explained in section 4.4.3, DM fluctuations entering the horizon before kinetic decoupling in the radiation-dominated era miss out on the amplitude boost due to the rapidly decaying gravitational potential. Further, atomic DM perturbations on scales smaller than the dark-photon diffusion length are strongly damped, leading to an absence of cosmological structure at these scales. The acoustic oscillations in the DM plasma which are one of the key feature of the atomic DM scenario remain imprinted on the late-time matter power spectrum. In configuration space, these oscillations point to an important length scale, the DAO

scale, at which the clustering of DM is enhanced and below which it is suppressed when compared with an equivalent Λ CDM model. For most atomic DM models that are in agreement with current observations, the DAO scale must lie today in the highly non-linear regime of cosmological fluctuations, hence making its impact on cosmology difficult to observe.

5.1.1 Matter Power Spectrum

The most dramatic and distinct cosmological implication of the atomic DM scenario is the modification of the small-scale matter power spectrum. Ultimately, this is a consequence of the relatively late kinetic decoupling of atomic DM compared to a standard WIMP CDM model. Indeed, the delayed kinetic decoupling of the dark plasma considerably impedes the growth of DM fluctuations for all subhorizon modes. Furthermore, fluctuations on length scales shorter than the diffusion distance of dark photons are *exponentially* damped compared to a CDM model, effectively prohibiting the formation of any late-time structure at these scales. Subhorizon scales that exceed the diffusion damping scale display acoustic oscillations that remain clearly imprinted on the late-time matter power spectrum, since DM forms the bulk of the non-relativistic matter. Fluctuations on length scales that cross into the horizon after DM kinematically decouples have a growth history similar to that of a vanilla Λ CDM model and we therefore expect no particular signature at these scales (see however a caveat at the end of this subsection).

In Figs. 5.1 and 5.2, we show examples of late-time linear matter power spectra for different models of atomic DM. The features discussed above are clearly visible in the spectra. We also observe that as the binding energy of the dark atoms is increased, the comoving wavenumber at which the power spectrum significantly departs from the Λ CDM case is increased. This makes sense since a higher binding energy implies an earlier dark recombination and kinetic decoupling, therefore pushing the impact of the DM-DR coupling toward higher comoving wavenumbers.

In the lowest panel of Fig. 5.1 and in Fig. 5.2, we keep the dark-atom

5.1. Cosmological Implications

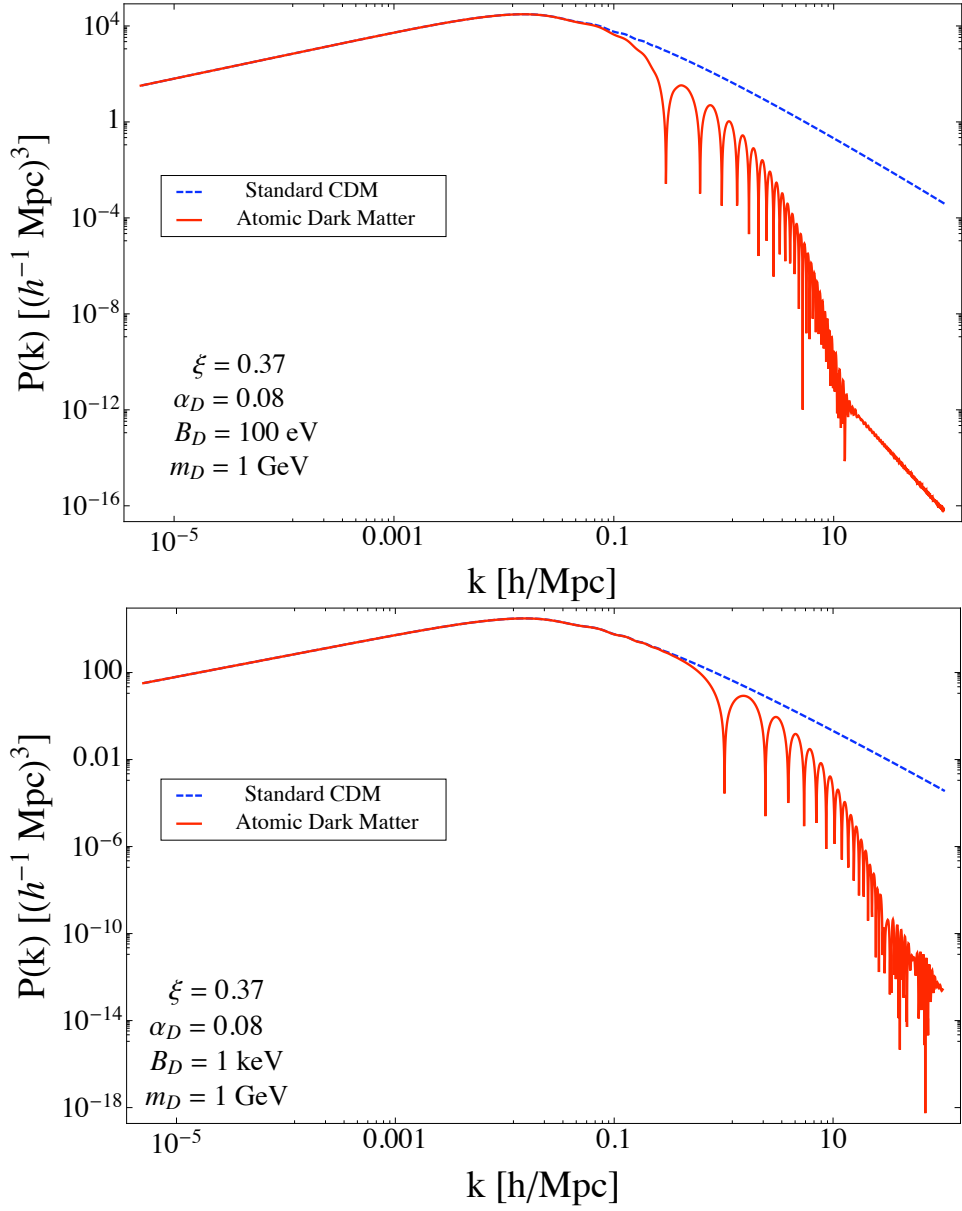


Figure 5.1: Total linear matter power spectrum at $z = 0$ for two atomic DM models. For reference, we also display the linear matter power spectrum for a vanilla Λ CDM model.

5.1. Cosmological Implications

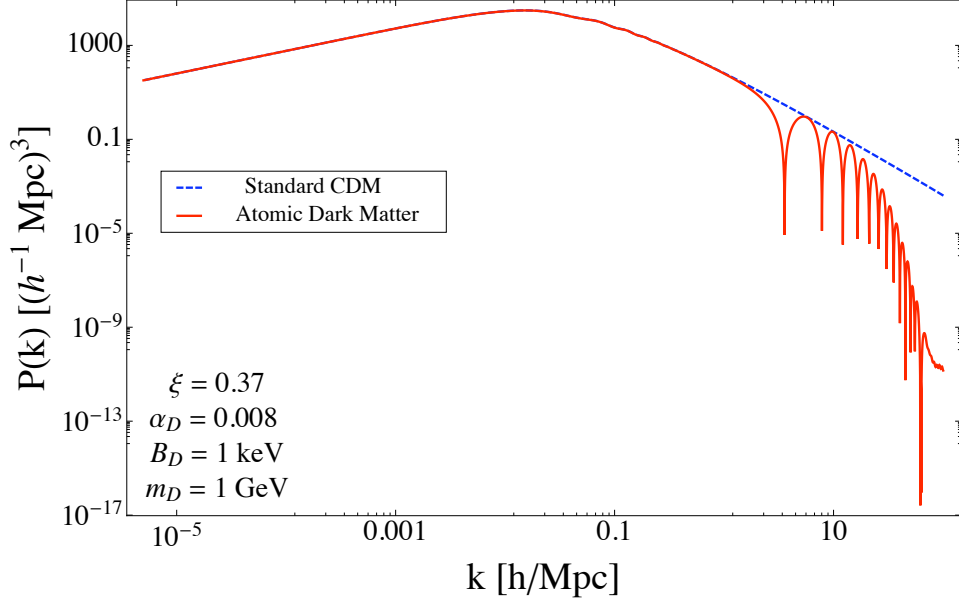


Figure 5.2: Total linear matter power spectrum at $z = 0$ for an atomic DM model. For reference, we also display the linear matter power spectrum for a vanilla Λ CDM model.

binding energy and mass constant but vary the dark fine-structure constant α_D . We observe that as α_D is decreased, the smallest comoving wavenumber affected by the DAOs moves toward higher values. At first, this seems counterintuitive, as a higher value of the dark coupling constant generally leads to a lower residual ionization fraction which in turns allows the dark photons to rapidly decouple from the DM. We must however remember that dark photons also interact with neutral dark atoms through Rayleigh scattering. For a fixed binding energy and DM mass, the Compton-scattering contribution to the dark-plasma opacity is roughly independent of α_D since $x_D(T_D \ll B_D) \propto \alpha_D^{-6}$ and $\sigma_{T,D} \propto \alpha_D^6$. On the other hand, the Rayleigh scattering contribution to τ_D is a steep function of α_D with $\tau_R^{-1} \propto \alpha_D^6$ after the onset of dark recombination. Thus, an increase of the dark fine-structure constant can considerably boost the Rayleigh-scattering contribution to the opacity of the dark plasma, hence significantly postponing its epoch of kinetic decoupling.

5.1. Cosmological Implications

It is also instructive to consider the correlation function of matter fluctuations in configuration space. The linear correlation function is related to the linear matter power spectrum via a 3D Fourier transform which, after simplification, can be reduced to

$$\xi_L(r) = \frac{1}{2\pi^2} \int dk k^2 P(k) j_0(kr), \quad (5.1)$$

where $j_0(kr)$ is the Spherical Bessel function of order 0. In Fig. 5.3, we display the linear correlation function computed from the three matter power spectra shown in Figs. 5.1 and 5.2 as well as the correlation expected from a standard Λ CDM model. In all cases, the usual BAO scale is clearly visible around $r \sim 104h^{-1}\text{Mpc}$. In a similar manner, the novel DAO length scale appears as a local enhancement of the correlation function at the scale corresponding to the sound horizon of the dark plasma at dark decoupling. On scales smaller than this sound horizon, the correlation function is significantly damped compared to the Λ CDM case, a consequence of the damping of small-scale fluctuations discussed above.

At late times, the key signature of these new features in the matter power spectrum and correlation function is a minimal DM halo mass. Indeed, since most of primordial fluctuations on scales smaller than the dark-plasma sound horizon are effectively wiped out by the diffusion of dark photons, no self-bound object can form at late times at these scales. The first regions that can collapse into self-bound DM halos must then have a minimal initial comoving size $\sim r_{\text{DAO}}$. Therefore, the first DM halos have a minimal mass given approximately by

$$M_{\text{min}} \approx \frac{4\pi}{3} r_{\text{DAO}}^3 \Omega_D \rho_{\text{crit}}. \quad (5.2)$$

In the hierarchical model of structure formation, these first halos are then accreted into larger, more massive halos. While some of these minimal-mass halos are destroyed through tidal stripping in larger halos, it is expected that a certain fraction of them remains as discrete sub-halos in larger bound objects such as galactic halos. These could potentially be detected through

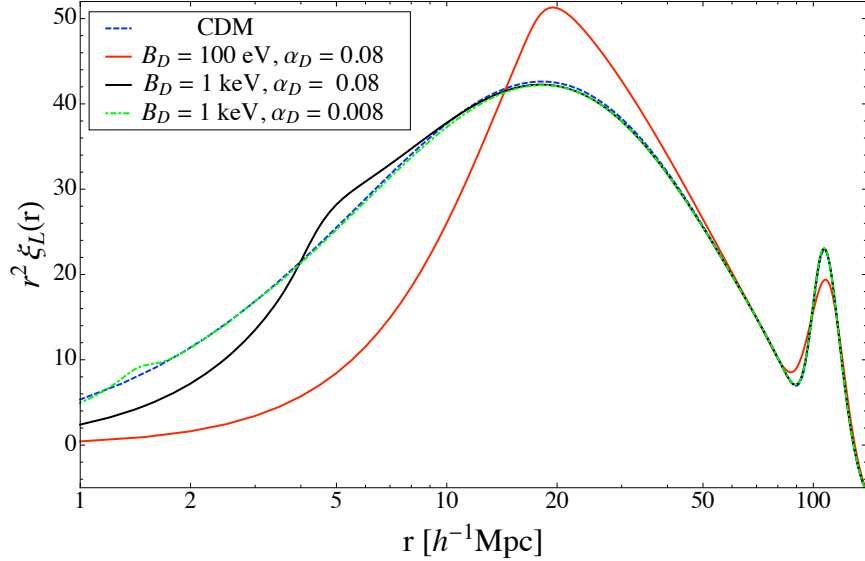


Figure 5.3: Linear correlation function for the three atomic DM models plotted in Figs. 5.1 and 5.2.

strong-lensing studies of substructures inside galactic halos (see e.g. [200]). Indeed, there is currently a growing scientific effort aimed at developing analytical methods and experimental techniques geared toward the detection of small-scale substructures inside galactic halos [201–207]. While current results mostly point out the existence of individual massive subhalos in galactic strong lenses [208–210], statistical analyses of multiple-image lenses have the potential to lead to strong constraints on the possible minimal subhalo mass. Thus, it is not unreasonable to think that this tell-tale signature of atomic DM might be detected in the near future.

Currently, the most stringent constraints on the small-scale matter power spectrum come from the Ly- α forest data [30, 211, 212]. There is however considerable systematic uncertainties in converting the Ly- α flux power spectrum to the actual linear matter power spectrum [213]. Most studies have assumed a power-law spectrum with a running spectral index. Since atomic DM predicts a much more complex shape of the matter power spectrum, it is not straightforward to apply these constraints to this scenario. In reality,

5.1. Cosmological Implications

hydrodynamical simulations of the Ly- α flux power spectrum in the atomic DM scenario will be required to derive the appropriate Ly- α constraints. We can nevertheless use the current measurements to obtain rough guidelines. Ref. [214] has found no deviation from the standard Λ CDM scenario on scales $k < 2 h \text{ Mpc}^{-1}$, while [211, 215, 216] have determined that the linear power spectrum is consistent with CDM on scales $k \lesssim 5 h \text{ Mpc}^{-1}$. Pending unforeseen physical effects, it is unlikely that atomic DM can have a large impact on these scales while leaving the Ly- α flux power spectrum unchanged. We therefore demand that the atomic DM linear power spectrum does not significantly deviate from that of a vanilla Λ CDM cosmology on those scales. More precisely, we compute two constraints: $k_{\text{DAO}} > 1 h \text{ Mpc}^{-1}$ and $k_{\text{DAO}} > 5 h \text{ Mpc}^{-1}$, where we have defined $k_{\text{DAO}} \equiv \pi/r_{\text{DAO}}$. These bounds correspond to $M_{\text{min}} \approx 10^{13} M_{\odot}$ and $M_{\text{min}} \approx 9.3 \times 10^{10} M_{\odot}$, respectively.

We show this constraint in Figs. 5.10, 5.11, and 5.12 where we display contours of constant minimal halo mass (dotted white lines) in the $\alpha_D - m_D$ plane for various values of the atomic binding energy. The dark and light gray regions correspond to $M_{\text{min}} > 10^{13} M_{\odot}$ and $M_{\text{min}} > 9.3 \times 10^{10} M_{\odot}$, respectively. We see that the Ly- α forest data only constrain models with $B_D \lesssim 10 \text{ keV}$. For higher values of the atomic binding energy, the kinetic decoupling of the DM happens very early (even for $\alpha_D \sim \mathcal{O}(1)$) and leads to a minimal halo mass $M_{\text{min}} \lesssim 10^7 M_{\odot}$ which is unconstrained by data.

To modify the faint-end of the galaxy luminosity function and bring it in agreement with the data, atomic DM needs to modify the properties of halos in the range $10^8 M_{\odot} \lesssim M_{\text{min}} \lesssim 10^{10} M_{\odot}$ [170]. According to the constraints in Figs. 5.10, 5.11, and 5.12, this is possible for model with $B_D \sim 10 \text{ keV}$, $m_D \sim 100 \text{ TeV}$ and $\alpha_D \sim 0.2$. Detailed N -body simulations will be required to assess how the atomic DM scenario exactly affects the halo mass function and density profile, but it is clear that there are allowed values of the dark parameters that can directly address some of the dwarf-galaxy problems.

For completeness, we also mention in passing that the dark radiation has a small impact on the evolution of DM perturbations even for modes that enter the horizon after dark kinetic decoupling in the radiation era.

Indeed, the free-streaming dark radiation amplifies the DM fluctuations as they enter the horizon due to their impact on the rapidly decaying gravitational potential. To illustrate this effect, we must however be careful since the presence of extra radiation shifts the epoch of matter-radiation equality z_{eq} and the angular scale of the CMB sound horizon at decoupling θ_s . Since these quantities have been precisely measured by experiments, we should keep them fixed as we vary the amount of dark radiation. This entails to adjusting the physical DM density ($\Omega_{\text{D}}h^2$) and the Hubble constant to keep the redshift of equality and the angular scale at decoupling unchanged. We keep $\Omega_{\text{b}}h^2$ fixed throughout since the CMB tightly constrains its value.

We illustrate in Fig. 5.4 the linear matter power spectrum for different values of the ratio of the DS temperature to the CMB temperature. We clearly observe that as ξ is increased, the amplitude of Fourier modes crossing into the Hubble scale in the radiation era are enhanced. In addition to the previously mentioned effect caused by the decaying gravitational potential, this enhancement is also caused by the larger DM density of model with high values of ξ . Indeed, the matter fluctuation spectrum is sensitive to the ratio $\Omega_{\text{b}}/\Omega_{\text{m}}$, since baryons are withheld from gravitational collapse prior to hydrogen recombination. As the total matter density is increased for a fixed amount of baryons, more matter can form gravitationally-bound structure and the fluctuation spectrum is therefore enhanced. Ref. [103] determined that about a third of the amplification comes from the increase in the radiation density while the rest can be attributed to the larger DM fraction.

5.1.2 Cosmic Microwave Background

We begin our study of the impact of the atomic DM scenario on the CMB by considering how the modified evolution of *cosmological perturbations* alter the spectra of temperature and polarization anisotropies. The CMB features caused by changes in the fluctuation evolution are more interesting than those resulting from the modified background cosmology since they are potentially *unique* to the atomic DM scenario (or, more generally, to theo-

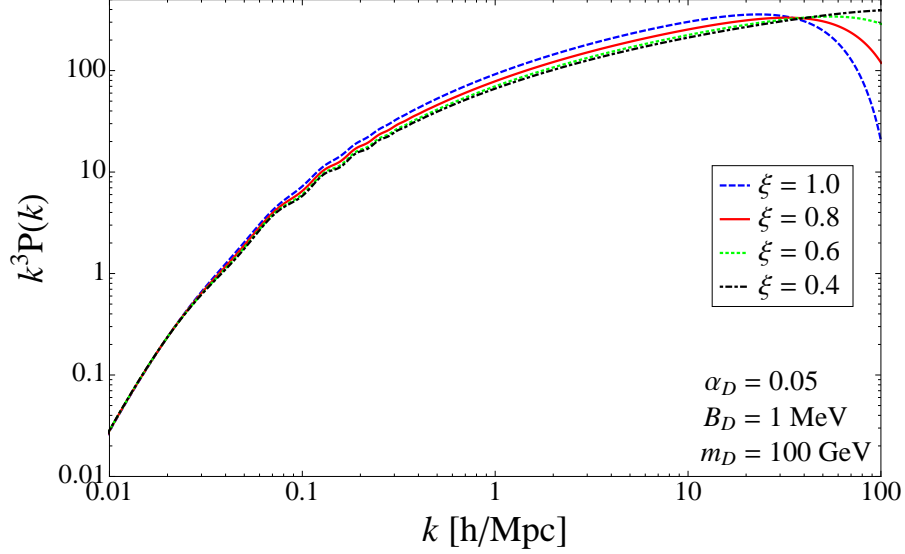


Figure 5.4: Dimensionless linear matter power spectrum at $z = 0$ for a single dark-atom model for different values of ξ . We plot $k^3 P(k)$ to magnify the small-scale region of the spectrum. Throughout the plot, we fix z_{eq} , $\Omega_b h^2$, and the angular scale of the CMB sound horizon at decoupling (θ_s).

ries incorporating dark plasmas). To isolate the impact of the fluctuations, it is important to keep fixed quantities that only depend on the background cosmology. These are z_{eq} , θ_s , the dark energy equation of state parameter w , the CMB acoustic damping scale r_d , and physical baryon density $\Omega_b h^2$. With these quantities fixed, we wish to determine if it is possible to distinguish an atomic DM model from a Λ CDM model containing an equivalent number of relativistic degrees of freedom. As we discuss below, the answer is positive.

To address the issue at hand, it is instructive to first review the impact of relativistic neutrinos on the CMB in the radiation-dominated era. The key point that distinguishes relativistic neutrinos from regular photons is their *free-streaming* nature. Indeed, while photons can only begin free-streaming after they decouple from the baryons at redshift $z \sim 1100$, neutrinos are generally assumed to have free-streamed since a very early epoch. This has

5.1. Cosmological Implications

two important consequences for the physics of the CMB [103]. First, the free-streaming of neutrinos causes a phase shift of the acoustic oscillations upon their entry into the horizon. Second, the impact of free-streaming radiation on the gravitational potential generates a uniform suppression of the CMB oscillation amplitude across all multipoles. Both outcomes can be traced back to the facts that: (1) neutrinos propagate supersonically with respect to the baryon-photon plasma and can thus establish metric fluctuations beyond the sound horizon of the CMB; and (2) the free propagation of neutrinos sources the growth of anisotropic stress on all scales (including superhorizon modes), hence affecting the gravitational source terms in the photon equations of motion.

We would like to determine how the above repercussions on the CMB change when we substitute a dark photon for a relativistic neutrino. As with the regular photons, the fundamental difference between the dark photons and the neutrinos is that the former can only start free-streaming after they decouple from the DM. This immediately suggests a possible way to distinguish the atomic DM scenario from a Λ CDM model containing extra relativistic neutrinos. Indeed, if the dark photons begin free-streaming while the length scales relevant to the CMB are entering the horizon, then the phase shift and amplitude suppression associated with the free-streaming of radiation will not be uniform across all the CMB multipoles. Small-scale modes entering the horizon while the dark photons are still coupled to the DM will not be affected by the phase shift and amplitude suppression while larger scales entering after dark-photon decoupling will be affected, as long as they become subhorizon during radiation domination. These non-uniform phase shifts and suppressions of power across multipoles constitute the tell-tale signature of a relativistic degrees of freedom decoupling from the plasma while the Fourier modes important to the the CMB are subhorizon.

In Figs. 5.5 and 5.6, we compare the temperature and polarization CMB power spectra for atomic DM models having different binding energy. We also show the CMB spectra of a Λ CDM model incorporating the same amount of additional relativistic degrees of freedom as the atomic DM models such that all the spectra shown have the same cosmological background

5.1. Cosmological Implications

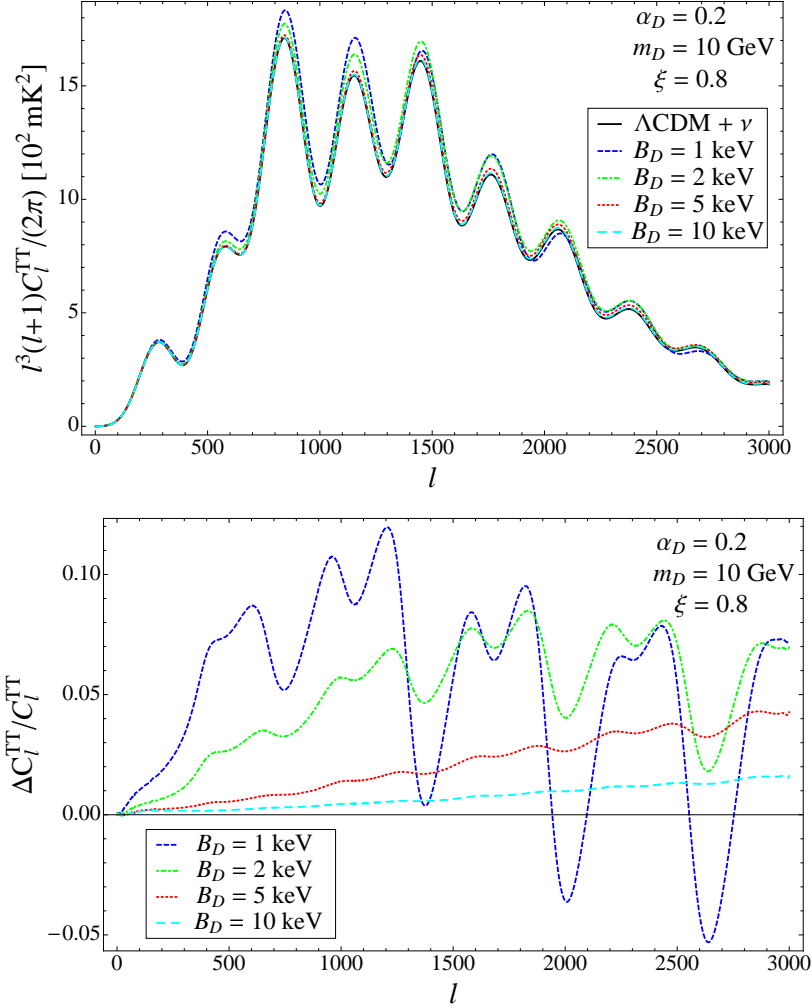


Figure 5.5: Comparison between the CMB angular power spectrum of atomic DM and that of a Λ CDM model with an equivalent number of extra neutrinos ($N_\nu = 4.849$ here). The various lines illustrate different values of the atomic binding energy, B_D . We fix all other dark parameters to the values indicated on the plot. The upper panel displays the TT spectra while the lower panel shows the fractional difference between the TT spectra of atomic DM and that of the Λ CDM model containing extra neutrinos. All other cosmological parameters are held fixed. Here, the helium fraction is fixed to $Y_p = 0.24$.

5.1. Cosmological Implications

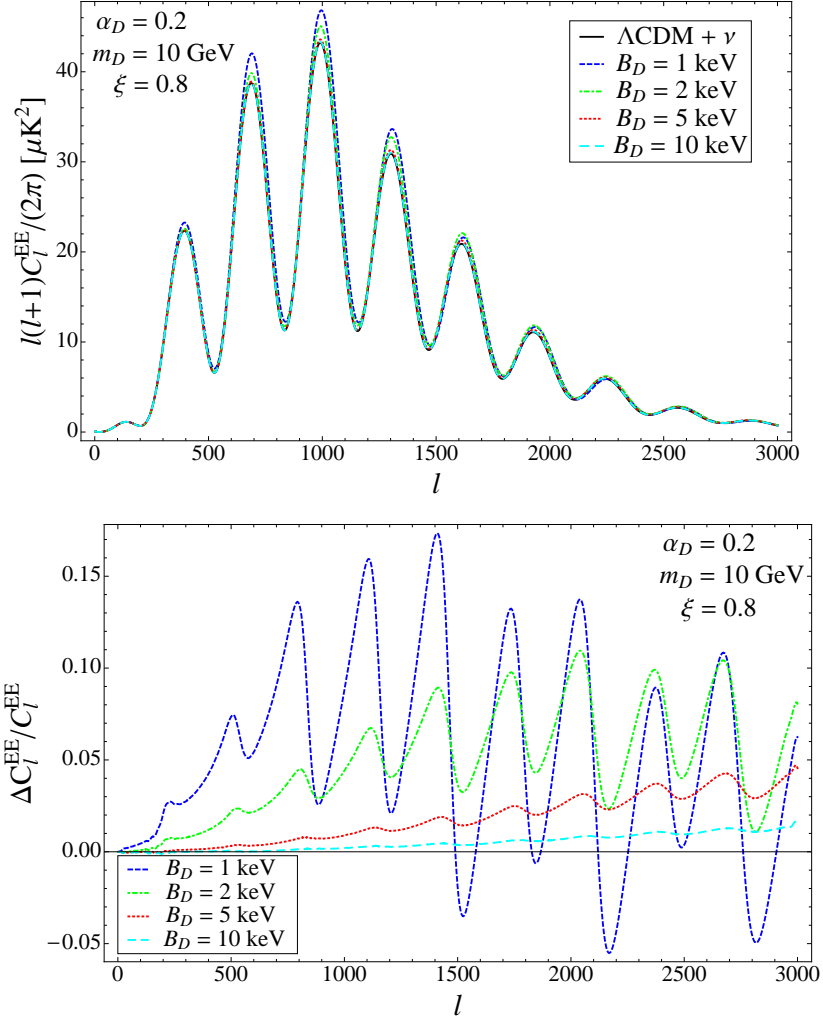


Figure 5.6: Similar to Fig. 5.5 but for the CMB EE polarization spectra.

evolution. The upper panels show the spectra themselves while the lower panels display the relative differences between the atomic DM spectra and the corresponding Λ CDM model. We immediately notice that as the binding energy is increased, both temperature and polarization power spectra converge toward the Λ CDM model containing extra neutrinos. Indeed, as the binding energy of dark atoms is made larger, dark photons decouple

5.1. Cosmological Implications

earlier from the DM and can therefore begin free-streaming at an earlier epoch, making them hard to distinguish from relativistic neutrinos.

For both temperature and polarization spectra, the key physical signatures that distinguish dark photons from neutrinos are clearly visible. First, let us discuss the amplitude suppression associated with the free-streaming radiation. We see that, compared with the Λ CDM model containing extra radiation, the amplitude of the CMB spectra for the atomic DM scenario are less suppressed, with the high- l multipoles being the least affected by the suppression. This is in line with our expectations since high multipoles enter the horizon before the dark photons have the chance to significantly free-stream and are therefore more immune to the suppression. The atomic DM models with $B_D = 5$ keV and 10 keV clearly display this behaviour. On the other hand, the scenarios with the lowest binding energies ($B_D = 1$ and 2 keV) exhibit a more complex l -dependence when compared with the Λ CDM model. To understand this difference, we need to invoke the important phase shifts between the atomic DM and Λ CDM models as well as the different growth history of the DM fluctuations in the two scenarios.

The effect of the phase shift is most visible for the $B_D = 1$ keV model. Indeed, since dark photons in this model are just beginning to free-stream when most Fourier modes contributing to the CMB enter the horizon, these do not experience the same phase shifts as the Λ CDM model. This can be most clearly discerned in the polarization spectrum (Fig. 5.6). There, we see that the phase difference between the atomic DM models and the Λ CDM containing extra neutrinos becomes progressively larger toward higher multipoles. This is exactly what we expect since the high multipoles enter the horizon before they can be affected by dark-photon free-streaming, while smaller multipoles experience a phase shift that progressively converges toward the pure neutrino case as l is lowered. One of the key feature of this drifting phase shift is that it converges toward constant values for both $l \gg l_{\text{dec}}$ and $l \ll l_{\text{dec}}$, where l_{dec} corresponds to the multipole that crosses into the horizon as dark photons begin free-streaming. This contrasts with phase shifts caused by a change in the angular scale of the sound horizon which act multiplicatively $l \rightarrow \alpha l$. We show in Fig. 5.7 the damping tail of

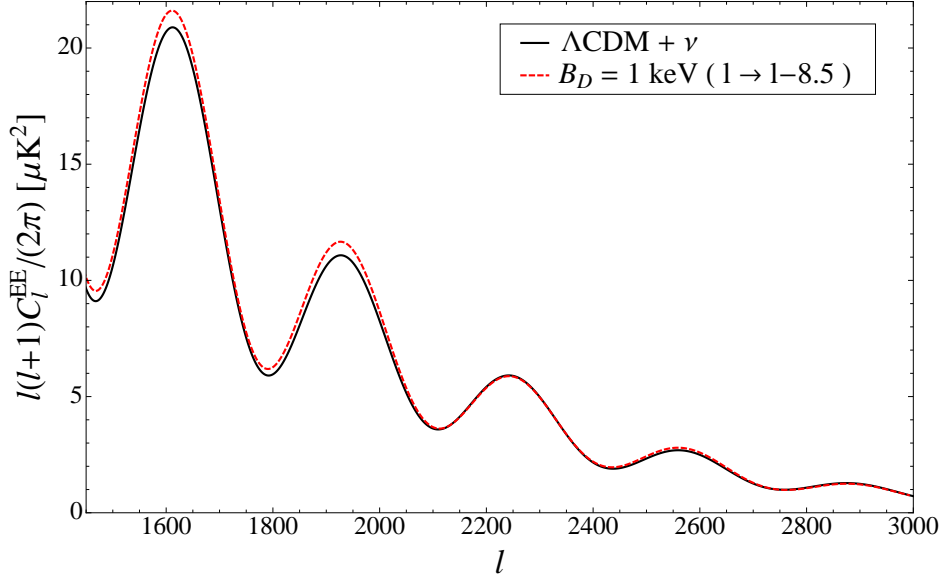


Figure 5.7: Illustration of the constant phase shift between an atomic DM model and a Λ CDM model containing an equivalent number of relativistic species. We show here that, in the atomic DM scenario, multipoles that enter the Hubble horizon before dark photons begin free-streaming do not experience the constant phase shift toward smaller l that usually characterizes models with extra relativistic degrees of freedom. To illustrate this, we have shifted the atomic DM spectrum by $\Delta l = -8.5$ and observed that the phases of both spectra coincide.

the EE -polarization spectrum for the $B_D = 1$ keV model. To illustrate the constant phase shift at $l \gg l_{\text{dec}} (\sim 500$ here), we have shifted its spectrum by $\Delta l \sim -8.5$. We see that the phase of the shifted spectrum matches very well that of the Λ CDM model containing extra relativistic neutrinos, hence showing the phase shift does asymptote to a constant at high multipoles.

There is an important ramification to the above observations. Since the CMB temperature anisotropies are sensitive to the DM-dominated gravitational potential at the epoch of last scattering, any significant modification to the growth history of DM density perturbations will be reflected in the C_l^{TT} power spectrum. As we discussed in section 4.4.3, DM fluctuations can-

5.1. Cosmological Implications

not grow as long as they are coupled to the DR. In the matter-dominated era, growing DM fluctuations are usually responsible for establishing the gravitational potentials that act as a restoring force to counterbalance the pressure of the photons. If DM perturbations are prohibited to grow by their coupling to the DR, then the gravitational potentials cannot be established and the gravitational source term acting on photon fluctuations is much weaker. Observationally, this has the consequence of altering the ratios of the odd and even peaks of the CMB spectrum, with the odd peaks being suppressed on scales where DM fluctuations cannot grow. Indeed, the odd peaks correspond to gravity-driven compression waves which are very sensitive to the size of the DM fluctuations. The lower panel of Fig. 5.5 clearly shows the deep troughs associated with the damping of the odd C_l^{TT} peaks caused by the late kinetic decoupling of DM for the models with $B_D = 1$ and 2 keV. Unfortunately, models displaying such significant suppression of odd C_l^{TT} peaks at high multipoles have very low values of σ_8 and violate the Ly- α bound on k_{DAO} , and are therefore ruled out by observations.

We now turn briefly our attention on how the atomic DM scenario affects the CMB through its impact on the *background* cosmology. Since atomic DM modifies the background evolution by the presence of the DR, the effects on the CMB are not unique but common to any theory incorporating extra relativistic degrees of freedom. For completeness, we nevertheless discuss their effects here. These include a modification of the primordial helium abundance, a change to the angular scale of the sound horizon at decoupling, a shift of the matter-radiation equality epoch, an enhanced early ISW effect and a modified CMB damping tail.

Primordial Helium Abundance The impact of the relativistic dark components on the expansion rate during BBN tends to increase the primordial

5.1. Cosmological Implications

helium fraction through the approximate relation [187]

$$Y_p \approx 0.2485 + 0.0016 \left[(273.9 \Omega_b h^2 - 6) + 100 \left(\sqrt{1 + \frac{4}{43} g_{*,D}^{\text{BBN}} \zeta_{\text{BBN}}^4} - 1 \right) \right], \quad (5.3)$$

where we have used the relation

$$\Delta N_\nu^{\text{BBN}} = \frac{8}{7} \frac{g_{*,D}^{\text{BBN}}}{2} \zeta_{\text{BBN}}^4 \quad (5.4)$$

between the number of additional neutrinos at BBN ($\Delta N_\nu \equiv N_\nu - 3$) and the relativistic degrees of freedom of the DS at that epoch. Since helium recombines before hydrogen at late times, a larger helium fraction leads to a net decrease in the free-electron fraction around $z \simeq 1100$. Consequently, the photons can diffuse more easily out of inhomogeneities and damp temperature and polarization anisotropies on scales smaller than the diffusion length. Therefore, we generically expect the CMB to display less power on small angular scales for atomic DM scenarios predicting a large primordial helium fraction [103, 199].

Angular size of Sound Horizon, Matter-Radiation Equality and Early ISW

The presence of the dark photons affects the size of the baryon-photon sound horizon through its impact on the Hubble expansion rate prior to hydrogen recombination. The sound horizon of the baryon-photon plasma is given by

$$r_s^{(b-\gamma)} = \int_0^{a_*} \frac{c_s^{(b-\gamma)} da}{a^2 H}, \quad (5.5)$$

where a_* is the scale factor at recombination and $c_s^{(b-\gamma)}$ is the sound speed of the baryon-photon plasma. Since the extra DR works to increase the Hubble rate, the net effect is a smaller value of $r_s^{(b-\gamma)}$. As the angular size of sounds horizon is given by $\theta_s = r_s^{(b-\gamma)}/D_A$, where D_A is the angular-diameter distance to the last-scattering surface, we therefore expect the CMB acoustic peaks to be shifted toward smaller angular scales (higher

5.1. Cosmological Implications

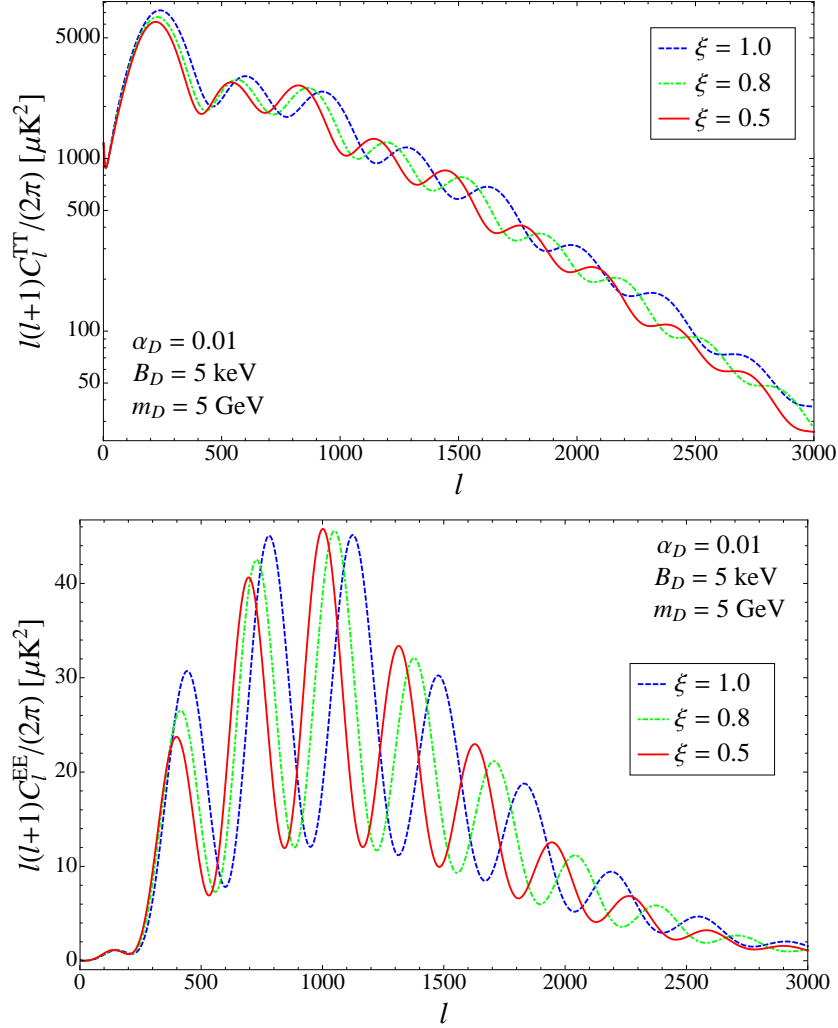


Figure 5.8: CMB angular power spectra in the atomic DM scenario for different values of ξ . We fix all other dark parameters to the values indicated on the plots. The upper panel displays the TT spectra while the lower panel shows the EE polarization spectra. All other cosmological parameters are held fixed. Here, the helium fraction is fixed to $Y_p = 0.24$ to isolate the effect from the changing sound horizon.

multipoles l). This effect is illustrated in Fig 5.8 where we display the temperature and E-polarization spectra for different values of ξ . The shift

5.1. Cosmological Implications

of the acoustic peaks to smaller angular scales is clearly visible for both types of spectra. Further, we see that the temperature anisotropies are amplified around the first acoustic peak as ξ increases. This is the result of the integrated Sachs-Wolfe (ISW) effect caused by the extra DR through its impact on the changing gravitational potential after recombination. Indeed, increasing ξ brings the epoch of matter-radiation equality closer to that of recombination, hence increasing the impact of radiation on the gravitational potential at late times.

Silk Damping Tail If we fix the epoch of matter-radiation equality, the primordial helium fraction and the angular scale of the sound horizon at decoupling, increasing the energy density of the dark photons leads to an enhanced damping of the CMB anisotropies [199]. To understand the origin of this effect, we need to remember that the photon diffusion distance scales as $r_d \propto H^{-0.5}$ (see Eq. (4.59)) while the angular diameter distance scales as H^{-1} . Thus, the damping angular scale $\theta_d \equiv r_d/D_A$ effectively increases if the Hubble rate is sped up due to the presence of extra radiation. We therefore expect that as the value of ξ is raised, the CMB spectrum will be increasingly affected by Silk damping. This effect is shown in Fig. 5.9 where we clearly observe the decline in amplitude associated with the increasing DR density. In addition, if the primordial helium fraction was allowed to vary according to Eq. (5.3), this would further increase the amount of Silk damping. Therefore, it is clear that measurements of the CMB damping tail provide strong constraint on ξ .

In summary, beyond the impact of the atomic DM scenario on the background cosmology caused by the DR, we have identified four key cosmological signatures that distinguish the atomic DM scenario from a Λ CDM model containing extra relativistic neutrinos. First, the emergence of the new DAO length scale in the late-time density field results in a minimal mass for the first DM protohalos that is generically larger than in the standard WIMP paradigm. Also, as the dark photons transition from being tightly-coupled to the dark plasma to a free-streaming state, they impart varying phase shifts and amplitude suppressions to the CMB multipoles entering the horizon. Importantly, these suppressions and phase shifts asymptote to constant

5.1. Cosmological Implications

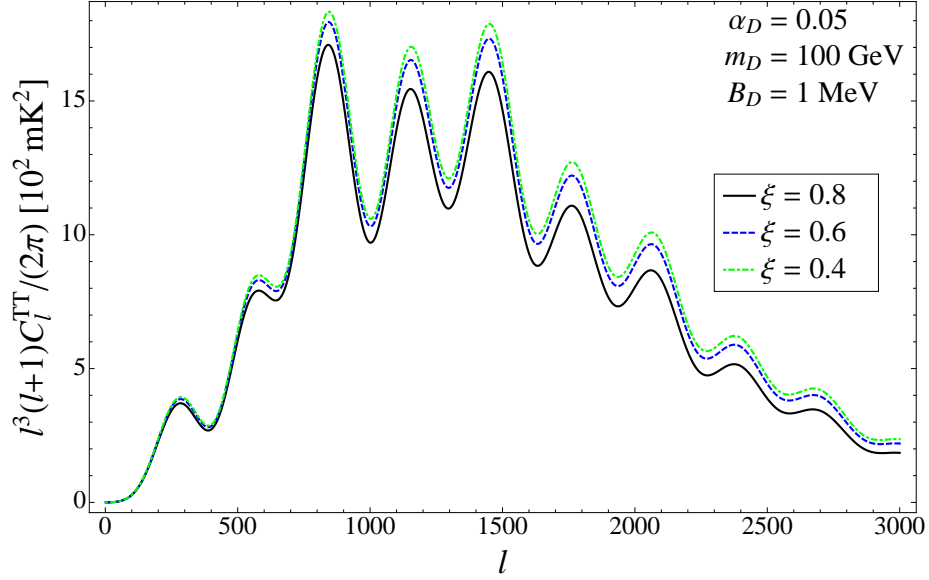


Figure 5.9: CMB temperature power spectra in the atomic DM scenario for different values of ξ . We fix all other dark parameters to the values indicated on the plots. We keep fixed throughout the redshift of matter-radiation equality and the angular size of the baryon-photon sound horizon at decoupling. Here, the helium fraction is fixed to $Y_p = 0.24$ to isolate the effect from the changing damping scale.

values for $l \gg l_{\text{dec}}$ and $l \ll l_{\text{dec}}$, a distinct feature of atomic DM that is not easily reproduced in the Λ CDM scenario. Furthermore, we have shown that the odd C_l^{TT} peaks are suppressed on scales that enter the causal horizon before DM kinematically decouples. It is therefore clear that precise measurements on the CMB damping tail could provide meaningful constraints on the parameter space of atomic DM. We should however keep in mind that the modified evolution of DM and DR *fluctuations* can only affect the CMB if the DS kinetic decoupling happens close enough to the epoch of last scattering. As such, a non-detection of these signatures effectively puts a lower bound on the redshift of kinetic decoupling which itself depends on a combination of α_D , B_D , m_D , and ξ .

5.2 Astrophysical Constraints on Atomic Dark Matter

As the Universe expands and cools down, non-linear structures begin to emerge and eventually form present-day astrophysical objects such as galaxies and clusters of galaxies. The internal dynamics of these objects is deeply influenced by the microphysics governing DM because the latter contributes the vast majority of the mass inside these objects. Since the atomic DM scenario naturally incorporates new interactions in the DS, it is important to discuss its implications for the dynamics of DM halos on a wide range of scales.

On one side, observations indicate that the DM halos of elliptical galaxies and clusters display a triaxial ellipsoidal shape [54, 165, 217–224]. This indicates that the relaxation (thermalization) time of their DM halos is much longer than the typical dynamical time of these celestial objects. From this observation, one can obtain a bound on the elastic collisional rate of DM particles. Similarly, detailed studies of the Bullet Cluster provide direct constraint on the self-interaction cross section of DM [55]. However, these constraints have been shown to be weaker than those derived from the halo ellipticity [181] and we therefore do not consider them here.

On the other side, due to the rich internal structure of dark atoms, the atomic DM scenario inherently includes dissipation mechanisms that could potentially have dramatic effects on the dynamics of DM halos. Indeed, collisional excitations of dark atoms followed by dark-photon emissions provide a cooling mechanisms for DM that could drastically alter the internal structure of halos. Further, the *chemistry* of the DS naturally provides other heat-dissipation mechanisms such as molecular cooling. Fortunately, demanding that DM particles be effectively collision-less to preserve the structure of halos strongly hinder the efficiency of the atomic dissipative processes, rendering them mostly irrelevant. Similarly, the requirement that very few actual particle collisions take place in the DS most likely shut off any chemical reactions inside halos. We therefore do not further consider the possibility of dark chemistry.

5.2.1 Ellipticity of DM Halos

Collisions among the different constituents of the DS lead to a redistribution of the linear and angular momentum inside a DM halo. This tends to erase velocity correlations on halo scales and brings the DM halo closer to isothermality, effectively altering the halo structure and making it roughly isotropic. Since observations indicate that halo iso-density contours are elliptical and thus significantly deviate from isotropy, we conclude that the DM thermalization time is much longer than the dynamical timescale of halos. This in turns tightly constrains the rate of particle collisions in which a significant amount of momentum is exchanged.

In the atomic DM scenario, we need to consider collisions between the dark atoms, the dark electrons, and the dark protons. In total, this amounts to six different types of collisions: **H-H**, **H-e**, **H-p**, **e-e**, **e-p**, and **p-p**. Here, **H** stands for the dark atoms. Since we are most interested in DS that are mostly neutral when non-linear structures form, the contribution from the first three types of collision is expected to dominate. To compute the rate of collisions with large momentum exchange, we need the momentum-transfer cross-section which is defined by

$$\sigma_{\text{mt}} \equiv \int d\Omega \frac{d\sigma}{d\Omega} (1 - \cos \theta), \quad (5.6)$$

where $d\sigma/d\Omega$ is the elastic differential cross-section. A detailed computation of the **H-H**, **H-e** and **H-p** momentum-transfer cross-section is beyond the scope of this chapter, but we can use the extensive literature (see e.g. [225]) on the corresponding visible-sector cross-sections to derive some general properties. We refer the reader to appendix B.4 for further details. To a good approximation, the **H-H**, **H-p**, and **H-e** momentum-transfer cross-sections are

$$\sigma_{\text{mt}}^{\mathbf{H-H}}(v) \approx \frac{30\pi\alpha_D^2}{B_D^2 v^{1/4}} \left[\frac{\mu_H m_D}{\mu_D B_D} \right]^{-\frac{1}{8}} e^{-\frac{\mu_H m_D v^2}{\mu_D B_D 300}}, \quad (5.7)$$

5.2. Astrophysical Constraints on Atomic Dark Matter

$$\sigma_{\text{mt}}^{\mathbf{H}-\mathbf{P}}(v) \approx \frac{60\pi\alpha_D^2}{B_D^2} \sqrt{\frac{m_{\mathbf{P}}}{m_D}} e^{-\frac{\mu_{\mathbf{H}}}{\mu_D} \frac{\mu_{D\mathbf{P}}}{B_D} \frac{v^2}{200}}, \quad (5.8)$$

$$\sigma_{\text{mt}}^{\mathbf{H}-\mathbf{e}}(v) \approx \frac{60\pi\alpha_D^2}{B_D^2} \sqrt{\frac{m_{\mathbf{e}}}{m_D}} e^{-\frac{\mu_{\mathbf{H}}}{\mu_D} \frac{\mu_{D\mathbf{e}}}{B_D} \frac{v^2}{200}}, \quad (5.9)$$

where $\mu_{D\mathbf{e}} = m_D m_{\mathbf{e}} / (m_D + m_{\mathbf{e}}) \simeq m_{\mathbf{e}}$ and v is the relative velocity of the colliding dark ions or atoms. The ion-ion differential cross sections are simply given by the Rutherford scattering cross-section. Performing the integral in Eq. 5.6 leads to

$$\sigma_{\text{mt}}^{\mathbf{P}-\mathbf{P}}(v) = \frac{8\pi\alpha_D^2}{m_{\mathbf{P}}^2 v^4} \ln [\csc^2 (\theta_{\text{min}}^{\mathbf{P}-\mathbf{P}}/2)], \quad (5.10)$$

$$\sigma_{\text{mt}}^{\mathbf{e}-\mathbf{e}}(v) = \frac{8\pi\alpha_D^2}{m_{\mathbf{e}}^2 v^4} \ln [\csc^2 (\theta_{\text{min}}^{\mathbf{e}-\mathbf{e}}/2)], \quad (5.11)$$

$$\sigma_{\text{mt}}^{\mathbf{e}-\mathbf{P}}(v) = \frac{2\pi\alpha_D^2}{\mu_D^2 v^4} \ln [\csc^2 (\theta_{\text{min}}^{\mathbf{e}-\mathbf{P}}/2)], \quad (5.12)$$

where $\theta_{\text{min}}^{\mathbf{i}-\mathbf{j}}$ is the minimum scattering angle. We take this angle to be given by the Debye screening length $\lambda_{D\mathbf{e}}$ of the dark plasma through the relation

$$\csc^2 (\theta_{\text{min}}^{\mathbf{i}-\mathbf{j}}/2) = \left(\frac{\lambda_{D\mathbf{e}} \mu_{\mathbf{i}\mathbf{j}} v^2}{\alpha_D} \right)^2 + 1, \quad (5.13)$$

where

$$\lambda_{D\mathbf{e}} \simeq \sqrt{\frac{\mu_D v^2}{8\pi\alpha_D n_{\mathbf{e}}}}, \quad (5.14)$$

and where $n_{\mathbf{e}}$ is the number density of free dark electrons inside a DM halo. The momentum-loss rate of dark species \mathbf{i} upon collisions with species \mathbf{j} in a DM halo is given by

$$\dot{p}_{\mathbf{i}\mathbf{j}} = n_{\mathbf{j}} \int dv v f(v) \sigma_{\text{mt}}^{\mathbf{i}-\mathbf{j}}(v) \Delta p_{\mathbf{i}}, \quad (5.15)$$

where $n_{\mathbf{j}} = n_{\mathbf{j}}(r)$ is the number density of specie \mathbf{j} inside a halo, v is the relative velocity of the collision, $\Delta p_{\mathbf{i}}$ is the momentum loss in a single collision and $f(v)$ is the velocity distribution which we take to be locally Maxwellian

5.2. Astrophysical Constraints on Atomic Dark Matter

with velocity dispersion v_0

$$f(v)dv = \frac{4}{\sqrt{\pi}v_0^3}v^2e^{-v^2/v_0^2}dv. \quad (5.16)$$

The momentum lost by particle \mathbf{i} upon colliding with particle \mathbf{j} is

$$\Delta p_{\mathbf{i}} = p_{\mathbf{i}} \frac{m_{\mathbf{j}}}{m_{\mathbf{i}} + m_{\mathbf{j}}}. \quad (5.17)$$

where $p_{\mathbf{i}}$ is the momentum of particle \mathbf{i} . Normally, the momentum loss is weighted by a factor $(1 - \cos \theta)$, but we have absorbed this factor into the momentum-transfer cross section. The rate of momentum-changing collisions between dark species \mathbf{i} and \mathbf{j} is defined as

$$\Gamma_{\mathbf{ij}} \equiv \frac{\dot{p}_{\mathbf{ij}}}{\bar{p}_{\mathbf{i}}}. \quad (5.18)$$

where $\bar{p}_{\mathbf{i}}$ is the momentum of particle \mathbf{i} averaged over the velocity distribution given in Eq. (5.16). With the help of the above momentum-transfer cross sections, these collisions rates are

$$\Gamma_{\mathbf{HH}} \simeq \frac{15\pi \Gamma(\frac{19}{8})\alpha_D^2 v_0^{3/4} n_{\mathbf{H}}}{B_D^2} \left[\frac{\mu_{\mathbf{H}} m_D}{\mu_D B_D} \right]^{-\frac{1}{8}} \left[1 + \frac{\mu_{\mathbf{H}} m_D v_0^2}{\mu_D B_D 300} \right]^{-\frac{19}{8}}, \quad (5.19)$$

$$\Gamma_{\mathbf{ep}} \simeq \frac{2\pi^{\frac{3}{2}}\alpha_D^2 n_{\mathbf{p}}}{\mu_D^2 v_0^3} \frac{m_{\mathbf{p}}}{m_{\mathbf{p}} + m_{\mathbf{e}}} \ln \left[1 + \frac{\mu_D^3 v_0^6}{4\pi^{\frac{3}{2}}\alpha_D^3 n_{\mathbf{e}}} \right], \quad (5.20)$$

$$\Gamma_{\mathbf{pp}} \simeq \frac{4\pi^{\frac{3}{2}}\alpha_D^2 n_{\mathbf{p}}}{m_{\mathbf{p}}^2 v_0^3} \ln \left[1 + \frac{\mu_D m_{\mathbf{p}}^2 v_0^6}{32\pi\alpha_D^3 n_{\mathbf{e}}} \right], \quad (5.21)$$

$$\Gamma_{\mathbf{ee}} \simeq \frac{4\pi^{\frac{3}{2}}\alpha_D^2 n_{\mathbf{e}}}{m_{\mathbf{e}}^2 v_0^3} \ln \left[1 + \frac{\mu_D m_{\mathbf{e}}^2 v_0^6}{32\pi\alpha_D^3 n_{\mathbf{e}}} \right], \quad (5.22)$$

$$\Gamma_{\mathbf{eH}} \simeq \frac{45\pi^{\frac{3}{2}}\alpha_D^2 v_0 n_{\mathbf{H}}}{B_D^2} \sqrt{\frac{m_{\mathbf{e}}}{m_D} \frac{m_D}{m_D + m_{\mathbf{e}}}} \left[1 + \frac{\mu_{\mathbf{H}} \mu_{D\mathbf{e}} v_0^2}{\mu_D B_D 200} \right]^{-\frac{5}{2}}, \quad (5.23)$$

$$\Gamma_{\mathbf{pH}} \simeq \frac{45\pi^{\frac{3}{2}}\alpha_D^2 v_0 n_{\mathbf{H}}}{B_D^2} \sqrt{\frac{m_{\mathbf{p}}}{m_D} \frac{m_D}{m_D + m_{\mathbf{p}}}} \left[1 + \frac{\mu_{\mathbf{H}} \mu_{D\mathbf{p}} v_0^2}{\mu_D B_D 200} \right]^{-\frac{5}{2}}. \quad (5.24)$$

In the above, $\Gamma(x)$ is the Gamma function. The rates for the opposite

5.2. Astrophysical Constraints on Atomic Dark Matter

processes are obtained by rescaling the above rates with the appropriate mass densities

$$\Gamma_{\mathbf{pe}} = \frac{n_{\mathbf{e}}m_{\mathbf{e}}}{n_{\mathbf{p}}m_{\mathbf{p}}}\Gamma_{\mathbf{ep}}, \quad (5.25)$$

$$\Gamma_{\mathbf{He}} = \frac{n_{\mathbf{e}}m_{\mathbf{e}}}{n_{\mathbf{H}}m_D}\Gamma_{\mathbf{eH}}, \quad (5.26)$$

$$\Gamma_{\mathbf{Hp}} = \frac{n_{\mathbf{p}}m_{\mathbf{p}}}{n_{\mathbf{H}}m_D}\Gamma_{\mathbf{pH}}. \quad (5.27)$$

In the case for which $m_{\mathbf{e}} \ll m_{\mathbf{p}}, m_D$, we see that $\Gamma_{\mathbf{pe}} \ll \Gamma_{\mathbf{ep}}$ and $\Gamma_{\mathbf{He}} \ll \Gamma_{\mathbf{eH}}$ if the abundance of dark atoms and dark ions is roughly similar. This is reasonable: a heavy dark proton needs to scatter off many light dark electrons before its momentum is significantly affected. Conversely, a dark electron's momentum can be dramatically changed by a single collision with a dark proton or a dark atom. However, since the dark electrons are usually much lighter than the dark protons and therefore carry a small fraction of the overall halo mass, these high-momentum-transfer collisions do not affect the ellipticity of DM halos. Therefore, we do not consider any further the scattering of dark electrons (that is, we neglect \mathbf{ee} , \mathbf{ep} and \mathbf{eH} collisions). In the case where the dark proton and the dark electron are nearly degenerate in mass, constraints on dark-proton collisions naturally engulf the dark electron constraints so we can still neglect them.

Detailed simulations of self-interacting DM halos have shown that DM particles forming the bulk of the matter density can undergo up to 10 hard scatters in a Hubble time before the ellipticity of halos is adversely affected [226]. Therefore, the ellipticity of DM halos is preserved if we have

$$\Gamma_{\text{coll}} < 10H_0, \quad (5.28)$$

where Γ_{coll} is the overall hard-scatter rate of the dark sector. The total collision rate inside a halo is the sum of the individual rates weighted by the relative abundance of each dark species

$$\Gamma_{\text{coll}} \simeq \bar{x}_D\Gamma_{\mathbf{p}} + (1 - \bar{x}_D)\Gamma_{\mathbf{H}}, \quad (5.29)$$

where

$$\Gamma_{\mathbf{p}} = \Gamma_{\mathbf{pp}} + \Gamma_{\mathbf{pH}} + \Gamma_{\mathbf{pe}}, \quad (5.30)$$

and

$$\Gamma_{\mathbf{H}} = \Gamma_{\mathbf{HH}} + \Gamma_{\mathbf{Hp}} + \Gamma_{\mathbf{He}}. \quad (5.31)$$

To compute the above constraint, we need to specify the density profile of both dark ions and dark atoms as well as the velocity dispersion $v_0(r)$. The main difficulty here is that the actual density profile of each dark constituents is itself determined by their collisional rates. For example, if the dark ions undergo many hard scatters among themselves within the typical dynamical time of a galaxy, they settle into their own isothermal density profile [126], while the neutral dark atoms maintain their CDM-like profile. This implies that the local ionized fraction inside a DM halo can vastly differs from the background values computed in section 4.3.2 (by several order of magnitudes in some cases). To complicate matters further, collisions between dark atoms in the central region of halos likely lead to the formation of a cored density profile. Therefore, it is clear that detailed N -body simulations would be required to determine the actual density profile of each dark constituent.

We can nevertheless derive conservative constraints on atomic DM by making some simple assumptions. We first assume halos to be locally neutral such that $n_{\mathbf{e}}(r) = n_{\mathbf{p}}(r)$. We further assume the ionized component of the DM follows the total density profile, that is, $n_{\mathbf{e}}(r) = n_{\mathbf{p}}(r) = \bar{x}_D n_D(r)$. Similarly, $n_{\mathbf{H}}(r) = (1 - \bar{x}_D) n_D(r)$. We take the halo ionized fraction (\bar{x}_D) to be equal to the late-time ionized fraction of the background, that is $\bar{x}_D = x_D(z = 0)$. It is important to emphasize that the above prescription is not accurate since the ionized and neutral components generally have different density profiles [126] and the ionized fraction inside halos may significantly differ from the overall background cosmological values. As such, the bounds derived from these assumptions should therefore be considered as upper limits on how limiting the ellipticity constraint can be. The actual bounds on the parameter space of atomic DM are potentially *much less* constraining. Nevertheless, the above treatment is expected to be fairly accurate for $\bar{x}_D \ll 1$ and $\bar{x}_D \sim 1$.

While it is true that the most stringent constraints on halo ellipticity (see e.g. [181]) come from the inner part of galactic halos, it is unclear how these bounds apply to atomic DM. Indeed, ellipticity constraints strongly depend on the local DM density in the inner central region of halos. The latter is usually obtained by fitting a predefined halo profile (e.g. NFW) to the data [227]. Since atomic DM generally admits a different halo shape, we cannot blindly apply these results to the atomic DM scenario. We therefore resort to typical values of the DM density and velocity dispersion inside galactic halos. Explicitly, we evaluate the above constraints using $\rho_D \simeq 3, 1$, and 0.3 GeV/cm^{-3} . We take the velocity dispersion to be $v_0 \simeq 250 \text{ km/s}$. The number density of DM particles is then given by $n_D = \rho_D/m_D$.

We display in Figs. 5.10, 5.11, and 5.12 the constraints on α_D and m_D for six different values of the atomic binding energy. We display the three disfavored contours corresponding $\rho_D \simeq 3, 1$, and 0.3 GeV/cm^{-3} . We observe that for $10 \text{ keV} \lesssim B_D \lesssim 100 \text{ keV}$, there is little parameter space for which the DS is mostly neutral *and* is not in tension with the ellipticity constraint. As the binding energy is increased above this threshold, a large allowed parameter space opens up since the atomic geometric cross section rapidly decreases as the binding energy climbs up in value. Below 10 keV , another unconstrained region opens up at large coupling constant values and masses. This is caused by the collision energy approaching the excitation threshold of the dark atoms. As this limit is approached, the momentum-transfer cross-section for atom-atom scattering become more and more suppressed, while the inelastic channels start to growth in importance. The inelastic cross-sections are however much smaller than the elastic ones ($\sim \pi a_{0,D}^2$ instead of $\sim 10^2 \pi a_{0,D}^2$) and we thus do not expect these collisions to severely affect the ellipticity of haloes.

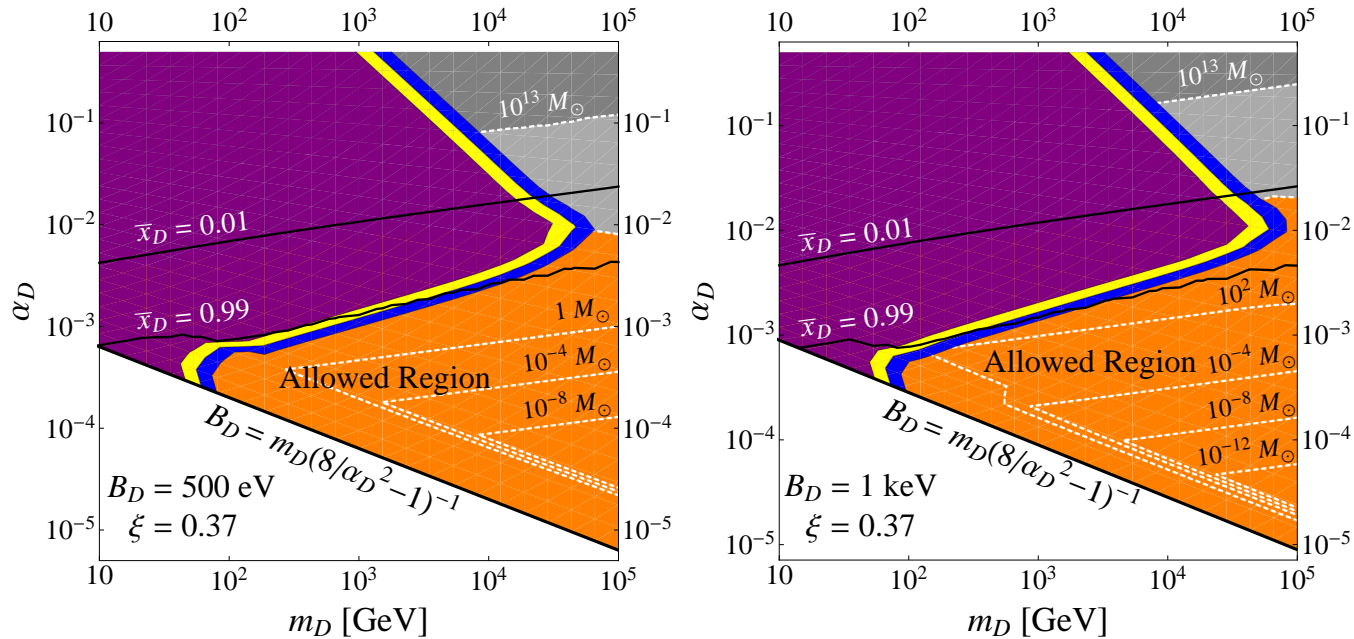


Figure 5.10: Halo ellipticity and Ly- α forest constraints on the parameter space of atomic DM. We display the constraint for two values of the atomic binding energy. The allowed region (orange) is clearly indicated on the plots. The blue, yellow and purple contours (outermost to innermost) display the disfavoured regions when $\rho_D \simeq 3, 1,$ and 0.3 GeV/cm $^{-3}$, respectively. The light and dark gray regions correspond to minimal halo masses $M_{\min} > 9.3 \times 10^{10} M_\odot$ and $M_{\min} > 10 \times 10^{13} M_\odot$, respectively. The white dashed lines indicate contours of constant minimal halo mass. We also show the contours (solid black) of constant background ionization fraction for $\bar{x}_D = 1\%$ and $\bar{x}_D = 99\%$.

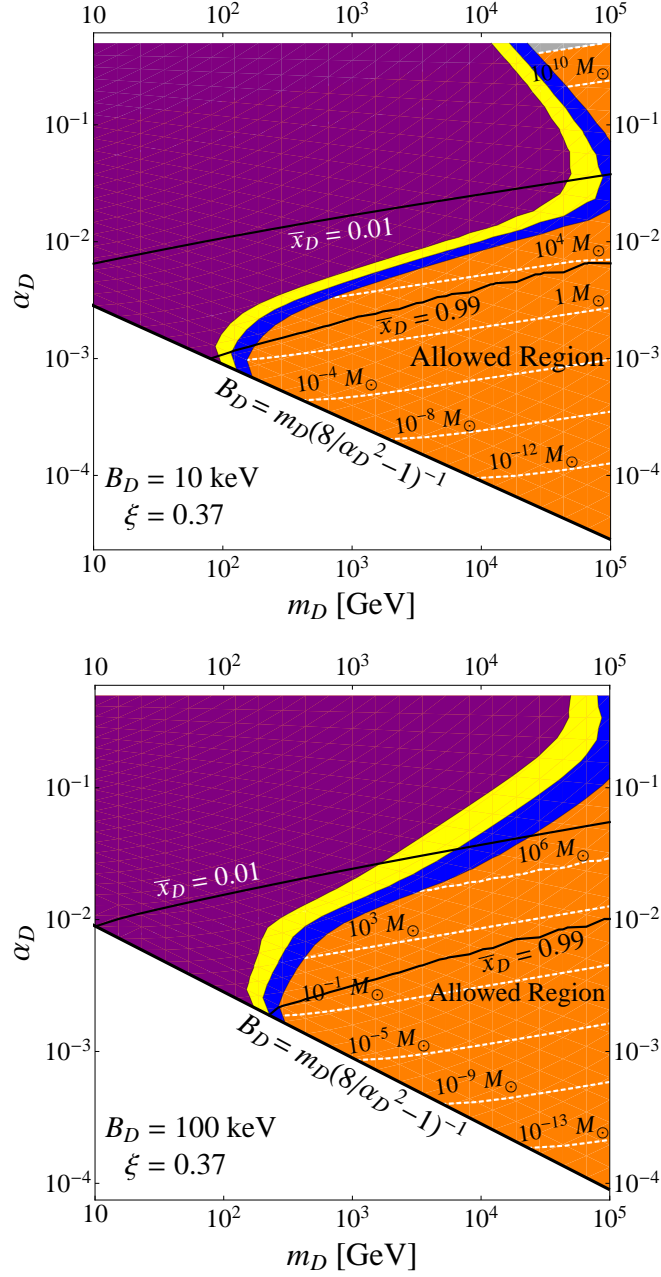


Figure 5.11: Same as Fig. 5.10 but for different values of the atomic binding energy.

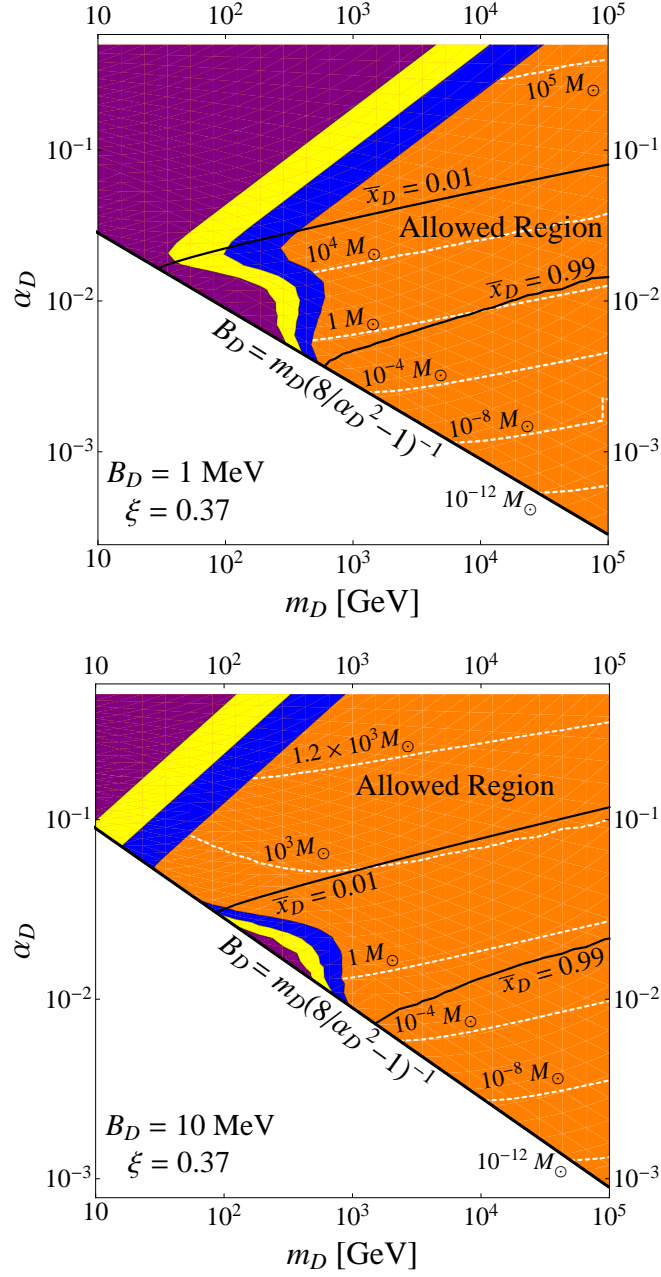


Figure 5.12: Same as Fig. 5.10 but for different values of the atomic binding energy.

Overall, the ellipticity constraint unambiguously disfavours dark atoms with mass $m_D \lesssim 1$ TeV, unless $B_D \gtrsim 1$ MeV. We however reiterate that the constraints shown in Figs. 5.10, 5.11, and 5.12 are *conservative*, especially in the regions where $1\% \lesssim \bar{x}_D \lesssim 99\%$ for which detailed simulations of dark-atomic halos will likely be required to assess the validity of the bounds. Indeed, if the typical hard-scatter timescale of dark ions is shorter than the dynamical time of a galaxy, we can safely assume that the dark ions settle into a separate isothermal density profile [126]. In the presence of a sizable population of neutral dark atoms, the overall DM halo can however still display significant ellipticity if the dark atoms are themselves mostly collisionless. Since the isothermal ionic halo is typically much more diffuse [126] than the neutral one, ion-ion and ion-atom interactions are probably much more suppressed than our naive estimate suggests. This is likely to open up much of the parameter space for $1\% \lesssim \bar{x}_D \lesssim 99\%$.

In the case where the dark ions form the majority of the matter density inside halos, the ellipticity constraints derived in the context of hidden charged DM apply [180, 181]. In this scenario, dark ions cannot settle into an isothermal profile without utterly violating the ellipticity of halos. Viable models can nevertheless be constructed by suppressing the dark fine-structure constant and by considering very large ions masses (such that the number density is low). Fortunately, as α_D is increased and m_D is decreased, more and more ions are bound into dark atoms hence softening the ion-scattering bound. In fact, since the early recombination rate scales as $\sim \alpha_D^3$ while the ion-ion hard-scatter rates scale as $\sim \alpha_D^2$, the ionized fraction drops faster than the ion-ion momentum-transfer rate is increasing as the the dark fine-structure constant is dialed up. Thus, the atomic DM scenario naturally provides a way to evade the halo ellipticity constraints on hidden-charged DM.

In summary, while detailed simulations of DM halo formation in the atomic DM scenario are likely required to determine the exact constraints, it is clear that dark atoms lighter than 1 TeV are likely to lead to collisional DM that is in tension with the observed internal structure of halos, unless $B_D \gtrsim 1$ MeV.

5.2.2 Cooling of DM Halos

Collisional excitation of dark atoms followed by the emission of a dark photon provides a natural cooling mechanism for DM. Since DM is observed to have very different properties than baryons (which are allowed to cool), collisional cooling of dark atoms must be suppressed. The easiest channel to excite a dark atom is through the hyperfine transition. The hyperfine splitting is given by

$$E_{\text{hf}} \approx \frac{4}{3} g_{\mathbf{e}} g_{\mathbf{p}} \alpha_D^2 \frac{m_{\mathbf{e}}}{m_{\mathbf{p}}} B_D, \quad (5.32)$$

where $g_{\mathbf{e}} \simeq 2$ and $g_{\mathbf{p}} \simeq 2$ are the gyromagnetic ratio of the dark electron and dark proton, respectively. This transition can be excited when a dark atom in a spin singlet state collides with a dark ion or atom and undergoes a spin-flip to the triplet state. The cross section for this process is somewhat smaller than the elastic scattering cross section [225]. Therefore, it is most likely that all regions of parameters space where hyperfine emission leads to significant cooling are already ruled by the ellipticity constraint. To verify this, we compute the typical timescale for a dark atom to lose an $\mathcal{O}(1)$ fraction of its kinetic energy due to hyperfine emission. Assuming that this process is approximately governed by the geometric cross-section, this timescale is

$$\tau_{\text{hf}} \simeq \frac{9m_D B_D m_{\mathbf{p}} v_0}{256 \sqrt{\pi} \alpha_D^4 m_{\mathbf{e}} n_D}. \quad (5.33)$$

Demanding that this timescale be longer than the age of the Universe leads to no new constraints beyond those already plotted in Figs. 5.10, 5.11, and 5.12.

Beyond the hyperfine transition, the other dissipative process that is relevant for dark atoms is the $1s \rightarrow 2s, 2p$ collisional excitation. Heuristically, such inelastic collisions can only happen when the timescale of the collision is shorter than the typical timescale of the dark atoms (i.e. adiabaticity is violated). The typical velocity of a dark electron inside an atom is $v_{\mathbf{e}} \sim \alpha_D$, leading to an atomic timescale $\tilde{\tau}_D \sim a_{0,D}/v_{\mathbf{e}}$. On the other hand, the collision timescale is of the order $\tau_{\text{coll}} \sim a_{0,D}/v$, where v is the relative velocity of the collision. Taking $\tau_{\text{coll}} < \tilde{\tau}_D$, inelastic collisions are only possible when

$$v \gtrsim \alpha_D. \quad (5.34)$$

According to Figs. 5.10, 5.11 and 5.12, all allowed regions of parameter space displaying a large fraction of neutral dark atoms have $\alpha_D \gtrsim 10^{-2}$. Taking v to be approximately equal to the typical velocity dispersion inside a DM halo, we have $v \sim 10^{-3}$ for galactic halos while $v \sim 10^{-2}$ for galaxy clusters. It is thus clear that inelastic collisions can play no major role inside galactic halos while they could play a marginal role inside clusters. In the latter case however, the small number density of dark atoms coupled with the typically small inelastic cross-sections (see e.g. [228]) likely render inelastic collisions completely negligible inside clusters. We therefore conclude that inelastic processes do not constrain the atomic DM scenario beyond the regions of parameter space already ruled out by the ellipticity and the matter power spectrum bounds.

5.3 Direct Detection

Most previous works on atomic DM [125, 126, 171] have focused their attention on the potential direct-detection signatures. Since atomic DM can naturally scatter inelastically, it offers a mechanism to reconcile the annual modulation seen by DAMA [82] and CoGeNT [85] with the null signal of the CDMS [229, 230] and Xenon10 [231–233] experiments. The actual direct-detection results strongly depend on how atomic DM couples to the SM. In this section, we compare the atomic DM models which provide a good fit to the direct-detection data to our cosmological and astrophysical constraints derived above.

In Ref. [125], the authors considered a model in which dark fermions are axially coupled to a broken $U(1)$ which mixes with the SM hypercharge. They found that dark atoms having an hyperfine splitting $E_{\text{hf}} \simeq 100$ keV, $70 \lesssim m_{\mathbf{p}} \lesssim 200$ GeV and $2.2 \gtrsim m_{\mathbf{e}} \gtrsim 1.6$ GeV can provide a good fit to the modulated spectrum of DAMA while evading the constraints from other direct-detection experiments. This corresponds to an atomic DM scenario

5.3. Direct Detection

with $27 \lesssim B_D \lesssim 45$ MeV, $0.16 \lesssim \alpha_D \lesssim 0.24$ and $72 \lesssim m_D \lesssim 201$ GeV. Extrapolating the constraints shown in Fig. 5.12 to the appropriate binding energies, we find that these values lie on the edge of the ellipticity bound and are therefore marginally allowed by our constraints.

In Ref. [126], the authors considered a similar broken axial $U(1)$ model which mixes with the SM hypercharge. In this work, they show that an atomic DM scenario with $E_{\text{hf}} \sim 5 - 15$ keV with dark fermion masses $m_e \sim m_p \sim 5$ GeV could reconcile the CoGeNT data with the count rate seen by the CRESST experiment [86]. This corresponds to an atomic DM scenario with $\alpha_D \sim 0.03$, $B_D \sim 1$ MeV and $m_D \sim 10$ GeV. This model is in serious tension with the halo constraint shown in Fig. 5.12 and is therefore likely to lead to collisional DM which would dramatically affect the structure of halos.

In Ref. [171], the authors considered an atomic DM model where the dark photon mixes with the regular photon. This effectively gives small standard electromagnetic charges to the dark fermions. The authors concluded that a scenario with $\alpha_D \sim 0.06$, $B_D \sim 5$ MeV and $m_D \sim 6$ GeV predicts the right cross section to explain the DM events recorded by the CoGeNT collaboration. These values are however clearly in tension with the halo ellipticity bound. Nevertheless, since they lie close to the boundary with the allowed region and since our constraints are conservative, detailed N -body simulations will be required to assess whether this model is ruled out or not.

We observe that dark-atom models capable of explaining the current direct-detection experiments are at best marginally allowed by our conservative astrophysical constraints. This stems from the fact that direct-detection experiments generally favor $m_D \sim 1 - 10$ GeV while the halo constraint typically imposes $m_D > 1$ TeV, unless $B_D \gtrsim 1$ MeV. From the point of view of direct detection, the main challenge for building a successful atomic DM theory is to avoid strong elastic scattering off nuclei while allowing for enough inelastic collisions to explain both DAMA and CoGeNT. The study of atomic DM models that could be in agreement with both the direct-detection data and the astrophysical constraints are left for future work.

5.4 Discussion

We have presented in this work a thorough study of a DS made up of atom-like bound states. This model naturally incorporates extra relativistic degrees of freedom whose presence are currently favored by CMB experiments. The observed primordial abundances of light elements constrain the temperature of DR to be somewhat cooler than the CMB, with an upper bound given approximately by $T_D/T_{\text{CMB}} < 0.8$ at $z = 0$. We have revisited the atomic physics necessary to describe the processes of dark recombination, thermal decoupling, and kinetic decoupling. We find that in some cases, the inclusion of physics beyond that of standard atomic hydrogen is required to properly describe these transitions. In particular, we find that bound-free processes such as photo-ionization heating and photo-recombination cooling are key to determine the thermal decoupling epoch of weakly-coupled atomic models. For strongly-coupled dark atoms, we have shown that the addition of Rayleigh scattering can significantly delay the kinetic and thermal decoupling of DM.

We have solved the linear cosmological perturbation equations, taking into account the interaction between DM and DR and showed that atomic DM can go through various regimes as time evolves and as the dark parameters are varied. In particular, the DR pressure leads to strong acoustic oscillations for Fourier modes entering the Hubble horizon prior to the dark drag epoch. Further, diffusion and acoustic damping severely suppress the amplitude of DM fluctuations on scales shorter than the sound horizon at kinetic decoupling. At late times, these features remain imprinted on the matter power spectrum. Importantly, the atomic DM scenario introduces the new DAO length scale in the density field which basically determines the minimal DM halo mass. We have shown that observations of Ly- α forest flux power spectrum put an upper bound on the size of the DAO scale and rule out a large fraction of atomic DM models with $B_D \lesssim 1$ keV.

We have performed a detailed study of the impact of the atomic DM scenario on the CMB. We have determined that the largest impact on the CMB in this model is due to the presence of dark photons. If dark pho-

tons begin free-streaming at a very early epoch, their impact on the CMB is likely indistinguishable from that of extra relativistic neutrinos. On the other hand, if dark photons decouple from DM when Fourier modes relevant for the CMB are inside the horizon, then the atomic DM scenario predicts CMB signatures that are difficult to reproduce with only relativistic neutrinos. These signatures include non-uniform phase shifts and amplitude suppressions of the temperature anisotropy power spectrum. The clearest CMB signature of the atomic DM scenario is a non-uniform phase shift of the polarization power spectrum that asymptotes to a constant at both large and small scales.

These signatures can only be present if the dark photons form a sizable fraction of the radiation energy density ($\xi \gtrsim 0.6$) and if they decouple at a late enough redshift, which usually requires $B_D \lesssim 10$ keV. These relatively low atomic binding energies are however strongly constrained by both the Ly- α data and the halo ellipticity requirement. For the remaining allowed parameter space, dark photons generically decouple too early to have an impact on the CMB that is noticeably different from that of standard relativistic neutrinos. It is therefore unlikely that the CMB can be used to learn about the simplest atomic DM model discussed here. Nevertheless, in a more general model where dark radiation only couples to a certain fraction of the DM, it is possible that the former could significantly affect the CMB without modifying the small-scale matter power spectrum. This is an intriguing possibility that we leave for future work.

The strongest constraint on atomic DM comes from requiring that DM is effectively collision-less inside galactic halos. This stems from the fact that atoms naturally have much larger geometric cross-sections than point particles. Since this geometric cross section scales as B_D^{-2} , the halo constraint favors a large binding energy, with models having $B_D \gtrsim 10$ MeV largely unconstrained. Unsurprisingly, this corresponds to the regime where atomic DM closely resembles a standard WIMP particle. For $B_D \lesssim 1$ keV, the ellipticity and Ly- α constraints favor a DS that is mostly ionized at all times. Our constraints in these regions of parameter space are similar to those found in Refs. [180, 181]. Importantly, we have shown that inelastic

processes are inefficient at dissipating the energy of dark atoms in all the regions that are not already ruled out by the halo and the small-scale power spectrum bounds. Overall, it is clear that preserving the observed ellipticity of halos severely limits the possible interactions between DM particles.

Since the atom-atom, ion-atom and ion-ion cross-sections are all velocity dependent, atomic DM can provide enough interactions to smooth out the central region of small satellites galaxies while retaining the ellipticity of large galactic and cluster halos. Furthermore, atomic DM scenarios predicting a minimal halo mass in the range $M_{\min} \sim 10^8 - 10^{10} M_{\odot}$ have the potential to affect the faint-end of the galaxy luminosity function and bring it in line with observations. In addition, the presence of an ionized component naturally makes the halo more diffuse and could potentially alleviate the so-called “too big to fail” problem [74, 75]. Interestingly, an atomic DM model with $B_D \sim 5$ keV, $m_D \sim 80$ TeV and $\alpha_D \sim 0.02$ could possibly address all three problems affecting dwarf galaxies. Indeed, this model has a late-time global ionized fraction of $\bar{x}_D \simeq 0.2$, a minimal halo mass of $M_{\min} \simeq 8 \times 10^8 M_{\odot}$ and lie at the boundary of the collisional constraint, meaning it could contain enough interactions to form cores in galactic halos while retaining their overall ellipticity. A detailed numerical study will be necessary to assess the success of this model.

Direct-detection data favor light atomic DM candidates which are in tension with the halo constraint. Nevertheless, the direct-detection signatures strongly depend on how dark atoms couple to the SM. Whether a successful model which agrees with both the halo and direct-detection constraint could be constructed remains an open question. While an explicit model would have to be specified in order to make quantitative predictions, we emphasize that dark atoms are still a viable DM candidate from the point of view of both astrophysics and direct detection.

One issue that we have not touched upon in this work is the possibility of dark magnetic fields. These have the potential to significantly alter structure formation unless there is a mechanism that naturally suppress their amplitude and range. The simplest way to achieve such suppression is to break the $U(1)_D$ gauge force by introducing a small dark-photon mass. This

5.4. Discussion

is an intriguing possibility since it would considerably alleviate the halo constraint by shrinking the size of the atomic cross-section and by limiting the range of ion-ion interactions. One would however have to revisit the atomic physics described in section 4.3 to make quantitative predictions about the thermal history of such a DS. We leave the study of such a model to future work.

Chapter 6

Oscillating Bispectra and Galaxy Clustering: A Novel Probe of Inflationary Physics with Large-Scale Structure

In this chapter, instead of studying possible new physics governing the DM sector, we use the *distribution* of DM and luminous matter in the Universe to study the physics of *inflation*. As such, this chapter constitutes a significant change of pace compared to the previous chapters. It is nevertheless completely aligned with the overall thesis goal of studying and constraining new physics in the DS. The reader may want to review sections 1.2 and 1.4.3 where numerous concepts discussed in this chapter are introduced.

6.1 Introduction

Since the publication of the seminal inflation papers [18, 19], a plethora of models have been proposed to explain why the Universe underwent a phase of exponential expansion at early times. Since most models offer very similar basic predictions, distinguishing between these models with today's data is not an easy task. One approach that has received a lot of attention recently is to look for departures from Gaussianity (see section 1.2) in the primordial cosmological perturbations [234]. Indeed, while a large class of models predicts that the non-Gaussian signature should be undetectably small, there also exist a number of models for which departures

from Gaussianity should be relatively large and observable [235]. Thus, any detection (or absence thereof) of non-Gaussianity in the primordial spectrum of perturbations could then rule out a large swath of inflation models.

Non-Gaussian signatures have been traditionally looked for in cosmic microwave background (CMB) anisotropies [1]. However, it has recently been shown that the initial departure from Gaussianity could be amplified in the clustering of dark-matter halos [111, 112, 236] (see [114] for a review and [237] for similar effects in another context). Indeed, mode coupling in non-Gaussian models induces a dependence of the local power spectrum on the long-wavelength potential perturbations. This can lead to a scale-dependent halo bias (see section 1.4.3) on large scales which is observable in large-scale-structure surveys, since galaxy clustering is closely connected to halo clustering on large scales. Competitive upper limits on non-Gaussianity have already been placed using this method [113].

While the non-Gaussian bias correction goes as k^{-2} in the local model, it has been shown in [238, 239] that the scale dependence of other types of non-Gaussian models can be significantly different. Furthermore, models could also differ by how the bias varies with halo mass. Therefore, measurements of the biasing of dark-matter halos could be used to distinguish among different non-Gaussian scenarios. So far, the bispectrum shapes for which large-scale-structure predictions have been worked out include the local [38], equilateral [39], orthogonal [40], and folded [41] shapes, all of which are scale independent. However, there are several classes of inflationary models which predict bispectra that have strongly scale-dependent oscillatory features [41, 127–132, 240–243]. These models can circumvent the tight limit on the bispectrum in the squeezed configuration [37] by breaking the slow-roll approximation. Since the squeezed triangle configuration is what determines the scale-dependent halo bias, such models potentially leave interesting signatures in halo clustering. The oscillatory bispectrum shapes are generally nonfactorizable and are therefore very computationally intensive to constrain with CMB data alone [244, 245]. We show here that these models can also be constrained by calculating their impact on halo clustering. Moreover, these models leave distinct features in the mass de-

pendence of the non-Gaussian halo bias, which allow us to distinguish them observationally from the smooth, scale-invariant shapes considered thus far.

In this chapter, we calculate the non-Gaussian correction to the dark-matter halo bias for two different oscillatory bispectra. We focus on models that display a sharp feature in their inflationary potential as well as models that have periodic features in the potential. Models with features in the potential have been invoked to explain deviations in the observed CMB power spectrum from the smooth prediction. On the other hand, periodic modulations of the potential are motivated by axion-monodromy models¹⁷ [130, 131]. While in both cases one obtains oscillatory three-point functions, the physics responsible for these modulations is very different. Indeed, the non-Gaussianities in the model with a feature are generated when the mode exits the horizon while for the resonant model, the non-Gaussianities are generated deep inside the horizon. As a consequence, we expect the two inflationary scenarios to make distinct predictions about the clustering of dark-matter halos. In particular, we anticipate that in the feature model, the non-Gaussian effect should be the largest around the mass scale that exited the horizon while the inflaton was crossing the feature. On the other hand, we expect non-Gaussian effects to be important for a broad range of scales in the resonant model since these were generated by causal physics inside the horizon. Our results support these qualitative predictions and most interestingly, they allow us to map properties of the inflaton potential to features of galaxy clustering.

The structure of this chapter is as follows. We begin by briefly reviewing halo biasing in the peak-background split formalism for general nonlocal quadratic non-Gaussianity. We then calculate the scale-dependent correction to the halo bias for the two inflation models considered here, emphasizing the effect of the new term unveiled in Refs. [246, 247]. We finally discuss our results in light of our qualitative predictions and physical expectations and conclude with a discussion on how these new effects could be detected

¹⁷Axion-monodromy inflation models are string-theory inspired inflation scenarios where the flatness of the potential is protected by a shift symmetry. Non-perturbative effects break this symmetry and lead to small oscillations in the potential driving inflation.

in large-scale-structure data.

6.2 Non-Gaussian Halo Bias in the Peak-Background Split Formalism

6.2.1 Nonlocal Kernel

Following [239], we consider the case for which the Bardeen potential during matter domination Φ is a general, nonlocal quadratic function of a Gaussian field ϕ

$$\Phi(\mathbf{x}) = \phi(\mathbf{x}) + f_{\text{NL}} \int d^3y \int d^3z W(\mathbf{y}, \mathbf{z}) \phi(\mathbf{x} + \mathbf{y}) \phi(\mathbf{x} + \mathbf{z}), \quad (6.1)$$

where the kernel $W(\mathbf{y}, \mathbf{z})$ is symmetric in its arguments and only depends on $y \equiv |\mathbf{y}|$ and $z \equiv |\mathbf{z}|$ as well as $\hat{\mathbf{y}} \cdot \hat{\mathbf{z}}$, where $\hat{\mathbf{y}} = \mathbf{y}/y$. In Fourier space, one can think of $\widetilde{W}(\mathbf{k}_1, \mathbf{k}_2)$ as a scale-dependent coupling between different modes. To conform to standard notation, we have pulled out an arbitrary factor of f_{NL} from the non-Gaussian kernel. Our results do not depend on this particular choice as they are only sensitive to the product $f_{\text{NL}}W(\mathbf{y}, \mathbf{z})$. Deviation from Gaussianity is usually parametrized by the bispectrum,

$$\langle \Phi(\mathbf{k}_1) \Phi(\mathbf{k}_2) \Phi(\mathbf{k}_3) \rangle = (2\pi)^3 \delta_{\text{D}}^3(\mathbf{k}_1 + \mathbf{k}_2 + \mathbf{k}_3) B_{\Phi}(k_1, k_2, k_3), \quad (6.2)$$

where δ_{D} is the Dirac delta function and $k_3 = |\mathbf{k}_1 + \mathbf{k}_2|$. In terms of the Fourier space kernel $\widetilde{W}(\mathbf{k}_1, \mathbf{k}_2)$, the bispectrum amplitude is given by

$$B_{\Phi}(k_1, k_2, k_3) = 2f_{\text{NL}} \left[\widetilde{W}(\mathbf{k}_1, \mathbf{k}_2) P_{\Phi}(k_1) P_{\Phi}(k_2) + 2 \text{ perm.} \right], \quad (6.3)$$

where $P_{\Phi}(k)$ stands for the power spectrum of Φ . The two permutations not written are the two remaining cyclic permutations of k_1, k_2, k_3 . Since the kernel $\widetilde{W}(\mathbf{k}_1, \mathbf{k}_2)$ is only required to be symmetric under the exchange of its two vectorial arguments, Eq. (6.3) does not uniquely specify \widetilde{W} . One

possible choice of kernel is

$$\widetilde{W}(\mathbf{k}_1, \mathbf{k}_2) = \frac{1}{2f_{\text{NL}}} \frac{B_{\Phi}(k_1, k_2, k_3)}{P_{\Phi}(k_1)P_{\Phi}(k_2) + 2 \text{ perm.}}, \quad (6.4)$$

which has the nice property of being fully symmetric under the exchange of the three momenta. For the halo bias calculation, we are mainly interested in the squeezed limit of the kernel where $k_2, k_3 \gg k_1$. In this limit, the bispectrum uniquely defines the kernel via the relation [239]

$$\widetilde{W}(\mathbf{k}_1, \mathbf{k}_2) \xrightarrow{k_2 \gg k_1} \frac{B_{\Phi}(k_1, k_2, k_3)}{4f_{\text{NL}}P_{\Phi}(k_1)P_{\Phi}(k_2)}. \quad (6.5)$$

Finally, to compute the dark-matter halo bias at late times, we need to consider the *processed* kernel $\widetilde{W}_0(\mathbf{k}_1, \mathbf{k}_2)$ defined via the transfer function $T(k)$,

$$\widetilde{W}_0(\mathbf{k}_1, \mathbf{k}_2) = \frac{T(|\mathbf{k}_1 + \mathbf{k}_2|)\widetilde{W}(\mathbf{k}_1, \mathbf{k}_2)}{T(k_1)T(k_2)}. \quad (6.6)$$

In the squeezed limit, this reduces to

$$\widetilde{W}_0(\mathbf{k}_1, \mathbf{k}_2) \xrightarrow{k_2 \gg k_1} \frac{1}{T(k_1)} \frac{B_{\Phi}(k_1, k_2, k_3)}{4f_{\text{NL}}P_{\Phi}(k_1)P_{\Phi}(k_2)}. \quad (6.7)$$

Note that we define our f_{NL} in terms of the Bardeen potential at last scattering, conforming to the convention usually adopted in CMB analyses.

6.2.2 Halo Bias in Peak-Background Split

We work in the Lagrangian picture of halo biasing where halos are identified as high-density regions in the initial linear matter field. As such, we focus here on deriving the Lagrangian halo bias b_{I} which relates the halo power spectrum to the linear matter power spectrum, $P_{\text{h}}(k) = b_{\text{I}}^2 P(k)$. The late-time linear Eulerian bias relevant for observations on large scales is simply given by $b_{\text{I}}^{\text{E}} = 1 + b_{\text{I}}$. In the Lagrangian picture, the number density of halos per unit logarithmic mass (also called halo mass function) is sensitive to the statistics of small-scale perturbations. In the Gaussian case, each Fourier mode evolves independently and therefore the small-scale

6.2. Non-Gaussian Halo Bias in the Peak-Background Split Formalism

matter power spectrum $P(k_s)$ (at some initial early time) is the same everywhere. However, non-Gaussianity introduces mode coupling, resulting in a dependence of the small-scale power spectrum on the local value of long-wavelength fluctuations. Non-Gaussian initial conditions thus generally rescale the local small-scale variance of the density field smoothed over a scale R_s , σ_{0s} , according to [246]

$$\hat{\sigma}_{0s}^2 \simeq \sigma_{0s}^2 + 4f_{\text{NL}}\phi_{\text{L}}(\mathbf{k})\sigma_{\text{W}}^2(k), \quad (6.8)$$

where the spectral moment σ_{W}^2 is

$$\sigma_{\text{W}}^2(k) = \int \frac{d^3k_s}{(2\pi)^3} F_{R_s}^2(k_s) \widetilde{W}_0(\mathbf{k}, \mathbf{k}_s) P(k_s), \quad (6.9)$$

and where $\phi_{\text{L}}(\mathbf{k})$ is a long-wavelength fluctuation of the gravitational potential. Here, F_{R_s} is the Fourier transform of a spherical top-hat with radius R_s , $P(k_s)$ is the matter power spectrum, and the “hat” denotes quantities that contain non-Gaussian contributions. Notice the appearance of the non-Gaussian kernel which indicates how a mode with wave number k_s couples to the long-wavelength mode k . Note also that σ_{W}^2 is not positive definite, as the sign depends on the shape of the non-Gaussian kernel. However, the second term in Eq. 6.8 is always much smaller than the Gaussian variance σ_{0s}^2 (since $\phi_{\text{L}} \sim 10^{-5}$), so that $\hat{\sigma}_{0s}^2$ is always positive.

Since the halo abundance \hat{n}_{h} generically depends on $\hat{\sigma}_{0s}$, this induces a scale-dependent dark-matter halo bias of the form [239, 246]

$$\begin{aligned} b_{\text{I}}(M, z; k) &\equiv \frac{1}{\hat{n}_{\text{h}}} \left. \frac{d\hat{n}_{\text{h}}}{d\delta_{\text{L}}(k)} \right|_{\delta_{\text{L}}=0} \\ &= \frac{\partial \ln \hat{n}_{\text{h}}}{\partial \ln \bar{\rho}} + \frac{\partial \ln \hat{n}_{\text{h}}}{\partial \ln \hat{\sigma}_{0s}} \frac{\partial \ln \hat{\sigma}_{0s}}{\partial \delta_{\text{L}}(k)}, \end{aligned} \quad (6.10)$$

where M stands for the halo mass, z for redshift, $\bar{\rho}$ is the average matter density of the Universe, \hat{n}_{h} is the average number density of halos of mass M and $\delta_{\text{L}}(k)$ is a long-wavelength density fluctuation. The halo mass M is related to the smoothing scale R_s through $M = (4\pi/3)\bar{\rho}R_s^3$ for a spherical

6.2. Non-Gaussian Halo Bias in the Peak-Background Split Formalism

tophat window function. In the following, we will drop the explicit z dependence. The first term in Eq. (6.10) is the usual Gaussian bias b_1 while the second term is induced by the non-Gaussian initial conditions. This last term can be expressed in a compact way when adopting a universal mass function prescription,

$$\hat{n}_h = \frac{\bar{\rho}}{M} f(\nu) \left| \frac{\partial \ln \hat{\sigma}_{0s}}{\partial \ln M} \right|, \quad (6.11)$$

where $\nu = \delta_c / \hat{\sigma}_{0s}$ is the significance, $\delta_c \approx 1.686$ is the linearly extrapolated collapse threshold, and $f(\nu)$ is a multiplicity function which we do not need to specify explicitly. A change in $\hat{\sigma}_{0s}$ thus changes halo abundance through a change in ν as well as a change in the Jacobian $|\partial \ln \hat{\sigma}_{0s} / \partial \ln M|$. The non-Gaussian halo bias correction can then be written in terms of the non-Gaussian kernel,

$$\Delta b_I(M, k) = 2f_{\text{NL}} \mathcal{M}^{-1}(k) \frac{\sigma_W^2(M, k)}{\sigma_{0s}^2(M)} [b_1(M) \delta_c + 2\epsilon_W(M, k)], \quad (6.12)$$

with

$$\epsilon_W(M, k) \equiv \frac{\partial \ln \sigma_W^2(M, k)}{\partial \ln \sigma_{0s}^2(M)} - 1, \quad (6.13)$$

where $\mathcal{M}(k) = 2k^2 g_*(z) / (3(1+z) H_0^2 \Omega_m)$. Here $g_*(z)$ is the potential growth function normalized to unity at last scattering. Since it is understood that $k_s \gg k$ in Eq. (6.9), we see that the bias correction depends on the non-Gaussian kernel evaluated in the squeezed limit. We note that the term proportional to $\epsilon_W(M, k)$ had been previously neglected in the literature until it was shown to be important in Ref. [246]. As we will see in the next section, this term is crucial for models displaying oscillatory features in their bispectrum. Examining Eq. (6.12), we observe that the scale dependence of the halo bias is determined by the product of $\mathcal{M}^{-1}(k) \propto k^{-2}$ with the leading k -dependent part of the processed non-Gaussian kernel evaluated in the squeezed limit. We now turn our attention to bispectra showing oscillatory behaviour and calculate the resulting scale-dependent bias. The numerical results presented in this paper assume a flat Λ CDM universe [28]

with $h = 0.72$, $\Omega_m = 0.28$, $n_s = 0.958$ and $\sigma_8 = 0.8$. The pivot scale for the primordial power spectrum amplitude is kept at $k_* = 0.002\text{Mpc}^{-1}$ throughout.

6.3 Oscillatory Bispectra and their Scale-dependent Bias

6.3.1 Resonant Non-Gaussianity

Resonant non-Gaussianity arises when periodic features in the inflationary potential (see section 1.2) lead to an oscillatory coupling between modes, which can trigger a resonance for modes oscillating with the same frequency inside the horizon [128–132, 241]. Such features arise, for example, in certain brane inflation models or in axion-monodromy inflation. For this class of models, the bispectrum has the generic form [132]

$$B_{\text{res}} = \left(\frac{5}{3}\right) (2\pi)^4 f_{\text{NL}}^{\text{res}} \Delta_{\Phi}^2 \frac{1}{k_1^2 k_2^2 k_3^2} \left(\sin(C_{\omega} \ln(k_t/k_p)) + \frac{1}{C_{\omega}} \cos(C_{\omega} \ln(k_t/k_p)) \sum_{i \neq j} \frac{k_i}{k_j} + \mathcal{O}\left(\frac{1}{C_{\omega}^2}\right) \right), \quad (6.14)$$

where Δ_{Φ} is the amplitude of primordial scalar power spectrum, $k_t = k_1 + k_2 + k_3$, k_p is a pivot scale which introduces a phase, and C_{ω} is related to the frequency ω of the periodic features of the inflationary potential by $C_{\omega} = \omega/H_1$. Here, H_1 stands for the Hubble parameter during inflation. The leading factor of $5/3$ comes from the conversion between the Bardeen primordial potential Φ and the gauge invariant curvature perturbation ζ at late times. Constraints from the matter power spectrum provide an upper bound on the value of $f_{\text{NL}}^{\text{res}}$. For the axion-monodromy scenario with a linear zero-order potential, this bound reads [132, 245]

$$f_{\text{NL}}^{\text{res}} \lesssim 10^{-3} C_{\omega}^{5/2}, \quad (6.15)$$

6.3. Oscillatory Bispectra and their Scale-dependent Bias

where it is assumed that the pivot scale $k_p = 0.002 \text{ Mpc}^{-1}$ exits the horizon about 60 e-folds before the end of inflation. Other zeroth-order inflaton potentials are likely to lead to a somewhat different constraint on $f_{\text{NL}}^{\text{res}}$ but we shall use Eq. (6.15) as a rough upper limit for this type of model. The resonant bispectrum can readily be evaluated in the squeezed limit [132]

$$B_{\text{res}} \xrightarrow{k_s \gg k} \left(\frac{5}{3}\right) \frac{(2\pi)^4 f_{\text{NL}}^{\text{res}} 2\Delta_{\Phi}^2}{C_\omega k_s^3 k^3} \cos \left\{ C_\omega \ln \left[\frac{2k_s}{k_p} \right] \right\}. \quad (6.16)$$

Note that the leading correction to this expression is suppressed by a factor of k/k_s , thus negligibly contributing to the bispectrum in the squeezed limit. Using Eq. (6.5), we obtain the leading-order non-Gaussian kernel,

$$\begin{aligned} \widetilde{W}(\mathbf{k}, \mathbf{k}_s) &\simeq \left(\frac{5}{3}\right) \frac{(2\pi)^4}{2C_\omega} \left(\frac{k}{k_*}\right)^{-\epsilon} \cos \left\{ C_\omega \ln \left[\frac{2k_s}{k_p} \right] \right\} \\ &\quad \times \left(\frac{k_s}{k_*}\right)^{-\epsilon} \left[1 - \frac{1}{2} \left(\frac{k}{k_s}\right)^{3-\epsilon} + \dots \right], \end{aligned} \quad (6.17)$$

where $\epsilon = n_s - 1$ and the ellipsis stands for terms that are higher order in k/k_s . We immediately see that the scale dependence of the non-Gaussian bias is given by

$$\Delta b_{\text{I,res}}(k) \propto k^{-2-\epsilon}, \quad (6.18)$$

that is, it is very similar to that of the local model. To calculate the amplitude of the bias correction, we first need to integrate Eq. (6.9) over the small-scale modes to obtain the non-Gaussian spectral moment $\sigma_W^2(k)$. The k_s integral is of the general form

$$\sigma_W^2 \propto \int k_s dk_s T^2(k_s) \frac{j_1^2(k_s R_s)}{R_s^2} \cos(C_\omega \ln(2k_s/k_p)). \quad (6.19)$$

For large values of the frequency C_ω , the integrand is rapidly oscillating and the resulting amplitude for the non-Gaussian bias is expected to be rather small. For a small enough value of the frequency ($C_\omega \lesssim 100$), the integral can be done numerically. To evaluate the second term in Eq. (6.12), we first

6.3. Oscillatory Bispectra and their Scale-dependent Bias

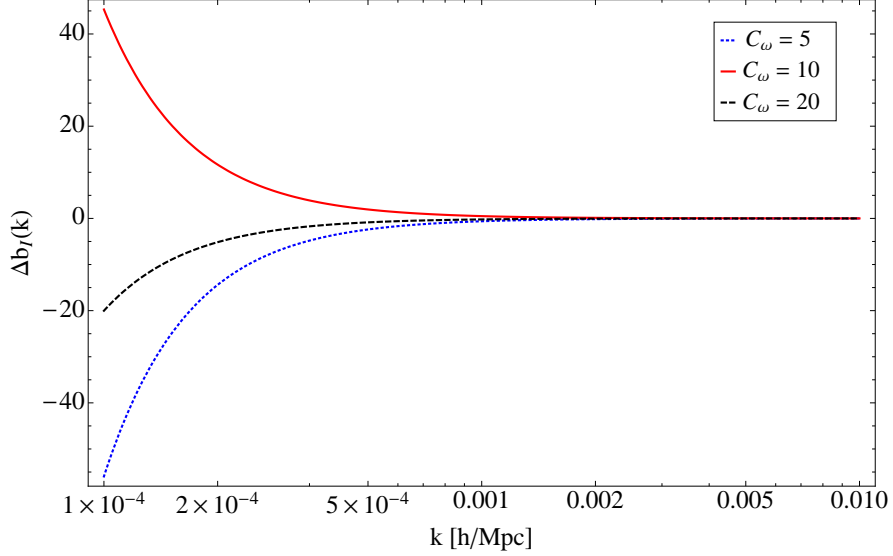


Figure 6.1: Non-Gaussian correction to the halo bias for the resonant non-Gaussianity model as a function of scale. We evaluate the bias for $M = 10^{13}M_{\odot}/h$ at $z = 0$. We take $f_{\text{NL}}^{\text{res}} = 10^{-3}C_{\omega}^{5/2}$ and evaluate the Gaussian bias b_1 using the Sheth-Tormen mass function [248].

use the chain rule to write it as

$$\frac{\partial \sigma_W^2(M, k)}{\partial \sigma_{0s}^2(M)} = \frac{\partial \sigma_W^2(M, k)}{\partial \ln M} \left(\frac{\partial \sigma_{0s}^2(M)}{\partial \ln M} \right)^{-1}. \quad (6.20)$$

The derivatives on the right can be calculated numerically. For all numerical computations, we use the complete expression for the bispectrum, Eq. (6.14). In Fig. 6.1, we show the scale dependence of the non-Gaussian halo bias correction for three values of C_{ω} evaluated for a halo mass of $10^{13}M_{\odot}/h$ at $z = 0$. We see that the non-Gaussian bias correction is small except for the largest scales where the scale dependence of $\Delta b_{\text{I, res}}(k) \propto k^{-2-\epsilon}$ becomes important. Interestingly, the non-Gaussian bias for these resonant models is completely dominated by the term proportional to $\epsilon_W(M, k)$ in Eq. (6.12), which was recently unveiled in Refs. [246, 247]. To understand why this new term is crucial for our analysis, we plot in Fig. 6.2 the non-Gaussian spectral

6.3. Oscillatory Bispectra and their Scale-dependent Bias

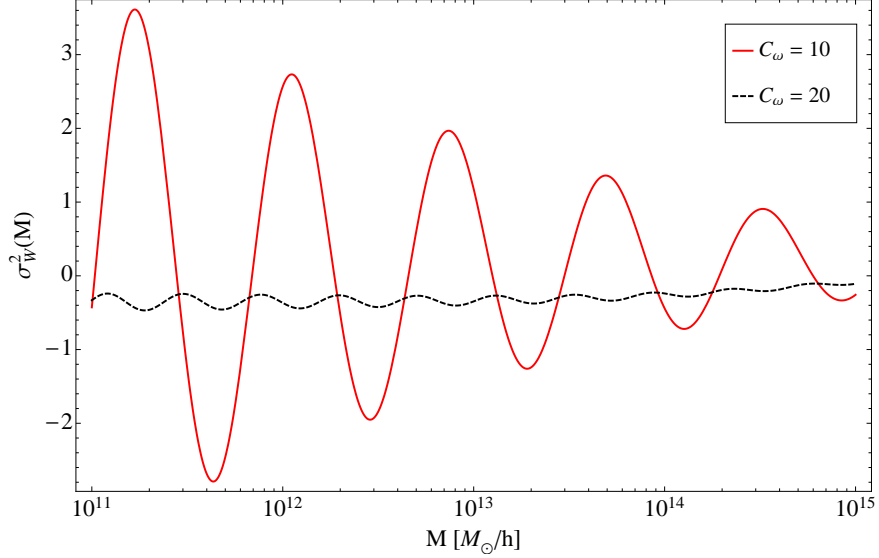


Figure 6.2: Non-Gaussian spectral moment σ_W^2 for the resonant model as a function of halo mass. We evaluate this spectral moment for $k = 10^{-3}h$ Mpc^{-1} at $z = 0$.

moment σ_W^2 as a function of halo mass for a fixed comoving scale. We see that σ_W^2 strongly oscillates with halo mass, leading to a large contribution to $\partial\sigma_W^2/\partial\ln M$, especially toward small masses. This highlights the importance of the newly discovered term for accurately predicting the non-Gaussian halo bias. We will discuss the relevance of this result for observations in Sec. 6.4.

An interesting feature of resonant non-Gaussianity models is that they predict a modulation of the halo bias with changing halo mass. In Fig. 6.3, we show the non-Gaussian halo bias as a function of halo mass evaluated at a scale $k = 10^{-3}h$ Mpc^{-1} . Again, the bias is dominated by the second term of Eq. (6.12) for $M \lesssim 10^{15}M_\odot/h$. We observe that the amplitude of the non-Gaussian bias decreases with increasing C_ω very rapidly and therefore this effect is likely to be unobservable unless C_ω is small. As expected, the non-Gaussian features of the halo bias show coherent modulations over a wide range of mass scales, an artifact of non-Gaussianities being produced by causal physics deep inside the horizon for these models. To contrast the

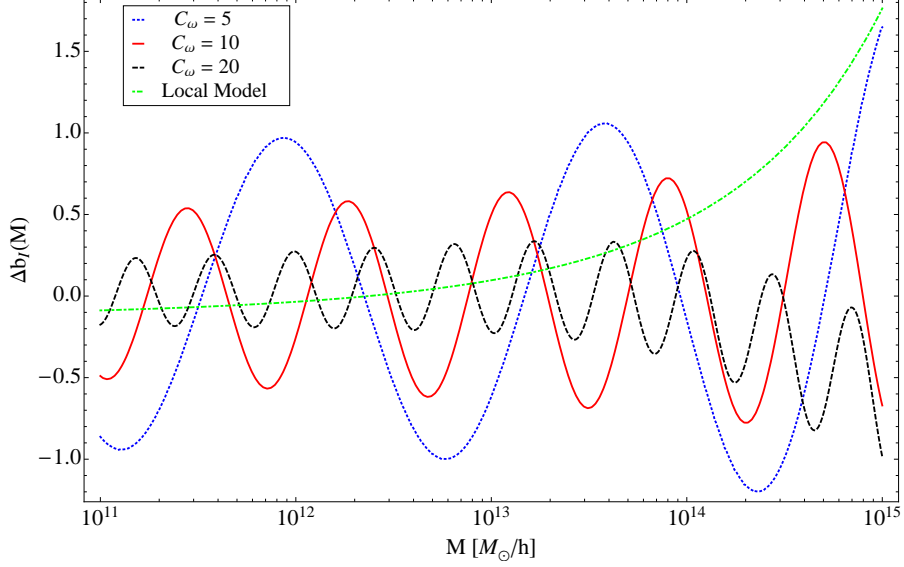


Figure 6.3: Non-Gaussian correction to the halo bias for the resonant non-Gaussianity model as a function of halo mass. We evaluate the bias for $k = 10^{-3}h \text{ Mpc}^{-1}$ at $z = 0$. We take $f_{\text{NL}}^{\text{res}} = 10^{-3}C_\omega^{5/2}$ and evaluate the Gaussian bias b_1 using the Sheth-Tormen mass function. For comparison, we also show the bias for local non-Gaussianity with $f_{\text{NL}}^{\text{local}} = 2$.

resonant model with the more traditional local model of non-Gaussianity, we also display the halo bias for a local model with $f_{\text{NL}}^{\text{local}} = 2$. At moderate halo masses ($M \sim 10^{12} - 10^{14} M_\odot/h$), the effect of resonant non-Gaussianity is comparable to that of a local model with $f_{\text{NL}}^{\text{local}}$ of order unity, for the values of C_ω chosen.

6.3.2 Features in the Inflaton Potential

The presence of a sharp feature in the inflaton potential can induce large primordial non-Gaussianities [127, 128, 240–242]. Indeed, modes that exit the horizon while the inflaton is crossing the feature get a boost in their three-point signal. Here, we shall focus on the case of a step in the inflaton potential, but our analysis could also be applied to the case of a bump in the potential. The exact form of the bispectrum can only be obtained

6.3. Oscillatory Bispectra and their Scale-dependent Bias

numerically but the authors of [128] suggested an approximate form:

$$B_{\text{feat}}(k_1, k_2, k_3) \approx - \left(\frac{5}{3}\right) (2\pi)^4 f_{\text{NL}}^{\text{feat}} \frac{\Delta_{\Phi}^2 k_f}{k_1^3 k_2^3 k_3^3} \quad (6.21)$$

$$\times \left\{ 2 \frac{\sum_{i \neq j} k_i k_j^2}{k_t} \sin \left[\frac{k_t}{k_f} \right] \sin \left[\frac{k_t \Delta k_f}{k_f^2} \right] \right\}.$$

Here, $k_t = k_1 + k_2 + k_3$ and $k_f \pm \Delta k_f$ are the Fourier modes that exit the horizon while the inflaton is crossing the feature (the sharper the feature in the inflaton potential, the larger Δk_f becomes). We fixed the phases such that $B_{\text{feat}} \rightarrow 0$ as $k_t \rightarrow 0$ which is physically motivated, since modes that exit the horizon long before the inflaton encounters the feature should not show significant non-Gaussianities. We choose the overall sign such that the non-Gaussian bias is positive for the scale exiting the horizon when the inflaton crosses the feature. In practice, this sign should be fixed by comparison to numerical simulations. In the squeezed limit, the bispectrum reads

$$B_{\text{feat}} \xrightarrow{k_s \gg k} - \left(\frac{5}{3}\right) (2\pi)^4 f_{\text{NL}}^{\text{feat}} \frac{\Delta_{\Phi}^2}{k_s^4 k^2} \left(\frac{k_f}{k}\right) \sin \left(\frac{2k_s}{k_f}\right) \sin \left(\frac{2k_s \Delta k_f}{k_f^2}\right). \quad (6.22)$$

For a narrow feature, we generally expect $\Delta k_f/k_f \ll 1$ and thus the last sinusoidal factor in Eq. (6.22) can be considered as an envelope function for the first rapidly oscillating sine factor. From Eq. (6.22), we see that at fixed k_s , non-Gaussianity becomes more important for modes k smaller than k_f (remember that k is the scale at which clustering of halos is measured). The non-Gaussian kernel can then readily be obtained as

$$\widetilde{W}(\mathbf{k}, \mathbf{k}_s) \simeq - \left(\frac{5}{3}\right) \frac{(2\pi)^4}{4} \left(\frac{k_f}{k_s}\right) \left(\frac{k}{k_*}\right)^{-\epsilon} \left(\frac{k_s}{k_*}\right)^{-\epsilon}$$

$$\times \sin \left(\frac{2k_s}{k_f}\right) \sin \left(\frac{2k_s \Delta k_f}{k_f^2}\right). \quad (6.23)$$

Note that \widetilde{W} approaches zero for $k_s \ll k_f$ and for $k_s \gg k_f$. This physically makes sense, since modes with $k_s \gg k_f$ are oscillating deep inside the horizon when the inflaton crosses the feature, and we expect their non-Gaussianities

6.3. Oscillatory Bispectra and their Scale-dependent Bias

to roughly cancel out. On the other hand, modes with $k_s \ll k_f$ are outside the horizon when non-Gaussianities are generated and we thus expect their contribution to the kernel to be small. We immediately see that the scale dependence of the halo bias is given by

$$\Delta b_{\text{I,feat}}(k) \propto k^{-2-\epsilon}, \quad (6.24)$$

which, at first glance, is similar to the resonant model. However, as we will see below, the two models predict very different behaviour for how the amplitude of Δb_{I} varies with halo mass. From Eq. (6.23), it is straightforward to compute numerically the non-Gaussian spectral moment σ_W^2 . In the feature model, the integral over small scale modes has the general form

$$\sigma_W^2 \propto \int k_s dk_s T^2(k_s) \frac{j_1^2(k_s R_s)}{R_s^2} \left(\frac{k_f}{k_s}\right) \sin\left(\frac{2k_s}{k_f}\right) \sin\left(\frac{2k_s \Delta k_f}{k_f^2}\right). \quad (6.25)$$

We see that for a given value of k_f , there will always be a scale R_s for which constructive interference between the first sine factor and the Bessel function happens (again, the second sine factor is considered to be slowly varying). Since the Bessel function peaks around $k_s \sim R_s^{-1}$, we naively expect $|\sigma_W^2|$ to have a maximum near $R_s = R_f \sim \mathcal{O}(1)/k_f$ or equivalently, near $M_f \sim \mathcal{O}(1)(4\pi/3)\bar{\rho}k_f^{-3}$. For $R_s \ll R_f$, the first sine factor is rapidly oscillating near the peak of the Bessel function and thus the only nonvanishing contribution comes from the low k_s tail. In this limit, the integrand becomes independent of R_s since $j_1^2(k_s R_s) \propto k_s^2 R_s^2$ for $k_s \ll R_s^{-1}$. We thus expect σ_W^2 to asymptote to a constant for small halo masses. On the other hand, for $R_s \gg R_f$, the integrand approaches zero and we therefore expect σ_W^2 to vanish for large halo masses.

Our numerical calculations support these qualitative conclusions. Indeed, Fig. 6.4 shows the absolute value of the non-Gaussian spectral moment for two values of k_f . The enhancement around $M_f \sim 1.5(4\pi/3)\bar{\rho}k_f^{-3}$ is clearly visible in both cases and $\sigma_W^2(M)$ rapidly vanishes for $M > M_f$. The latter point is expected on physical grounds since halos with $M > M_f$ correspond to scales (in the initial density field) that were outside the horizon

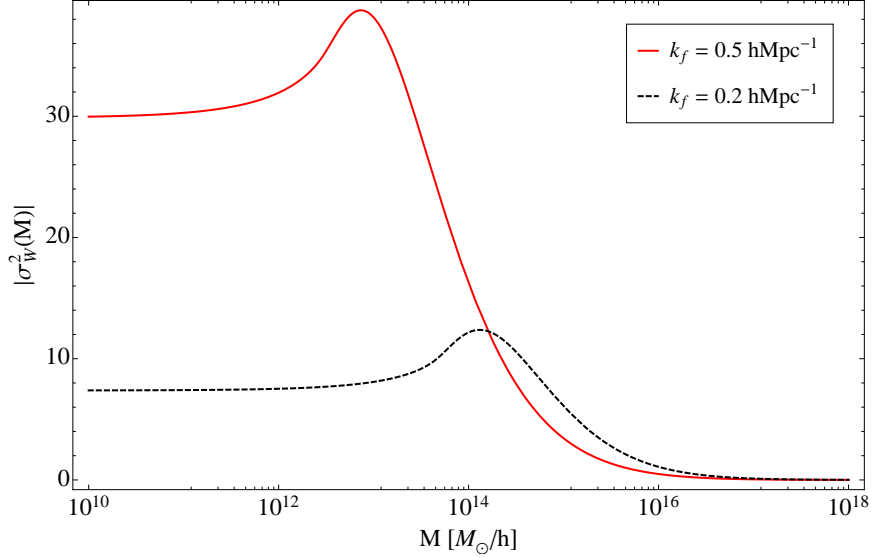


Figure 6.4: Absolute value of the non-Gaussian spectral moment σ_W^2 for the feature model as a function of halo mass. We evaluate this spectral moment for $k = 10^{-3}h \text{ Mpc}^{-1}$ at $z = 0$ and use $\Delta k_f/k_f = 0.01$.

when the non-Gaussianities were generated. Therefore, the non-Gaussian correction to the variance of the density field smoothed on these scales must be somewhat suppressed.

We can now use Eq. (6.12) to compute the scale-dependent non-Gaussian correction to the halo bias. From the functional form of σ_W^2 , we expect the term proportional to ϵ_W to dominate around the feature at $M = M_f$ since $\partial \ln \sigma_W^2 / \partial \ln M$ is largest there. To verify this, it is instructive to consider the two distinct contributions to the bias as a function of halo mass. In Fig. 6.5, we show both the contribution proportional to the Gaussian bias b_1 , as well as the recently unveiled contribution proportional to ϵ_W for a feature at $k_f = 0.5 \text{ hMpc}^{-1}$. We observe that the ϵ_W term clearly displays a feature at $M_f \sim 1.5(4\pi/3)\bar{\rho}k_f^{-3} \simeq 4 \times 10^{12}M_\odot/h$ and that it dominates the overall bias for halo masses $M \lesssim 10^{14}M_\odot/h$. This once again highlights the importance of the ϵ_W term for models with strongly scale-dependent bispectra [247].

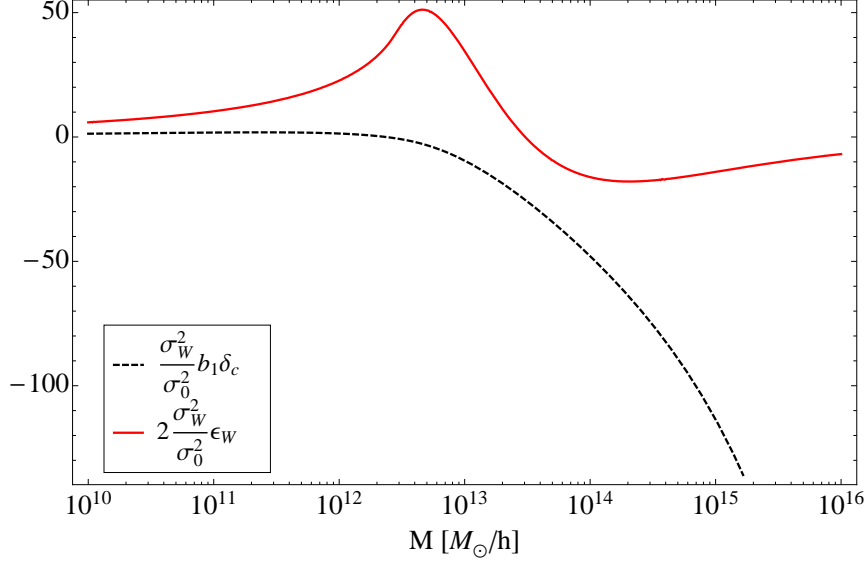


Figure 6.5: The two contributions to the non-Gaussian halo bias correction as a function of mass for the model with a feature at $k_f = 0.5 \text{hMpc}^{-1}$. We evaluate σ_W^2 for $k = 10^{-3} \text{hMpc}^{-1}$ at $z = 0$ and use $\Delta k_f / k_f = 0.01$. The Gaussian bias b_1 is derived using the Sheth-Tormen mass function.

In Fig. 6.6, we show the amplitude of the non-Gaussian bias correction as a function of halo mass for three different values of k_f . Note that while we assumed a value of $f_{\text{NL}}^{\text{feat}} = 10$ here, still within the allowed range of power spectrum constraints [128], this parameter is in reality fixed for a given inflation potential by the numerical calculation. For comparison, we also plot the halo bias correction for local quadratic non-Gaussianity, $\Delta b_{\text{I,local}} = 2f_{\text{NL}}^{\text{local}} b_1 \delta_c \mathcal{M}^{-1}(k)$. We immediately see that the bias correction for models with a feature in the potential displays a large enhancement around $M = M_f$ when compared to the monotonic and featureless bias of a local-type model. Observations of this tell-tale signature in large-scale-structure data provide us with an exciting new window to probe microscopic inflationary physics with observations of galaxy clustering on the largest scales.

For halo masses $M \gg M_f$, the bias becomes dominated by the first term of Eq. (6.12) since b_1 is large for very massive halos. In this limit, Δb_{I} is

6.3. Oscillatory Bispectra and their Scale-dependent Bias

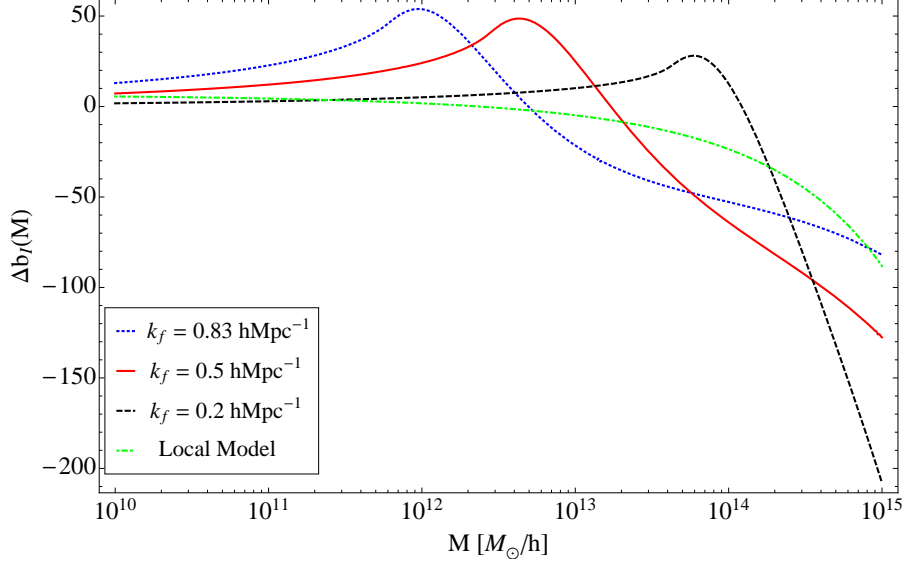


Figure 6.6: Mass dependence of the non-Gaussian correction to the halo bias for the model with a feature in the inflaton potential. We evaluate the bias for $k = 10^{-3}h \text{ Mpc}^{-1}$ at $z = 0$ and use $\Delta k_f/k_f = 0.01$. We take $f_{\text{NL}}^{\text{feat}} = 10$ and evaluate the Gaussian bias b_1 using the Sheth-Tormen mass function. For comparison, we also show the bias for the local model of non-Gaussianity with $f_{\text{NL}}^{\text{local}} = -10$.

very sensitive to the small k behaviour of the bispectrum which may not be accurately captured by our ansatz, Eq. (6.22). Thus, a complete numerical computation of the bispectrum is likely to be required to accurately predict the large-mass limit of the halo bias. We leave this for future work. However, since halos above $M \gtrsim 10^{15}M_{\odot}/h$ are very rare, especially at higher redshifts, we do not expect the observational constraints to be dominated by this mass range.

In Fig. 6.7, we show the absolute value of the non-Gaussian bias correction as a function of scale for three values of k_f . We evaluate the amplitude of the bias at $M = M_f$, that is, at the peak of the feature in ϵ_W . At this mass scale, we see that the halo bias can reach a very wide amplitude on large cosmological scales. The scale dependence proportional to $k^{-2-\epsilon}$ derived

6.3. Oscillatory Bispectra and their Scale-dependent Bias

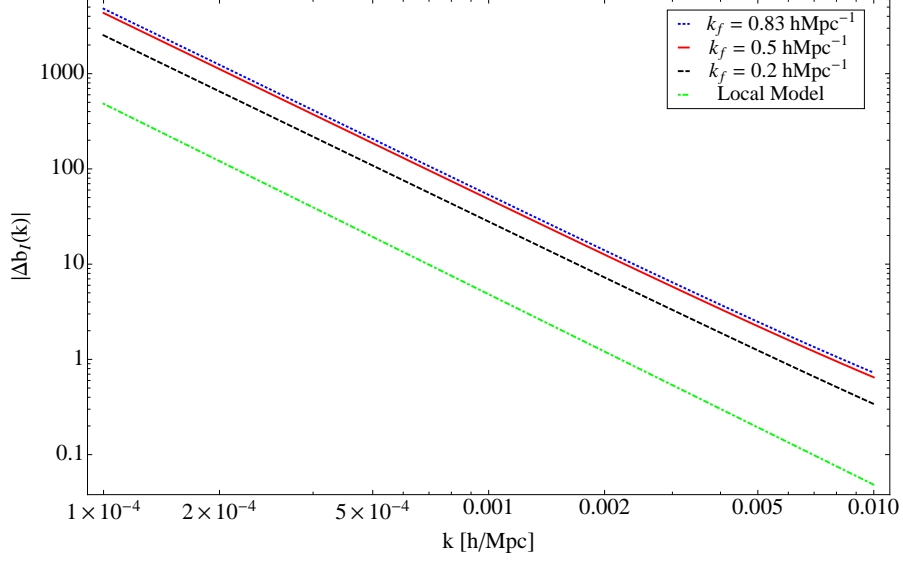


Figure 6.7: Scale dependence of the non-Gaussian correction to the halo bias for the model with a feature in the inflaton potential. We evaluate the bias for $M = 1.5(4\pi/3)\bar{\rho}k_f^{-3}$ at $z = 0$ and use $\Delta k_f/k_f = 0.01$. We take $f_{\text{NL}}^{\text{feat}} = 10$ and evaluate the Gaussian bias b_1 using the Sheth-Tormen mass function. For comparison, we also show the non-Gaussian bias correction from the local model evaluated at $M = 10^{13}M_{\odot}/h$ and $f_{\text{NL}}^{\text{local}} = 100$.

in Eq. (6.23) is readily visible. For comparison, we also plot the halo bias correction for the local-model of non-Gaussianity which displays a similar scale dependence but a much smaller amplitude even for $f_{\text{NL}}^{\text{local}} = 100$.

We note in passing that varying $\Delta k_f/k_f$ corresponds to changing the overall scale of the bispectrum. This can readily be seen from Eq. (6.22) where $\Delta k_f/k_f$ only appears in the modulating envelope. For $\Delta k_f/k_f \ll 1$ and $2k_s \lesssim k_f$ (i.e. for the modes that contribute most to σ_W^2), one can Taylor expand the second sine factor to obtain, after simplification, $B_{\text{feat}} \propto \Delta k_f/k_f$. Therefore, the overall amplitude of the bias correction is determined by the product $f_{\text{NL}}^{\text{feat}}(\Delta k_f/k_f)$. This scaling agrees with the result of Ref. [127], where it was shown that the overall amplitude of the bispectrum is inversely proportional to the width of the step in the potential. To see this, we note

that the sharper is the step, the more kinetic energy is acquired by the inflaton and as a consequence, the longer slow roll is violated. Therefore, we expect that the sharper is the step (corresponding to larger bispectrum amplitude), the larger the band of Fourier modes affected (Δk_f), hence the above result.

In summary, we have shown that the presence of a feature in the inflaton potential leads to a corresponding feature in the mass dependence of the non-Gaussian halo bias. Ultimately, this is a consequence of non-Gaussianity being generated at a specific scale during inflation in these models. Finally, we reiterate that the numerical results presented in this section were computed using the analytical expression for the bispectrum given in Eq. 6.21. It is important to keep in mind that this expression is approximate. However, it most likely captures the important physics. As such, we expect our conclusions to be robust to the inclusion of a more accurate bispectrum.

6.4 Discussion

We have analyzed the non-Gaussian halo bias resulting from two inflation models displaying oscillatory bispectra. Even though the two models predict the same scale dependence as local quadratic non-Gaussianity, we find that they make very different predictions concerning how the amplitude of the bias varies with halo mass. Indeed, while the resonant model predicts an oscillatory amplitude as a function of halo mass, models with a feature in the potential predict an enhancement of the bias for halos with mass that corresponds to the scale that exited the horizon at the time when the inflaton was crossing the feature in the potential. Ultimately, these very different outcomes can be traced back to the distinct physics that is responsible for generating non-Gaussianities in the first place.

For the resonant model, non-Gaussianity is generated well inside the horizon, when the modes are rapidly oscillating. As explained in Ref. [128], oscillations in the inflaton potential lead to an oscillatory coupling between different Fourier modes. As the physical frequency of each mode $k/a(t)$ decreases, there will be a time when $k/a(t_{\text{res}}) \sim \omega$ and the oscillating mode

can resonate with the coupling and generate a departure from Gaussianity. As a large number of modes eventually passes through the resonance, we naturally expect the non-Gaussian effects to be present on a broad range of scales, as can be seen in Fig. 6.3. A crucial consequence of this subhorizon generation mechanism is that the resulting modulation of the halo bias is *in phase* over a broad range of masses. This is a tell-tale signature that could be looked for in large-scale-structure data and used to put constraints on these resonant-type inflation models.

For models with a feature in the inflaton potential, non-Gaussianity is generated during slow-roll violation associated with the inflaton suddenly accelerating as it crosses the step or the bump in the potential. Consequently, different Fourier modes within a limited range of scales are coupled, hence generating a nonvanishing three-point function. However, modes deep inside the horizon are rapidly oscillating and we thus expect their non-Gaussian signature to average out to zero. On the other hand, modes that exit the horizon as slow roll is violated are frozen-in before causal physics could erase their correlation with other Fourier modes. We thus expect the bispectrum to be significant when at least one side of the triangle has $k \sim k_f$ (and no side has $k \gg k_f$). As a consequence, modes that exit the horizon during slow-roll violation get an enhanced coupling to the long-wavelength perturbations, resulting in an amplified clustering of halos at the corresponding mass scale. Conversely, modes that are superhorizon when slow-roll is violated become correlated with modes that have $k \sim k_f$. This induces a rescaling of the variance of the density field according to Eq. (6.8), which results in a nonvanishing halo bias at these mass scales. As mentioned earlier, this rescaling of the variance is very sensitive to the small- k limit of the bispectrum and a complete numerical computation will be required to accurately predict the halo bias for $M \gg M_f$. Nevertheless, since very massive halos are rare and restricted to low redshifts, it is unlikely that observational constraints will depend sensitively on the high-mass tail.

For both classes of models, we find that the term coming from the Jacobian $d \ln \sigma_{0s} / d \ln M$ (see Ref. [246] for details) is an important and often dominant contribution to the non-Gaussian halo bias. This term comes

about because the non-Gaussian mode-coupling induces a modulation with ϕ_L of the significance *interval* $d \ln \nu = d \ln \sigma_{0s}$ that corresponds to a fixed logarithmic mass interval $d \ln M$. This term is strictly present because we have assumed throughout that halos are selected by mass, which is appropriate e.g. when comparing to N -body simulations. In practice, however, galaxies are selected by more complex criteria which are only indirectly related to the host halo mass. If we divide the total galaxy sample into different subsamples (e.g., by luminosity, colour, light profile, ...), then the mass dependence shown in Figs. 6.3 and 6.6 will be observable as long as the scatter in the mass-observable relation is not much larger than the width of the features. Fortunately, the latter typically corresponds to a factor of 2 or more in mass, which should make these features detectable for a wide range of large-scale structure tracers. Note that the precise shape of $\Delta b_I(M)$ depends on the filter chosen for the small-scale density field. In principle, one could use a filter matched to the Lagrangian profiles of dark-matter halos [249]. We have tried replacing the top-hat filter with a Gaussian, and found only relatively minor differences, at the 7% level for $\Delta b_I(M)$ (see Fig. 6.8).

6.5 Conclusion

We have shown that measurements of galaxy clustering could potentially be used as a probe of features in the inflationary potential. By computing the non-Gaussian correction to the halo bias, we revealed that features in the inflationary potential such as oscillations, bumps, or steps get imprinted onto the clustering properties of dark-matter halos. While we have restricted ourselves to two generic models for which approximate forms of the oscillatory bispectrum are known, we expect this effect to be robust to the inclusion of more detailed bispectra. We note that this probe of primordial non-Gaussianity is complementary to CMB constraints, as it probes very small scales where the microwave background becomes foreground dominated. On intermediate scales, the two approaches could be used in conjunction to cross correlate a possible feature in CMB data with a corresponding attribute in the clustering of dark-matter halos.

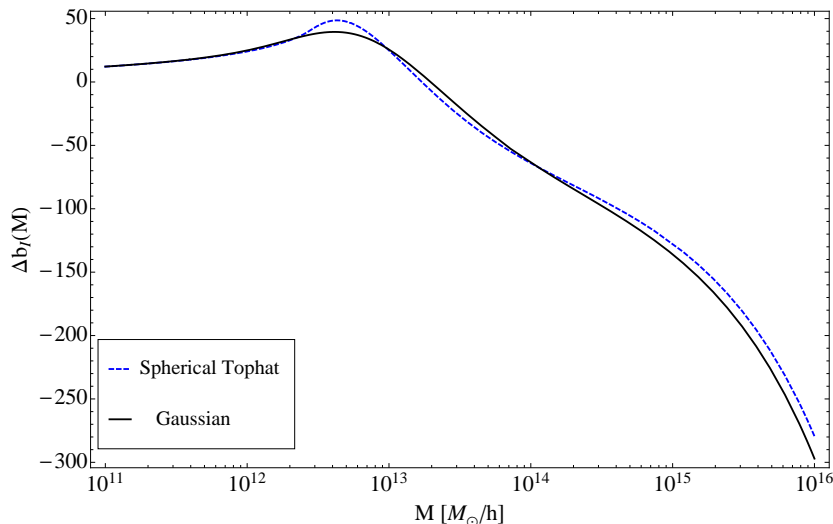


Figure 6.8: Comparison between $\Delta b_I(M)$ obtained with a spherical tophat filter and with a Gaussian filter. We evaluate the bias for $k = 10^{-3} h \text{ Mpc}^{-1}$ at $z = 0$ and use $\Delta k_f/k_f = 0.01$ and $k_f = 0.5 h \text{ Mpc}^{-1}$. We take $f_{\text{NL}}^{\text{feat}} = 10$.

While showing the same scale dependence $\propto k^{-2}$, the predictions of the models considered here are strikingly different from the usually considered local model. In particular, they show significantly stronger effects for moderate halo masses ($10^{12} - 10^{14} M_\odot/h$) than the local model, as compared to the effect at the high-mass end ($> 10^{14} M_\odot/h$). Thus, focusing on the most massive, highly biased halos might not in general be the best way to design or optimize surveys for the search for primordial non-Gaussianity.

The non-Gaussian models discussed here also make other predictions which are potentially observable with large-scale structure. While the study of these effects is beyond the scope of this paper, it would be interesting to correlate the non-Gaussian halo bias with features in the matter power spectrum and in the mass function of dark-matter halos. The former could in principle be probed by weak lensing observations, and the latter through the abundance of galaxy clusters. The bispectrum of galaxies would also be a precise, albeit more complex and computationally expensive, approach to testing these inflationary models. The key advantage of the scale-dependent

6.5. Conclusion

bias is, however, that it is a unique signature of primordial non-Gaussianity which is not easily mimicked by other effects. We thus anticipate this observable to be a robust probe of features in the inflaton potential.

Chapter 7

Conclusions

In this final chapter, we summarize the key results obtained in this thesis, emphasizing their contributions to the field of theoretical cosmology.

In chapter 2, we have shown that the resonant annihilation of DM to e^+e^- pairs is in tension with data from the diffuse gamma-ray background and limits on energy injection into the primeval gas. We determined that the regions of parameter space corresponding to the largest enhancements are problematic and likely ruled out by these bounds. Our results contributed to disfavouring DM annihilation as the main source of the positron excess seen by cosmic-ray experiments. Other works have reached similar conclusions [89, 250–252].

In chapter 3, we derived a second-order tight-coupling approximation scheme. We showed that this second-order scheme leads to an improvement in the accuracy of numerical computations and can be used to reduce the speed of CMB Boltzmann codes. The equations derived in this chapter are now implemented in common CMB codes such as `CAMB` and `CLASS`, for use by the greater cosmological-science community. We have also derived the higher-order terms in the initial-condition expansion and computed, for the first time, the tight-coupling corrections to these initial conditions. These higher-order terms are required in order to solve the exact equations from early times.

In chapters 4 and 5, we presented an exhaustive study of atomic DM. This scenario naturally includes a DR component which could explain the relatively high apparent number of relativistic species implied by recent CMB data. We have determined that this DR needs to be cooler than the CMB in order to leave the abundances of primordial elements unchanged. We have revisited the atomic physics necessary to characterize the dark

atoms and pointed out a few improvements that are required to accurately describe the thermal history of the dark sector. We have studied the solutions to the Boltzmann equations in the atomic DM scenario and shown how they differ from the vanilla CDM case. In particular, we have determined that the growth of DM fluctuations is seriously impeded on scales that enter the horizon before the epoch of DM kinetic decoupling.

In chapter 5, we have computed the linear matter power spectrum and revealed that it displays strong acoustic oscillations and a cutoff on small scales. In configuration space, these oscillations point to the DAO scale which corresponds to the size of the DM sound horizon at the dark drag epoch. We have shown that the DAO scale selects a minimal DM halo mass which could potentially alleviate the current tension regarding the faint-end of the galaxy luminosity function. We have similarly computed the CMB angular power spectra and showed that it is sensitive to the dark-photon decoupling epoch, if the latter happens close enough to the surface of last-scattering of CMB photons.

We have presented a careful and realistic analysis of DM collisions inside halos and showed that they constrain the parameter space of atomic DM. We have determined that a viable atomic DM model is typically very massive and has a binding energy that is much larger than that of standard atomic hydrogen. We have finally identified a region of parameter space where atomic DM could potentially mitigate the recent satellite-galaxy problems. Detailed N -body simulations will be required to accurately determine whether this latter model can successfully address this issue.

Essentially, we have shown in chapters 4 and 5 that the dark sector can contain very rich physics and still obey all known cosmological and astrophysical constraints. Despite a minimal set of ingredients, this model displays a very complex phenomenology, of which we have only explored a small subset. It would indeed be interesting to investigate other aspects of the atomic DM scenario such as black-hole formation and possible couplings to the SM in light of the constraints presented here.

In chapter 6, we have considered the impact of oscillations in the bispectrum of primordial fluctuations on the clustering of DM halos. Interestingly,

we have identified a novel signature that had not been previously discussed in the literature. Indeed, we have determined that features in the inflaton potential such as oscillations or bumps become imprinted at late times on the mass dependence of the halo bias. This finding could potentially open up a new way of exploring and constraining the physics governing the very early Universe.

The research presented in this thesis contributes to the larger ongoing scientific effort aimed at improving our knowledge of the world we live in. As our theoretical understanding of the Universe expands and as more data becomes available, the physics governing the DS might be unveiled. In particular, we believe that the next decade will certainly be crucial for our understanding of DM physics.

For direct-detection experiments, the constantly increasing sensitivity of detectors coupled with the experience accumulated in the last decade of DM searches will either lead to a tell-tale detection of DM or will severely constrain the WIMP hypothesis. Indeed, direct-detection experiments are just beginning to probe the range of cross sections expected from a weakly-coupled DM particle. An outright detection would directly inform us about how DM couples to the SM of particle physics, which would constitute a giant leap forward in our understanding of the Universe. Such detection could also point us to possible particle-collider signatures that could be looked for in the data, and used to cross-check the direct-detection signal and possibly provide us with extra information about the properties of DM. Conversely, a null detection would force us to rethink the vanilla WIMP paradigm and focus our attention on more general DM scenarios. For this latter outcome, cosmological and astrophysical observations become the only way of inferring information about the physics governing DM.

The searches for a possible DM annihilation (or decay) signal in gamma-ray and cosmic-ray data provide us with another window to explore the physics of DM. Unfortunately, disentangling the DM signal from all the astrophysical foregrounds and backgrounds is a rather tricky business. Even if a tell-tale signature of DM annihilation such as a sharp gamma-ray line would be found in the data, one would have to carefully rule out all pos-

sible standard astrophysical explanations for the signal before claiming a discovery. However, if one could cross-correlate the potential DM signal with another independent observation such as a direct-detection or collider signal, this would considerably boost our confidence that we are closing in on the nature of DM.

Beyond the direct and indirect DM searches, studies of the internal structure of DM halos and of their substructure content could provide us with key information about interactions between DM particles. In particular, strong-lensing studies of galactic halos have the potential to enlighten us about the low-mass end of the halo mass function. The detection of a minimal subhalo mass (such as that predicted by atomic DM) would constitute a tell-tale signature of the interactions taking place in the DM sector. It remains unclear however if such observation could directly pinpoint the particle nature of DM. Again, it might be necessary to cross-correlate any potential signal with other cosmological observables such as the CMB or galaxy clustering data to bring the nature of DM into focus.

In conclusion, the unambiguous identification of the physics governing the DM sector will most likely require many complementary observations that all point to the same DM paradigm. Given the large ongoing scientific effort aimed at pinpointing the physics of DM and all the theoretical knowledge accumulated in the last three decades, mankind may well be on the verge of a discovery that could revolutionize our understanding of the Universe. It is just a matter of time before we can shed light on the dark sector of the Universe.

Bibliography

- [1] E. Komatsu *et al.*, “Seven-Year Wilkinson Microwave Anisotropy Probe (WMAP) Observations: Cosmological Interpretation,” *Astrophys.J.Suppl.*, vol. 192, p. 18, 2011.
- [2] A. Einstein, “Die Grundlage der allgemeinen Relativitätstheorie,” *Annalen der Physik*, vol. 354, pp. 769–822, 1916.
- [3] E. Hubble, “A Relation between Distance and Radial Velocity among Extra-Galactic Nebulae,” *Proceedings of the National Academy of Science*, vol. 15, pp. 168–173, Mar. 1929.
- [4] F. Zwicky, “Die Rotverschiebung von extragalaktischen Nebeln,” *Helvetica Physica Acta*, vol. 6, pp. 110–127, 1933.
- [5] F. Zwicky, “On the Masses of Nebulae and of Clusters of Nebulae,” *Astrophys. J.*, vol. 86, p. 217, Oct. 1937.
- [6] A. Friedman, “Über die Krümmung des Raumes,” *Zeitschrift für Physik*, vol. 10, pp. 377–386, Dec. 1922.
- [7] G. Lemaître, “Un Univers homogène de masse constante et de rayon croissant rendant compte de la vitesse radiale des nébuleuses extragalactiques,” *Annales de la Societe Scietifique de Bruxelles*, vol. 47, pp. 49–59, 1927.
- [8] G. Gamow, “The Evolution of the Universe,” *Nature*, vol. 162, pp. 680–682, Oct. 1948.
- [9] R. A. Alpher, H. Bethe, and G. Gamow, “The Origin of Chemical Elements,” *Physical Review*, vol. 73, pp. 803–804, Apr. 1948.
- [10] R. H. Dicke, R. Beringer, R. L. Kyhl, and A. B. Vane, “Atmospheric Absorption Measurements with a Microwave Radiometer,” *Physical Review*, vol. 70, pp. 340–348, Sept. 1946.

Bibliography

- [11] R. A. Alpher and R. C. Herman, "Remarks on the Evolution of the Expanding Universe," *Physical Review*, vol. 75, pp. 1089–1095, Apr. 1949.
- [12] A. G. Doroshkevich and I. D. Novikov, "Mean Density of Radiation in the Metagalaxy and Certain Problems in Relativistic Cosmology," *Soviet Physics Doklady*, vol. 9, p. 111, Aug. 1964.
- [13] A. A. Penzias and R. W. Wilson, "A Measurement of Excess Antenna Temperature at 4080 Mc/s.," *Astrophys. J.*, vol. 142, pp. 419–421, July 1965.
- [14] R. H. Dicke, P. J. E. Peebles, P. G. Roll, and D. T. Wilkinson, "Cosmic Black-Body Radiation.," *Astrophys. J.*, vol. 142, pp. 414–419, July 1965.
- [15] V. C. Rubin, W. K. J. Ford, and N. . Thonnard, "Rotational properties of 21 SC galaxies with a large range of luminosities and radii, from NGC 4605 (R = 4kpc) to UGC 2885 (R = 122 kpc)," *Astrophys. J.*, vol. 238, pp. 471–487, June 1980.
- [16] W. Rindler, "Visual horizons in world models," *Mon. Not. Roy. Astron. Soc.*, vol. 116, p. 662, 1956.
- [17] R. H. Dicke, ed., *Gravitation and the universe*, 1970.
- [18] A. H. Guth, "The Inflationary Universe: A Possible Solution to the Horizon and Flatness Problems," *Phys.Rev.*, vol. D23, pp. 347–356, 1981.
- [19] A. A. Starobinsky, "A New Type of Isotropic Cosmological Models Without Singularity," *Phys.Lett.*, vol. B91, pp. 99–102, 1980.
- [20] M. B. Einhorn and K. Sato, "Monopole production in the very early universe in a first-order phase transition," *Nuclear Physics B*, vol. 180, pp. 385–404, May 1981.
- [21] A. D. Linde, "A new inflationary universe scenario: A possible solution of the horizon, flatness, homogeneity, isotropy and primordial monopole problems," *Physics Letters B*, vol. 108, pp. 389–393, Feb. 1982.
- [22] A. Albrecht and P. J. Steinhardt, "Cosmology for grand unified theories with radiatively induced symmetry breaking," *Physical Review Letters*, vol. 48, pp. 1220–1223, Apr. 1982.

Bibliography

- [23] A. A. Starobinsky, “Dynamics of phase transition in the new inflationary universe scenario and generation of perturbations,” *Physics Letters B*, vol. 117, pp. 175–178, Nov. 1982.
- [24] J. M. Bardeen, P. J. Steinhardt, and M. S. Turner, “Spontaneous creation of almost scale-free density perturbations in an inflationary universe,” *Phys. Rev. D*, vol. 28, pp. 679–693, Aug. 1983.
- [25] G. F. Smoot, C. L. Bennett, *et al.*, “Structure in the COBE differential microwave radiometer first-year maps,” *Astrophys. J. Lett.*, vol. 396, pp. L1–L5, Sept. 1992.
- [26] A. G. Riess *et al.*, “Observational Evidence from Supernovae for an Accelerating Universe and a Cosmological Constant,” *Astron.J.*, vol. 116, pp. 1009–1038, Sept. 1998.
- [27] S. Perlmutter *et al.*, “Measurements of Omega and Lambda from 42 High-Redshift Supernovae,” *Astrophys. J.*, vol. 517, pp. 565–586, June 1999.
- [28] D. N. Spergel *et al.*, “First-Year Wilkinson Microwave Anisotropy Probe (WMAP) Observations: Determination of Cosmological Parameters,” *Astrophys.J.Suppl.*, vol. 148, pp. 175–194, Sept. 2003.
- [29] A. G. Sanchez *et al.*, “The clustering of galaxies in the SDSS-III Baryon Oscillation Spectroscopic Survey: cosmological implications of the large-scale two-point correlation function,” *ArXiv e-prints*, Mar. 2012.
- [30] P. McDonald *et al.*, “The Lyman-alpha forest power spectrum from the Sloan Digital Sky Survey,” *Astrophys.J.Suppl.*, vol. 163, pp. 80–109, 2006.
- [31] L. Van Waerbeke *et al.*, “Detection of correlated galaxy ellipticities from CFHT data: first evidence for gravitational lensing by large-scale structures,” *Astron.Astrophys.*, vol. 358, pp. 30–44, June 2000.
- [32] D. J. Bacon, A. R. Refregier, and R. S. Ellis, “Detection of weak gravitational lensing by large-scale structure,” *Mon. Not. Roy. Astron. Soc.*, vol. 318, pp. 625–640, Oct. 2000.
- [33] D. M. Wittman, J. A. Tyson, D. Kirkman, I. Dell’Antonio, and G. Bernstein, “Detection of weak gravitational lensing distortions

Bibliography

- of distant galaxies by cosmic dark matter at large scales,” *Nature*, vol. 405, pp. 143–148, May 2000.
- [34] N. Kaiser, G. Wilson, and G. A. Luppino, “Large-Scale Cosmic Shear Measurements,” *ArXiv Astrophysics e-prints*, Mar. 2000.
- [35] W. Freedman *et al.*, “Final results from the Hubble Space Telescope key project to measure the Hubble constant,” *Astrophys.J.*, vol. 553, pp. 47–72, 2001.
- [36] S. Dodelson, *Modern cosmology*. Academic Press, 2003.
- [37] J. M. Maldacena, “Non-Gaussian features of primordial fluctuations in single field inflationary models,” *JHEP*, vol. 0305, p. 013, 2003.
- [38] D. Salopek and J. Bond, “Nonlinear evolution of long wavelength metric fluctuations in inflationary models,” *Phys.Rev.*, vol. D42, pp. 3936–3962, 1990.
- [39] P. Creminelli, A. Nicolis, L. Senatore, M. Tegmark, and M. Zaldarriaga, “Limits on non-gaussianities from wmap data,” *JCAP*, vol. 0605, p. 004, 2006.
- [40] L. Senatore, K. M. Smith, and M. Zaldarriaga, “Non-Gaussianities in Single Field Inflation and their Optimal Limits from the WMAP 5-year Data,” *JCAP*, vol. 1001, p. 028, 2010.
- [41] P. D. Meerburg, J. P. van der Schaar, and P. S. Corasaniti, “Signatures of Initial State Modifications on Bispectrum Statistics,” *JCAP*, vol. 0905, p. 018, 2009.
- [42] S. Tremaine and J. Gunn, “Dynamical Role of Light Neutral Leptons in Cosmology,” *Phys.Rev.Lett.*, vol. 42, pp. 407–410, 1979.
- [43] P. Bode, J. P. Ostriker, and N. Turok, “Halo formation in warm dark matter models,” *Astrophys.J.*, vol. 556, pp. 93–107, 2001.
- [44] J. J. Dalcanton and C. J. Hogan, “Halo cores and phase space densities: Observational constraints on dark matter physics and structure formation,” *Astrophys.J.*, vol. 561, pp. 35–45, 2001.
- [45] A. R. Zentner and J. S. Bullock, “Halo substructure and the power spectrum,” *Astrophys.J.*, vol. 598, p. 49, 2003.

Bibliography

- [46] R. E. Smith and K. Markovic, “Testing the Warm Dark Matter paradigm with large-scale structures,” *Phys.Rev.*, vol. D84, p. 063507, 2011.
- [47] G. R. Blumenthal, S. Faber, J. R. Primack, and M. J. Rees, “Formation of Galaxies and Large Scale Structure with Cold Dark Matter,” *Nature*, vol. 311, pp. 517–525, 1984.
- [48] M. Davis, G. Efstathiou, C. S. Frenk, and S. D. White, “The Evolution of Large Scale Structure in a Universe Dominated by Cold Dark Matter,” *Astrophys.J.*, vol. 292, pp. 371–394, 1985.
- [49] R. Peccei and H. R. Quinn, “Constraints Imposed by CP Conservation in the Presence of Instantons,” *Phys.Rev.*, vol. D16, pp. 1791–1797, 1977.
- [50] D. E. Kaplan, M. A. Luty, and K. M. Zurek, “Asymmetric Dark Matter,” *Phys.Rev.*, vol. D79, p. 115016, 2009.
- [51] S. D. White, C. Frenk, and M. Davis, “Clustering in a Neutrino Dominated Universe,” *Astrophys.J.*, vol. 274, pp. L1–L5, 1983.
- [52] D. N. Spergel and P. J. Steinhardt, “Observational evidence for self-interacting cold dark matter,” *Phys.Rev.Lett.*, vol. 84, pp. 3760–3763, 2000.
- [53] J. L. Feng, “Dark Matter Candidates from Particle Physics and Methods of Detection,” *Ann.Rev.Astron.Astrophys.*, vol. 48, p. 495, 2010.
- [54] D. A. Buote, T. E. Jeltema, C. R. Canizares, and G. P. Garmire, “Chandra evidence for a flattened, triaxial dark matter halo in the elliptical galaxy ngc 720,” *Astrophys.J.*, vol. 577, pp. 183–196, 2002.
- [55] M. Markevitch *et al.*, “Direct Constraints on the Dark Matter Self-Interaction Cross Section from the Merging Galaxy Cluster 1E 0657-56,” *Astrophys. J.*, vol. 606, pp. 819–824, May 2004.
- [56] A. A. Klypin, A. V. Kravtsov, O. Valenzuela, and F. Prada, “Where are the missing Galactic satellites?,” *Astrophys.J.*, vol. 522, pp. 82–92, 1999.
- [57] B. Moore, S. Ghigna, F. Governato, G. Lake, T. R. Quinn, *et al.*, “Dark matter substructure within galactic halos,” *Astrophys.J.*, vol. 524, pp. L19–L22, 1999.

Bibliography

- [58] A. Kravtsov, “Dark Matter Substructure and Dwarf Galactic Satellites,” *Advances in Astronomy*, vol. 2010, 2010.
- [59] Z. Haiman, M. J. Rees, and A. Loeb, “Destruction of molecular hydrogen during cosmological reionization,” *Astrophys.J.*, vol. 476, p. 458, 1997.
- [60] A. A. Thoul and D. H. Weinberg, “Hydrodynamic simulations of galaxy formation. 2. Photoionization and the formation of low mass galaxies,” *Astrophys.J.*, vol. 465, p. 608, 1996.
- [61] M.-M. Mac Low and A. Ferrara, “Starburst - driven mass loss from dwarf galaxies: Efficiency and metal ejection,” *Astrophys.J.*, vol. 513, p. 142, 1999.
- [62] R. Barkana and A. Loeb, “The photoevaporation of dwarf galaxies during reionization,” *Astron.J.*, vol. 523, pp. 54–65, 1999.
- [63] R. S. Somerville, “Can photoionization squelching resolve the substructure crisis?,” *Astrophys.J.*, vol. 572, pp. L23–L26, 2002.
- [64] P. R. Shapiro, I. T. Iliev, and A. C. Raga, “Photoevaporation of cosmological minihalos during reionization,” *Mon.Not.Roy.Astron.Soc.*, vol. 348, p. 753, 2004.
- [65] K. Tassis, A. V. Kravtsov, and N. Y. Gnedin, “Scaling Relations of Dwarf Galaxies without Supernova-Driven Winds,” *Astrophys.J.*, vol. 672, pp. 888–903, 2008.
- [66] C. Pfrommer, P. Chang, and A. E. Broderick, “The Cosmological Impact of Luminous TeV Blazars III: Implications for Galaxy Clusters and the Formation of Dwarf Galaxies,” *Astrophys.J.*, vol. 752, p. 24, 2012.
- [67] W. de Blok, “The Core-Cusp Problem,” *Advances in Astronomy*, vol. 2010, p. 789293, 2010.
- [68] M. G. Walker and J. Penarrubia, “A Method for Measuring (Slopes of) the Mass Profiles of Dwarf Spheroidal Galaxies,” *Astrophys.J.*, vol. 742, p. 20, 2011.
- [69] R. K. de Naray and K. Spekkens, “Do Baryons Alter the Halos of Low Surface Brightness Galaxies?,” *Astrophys.J.*, vol. 741, p. L29, 2011.

Bibliography

- [70] A. Pontzen and F. Governato, “How supernova feedback turns dark matter cusps into cores,” *Mon.Not.Roy.Astron.Soc.*, vol. 421, pp. 3464–3471, Apr. 2012.
- [71] T. Sawala, C. Scannapieco, U. Maio, and S. White, “Formation of isolated dwarf galaxies with feedback,” *Mon. Not. Roy. Astron. Soc.*, vol. 402, pp. 1599–1613, Mar. 2010.
- [72] M. A. Breddels, A. Helmi, R. van den Bosch, G. van de Ven, and G. Battaglia, “Orbit-based dynamical models of the Sculptor dSph galaxy,” 2012.
- [73] M. Vogelsberger, J. Zavala, and A. Loeb, “Subhaloes in self-interacting galactic dark matter haloes,” *Mon.Not.Roy.Astron.Soc.*, p. 3127, May 2012.
- [74] M. Boylan-Kolchin, J. S. Bullock, and M. Kaplinghat, “Too big to fail? The puzzling darkness of massive Milky Way subhaloes,” *Mon.Not.Roy.Astron.Soc.*, vol. 415, p. L40, 2011.
- [75] M. Boylan-Kolchin, J. S. Bullock, and M. Kaplinghat, “The Milky Way’s bright satellites as an apparent failure of LCDM,” *Mon.Not.Roy.Astron.Soc.*, vol. 422, pp. 1203–1218, 2012.
- [76] A. Zolotov, A. M. Brooks, B. Willman, F. Governato, A. Pontzen, C. Christensen, A. Dekel, T. Quinn, S. Shen, and J. Wadsley, “Baryons Matter: Why Luminous Satellite Galaxies Have Reduced Central Masses,” *ArXiv e-prints*, June 2012.
- [77] C. A. Vera-Ciro, A. Helmi, E. Starkeburg, and M. A. Breddels, “Not too big, not too small: the dark halos of the dwarf spheroidals in the Milky Way,” 2012.
- [78] Q. Guo, S. White, C. Li, and M. Boylan-Kolchin, “How do galaxies populate Dark Matter halos?,” *Mon.Not.Roy.Astron.Soc.*, vol. 404, p. 1111, 2010.
- [79] M. R. Lovell, V. Eke, C. S. Frenk, L. Gao, A. Jenkins, *et al.*, “The Haloes of Bright Satellite Galaxies in a Warm Dark Matter Universe,” *Mon.Not.Roy.Astron.Soc.*, vol. 420, pp. 2318–2324, 2012.
- [80] G. D’Amico, M. Kamionkowski, and K. Sigurdson, “Dark Matter Astrophysics,” 2009.

Bibliography

- [81] A. Loeb and M. Zaldarriaga, “The Small-scale power spectrum of cold dark matter,” *Phys.Rev.*, vol. D71, p. 103520, 2005.
- [82] R. Bernabei *et al.*, “First results from DAMA/LIBRA and the combined results with DAMA/NaI,” *Eur.Phys.J.*, vol. C56, pp. 333–355, 2008.
- [83] Z. Ahmed *et al.*, “Dark Matter Search Results from the CDMS II Experiment,” *Science*, vol. 327, pp. 1619–1621, 2010.
- [84] E. Aprile *et al.*, “First Dark Matter Results from the XENON100 Experiment,” *Phys.Rev.Lett.*, vol. 105, p. 131302, 2010.
- [85] C. Aalseth *et al.*, “Results from a Search for Light-Mass Dark Matter with a P-type Point Contact Germanium Detector,” *Phys.Rev.Lett.*, vol. 106, p. 131301, 2011.
- [86] G. Angloher, M. Bauer, I. Bavykina, A. Bento, C. Bucci, *et al.*, “Results from 730 kg days of the CRESST-II Dark Matter Search,” *Eur.Phys.J.*, vol. C72, p. 1971, 2012.
- [87] O. Adriani *et al.*, “An anomalous positron abundance in cosmic rays with energies 1.5–100 GeV,” *Nature*, vol. 458, pp. 607–609, 2009.
- [88] A. A. Abdo *et al.*, “Measurement of the cosmic ray e^+e^- spectrum from 20 GeV to 1 TeV with the Fermi Large Area Telescope,” *Physical Review Letters*, vol. 102, no. 18, p. 181101, 2009.
- [89] P. Meade, M. Papucci, A. Strumia, and T. Volansky, “Dark Matter Interpretations of the e^+e^- Excesses after FERMI,” *Nucl.Phys.*, vol. B831, pp. 178–203, 2010.
- [90] D. Grasso *et al.*, “On possible interpretations of the high energy electron-positron spectrum measured by the Fermi Large Area Telescope,” *Astropart.Phys.*, vol. 32, pp. 140–151, 2009.
- [91] A. Abdo *et al.*, “Constraints on Cosmological Dark Matter Annihilation from the Fermi-LAT Isotropic Diffuse Gamma-Ray Measurement,” *JCAP*, vol. 1004, p. 014, 2010.
- [92] D. Hooper and L. Goodenough, “Dark Matter Annihilation in The Galactic Center As Seen by the Fermi Gamma Ray Space Telescope,” *Phys.Lett.*, vol. B697, pp. 412–428, 2011.

Bibliography

- [93] D. Hooper and T. Linden, “On The Origin Of The Gamma Rays From The Galactic Center,” *Phys.Rev.*, vol. D84, p. 123005, 2011.
- [94] T. Bringmann, X. Huang, A. Ibarra, S. Vogl, and C. Weniger, “Fermi LAT Search for Internal Bremsstrahlung Signatures from Dark Matter Annihilation,” 2012.
- [95] C. Weniger, “A Tentative Gamma-Ray Line from Dark Matter Annihilation at the Fermi Large Area Telescope,” 2012.
- [96] L. Bergstrom, “Dark Matter Evidence, Particle Physics Candidates and Detection Methods,” 2012.
- [97] J. Lavallo and P. Salati, “Dark Matter Indirect Signatures,” 2012.
- [98] J. Dunkley, R. Hlozek, J. Sievers, V. Acquaviva, P. Ade, *et al.*, “The Atacama Cosmology Telescope: Cosmological Parameters from the 2008 Power Spectra,” *Astrophys.J.*, vol. 739, p. 52, 2011.
- [99] R. Keisler, C. Reichardt, K. Aird, B. Benson, L. Bleem, *et al.*, “A Measurement of the Damping Tail of the Cosmic Microwave Background Power Spectrum with the South Pole Telescope,” *Astrophys.J.*, vol. 743, p. 28, 2011.
- [100] C.-P. Ma and E. Bertschinger, “Cosmological perturbation theory in the synchronous and conformal Newtonian gauges,” *Astrophys.J.*, vol. 455, pp. 7–25, 1995.
- [101] P. Peebles, “Recombination of the Primeval Plasma,” *Astrophys.J.*, vol. 153, p. 1, 1968.
- [102] S. Seager, D. D. Sasselov, and D. Scott, “How exactly did the universe become neutral?,” *Astrophys.J.Suppl.*, vol. 128, pp. 407–430, 2000.
- [103] S. Bashinsky and U. Seljak, “Signatures of relativistic neutrinos in CMB anisotropy and matter clustering,” *Phys. Rev. D*, vol. 69, p. 083002, Apr. 2004.
- [104] P. J. E. Peebles and J. T. Yu, “Primeval Adiabatic Perturbation in an Expanding Universe,” *Astrophys.J.*, vol. 162, p. 815, Dec. 1970.
- [105] U. Seljak, “A two-fluid approximation for calculating the cosmic microwave background anisotropies,” *Astrophys. J. Lett.*, vol. 435, pp. L87–L90, Nov. 1994.

Bibliography

- [106] W. Hu and N. Sugiyama, “Anisotropies in the cosmic microwave background: an analytic approach,” *Astrophys. J.*, vol. 444, pp. 489–506, May 1995.
- [107] R. K. Sachs and A. M. Wolfe, “Perturbations of a Cosmological Model and Angular Variations of the Microwave Background,” *Astrophys. J.*, vol. 147, p. 73, Jan. 1967.
- [108] U. Seljak and M. Zaldarriaga, “A Line of sight integration approach to cosmic microwave background anisotropies,” *Astrophys. J.*, vol. 469, pp. 437–444, 1996.
- [109] Planck Collaboration, P. A. R. Ade, N. Aghanim, M. Arnaud, M. Ashdown, J. Aumont, C. Baccigalupi, M. Baker, A. Balbi, A. J. Banday, and et al., “Planck early results. I. The Planck mission,” *Astron. Astrophys.*, vol. 536, p. A1, Dec. 2011.
- [110] N. Kaiser, “On the spatial correlations of Abell clusters,” *Astrophys. J. Lett.*, vol. 284, pp. L9–L12, Sept. 1984.
- [111] S. Matarrese and L. Verde, “The effect of primordial non-Gaussianity on halo bias,” *Astrophys. J.*, vol. 677, pp. L77–L80, 2008.
- [112] N. Dalal, O. Dore, D. Huterer, and A. Shirokov, “The imprints of primordial non-gaussianities on large-scale structure: scale dependent bias and abundance of virialized objects,” *Phys. Rev.*, vol. D77, p. 123514, 2008.
- [113] A. Slosar, C. Hirata, U. Seljak, S. Ho, and N. Padmanabhan, “Constraints on local primordial non-Gaussianity from large scale structure,” *JCAP*, vol. 0808, p. 031, 2008.
- [114] V. Desjacques and U. Seljak, “Primordial non-Gaussianity in the large scale structure of the Universe,” *Adv. Astron.*, vol. 2010, p. 908640, 2010.
- [115] J. Chang *et al.*, “An excess of cosmic ray electrons at energies of 300.800 GeV,” *Nature*, vol. 456, pp. 362–365, 2008.
- [116] S. Torii *et al.*, “High-energy electron observations by PPB-BETS flight in Antarctica,” 2008.
- [117] N. Arkani-Hamed, D. P. Finkbeiner, T. R. Slatyer, and N. Weiner, “A Theory of Dark Matter,” *Phys. Rev.*, vol. D79, p. 015014, 2009.

Bibliography

- [118] M. Ibe, H. Murayama, and T. T. Yanagida, “Breit-Wigner Enhancement of Dark Matter Annihilation,” *Phys. Rev.*, vol. D79, p. 095009, 2009.
- [119] W.-L. Guo and Y.-L. Wu, “Enhancement of Dark Matter Annihilation via Breit-Wigner Resonance,” *Phys. Rev.*, vol. D79, p. 055012, 2009.
- [120] M. Kamionkowski and S. Profumo, “Early Annihilation and Diffuse Backgrounds in Models of Weakly Interacting Massive Particles in Which the Cross Section for Pair Annihilation Is Enhanced by $1/v$,” *Phys. Rev. Lett.*, vol. 101, p. 261301, 2008.
- [121] P. Peebles and J. Yu, “Primeval adiabatic perturbation in an expanding universe,” *Astrophys.J.*, vol. 162, pp. 815–836, 1970.
- [122] A. Lewis, A. Challinor, and A. Lasenby, “Efficient computation of CMB anisotropies in closed FRW models,” *Astrophys.J.*, vol. 538, pp. 473–476, 2000.
- [123] D. Blas, J. Lesgourgues, and T. Tram, “The Cosmic Linear Anisotropy Solving System (CLASS) II: Approximation schemes,” *JCAP*, vol. 1107, p. 034, 2011.
- [124] H. Goldberg and L. J. Hall, “A New Candidate for Dark Matter,” *Phys.Lett.*, vol. B174, p. 151, 1986.
- [125] D. E. Kaplan, G. Z. Krnjaic, K. R. Rehermann, and C. M. Wells, “Atomic Dark Matter,” *JCAP*, vol. 1005, p. 021, 2010.
- [126] D. E. Kaplan, G. Z. Krnjaic, K. R. Rehermann, and C. M. Wells, “Dark Atoms: Asymmetry and Direct Detection,” *JCAP*, vol. 1110, p. 011, 2011.
- [127] X. Chen, R. Easther, and E. A. Lim, “Large Non-Gaussianities in Single Field Inflation,” *JCAP*, vol. 0706, p. 023, 2007.
- [128] X. Chen, R. Easther, and E. A. Lim, “Generation and Characterization of Large Non-Gaussianities in Single Field Inflation,” *JCAP*, vol. 0804, p. 010, 2008.
- [129] R. Bean, X. Chen, G. Hailu, S.-H. H. Tye, and J. Xu, “Duality Cascade in Brane Inflation,” *JCAP*, vol. 0803, p. 026, 2008.

Bibliography

- [130] L. McAllister, E. Silverstein, and A. Westphal, “Gravity Waves and Linear Inflation from Axion Monodromy,” *Phys.Rev.*, vol. D82, p. 046003, 2010.
- [131] R. Flauger, L. McAllister, E. Pajer, A. Westphal, and G. Xu, “Oscillations in the CMB from Axion Monodromy Inflation,” *JCAP*, vol. 1006, p. 009, 2010.
- [132] R. Flauger and E. Pajer, “Resonant Non-Gaussianity,” *JCAP*, vol. 1101, p. 017, 2011.
- [133] D. Feldman, Z. Liu, and P. Nath, “PAMELA Positron Excess as a Signal from the Hidden Sector,” *Phys. Rev.*, vol. D79, p. 063509, 2009.
- [134] M. Ibe, Y. Nakayama, H. Murayama, and T. T. Yanagida, “Nambu-Goldstone Dark Matter and Cosmic Ray Electron and Positron Excess,” *JHEP*, vol. 04, p. 087, 2009.
- [135] M. Kakizaki, S. Matsumoto, Y. Sato, and M. Senami, “Significant effects of second KK particles on LKP dark matter physics,” *Phys.Rev.*, vol. D71, p. 123522, 2005.
- [136] T. Oda, T. Totani, and M. Nagashima, “Gamma-ray background from neutralino annihilation in the first cosmological objects,” *Astrophys. J.*, vol. 633, pp. L65–L68, 2005.
- [137] S. Profumo, K. Sigurdson, and M. Kamionkowski, “What mass are the smallest protohalos?,” *Phys. Rev. Lett.*, vol. 97, p. 031301, 2006.
- [138] X.-L. Chen and M. Kamionkowski, “Particle decays during the cosmic dark ages,” *Phys. Rev.*, vol. D70, p. 043502, 2004.
- [139] M. Kamionkowski and S. M. Koushiappas, “Galactic Substructure and Direct Detection of Dark Matter,” *Phys. Rev.*, vol. D77, p. 103509, 2008.
- [140] A. Cooray and R. K. Sheth, “Halo models of large scale structure,” *Phys. Rept.*, vol. 372, pp. 1–129, 2002.
- [141] P. Sreekumar *et al.*, “EGRET observations of the extragalactic gamma ray emission,” *Astrophys. J.*, vol. 494, pp. 523–534, 1998.
- [142] L. Zhang, X. Chen, M. Kamionkowski, Z.-g. Si, and Z. Zheng, “Constraints on radiative dark-matter decay from the cosmic microwave background,” *Phys. Rev.*, vol. D76, p. 061301, 2007.

Bibliography

- [143] P. Gondolo *et al.*, “DarkSUSY: Computing supersymmetric dark matter properties numerically,” *JCAP*, vol. 0407, p. 008, 2004.
- [144] P. S. Coppi and R. D. Blandford, “Reaction rates and energy distributions for elementary processes in relativistic pair plasmas,” *Mon. Not. R. astr. Soc.*, vol. 245, pp. 453–469, Aug. 1990.
- [145] J. Mardon, Y. Nomura, D. Stolarski, and J. Thaler, “Dark Matter Signals from Cascade Annihilations,” *JCAP*, vol. 0905, p. 016, 2009.
- [146] S. Profumo and T. E. Jeltema, “Extragalactic Inverse Compton Light from Dark Matter Annihilation and the Pamela Positron Excess,” *JCAP*, vol. 0907, p. 020, 2009.
- [147] M. Wilson and J. Silk, “On the Anisotropy of the cosmological background matter and radiation distribution. 1. The Radiation anisotropy in a spatially flat universe,” *Astrophys.J.*, vol. 243, pp. 14–25, 1981.
- [148] J. Bond and G. Efstathiou, “Cosmic background radiation anisotropies in universes dominated by nonbaryonic dark matter,” *Astrophys.J.*, vol. 285, pp. L45–L48, 1984.
- [149] N. Vittorio and J. Silk, “Fine-scale anisotropy of the cosmic microwave background in a universe dominated by cold dark matter,” *Astrophys.J.*, vol. 285, pp. L39–L43, 1984.
- [150] J. Bond and G. Efstathiou, “The statistics of cosmic background radiation fluctuations,” *Mon.Not.Roy.Astron.Soc.*, vol. 226, pp. 655–687, 1987.
- [151] N. Sugiyama and N. Gouda, “Perturbations of the cosmic microwave background radiation and structure formations,” *Progress of Theoretical Physics*, vol. 88, no. 5, pp. 803–844, 1992.
- [152] D. Grin and C. M. Hirata, “Cosmological hydrogen recombination: The effect of extremely high- n states,” *Phys.Rev.*, vol. D81, p. 083005, 2010.
- [153] J. Rubino-Martin, J. Chluba, W. Fendt, and B. Wandelt, “Estimating the impact of recombination uncertainties on the cosmological parameter constraints from cosmic microwave background experiments,” 2009.

- [154] W. Y. Wong, A. Moss, and D. Scott, “How well do we understand cosmological recombination?,” *Mon.Not.Roy.Astron.Soc.*, 2007.
- [155] A. C. Hindmarsh, *ODEPACK, A Systematized Collection of ODE Solvers*. Scientific Publishing, North Holland, 1983.
- [156] M. Bucher, K. Moodley, and N. Turok, “The General primordial cosmic perturbation,” *Phys.Rev.*, vol. D62, p. 083508, 2000.
- [157] J. Hamann, A. Balbi, J. Lesgourgues, and C. Quercellini, “Optimising Boltzmann codes for the Planck era,” *JCAP*, vol. 0904, p. 011, 2009.
- [158] M. Doran, “Speeding up cosmological Boltzmann codes,” *JCAP*, vol. 0506, p. 011, 2005.
- [159] T. Kobayashi, R. Maartens, T. Shiromizu, and K. Takahashi, “Cosmological magnetic fields from nonlinear effects,” *Phys.Rev.*, vol. D75, p. 103501, 2007.
- [160] A. Challinor and A. Lasenby, “Cosmic microwave background anisotropies in the CDM model: A Covariant and gauge invariant approach,” *Astrophys.J.*, vol. 513, pp. 1–22, 1999.
- [161] A. Lewis and S. Bridle, “Cosmological parameters from CMB and other data: A Monte Carlo approach,” *Phys.Rev.*, vol. D66, p. 103511, 2002.
- [162] A. Gelman and D. B. Rubin, “Inference from Iterative Simulation Using Multiple Sequences,” *Statist.Sci.*, vol. 7, pp. 457–472, 1992.
- [163] P. F. Hopkins, E. Quataert, and N. Murray, “Stellar feedback in galaxies and the origin of galaxy-scale winds,” *Mon.Not.Roy.Astron.Soc.*, vol. 421, pp. 3522–3537, Apr. 2012.
- [164] M. Uhlig, C. Pfrommer, M. Sharma, B. Nath, T. Ensslin, *et al.*, “Galactic winds driven by cosmic-ray streaming,” 2012.
- [165] J. Miralda-Escude, “A test of the collisional dark matter hypothesis from cluster lensing,” 2000.
- [166] N. Yoshida, V. Springel, S. D. White, and G. Tormen, “Collisional dark matter and the structure of dark halos,” *Astrophys.J.*, vol. 535, p. L103, 2000.

Bibliography

- [167] O. Y. Gnedin and J. P. Ostriker, “Limits on collisional dark matter from elliptical galaxies in clusters,” *Astrophys.J.*, 2000.
- [168] A. V. Maccio, S. Paduroiu, D. Anderhalden, A. Schneider, and B. Moore, “Cores in warm dark matter haloes: a Catch 22 problem,” 2012.
- [169] A. Loeb and N. Weiner, “Cores in Dwarf Galaxies from Dark Matter with a Yukawa Potential,” *Phys.Rev.Lett.*, vol. 106, p. 171302, 2011.
- [170] L. G. d. Aarssen, T. Bringmann, and C. Pfrommer, “Dark matter with long-range interactions as a solution to all small-scale problems of Λ CDM cosmology?,” 2012.
- [171] J. M. Cline, Z. Liu, and W. Xue, “Millicharged Atomic Dark Matter,” *Phys.Rev.*, vol. D85, p. 101302, 2012.
- [172] E. Bertschinger, “The Effects of Cold Dark Matter Decoupling and Pair Annihilation on Cosmological Perturbations,” *Phys.Rev.*, vol. D74, p. 063509, 2006.
- [173] R. Foot, “Mirror matter-type dark matter,” *Int.J.Mod.Phys.*, vol. D13, pp. 2161–2192, 2004.
- [174] P. Ciarcelluti, “Cosmology with mirror dark matter,” *Int.J.Mod.Phys.*, vol. D19, pp. 2151–2230, 2010.
- [175] M. Y. Khlopov, A. G. Mayorov, and E. Y. Soldatov, “Composite Dark Matter and Puzzles of Dark Matter Searches,” *Int.J.Mod.Phys.*, vol. D19, pp. 1385–1395, 2010.
- [176] M. Y. Khlopov, A. G. Mayorov, and E. Y. Soldatov, “The dark atoms of dark matter,” *Prespace.J.*, vol. 1, pp. 1403–1417, 2010.
- [177] S. R. Behbahani, M. Jankowiak, T. Rube, and J. G. Wacker, “Nearly Supersymmetric Dark Atoms,” *Adv.High Energy Phys.*, vol. 2011, p. 709492, 2011.
- [178] H. Davoudiasl, D. E. Morrissey, K. Sigurdson, and S. Tulin, “Hylogenesis: A Unified Origin for Baryonic Visible Matter and Antibaryonic Dark Matter,” *Phys.Rev.Lett.*, vol. 105, p. 211304, 2010.
- [179] K. Petraki, M. Trodden, and R. R. Volkas, “Visible and dark matter from a first-order phase transition in a baryon-symmetric universe,” *JCAP*, vol. 1202, p. 044, 2012.

Bibliography

- [180] L. Ackerman, M. R. Buckley, S. M. Carroll, and M. Kamionkowski, “Dark Matter and Dark Radiation,” *Phys.Rev.*, vol. D79, p. 023519, 2009.
- [181] J. L. Feng, M. Kaplinghat, H. Tu, and H.-B. Yu, “Hidden Charged Dark Matter,” *JCAP*, vol. 0907, p. 004, 2009.
- [182] R. H. Cyburt, B. D. Fields, K. A. Olive, and E. Skillman, “New BBN limits on physics beyond the standard model from He-4,” *Astropart.Phys.*, vol. 23, pp. 313–323, 2005.
- [183] G. Mangano and P. D. Serpico, “A robust upper limit on N_{eff} from BBN, circa 2011,” *Phys. Lett.*, vol. B701, pp. 296–299, 2011.
- [184] K. M. Nollett and G. P. Holder, “An analysis of constraints on relativistic species from primordial nucleosynthesis and the cosmic microwave background,” 2011.
- [185] E. Aver, K. A. Olive, and E. D. Skillman, “A New Approach to Systematic Uncertainties and Self-Consistency in Helium Abundance Determinations,” *JCAP*, vol. 1005, p. 003, 2010.
- [186] Y. Izotov and T. Thuan, “The primordial abundance of 4He: evidence for non-standard big bang nucleosynthesis,” *Astrophys.J.*, vol. 710, pp. L67–L71, 2010.
- [187] V. Simha and G. Steigman, “Constraining The Early-Universe Baryon Density And Expansion Rate,” *JCAP*, vol. 0806, p. 016, 2008.
- [188] Y. Ali-Haïmoud and C. M. Hirata, “Ultrafast effective multi-level atom method for primordial hydrogen recombination,” *Phys.Rev.*, vol. D82, p. 063521, 2010.
- [189] L. Spitzer, Jr. and J. L. Greenstein, “Continuous Emission from Planetary Nebulae,” *Astrophys.J.*, vol. 114, p. 407, Nov. 1951.
- [190] S. Goldman and G. Drake, “Relativistic two-photon decay rates of 2s12 hydrogenic ions,” *Phys.Rev.*, vol. A24, pp. 183–191, 1981.
- [191] S. Goldman, “Generalized Laguerre representation: Application to relativistic two-photon decay rates,” *Phys.Rev.*, vol. A40, pp. 1185–1193, 1989.
- [192] L. Spitzer, *Physical Processes in the Interstellar Medium*. Wiley, May 1978.

Bibliography

- [193] A. Burgess, “Tables of hydrogenic photoionization cross-sections and recombination coefficient,” *Mem. R. Ast. Soc.*, vol. 69, p. 1, 1965.
- [194] S. Seager, D. D. Sasselov, and D. Scott, “A new calculation of the recombination epoch,” *Astrophys.J.*, vol. 523, pp. L1–L5, 1999.
- [195] D. Pequignot, P. Petitjean, and C. Boisson, “Total and effective radiative recombination coefficients,” *A. and A.*, vol. 251, pp. 680–688, Nov. 1991.
- [196] J. Stepanek, “Electron and positron atomic elastic scattering cross sections,” *Radiation Physics and Chemistry*, vol. 66, no. 2, pp. 99 – 116, 2003.
- [197] F.-Y. Cyr-Racine and K. Sigurdson, “Photons and baryons before atoms: Improving the tight-coupling approximation,” *Phys. Rev. D*, vol. 83, p. 103521, May 2011.
- [198] C. Pitrou, “The tight-coupling approximation for baryon acoustic oscillations,” *Phys.Lett.*, vol. B698, pp. 1–5, 2011.
- [199] Z. Hou, R. Keisler, L. Knox, M. Millea, and C. Reichardt, “How Additional Massless Neutrinos Affect the Cosmic Microwave Background Damping Tail,” *ArXiv e-prints*, Apr. 2011.
- [200] N. Dalal and C. S. Kochanek, “Direct Detection of Cold Dark Matter Substructure,” *Astrophys. J.*, vol. 572, pp. 25–33, June 2002.
- [201] L. A. Moustakas, A. J. Bolton, J. T. Booth, J. S. Bullock, E. Cheng, *et al.*, “The Observatory for Multi-Epoch Gravitational Lens Astrophysics (OMEGA),” 2008.
- [202] C. R. Keeton and L. A. Moustakas, “A New Channel for Detecting Dark Matter Substructure in Galaxies: Gravitational Lens Time Delays,” *Astrophys.J.*, vol. 699, pp. 1720–1731, 2009.
- [203] L. A. Moustakas, K. Abazajian, A. Benson, A. S. Bolton, J. S. Bullock, *et al.*, “Strong gravitational lensing probes of the particle nature of dark matter,” 2009.
- [204] L. Koopmans, M. Auger, M. Barnabe, A. Bolton, M. Bradac, *et al.*, “Strong Gravitational Lensing as a Probe of Gravity, Dark-Matter and Super-Massive Black Holes,” 2009.

- [205] P. Marshall, M. Auger, J. Bartlett, M. Bradac, A. Cooray, *et al.*, “Dark Matter Structures in the Universe: Prospects for Optical Astronomy in the Next Decade,” 2009.
- [206] S. Vegetti and L. V. E. Koopmans, “Statistics of mass substructure from strong gravitational lensing: quantifying the mass fraction and mass function,” *Mon. Not. R. Astron. Soc.*, vol. 400, pp. 1583–1592, Dec. 2009.
- [207] S. Vegetti and L. V. E. Koopmans, “Bayesian strong gravitational-lens modelling on adaptive grids: objective detection of mass substructure in Galaxies,” *Mon. Not. R. Astron. Soc.*, vol. 392, pp. 945–963, Jan. 2009.
- [208] S. Vegetti, D. J. Lagattuta, J. P. McKean, M. W. Auger, C. D. Fassnacht, and L. V. E. Koopmans, “Gravitational detection of a low-mass dark satellite galaxy at cosmological distance,” *Nature*, vol. 481, pp. 341–343, Jan. 2012.
- [209] R. Fadely and C. R. Keeton, “Substructure in the lens HE 0435-1223,” *Mon. Not. R. Astron. Soc.*, vol. 419, pp. 936–951, Jan. 2012.
- [210] S. Vegetti, L. V. E. Koopmans, A. Bolton, T. Treu, and R. Gavazzi, “Detection of a dark substructure through gravitational imaging,” *Mon. Not. R. Astron. Soc.*, vol. 408, pp. 1969–1981, Nov. 2010.
- [211] M. Tegmark and M. Zaldarriaga, “Separating the early universe from the late universe: Cosmological parameter estimation beyond the black box,” *Phys.Rev.*, vol. D66, p. 103508, 2002.
- [212] U. Seljak *et al.*, “Cosmological parameter analysis including SDSS Ly-alpha forest and galaxy bias: Constraints on the primordial spectrum of fluctuations, neutrino mass, and dark energy,” *Phys.Rev.*, vol. D71, p. 103515, 2005.
- [213] S. Bird, H. V. Peiris, M. Viel, and L. Verde, “Minimally Parametric Power Spectrum Reconstruction from the Lyman-alpha Forest,” *Mon.Not.Roy.Astron.Soc.*, vol. 413, pp. 1717–1728, 2011.
- [214] U. Seljak, A. Makarov, P. McDonald, and H. Trac, “Can sterile neutrinos be the dark matter?,” *Phys.Rev.Lett.*, vol. 97, p. 191303, 2006.

- [215] R. A. Croft, D. H. Weinberg, M. Bolte, S. Burles, L. Hernquist, *et al.*, “Towards a precise measurement of matter clustering: Lyman alpha forest data at redshifts 2-4,” *Astrophys.J.*, vol. 581, pp. 20–52, 2002.
- [216] N. Y. Gnedin and A. J. Hamilton, “Matter power spectrum from the Lyman-alpha forest: Myth or reality?,” *Mon.Not.Roy.Astron.Soc.*, vol. 334, pp. 107–116, 2002.
- [217] N. Inada *et al.*, “A Gravitationally lensed quasar with quadruple images separated by 14.62 arcseconds,” *Nature*, vol. 426, pp. 810–812, 2003.
- [218] H. Hoekstra, H. K. Yee, and M. D. Gladders, “Properties of galaxy dark matter halos from weak lensing,” *Astrophys.J.*, vol. 606, pp. 67–77, 2004.
- [219] R. Mandelbaum, C. M. Hirata, T. Broderick, U. Seljak, and J. Brinkmann, “Ellipticity of dark matter halos with galaxy-galaxy weak lensing,” *Mon.Not.Roy.Astron.Soc.*, vol. 370, pp. 1008–1024, 2006.
- [220] L. V. Koopmans, T. Treu, A. S. Bolton, S. Burles, and L. A. Moustakas, “The sloan lens acs survey. 3. the structure and formation of early-type galaxies and their evolution since $z = 1$,” *Astrophys.J.*, vol. 649, pp. 599–615, 2006.
- [221] T. Morokuma, N. Inada, M. Oguri, S.-I. Ichikawa, Y. Kawano, *et al.*, “Discovery of a Gravitationally Lensed Quasar from the Sloan Digital Sky Survey: SDSS J133222.62+034739.9,” *Astron.J.*, vol. 133, pp. 214–219, 2007.
- [222] T. Fang, P. J. Humphrey, and D. A. Buote, “Rotation and Turbulence of the Hot ICM in Galaxy Clusters,” *Astrophys.J.*, vol. 691, pp. 1648–1659, 2009.
- [223] A. K. D. Evans and S. Bridle, “A Detection of Dark Matter Halo Ellipticity using Galaxy Cluster Lensing in SDSS,” *Astrophys.J.*, vol. 695, pp. 1446–1456, 2009.
- [224] O. Host, S. H. Hansen, R. Piffaretti, A. Morandi, S. Ettori, *et al.*, “Measurement of the dark matter velocity anisotropy in galaxy clusters,” *Astrophys.J.*, vol. 690, pp. 358–366, 2009.

- [225] P. S. Krstic and D. R. Schultz, “Elastic scattering and charge transfer in slow collisions: isotopes of H and H⁺ colliding with isotopes of H and with He,” *Journal of Physics B: Atomic, Molecular and Optical Physics*, vol. 32, no. 14, p. 3485, 1999.
- [226] A. H. G. Peter, M. Rocha, J. S. Bullock, and M. Kaplinghat, “In prep.,” 2012.
- [227] P. J. Humphrey, D. A. Buote, F. Gastaldello, L. Zappacosta, J. S. Bullock, *et al.*, “A chandra view of dark matter in early-type galaxies,” *Astrophys.J.*, vol. 646, pp. 899–918, 2006.
- [228] M. R. Flannery, “Impact-parameter treatment of hydrogen-hydrogen excitation collisions. ii. four-state approximation,” *Phys. Rev.*, vol. 183, pp. 241–244, Jul 1969.
- [229] Z. Ahmed *et al.*, “Search for Weakly Interacting Massive Particles with the First Five-Tower Data from the Cryogenic Dark Matter Search at the Soudan Underground Laboratory,” *Phys.Rev.Lett.*, vol. 102, p. 011301, 2009.
- [230] Z. Ahmed *et al.*, “Results from a Low-Energy Analysis of the CDMS II Germanium Data,” *Phys.Rev.Lett.*, vol. 106, p. 131302, 2011.
- [231] J. Angle *et al.*, “First Results from the XENON10 Dark Matter Experiment at the Gran Sasso National Laboratory,” *Phys.Rev.Lett.*, vol. 100, p. 021303, 2008.
- [232] J. Angle *et al.*, “Constraints on inelastic dark matter from XENON10,” *Phys.Rev.*, vol. D80, p. 115005, 2009.
- [233] J. Angle *et al.*, “A search for light dark matter in XENON10 data,” *Phys.Rev.Lett.*, vol. 107, p. 051301, 2011.
- [234] F. Bernardeau, S. Colombi, E. Gaztanaga, and R. Scoccimarro, “Large scale structure of the universe and cosmological perturbation theory,” *Phys.Rept.*, vol. 367, pp. 1–248, 2002.
- [235] N. Bartolo, E. Komatsu, S. Matarrese, and A. Riotto, “Non-Gaussianity from inflation: Theory and observations,” *Phys.Rept.*, vol. 402, pp. 103–266, 2004.
- [236] N. Afshordi and A. J. Tolley, “Primordial non-gaussianity, statistics of collapsed objects, and the Integrated Sachs-Wolfe effect,” *Phys.Rev.*, vol. D78, p. 123507, 2008.

- [237] S. G. Rubin, A. S. Sakharov, and M. Y. Khlopov, “The Formation of primary galactic nuclei during phase transitions in the early universe,” *J.Exp.Theor.Phys.*, vol. 91, pp. 921–929, 2001.
- [238] L. Verde and S. Matarrese, “Detectability of the effect of Inflationary non-Gaussianity on halo bias,” *Astrophys.J.*, vol. 706, pp. L91–L95, 2009.
- [239] F. Schmidt and M. Kamionkowski, “Halo Clustering with Non-Local Non-Gaussianity,” *Phys.Rev.*, vol. D82, p. 103002, 2010.
- [240] L.-M. Wang and M. Kamionkowski, “The Cosmic microwave background bispectrum and inflation,” *Phys.Rev.*, vol. D61, p. 063504, 2000.
- [241] X. Chen, “Primordial Non-Gaussianities from Inflation Models,” *Adv.Astron.*, vol. 2010, p. 638979, 2010.
- [242] X. Chen, “Primordial Features as Evidence for Inflation,” *JCAP*, vol. 1201, p. 038, 2012.
- [243] P. D. Meerburg, J. P. van der Schaar, and M. G. Jackson, “Bispectrum signatures of a modified vacuum in single field inflation with a small speed of sound,” *JCAP*, vol. 1002, p. 001, 2010.
- [244] J. Fergusson, M. Liguori, and E. Shellard, “General CMB and Primordial Bispectrum Estimation I: Mode Expansion, Map-Making and Measures of f_{NL} ,” *Phys.Rev.*, vol. D82, p. 023502, 2010.
- [245] P. D. Meerburg, “Oscillations in the Primordial Bispectrum I: Mode Expansion,” *Phys.Rev.*, vol. D82, p. 063517, 2010.
- [246] V. Desjacques, D. Jeong, and F. Schmidt, “Non-Gaussian Halo Bias Re-examined: Mass-dependent Amplitude from the Peak-Background Split and Thresholding,” *Phys.Rev.*, vol. D84, p. 063512, 2011.
- [247] V. Desjacques, D. Jeong, and F. Schmidt, “Accurate Predictions for the Scale-Dependent Galaxy Bias from Primordial Non-Gaussianity,” *Phys.Rev.*, vol. D84, p. 061301, 2011.
- [248] R. K. Sheth and G. Tormen, “Large scale bias and the peak background split,” *Mon.Not.Roy.Astron.Soc.*, vol. 308, p. 119, 1999.
- [249] N. Dalal, Y. Lithwick, and M. Kuhlen, “The Origin of Dark Matter Halo Profiles,” 2010.

Bibliography

- [250] G. Bertone, M. Cirelli, A. Strumia, and M. Taoso, “Gamma-ray and radio tests of the e^+e^- excess from DM annihilations,” *JCAP*, vol. 0903, p. 009, 2009.
- [251] L. Bergstrom, G. Bertone, T. Bringmann, J. Edsjo, and M. Taoso, “Gamma-ray and Radio Constraints of High Positron Rate Dark Matter Models Annihilating into New Light Particles,” *Phys.Rev.*, vol. D79, p. 081303, 2009.
- [252] E. Borriello, A. Cuoco, and G. Miele, “Secondary radiation from the Pamela/ATIC excess and relevance for Fermi,” *Astrophys.J.*, vol. 699, pp. L59–L63, 2009.
- [253] A. Lewis, “CAMB Notes,” *Unpublished*, 2011.
- [254] E. W. Kolb and M. S. Turner, *The early universe*. Addison-Wesley, 1990.
- [255] L. D. Landau and E. M. Lifshitz, *The classical theory of fields*. Oxford: Pergamon Press, 1975.
- [256] G. B. Rybicki and A. P. Lightman, *Radiative processes in astrophysics*. New York, Wiley-Interscience, 1979.
- [257] H.-W. Lee, “Exact low-energy expansion of the Rayleigh scattering cross-section by atomic hydrogen,” *Mon.Not.Roy.Astron.Soc.*, vol. 358, pp. 1472–1476, Apr. 2005.
- [258] M. J. Jamieson, A. Dalgarno, and J. N. Yukich, “Elastic scattering of hydrogen atoms at low temperatures,” *Phys. Rev. A*, vol. 46, pp. 6956–6961, Dec 1992.
- [259] A. Dalgarno, M. R. C. McDowell, and A. Williams, “The mobilities of ions in unlike gases,” *Phil. Trans. R. Soc. Lond. A*, vol. 250, no. 982, pp. 411–425, 1958.
- [260] J. E. Jones, “On the Determination of Molecular Fields. II. From the Equation of State of a Gas,” *Royal Society of London Proceedings Series A*, vol. 106, pp. 463–477, Oct. 1924.
- [261] P. S. Krstic and D. R. Schultz, “Elastic and related transport cross sections for collisions among isotopomers of $H^+ + H$, $H^+ + H_2$, $H^+ + He$, $H + H$, and $H + H_2$,” *Atomic and Plasma-Material Data for Fusion*, vol. 8, no. 1, 1998.

- [262] I. A. Ivanov, J. Mitroy, and K. Varga, “Positronium-positronium scattering using the stochastic variational method,” *Phys. Rev. A*, vol. 65, p. 022704, Jan 2002.
- [263] S. J. Ward, J. W. Humberston, and M. R. C. McDowell, “Elastic scattering of electrons (or positrons) from positronium and the photodetachment of the positronium negative ion,” *J. Phys. B*, vol. 20, no. 1, p. 127, 1987.
- [264] K. Smith, R. P. McEachran, and P. A. Fraser, “Effect of virtual excitation of the $2s$ state on the elastic scattering of electrons by atomic hydrogen,” *Phys. Rev.*, vol. 125, pp. 553–558, Jan 1962.
- [265] P. Banks, “Collision frequencies and energy transfer electrons,” *Planetary and Space Science*, vol. 14, no. 11, pp. 1085 – 1103, 1966.

Appendix A

Second-Order Tight-Coupling Appendices

A.1 Perturbation Equations

In this Appendix, we list the perturbation equations used to solve for the initial conditions found in Appendix A.2. We closely follow the notation of Ref. [100]. Here, η and h stand for the synchronous gauge curvature perturbation variables, a is the scale factor, K is the inverse of the squared curvature radius, $\beta_l = 1 - l(l+2)K/k^2$, ρ_i is the energy density of the i^{th} species, $w_i \equiv p_i/\rho_i$, where p_i is the pressure, and a dot denotes differentiation with respect to conformal time. The subscripts “c”, “ ν ”, “ γ ”, and “b” stand for the CDM, the neutrinos, the photons, and the baryons, respectively. δ_i stands for a perturbation in the energy density of species i , θ_i is the divergence of the velocity and F_{il} the l^{th} multipole moment of species i .

$$k^2\beta_1\eta - \frac{1}{2}\frac{\dot{a}}{a}\dot{h} + 4\pi Ga^2 \sum_i \rho_i \delta_i = 0 \quad (\text{A.1})$$

$$k^2\beta_1\dot{\eta} - \frac{K\dot{h}}{2} - 4\pi Ga^2 \sum_i (1+w_i)\rho_i\theta_i = 0 \quad (\text{A.2})$$

$$\dot{\delta}_c + \frac{1}{2}\dot{h} = 0 \quad (\text{A.3})$$

$$\dot{\delta}_\nu + \frac{4}{3}\theta_\nu + \frac{2}{3}\dot{h} = 0 \quad (\text{A.4})$$

$$\dot{\theta}_\nu - \frac{k^2}{4}(\delta_\nu - 2\beta_1 F_{\nu 2}) = 0 \quad (\text{A.5})$$

$$\dot{F}_{\nu 2} - \frac{8}{15}\theta_\nu + \frac{3}{5}\beta_2 k F_{\nu 3} - \frac{4}{5}\left(\frac{\dot{h}}{3} + 2\dot{\eta}\right) = 0 \quad (\text{A.6})$$

A.2. Initial Conditions

$$\dot{\delta}_\gamma + \frac{4}{3}\theta_\gamma + \frac{2}{3}\dot{h} = 0 \quad (\text{A.7})$$

$$\dot{\theta}_\gamma - \frac{k^2}{4}(\delta_\gamma - 2\beta_1 F_{\gamma 2}) - \frac{1}{\tau_c} S_b = 0 \quad (\text{A.8})$$

$$\begin{aligned} \dot{F}_{\gamma 2} - \frac{8}{15}\theta_\gamma + \frac{3}{5}\beta_2 k F_{\gamma 3} - \frac{4}{5}\left(\frac{\dot{h}}{3} + 2\dot{\eta}\right) \\ - \frac{1}{\tau_c}\left(F_{\gamma 2} - \frac{2}{15}\left(\frac{3}{4}F_{\gamma 2} + \frac{9}{2}G_{\gamma 2}\right)\right) = 0 \end{aligned} \quad (\text{A.9})$$

$$\dot{\delta}_b + \theta_b + \frac{1}{2}\dot{h} = 0 \quad (\text{A.10})$$

$$S_b - \frac{\tau_c}{1+R}\left[-\frac{\dot{a}}{a}(S_b + \theta_\gamma) - \dot{S}_b + k^2\left(c_s^2\delta_b - \frac{1}{4}\delta_\gamma + \beta_1\frac{F_{\gamma 2}}{2}\right)\right] = 0 \quad (\text{A.11})$$

Here, $R = (4/3)\rho_\gamma/\rho_b$. Our approach to solve these equations follow closely that of Ref. [253]. We first use Eq. (A.1) to eliminate \dot{h} in favor of the curvature perturbation η . For simplicity, we set $c_s^2 = 0$. We then approximate the octupole moment of the neutrinos and photons as:

$$F_{\nu 3} \simeq \frac{k\tau}{7}\left(1 - \frac{4}{315}k^2\tau^2\right)F_{\nu 2}, \quad (\text{A.12})$$

$$F_{\gamma 3} \simeq \frac{3}{7}k\tau_c F_{\gamma 2}. \quad (\text{A.13})$$

Finally, we eliminate the photon polarization moments from (A.9) using

$$G_{\gamma 2} \simeq \frac{1}{4}\left(F_{\gamma 2} - \frac{5\tau_c}{2}\dot{F}_{\gamma 2}\right). \quad (\text{A.14})$$

A.2 Initial Conditions

In this Appendix, we list the initial conditions obtained by the method outlined in Sec. 3.2.1. Here, $R_\nu = \rho_\nu/(\rho_\nu + \rho_\gamma)$, $R_b = \rho_b/\rho_m$, $\omega = H_0\Omega_m/\sqrt{\Omega_r}$, $\epsilon = \tau_c/\tau$, $S_b(\tau) \equiv \theta_b(\tau) - \theta_\gamma(\tau)$ is the velocity difference between baryons and photons. Note that our convention for the normalization of perturbations differs from Ref. [253] by $\beta_1 \rightarrow -\beta_1/2$. Note also that what we label β_1 here is denoted by β_2 in Ref. [253].

1. Photons

$$\begin{aligned} \delta_\gamma(\tau) = & -\frac{2\beta_1}{3}k^2\tau^2 + \frac{2\beta_1}{15}\omega k^2\tau^3 \\ & + \frac{\beta_1(4\beta_1 R_\nu + 15\beta_1 - 5)}{27(4R_\nu + 15)}k^4\tau^4 - \frac{\beta_1}{24}\omega^2 k^2\tau^4 \quad (\text{A.15}) \end{aligned}$$

$$\begin{aligned} \theta_\gamma(\tau) = & -\frac{\beta_1}{18}k^4\tau^3 - \frac{8\beta_1}{36R_\nu + 135}k^4\tau^3\epsilon + \frac{\beta_1(1 + 5R_b - R_\nu)}{120(1 - R_\nu)}\omega k^4\tau^4 \\ & - \frac{2\beta_1(2(5R_b - 9)R_\nu + 75R_b + 8R_\nu^2 + 10)}{15(R_\nu - 1)(2R_\nu + 15)(4R_\nu + 15)}\omega k^4\tau^4\epsilon \\ & + \frac{16\beta_1(6R_\nu + 181)}{45(2R_\nu + 15)(4R_\nu + 15)}k^4\tau^3\epsilon^2 \quad (\text{A.16}) \end{aligned}$$

$$\begin{aligned} F_{\gamma 2}(\tau) = & \frac{64}{9(4R_\nu + 15)}k^2\tau^2\epsilon + \frac{4(8R_\nu - 5)}{3(2R_\nu + 15)(4R_\nu + 15)}\omega k^2\tau^3\epsilon \\ & - \frac{32(6R_\nu + 181)}{9(2R_\nu + 15)(4R_\nu + 15)}k^2\tau^2\epsilon^2 \\ & - \frac{16(2R_\nu(12R_\nu + 767) - 1855)}{9(2R_\nu + 15)(2R_\nu + 25)(4R_\nu + 15)}\omega k^2\tau^3\epsilon^2 \quad (\text{A.17}) \end{aligned}$$

2. Baryons

$$\delta_b(\tau) = \frac{3}{4}\delta_\gamma(\tau) \quad (\text{A.18})$$

$$\begin{aligned} S_b(\tau) = & \frac{\beta_1 R_b}{6(1 - R_\nu)}\omega k^4\tau^4\epsilon + \frac{10\beta_1 R_b}{3(1 - R_\nu)(4R_\nu + 15)}\omega k^4\tau^4\epsilon^2 \\ & - \frac{\beta_1 R_b(15R_b + 2R_\nu - 2)}{96(R_\nu - 1)^2}\omega^2 k^4\tau^5\epsilon \quad (\text{A.19}) \end{aligned}$$

3. Cold Dark Matter

$$\begin{aligned} \delta_c(\tau) = & -\frac{\beta_1}{2}k^2\tau^2 + \frac{\beta_1}{10}\omega k^2\tau^3 \quad (\text{A.20}) \\ & + \frac{1}{72}\beta_1\left(-\frac{10}{4R_\nu + 15} + 2\beta_1 - 1\right)k^4\tau^4 - \frac{\beta_1}{32}\omega^2 k^2\tau^4 \end{aligned}$$

4. Neutrinos

$$\begin{aligned} \delta_\nu(\tau) = & -\frac{2\beta_1}{3}k^2\tau^2 + \frac{2\beta_1}{15}\omega k^2\tau^3 \\ & + \frac{1}{27}\beta_1 \left(\beta_1 - \frac{1}{4R_\nu + 15} \right) k^4\tau^4 - \frac{\beta_1}{24}\omega^2 k^2\tau^4 \quad (\text{A.21}) \end{aligned}$$

$$\begin{aligned} \theta_\nu(\tau) = & -\frac{\beta_1(4R_\nu + 23)}{18(4R_\nu + 15)}k^4\tau^3 + \frac{16\beta_1(1 - R_\nu)}{9(2R_\nu + 15)(4R_\nu + 15)}k^4\tau^3\epsilon \\ & + \frac{\beta_1(8R_\nu^2 + 50R_\nu + 275)}{120(2R_\nu + 15)(4R_\nu + 15)}\omega k^4\tau^4 \\ & - \frac{16\beta_1(R_\nu - 1)(2R_\nu - 15)}{15(2R_\nu + 15)(2R_\nu + 25)(4R_\nu + 15)}\omega k^4\tau^4\epsilon \\ & + \frac{32\beta_1(R_\nu - 1)(6R_\nu + 181)}{45(2R_\nu + 15)(2R_\nu + 25)(4R_\nu + 15)}k^4\tau^3\epsilon^2 \quad (\text{A.22}) \end{aligned}$$

$$\begin{aligned} \frac{F_{\nu 2}(\tau)}{2} = & \frac{4}{12R_\nu + 45}k^2\tau^2 + \frac{(4R_\nu - 5)}{3(2R_\nu + 15)(4R_\nu + 15)}\omega k^2\tau^3 \\ & + \frac{64(R_\nu - 1)}{9(2R_\nu + 15)(4R_\nu + 15)}k^2\tau^2\epsilon \\ & - \frac{28(7\beta_1 - 3)R_\nu + 5(175\beta_1 + 27\beta_2 - 84)}{189(25 + 2R_\nu)(15 + 4R_\nu)}k^4\tau^4 \\ & + \frac{(4R_\nu(2R_\nu - 65) + 225)}{24(2R_\nu + 15)(2R_\nu + 25)(4R_\nu + 15)}\omega^2 k^2\tau^4 \\ & + \frac{16(R_\nu - 1)(2R_\nu - 15)}{3(2R_\nu + 15)(2R_\nu + 25)(4R_\nu + 15)}\omega k^2\tau^3\epsilon \\ & - \frac{32(R_\nu - 1)(6R_\nu + 181)}{9(2R_\nu + 15)(2R_\nu + 25)(4R_\nu + 15)}k^2\tau^2\epsilon^2 \quad (\text{A.23}) \end{aligned}$$

$$F_{\nu 3}(\tau) = \frac{4}{7(12R_\nu + 45)}k^3\tau^3 \quad (\text{A.24})$$

5. Curvature (synchronous gauge)

$$\begin{aligned} \eta(\tau) = & 2 + \left(\frac{5}{12R_\nu + 45} - \frac{\beta_1}{6} \right) k^2 \tau^2 & (\text{A.25}) \\ & + \frac{80(R_\nu - 1)}{9(2R_\nu + 15)(4R_\nu + 15)} k^2 \tau^2 \epsilon \\ & + \frac{(16\beta_1 R_\nu^2 + 20(9\beta_1 + 5)R_\nu + 25(18\beta_1 - 5))}{60(2R_\nu + 15)(4R_\nu + 15)} \omega k^2 \tau^3 \end{aligned}$$

A.3 Tight-Coupling Approximation to Second Order in τ_c

In this Appendix, we give the key result of our improved tight-coupling approximation scheme: the photon-baryon slip to second order in τ_c .

$$\begin{aligned} \dot{S}_b = & \left[\frac{\dot{\tau}_c}{\tau_c} - \mathcal{H} \frac{2}{1+R} \right] S_b + \frac{\tau_c}{1+R} \left[-\frac{\ddot{a}}{a} \theta_b - k^2 \mathcal{H} \left(\frac{1}{2} \delta_\gamma - \beta_1 F_{\gamma 2} \right) \right] & (\text{A.26}) \\ & + k^2 \left(c_s^2 \dot{\delta}_b - \frac{1}{4} \dot{\delta}_\gamma + \beta_1 \frac{\dot{F}_{\gamma 2}}{2} \right) - \left[\frac{2R(3\mathcal{H}^2 c_s^2 + (R+1)\dot{\mathcal{H}} - 3\mathcal{H}^2)}{(R+1)^3} \right] S_b \tau_c \\ & + \frac{\tau_c^2}{(1+R)^2} \left[\frac{\ddot{a}}{a} \mathcal{H} \frac{((2-3c_s^2)R-2)\theta_b}{(R+1)} + \frac{\mathcal{H}k^2(1-3c_s^2)\theta_b}{3(R+1)} \right. \\ & + \frac{\ddot{a}}{a} \frac{k^2 c_s^2 \delta_b}{(R+1)} + \frac{k^4(3c_s^2-1)c_s^2 \delta_b}{3(R+1)} + \frac{k^4 R(3c_s^2-1)\delta_\gamma}{12(R+1)} + \frac{\ddot{a}}{a} \frac{k^2(2+3R)\delta_\gamma}{4(R+1)} \\ & + \frac{\mathcal{H}^2 k^2 ((2-3c_s^2)R-1)\delta_\gamma}{2(R+1)} + \frac{\mathcal{H}k^2 c_s^2 (1+(3c_s^2-2)R)\dot{\delta}_b}{R+1} \\ & + \frac{\mathcal{H}k^2 (2+(5-3c_s^2)R)\dot{\delta}_\gamma}{4(R+1)} + \frac{2\mathcal{H}(1-3c_s^2)k^3 \sigma}{3} + \frac{k^4(3c_s^2-1)\beta_1 \eta}{3} \\ & \left. + 2\mathcal{H}k^2(3c_s^2-1)\dot{\eta} + \frac{k^2(1-3c_s^2)\Delta}{6} \right] \\ & + \left[\frac{4\ddot{a}\theta_b - 4k^2 c_s^2 \dot{\delta}_b + 2\mathcal{H}k^2 \delta_\gamma + k^2 \dot{\delta}_\gamma}{2(R+1)^2} \right] \tau_c \dot{\tau}_c - \frac{4\mathcal{H}R}{(R+1)^2} \dot{\tau}_c S_b + \mathcal{O}(\tau_c^3) \end{aligned}$$

Here, $\Delta = 8\pi G a^2 (\rho_\gamma \delta_\gamma + \rho_\nu \delta_\nu + 3c_s^2 \rho_b \delta_b)$.

Appendix B

Atomic Dark-Matter Appendices

B.1 Relations between Dark Parameters

In this appendix, we relate the dark electron mass m_e , the dark proton mass m_p , and the atomic reduced mass μ_D to the DS parameters. These relations are obtained from the definition of the binding energy $B_D = (1/2)\alpha_D^2\mu_D$ and from the mass-balance equation $m_e + m_p - B_D = m_D$.

$$\mu_D = \frac{2B_D}{\alpha_D^2} \quad m_e = \frac{\mu_D m_p}{m_p - \mu_D} \quad (\text{B.1})$$

$$m_p = \frac{m_D + B_D + \sqrt{(m_D + B_D)^2 - 4(m_D + B_D)\mu_D}}{2} \quad (\text{B.2})$$

B.2 Effective Number of Relativistic Degrees of Freedom

The effective number of degrees of freedom contributing to the entropy density of the DS at a temperature T_D is [254]

$$g_{*S,D}(T_D) = 2 + \frac{45}{\pi^4} \left[\int_{y_e}^{\infty} \frac{(u^2 - y_e^2)^{\frac{1}{2}}}{e^u + 1} du + \frac{1}{3} \int_{y_e}^{\infty} \frac{(u^2 - y_e^2)^{\frac{3}{2}}}{e^u + 1} du \right], \quad (\text{B.3})$$

where $y_e \equiv \frac{m_e}{T_D}$ and the first term corresponds to the dark-photon contribution while the term in square brackets denote the dark-electron contribution.

Performing the integrals, we obtain, to a very good approximation,

$$g_{*S,D}(T_D) \simeq 2 + \frac{7}{2}(1 + y_e^{1.394})^{0.247} e^{-0.277y_e^{1.384}}. \quad (\text{B.4})$$

B.3 Thermal Rates

In this appendix, we compute the rates governing the energy exchange between the DM and the DR.

B.3.1 Photo-Ionization Heating Rate

The photo-ionization heating rate is given by [102]:

$$\Pi_{\text{p-i}} = \sum_{n,l} n_{nl} B_D \int_0^\infty \frac{\kappa^2 \gamma_{nl}(\kappa)}{e^{B_D(\kappa^2+n^{-2})/T_D} - 1} d(\kappa^2), \quad (\text{B.5})$$

where the sum runs over all atomic states specified by the quantum numbers $n \geq 2$ and $l \leq n - 1$, n_{nl} represents the number density of dark atoms in state nl and $\gamma_{nl}(\kappa)$ is defined in Eq. (4.16). We do not include bound-free transitions to and from the ground state since recombination directly to the $1s$ state results in the emission of an energetic photon that is immediately reabsorbed by a nearby neutral atom, hence resulting in no net cooling or heating. We assume that the occupations numbers of excited states are in Boltzmann equilibrium with the $2s$ state

$$n_{nl} = n_{2s} \frac{g_{nl}}{g_{2s}} e^{-B_D(1/4-n^{-2})/T_D}, \quad (\text{B.6})$$

where g_{nl} is the degeneracy of the energy level with quantum numbers nl . This approximation is valid as long as $\mathcal{B}_D(T_D) \gtrsim H$. Performing the momentum integration in Eq. (B.5) and computing the sum over atomic states up to $n_{\text{max}} = 250$ yield a photo-ionization heating rate of the form

$$\Pi_{\text{p-i}}(T_D) = \frac{\alpha_D^3 T_D^2}{3\pi} x_{2s} n_D e^{-\frac{B_D}{4T_D}} F_{\text{p-i}}(T_D/B_D), \quad (\text{B.7})$$

B.3. Thermal Rates

$F_{p-i}(y)$ is a dimensionless universal function encoding the remaining of the temperature dependence of the photo-ionization heating rate. It is shown in Fig. B.1. This function is well-fitted by

$$F_{p-i}(y) = \frac{3973.6 y^{-0.0222}}{(2.012 + y^{0.2412})^{6.55}}, \quad (\text{B.8})$$

for $4 \times 10^{-4} \lesssim y \lesssim 10^2$.

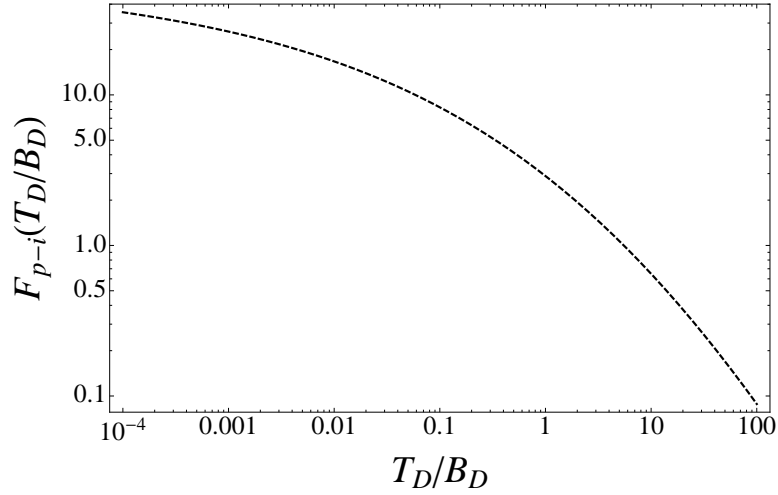


Figure B.1: Universal dimensionless fitting functions F_{p-i} for the photo-ionization heating rate, plotted as a function of T_D/B_D .

B.3.2 Photo-Recombination Cooling Rate

The rate of photo-recombination cooling is given by [102]

$$\begin{aligned} \Pi_{p-r} &= \sum_{n,l} x_D^2 n_D^2 \frac{(2\pi)^{3/2} B_D}{(\mu_D T_{DM})^{3/2}} \int_0^\infty e^{-B_D \kappa^2 / T_{DM}} \kappa^2 \gamma_{nl}(\kappa) \\ &\quad \times [1 + f_{BB}(B_D(\kappa^2 + n^{-2}), T_D)] d(\kappa^2). \end{aligned} \quad (\text{B.9})$$

As before, we do not consider recombination directly to the ground state. Computing the momentum integral and summing over all atomic states up

B.3. Thermal Rates

to $n_{\max} = 250$ yield a photo-recombination cooling rate of the form

$$\Pi_{\text{p-r}} = \frac{2\alpha_D^3 \sqrt{2\pi T_{\text{DM}}}}{3\mu_D^{3/2}} x_D^2 n_D^2 F_{\text{p-r}}\left(\frac{T_D}{B_D}, \frac{T_{\text{DM}}}{T_D}\right), \quad (\text{B.10})$$

where $F_{\text{p-r}}$ is a dimensionless universal function. We illustrate its behaviour in Fig. B.2.

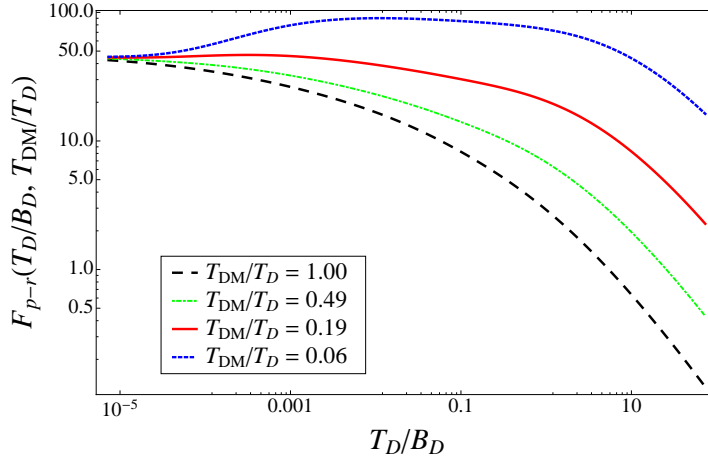


Figure B.2: Universal dimensionless fitting function $F_{\text{p-r}}$ for the photo-recombination cooling rate, plotted as a function of T_D/B_D for 4 different constant values of T_{DM}/T_D .

B.3.3 Free-Free Cooling and Heating

The free-free emission (absorption) process refers to the emission (absorption) of a dark photon by a dark electron due to its acceleration in the Coulomb field created by a dark proton. For atomic DM, we are mostly interested in the emission and absorption of dark radiation by thermal dark electron obeying a Maxwell-Boltzmann velocity distribution. The rate for thermal Bremsstrahlung cooling is [255, 256]

$$\Pi_{\text{ff-c}} = \frac{16\alpha_D^3 \bar{g}_{\text{ff}} \sqrt{2\pi T_{\text{DM}}} x_D^2 n_D^2}{(3\mu_D)^{3/2}}, \quad (\text{B.11})$$

B.3. Thermal Rates

where \bar{g}_{ff} is the free-free velocity-averaged and frequency-averaged Gaunt factor, which is of order unity. The inverse process of thermal free-free absorption is characterized by the following absorption coefficient [256]

$$a_{\nu}^{\text{ff}}(T_{\text{DM}}) = \frac{2\alpha_D^3 n_D^2 x_D^2 (1 - e^{-2\pi\nu/T_{\text{DM}}}) g_{\nu}^{\text{ff}}}{(3\mu_D)^{3/2} \sqrt{2\pi T_{\text{DM}}} \nu^3}, \quad (\text{B.12})$$

where g_{ν}^{ff} is the velocity-averaged free-free Gaunt factor and ν is the frequency of the incoming dark photons. The total amount of energy absorbed through free-free interactions per unit volume per unit time is then

$$\begin{aligned} \Pi_{\text{ff-h}} &= 4\pi \int_0^{\infty} a_{\nu}^{\text{ff}}(T_{\text{DM}}) B_{\nu}(T_D) d\nu \\ &\simeq \frac{2^5 \pi \sqrt{2\pi} \alpha_D^3 \bar{g}_{\text{ff}} x_D^2 n_D^2}{(3\mu_D)^{3/2} \sqrt{T_{\text{DM}}}} \int_0^{\infty} e^{-2\pi\nu/T_{\text{DM}}} \frac{e^{2\pi\nu/T_{\text{DM}}} - 1}{e^{2\pi\nu/T_D} - 1} d\nu, \end{aligned} \quad (\text{B.13})$$

where $B_{\nu}(T_D)$ is the Planck function. To evaluate this integral, we first note that the integrand only depends on T_{DM} itself and on the fractional temperature difference between the DM and DR, $\epsilon \equiv (T_D - T_{\text{DM}})/T_D$

$$e^{-2\pi\nu/T_{\text{DM}}} \frac{e^{2\pi\nu/T_{\text{DM}}} - 1}{e^{2\pi\nu/T_D} - 1} = \frac{e^{-2\pi\nu/T_{\text{DM}}} - e^{-4\pi\nu/T_{\text{DM}}}}{e^{-2\pi\nu\epsilon/T_{\text{DM}}} - e^{-2\pi\nu/T_{\text{DM}}}}. \quad (\text{B.14})$$

In the limit of quasi thermal equilibrium, $\epsilon \ll 1$, we can expand the integrand as a power series in ϵ and compute the frequency integral order-by-order in the fractional temperature difference. This leads to

$$\begin{aligned} \int_0^{\infty} e^{-2\pi\nu/T_{\text{DM}}} \frac{e^{2\pi\nu/T_{\text{DM}}} - 1}{e^{2\pi\nu/T_D} - 1} d\nu &\approx \\ &\frac{T_{\text{DM}}}{12\pi} (6 + \pi^2 \epsilon (1 + 2\epsilon) - 6\epsilon^2 \zeta(3) + \mathcal{O}(\epsilon^3)), \end{aligned} \quad (\text{B.15})$$

where $\zeta(x)$ is the Riemann zeta function. The net rate at which DM gains energy due to free-free interactions, $\Pi_{\text{ff}} \equiv \Pi_{\text{ff-h}} - \Pi_{\text{ff-c}}$, is the given by

$$\Pi_{\text{ff}} \simeq \frac{16\alpha_D^3 \bar{g}_{\text{ff}} \sqrt{2\pi T_{\text{DM}}} x_D^2 n_D^2}{(3\mu_D)^{3/2}} \left(\frac{\pi^2 \epsilon (1 + 2\epsilon) - 6\zeta(3) \epsilon^2}{6} \right). \quad (\text{B.16})$$

For numerical computation, we take $\bar{g}_{\text{ff}} \simeq 1.3$.

B.3.4 Rayleigh Heating

After the onset of recombination, dark photons can transfer energy to the DM sector via Rayleigh scattering off neutral dark atoms. The scattering cross-section for this process is given by [257]

$$\sigma_{\text{R}}(\nu) \approx \sigma_{\text{T},D} \frac{81}{64} \left(\frac{\nu}{\nu_{\text{Ly}\alpha}} \right)^4, \quad (\text{B.17})$$

where $\sigma_{\text{T},D} \equiv 8\pi\alpha_D^2/(3m_{\text{e}}^2)$ is the dark Thomson cross-section and $\nu_{\text{Ly}\alpha}$ is the frequency of dark Lyman- α photons. This expression is valid for $\nu \ll \nu_{\text{Ly}\alpha}$, which is realized for the large majority of dark photons after the onset of dark recombination. The net rate of energy transfer between dark photons and DM due to Rayleigh scattering is

$$\Pi_{\text{R}} = 2n_D(1 - x_D) \int \sigma_{\text{R}}(\nu) B_{\nu}(T_D) \Delta E_{\text{R}} \frac{d\nu}{\nu}, \quad (\text{B.18})$$

where $B_{\nu}(T_D)$ is the Planck function and ΔE_{R} is the average net energy gained by a dark atoms in a Rayleigh scattering event. It is given by

$$\Delta E_{\text{R}} = \frac{2\pi\nu}{m_D} (2\pi\nu - wT_{\text{DM}}), \quad (\text{B.19})$$

where $w = 75600\zeta(9)/\pi^8$ is a constant that can be determined using detailed balance. Substituting Eq. (B.19) into Eq. (B.18) and performing the integral over frequency yields the effective heating rate

$$\Pi_{\text{R}} \simeq \frac{430080\zeta(9)\alpha_D^2 n_D (1 - x_D) T_D^8 (T_D - T_{\text{DM}})}{\pi^2 B_D^4 m_D m_{\text{e}}^2}, \quad (\text{B.20})$$

where $\zeta(y)$ stands for the Riemann Zeta function. This expression is valid for $T_D \ll B_D$ which is always realized when a large population of neutral dark atoms is present.

B.4 Atomic Cross-Sections

In this appendix, we justify the form of the cross sections used to describe collisions of DM particles.

B.4.1 H-H Cross-Section

We consider the elastic scattering of two identical hydrogen-like atoms. This problem requires one to solve for the joint wavefunction of the two atoms interacting via the singlet gerade and triplet ungerade molecular potentials [225, 258]. The elastic differential cross section for indistinguishable hydrogen-like atom is given by

$$\frac{d\sigma_{\text{el}}^{\text{H-H}}}{d\Omega} = \frac{1}{4} \frac{d\sigma_{\text{s}}^{\text{H-H}}}{d\Omega} + \frac{3}{4} \frac{d\sigma_{\text{t}}^{\text{H-H}}}{d\Omega}, \quad (\text{B.21})$$

where the subscripts “s” and “t” refer to the singlet and triplet states, respectively. The singlet and triplet contributions take the form [225]

$$\frac{d\sigma_{\text{s,t}}^{\text{H-H}}}{d\Omega} = \frac{1}{4} |f_{\text{s,t}}(\theta) \pm f_{\text{s,t}}(\pi - \theta)|^2 + \frac{3}{4} |f_{\text{s,t}}(\theta) \mp f_{\text{s,t}}(\pi - \theta)|^2, \quad (\text{B.22})$$

where the uppermost sign is for the singlet and the lower sign for the triplet. Here, $f_{\text{s,t}}(\theta)$ is the scattering amplitude for the centre-of-mass (CM) scattering angle θ and is given by

$$f_{\text{s,t}}(\theta) = \frac{1}{2ik} \sum_{l=0}^{\infty} (2l+1)(e^{2i\delta_l^{\text{s,t}}} - 1)P_l(\cos\theta), \quad (\text{B.23})$$

where k is the wavenumber in the CM frame, l is the orbital angular momentum, $P_l(\cos\theta)$ is the l^{th} Legendre polynomial, and $\delta_l^{\text{s,t}}$ is the scattering phase shift from either the singlet or the triplet molecular potential. From Eqs. (B.22) and (B.23), one can obtain the important result

$$\begin{aligned} \sigma_{\text{mt}}^{\text{H-H}} &\equiv \int d\Omega \frac{d\sigma_{\text{el}}^{\text{H-H}}}{d\Omega} (1 - \cos\theta) \\ &= \sigma_{\text{el}}^{\text{H-H}}, \end{aligned} \quad (\text{B.24})$$

B.4. Atomic Cross-Sections

where $\sigma_{\text{mt}}^{\mathbf{H}-\mathbf{H}}$ and $\sigma_{\text{el}}^{\mathbf{H}-\mathbf{H}}$ are the momentum-transfer and the total elastic cross-section, respectively. This result can easily be proven using the orthogonality of the Legendre polynomial and follows from the symmetry of scattering two identical atoms.

All the information about the atomic physics is encoded in the phase shifts $\delta_l^{\text{s,t}}$. These can be found by solving the Schrödinger equation

$$\left[\frac{d^2}{dR^2} - \frac{l(l+1)}{R^2} + 2\mu[E - V^{\text{s,t}}(R)] \right] Ru_l^{\text{s,t}}(R) = 0, \quad (\text{B.25})$$

such that the asymptotic behavior at large R is

$$u_l^{\text{s,t}}(R) \simeq R^{-1} \sin(kR - l\pi/2 + \delta_l^{\text{s,t}}). \quad (\text{B.26})$$

Here, μ is the reduced mass of the colliding atoms, $V^{\text{s,t}}(R)$ is the interatomic potential in the singlet or triplet state, E is the relative energy of the collision and $k = \sqrt{2\mu E}$. In the semi-classical limit, the phase shift can be written as [225, 259]

$$\begin{aligned} \delta_l^{\text{s,t}} \approx & \int_{R_0}^{\infty} \left(k^2 - 2\mu V^{\text{s,t}}(R) - \frac{l(l+1)}{R^2} \right)^{\frac{1}{2}} dR \\ & - \int_{R'_0}^{\infty} \left(k^2 - \frac{l(l+1)}{R^2} \right)^{\frac{1}{2}} dR, \end{aligned} \quad (\text{B.27})$$

where R_0 and R'_0 are the outermost zeros of the respective integrands.

Now focusing on the atomic DM scenario, we would like to understand how the phase shifts are affected when the dark parameters α_D , B_D and m_D are varied. These parameters enter the phase shifts through their contributions to the wave number k and to the molecular potentials $V^{\text{s,t}}(R)$. While it is out of the scope of this appendix to compute the molecular potentials of dark atoms, we can nonetheless extract general properties of these potentials by studying the case of standard molecular hydrogen. To gain insights into the scaling of the molecular potential with the dark parameters, let us

briefly consider the Lennard-Jones potential [260]

$$V(R) = \epsilon \left[\left(\frac{R_m}{R} \right)^{12} - 2 \left(\frac{R_m}{R} \right)^6 \right], \quad (\text{B.28})$$

where the first term accounts for the short-range repulsive force due to Pauli blocking while the second term describes the long-range behaviour of the interaction. Here, ϵ is a constant setting the depth of the potential well and R_m is the distance where the potential admits a minimum.

On purely dimensional ground, the typical energy scale of the molecular potential should be proportional to the atomic binding energy, that is, $\epsilon \propto B_D$. Also, the typical atomic separation R_m should be of the order of the dark atomic Bohr radius, $R_m \propto a_{0,D} = 2\alpha_D/B_D$. We can thus write

$$V_D(R/a_{0,D}) \sim \frac{B_D}{B_H} V_H(R/a_0), \quad (\text{B.29})$$

where the ‘‘H’’ subscript stands for the standard atomic hydrogen. Defining the dimensionless distance $r \equiv R/a_{0,D}$, we can write Eq. (B.27) as

$$\begin{aligned} \delta_{l,D} &\approx \int_{r_0}^{\infty} \left(\frac{\alpha_D^2 m_D}{B_D^2} [E - V_D(r)] - \frac{l(l+1)}{r^2} \right)^{\frac{1}{2}} dr \\ &\quad - \int_{r'_0}^{\infty} \left(\frac{\alpha_D^2 m_D}{B_D^2} E - \frac{l(l+1)}{r^2} \right)^{\frac{1}{2}} dr, \end{aligned} \quad (\text{B.30})$$

where we have substituted the two-atom reduced mass $\mu = m_D/2$. We therefore observe that the phase shifts only depend on two dimensionless combinations of the dark parameters

$$\begin{aligned} \delta_{l,D} &= \delta_{l,D} \left(\frac{\alpha_D^2 m_D E}{B_D^2}, \frac{\alpha_D^2 m_D V_D}{B_D^2} \right) \\ &\simeq \delta_{l,D} \left(\frac{\alpha_D^2 m_D E}{B_D^2}, \frac{\alpha_D^2 m_D V_H}{B_D B_H} \right), \end{aligned} \quad (\text{B.31})$$

where we used Eq. (B.29) in the last line. Since V_H/B_H is known, one could then use Eq. (B.30) to obtain the phase shifts for dark atoms. However,

B.4. Atomic Cross-Sections

Eq. (B.31) suggests that one could obtain approximate $\delta_{l,D}$ directly from the baryonic hydrogen phase shifts by rescaling the collision energy as

$$E \rightarrow \left(\frac{\alpha_D}{\alpha_{\text{em}}} \right)^2 \frac{m_D}{m_H} \left(\frac{B_H}{B_D} \right)^2 E, \quad (\text{B.32})$$

where α_{em} is the fine-structure constant of standard electromagnetism. Of course, this is only an approximation since the molecular potential would also have to be rescaled according to Eq. (B.31). Moreover, the molecular potential itself depends non-trivially on α_D and μ_D and would have to be modified accordingly. Nevertheless, studies of deuterium, tritium [261] and positronium [262] self-scattering support the above approximate rescaling. We therefore take our atom-atom momentum-transfer cross section to be

$$\sigma_{\text{mt}}^{\text{H-H}}[E] \approx \left(\frac{a_{0,D}}{a_0} \right)^2 \sigma_{\text{mt}}^{\text{H-H}} \left[\left(\frac{\alpha_D}{\alpha_{\text{em}}} \right)^2 \frac{m_D}{m_H} \left(\frac{B_H}{B_D} \right)^2 E \right], \quad (\text{B.33})$$

where the leading factor accounts for the change in the geometric cross section. A numerical fit to the calculations found in Refs. [225, 261] leads to

$$\sigma_{\text{mt}}^{\text{H-H}}(E_{\text{CM}}) \approx 10^2 \pi a_0^2 \left(\frac{E_{\text{CM}}}{B_H} \right)^{-\frac{1}{8}} e^{-\frac{E_{\text{CM}}}{75B_H}}, \quad (\text{B.34})$$

which is valid for $10^{-3} \lesssim E_{\text{CM}}/B_H \lesssim 10$. At high energy, inelastic collisions begin to dominate over the elastic channel and this explain the much steeper energy dependence in that regime. Using Eq. (B.33), we can finally obtain an approximate momentum-transfer cross section for the neutral dark atoms

$$\sigma_{\text{mt}}^{\text{H-H}}(E) \approx \frac{25\pi\alpha_D^2}{B_D^2} \left[\frac{\mu_H}{\mu_D} \frac{m_D}{m_H} \frac{E}{B_D} \right]^{-\frac{1}{8}} e^{-\frac{\mu_H}{\mu_D} \frac{m_D}{m_H} \frac{E}{75B_D}}, \quad (\text{B.35})$$

where we have use the definition of binding energy to simplify the energy rescaling. Here, μ_H is the reduced mass of the regular proton-electron system. In terms of the relative velocity between the two dark atoms, the cross

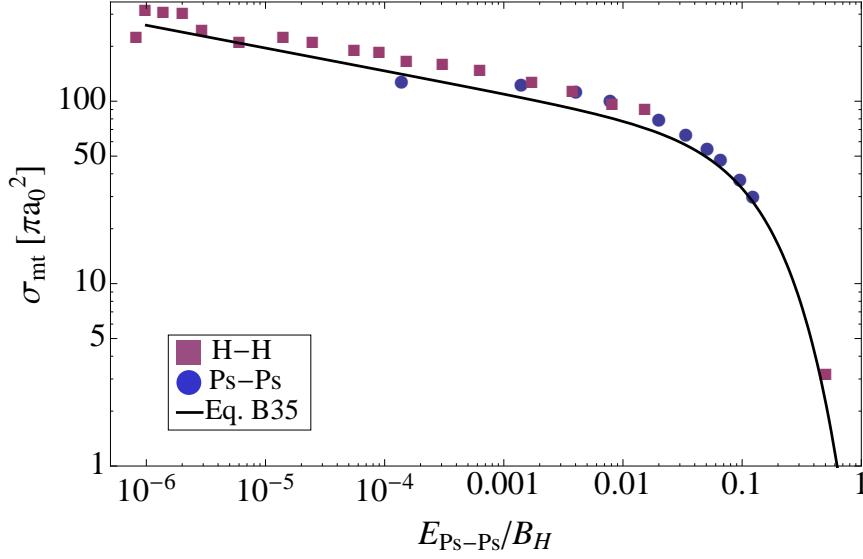


Figure B.3: Momentum-transfer cross-section for hydrogen [261] (purple squares) and positronium (Ps) [262] (blue disks) self-scattering. We have rescaled the energy dependence of the H-H cross-section according to Eq. (B.32) to compare it to the positronium cross-section. We also display the momentum-transfer cross-section we use for dark-atom scattering (Eq. (B.35)).

section reads

$$\sigma_{\text{mt}}^{\text{H-H}}(v) \approx \frac{30\pi\alpha_D^2}{B_D^2 v^{1/4}} \left[\frac{\mu_{\text{H}} m_D}{\mu_D B_D} \right]^{-\frac{1}{8}} e^{-\frac{\mu_{\text{H}} m_D}{\mu_D B_D} \frac{v^2}{300}}, \quad (\text{B.36})$$

where we used $E = m_{\text{H}}v^2/4$. In the limit where $m_{\text{e}} = m_{\text{p}}$, Eq. (B.36) agrees within a factor of order unity with the positronium (Ps) self-scattering cross section [262] (see Fig. B.3). At very low velocities ($v \lesssim 10^{-4}$), the above expression likely overestimates the momentum-transfer cross section. However, since very little energy is transferred in these low velocity collisions, we do not expect this to have a large impact on our results.

B.4.2 H-p and H-e Cross-Sections

When a dark proton collides with a neutral dark atom such that no atomic transitions are excited, two distinct processes must be taken into account. The dark proton can either collide elastically on the dark atom or it can capture the dark electron in a symmetric charge transfer. Similarly, when a dark electron encounters a neutral atom at low energy, it can either scatter elastically or eject the atomic dark electron and be captured by the atomic nucleus. Since the final products of these two types of processes are indistinguishable, they both need to be taken into account to accurately calculate the differential elastic cross section [225]

$$\frac{d\sigma_{\text{el}}^{\text{H-p,e}}}{d\Omega} = \frac{3}{4}|f_{\text{d}}(\theta) - f_{\text{ex}}(\pi - \theta)|^2 + \frac{1}{4}|f_{\text{d}}(\theta) + f_{\text{ex}}(\pi - \theta)|^2, \quad (\text{B.37})$$

where $f_{\text{d}}(\theta)$ is the amplitude for the direct elastic scattering while $f_{\text{ex}}(\theta)$ is the amplitude for the charge-exchange process. Quantum interference between these two types of elastic scattering generally implies that $\sigma_{\text{mt}}^{\text{H-p,e}} \neq \sigma_{\text{el}}^{\text{H-p,e}}$, in contrast to the symmetric atom-atom case.

Much of the above discussion for the atom-atom case applies here and we can relate the dark proton-atom and electron-atom momentum-transfer cross-section to that of standard proton-hydrogen and electron-hydrogen scattering as

$$\sigma_{\text{mt}}^{\text{H-p,e}}[E] \approx \left(\frac{a_{0,D}}{a_0}\right)^2 \sigma_{\text{mt}}^{\text{H-p,e}} \left[\left(\frac{\alpha_D}{\alpha_{\text{em}}}\right)^2 \frac{\mu_{D\text{p,e}}}{\mu_{\text{Hp,e}}} \left(\frac{B_{\text{H}}}{B_D}\right)^2 E \right], \quad (\text{B.38})$$

where $\mu_{D\text{p,e}} = m_D m_{\text{p,e}} / (m_D + m_{\text{p,e}})$ and similarly for $\mu_{\text{Hp,e}}$. From the results presented in Ref. [225], we can obtain an approximate expression for the proton-hydrogen momentum-transfer cross-section (obtained through a numerical fit)

$$\sigma_{\text{mt}}^{\text{H-p}}(E_{\text{CM}}) \approx 240 \pi a_0^2 \left(\frac{E_{\text{CM}}}{B_{\text{H}}}\right)^{-\frac{1}{8}} e^{-\frac{E_{\text{CM}}}{100 B_{\text{H}}}}, \quad (\text{B.39})$$

again valid for $10^{-3} \lesssim E_{\text{CM}}/B_{\text{H}} \lesssim 10$. In the case of electron-hydrogen

B.4. Atomic Cross-Sections

scattering, the momentum-transfer cross-section is smaller by almost two orders of magnitude

$$\sigma_{\text{mt}}^{\text{H-e}}(E_{\text{CM}} \ll B_{\text{H}}) \approx 7\pi a_0^2. \quad (\text{B.40})$$

The main reason for this large difference is that the electron-hydrogen differential cross-section is strongly peaked in the forward direction, which implies small momentum transfer. On the other hand, the proton-hydrogen differential cross-section has a significant backward peak which contributes substantially to the overall momentum-transfer cross-section. Phenomenologically, we can take this into account by rescaling the cross sections by the ratio of the masses of the two colliding bodies, that is

$$\sigma_{\text{mt}}^{\text{H-e}}(E) \approx \sqrt{\frac{m_{\text{e}}}{m_{\text{H}}}} \sigma_{\text{mt}}^{\text{H-p}}\left(\frac{m_{\text{p}}}{2m_{\text{e}}}E\right), \quad (\text{B.41})$$

where we have used Eq. (B.32) to appropriately rescale the collision energy. To obtain insight on the case $m_{\text{e}} \sim m_{\text{p}}$, we also consider the case of an electron elastically scattering off positronium [263]. In this case, we expect the low-energy cross-section to be somewhat suppressed since the first Born approximation for the scattering amplitude exactly vanishes. Existing computations support this fact and predict a roughly constant cross-section at low energy. With this in mind, we conservatively neglect the small energy dependence of the H-p cross-section at low energy and write

$$\sigma_{\text{mt}}^{\text{H-p}}(E) \approx \frac{60\pi\alpha_D^2}{B_D^2} \sqrt{\frac{m_{\text{p}}}{m_D}} e^{-\frac{\mu_{\text{H}}}{\mu_D} \frac{\mu_{D\text{p}}}{\mu_{\text{Hp}}} \frac{E}{100B_D}}, \quad (\text{B.42})$$

$$\sigma_{\text{mt}}^{\text{H-e}}(E) \approx \frac{60\pi\alpha_D^2}{B_D^2} \sqrt{\frac{m_{\text{e}}}{m_D}} e^{-8\frac{\mu_{\text{H}}}{\mu_D} \frac{\mu_{D\text{e}}}{\mu_{\text{He}}} \frac{E}{100B_D}}, \quad (\text{B.43})$$

or in terms of the relative velocity between the ions and the dark atom

$$\sigma_{\text{mt}}^{\text{H-p}}(v) \approx \frac{60\pi\alpha_D^2}{B_D^2} \sqrt{\frac{m_{\text{p}}}{m_D}} e^{-\frac{\mu_{\text{H}}}{\mu_D} \frac{\mu_{D\text{p}}}{B_D} \frac{v^2}{200}}, \quad (\text{B.44})$$

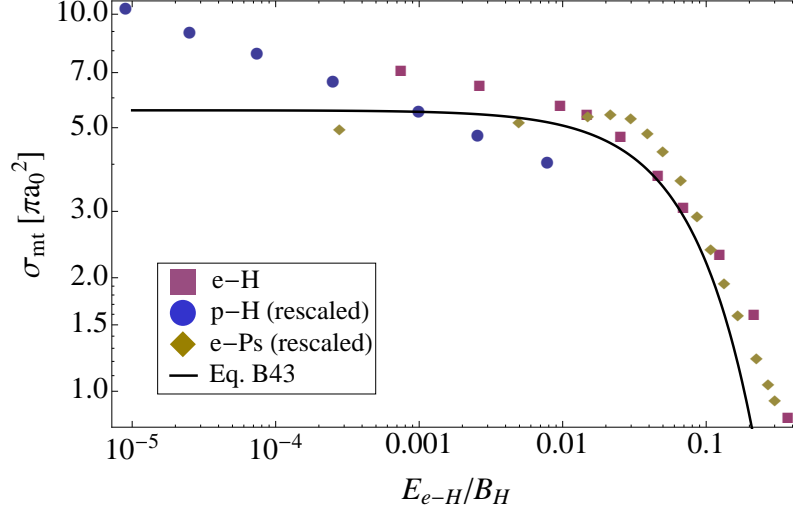


Figure B.4: Momentum-transfer cross-section for electron-hydrogen scattering obtained from direct computation [264, 265] (purple squares), from rescaling the proton-hydrogen cross-section [261] (blue disks), and from rescaling the electron-positronium cross-section [263] (yellow diamonds). We also display the momentum-transfer cross section we use for dark electron-atom scattering (Eq. (B.43)).

$$\sigma_{\text{mt}}^{\text{H-e}}(v) \approx \frac{60\pi\alpha_D^2}{B_D^2} \sqrt{\frac{m_e}{m_D}} e^{-\frac{\mu_H}{\mu_D} \frac{\mu_{De}}{B_D} \frac{v^2}{200}}, \quad (\text{B.45})$$

where we have used $E = \mu_{\text{He,p}} v^2/2$. In Fig. B.4, we display the H-e momentum-transfer cross-section, both from direct computation and from rescaling the p-H and electron-positronium cross-sections according to Eq. (B.41). We see that this rescaling is accurate up to a factor of order unity over the energy range of interest and thus provide the correct order of magnitude for the cross section. We also display in the figure our approximate expression for the dark electron-atom cross-section Eq. (B.43).